# Contract Work Performed Under the Auspices of The United States Department of Energy

Final Technical Report for Award Number #DE-NE0008312 Project Period: Oct. 1, 2014 – Sept. 30, 2017 Reporting Period: Oct. 1, 2014 – Sept. 30, 2017

# MULTI-PHASE MODEL DEVELOPMENT TO ASSESS RCIC SYSTEM CAPABILITIES UNDER SEVERE ACCIDENT CONDITIONS

## Recipient:

Texas A&M Engineering Experiment Station 400 Harvey Mitchell Parkway, South Suite 300 College Station, TX 77845-43 75

Project Director/Principal Investigator:
Karen Vierow Kirkland (PI)
Department of Nuclear Engineering
Texas A&M University
MS 3133
College Station, TX 77843-3133
vierow@tamu.edu
(979) 458-0600

Consortium/Teaming Members:
K. W. Ross (Sandia National Laboratories)
B. A. Beeny (Texas A&M University)
N. Luthman (Texas A&M University)
Z. Strater (Texas A&M University)

Submitted to the US DOE on December 23, 2017

#### **Executive Summary**

The Reactor Core Isolation Cooling (RCIC) System is a safety-related system that provides makeup water for core cooling of some Boiling Water Reactors (BWRs) with a Mark I containment. The RCIC System consists of a steam-driven Terry turbine that powers a centrifugal, multi-stage pump for providing water to the reactor pressure vessel.

The Fukushima Dai-ichi accidents demonstrated that the RCIC System can play an important role under accident conditions in removing core decay heat. The RCIC System is believed to have successfully removed decay heat for almost 70 hours in Unit 2 and 20 hours in Unit 3. These durations greatly exceeds the 4 to 8-hour operation that the RCIC System is given credit for in US BWRs. The unexpectedly sustained, good performance of the RCIC System in the Fukushima reactor demonstrates, firstly, that its capabilities are not well understood, and secondly, that the system has high potential for extended core cooling in accident scenarios. Better understanding and analysis tools would allow for more options to cope with a severe accident situation and to reduce the consequences.

The objectives of this project were to develop physics-based models of the RCIC System, incorporate them into a multi-phase code and validate the models. The project tackled the current major challenges in RCIC System analysis to enable evaluation of the following two-phase thermodynamic aspects of the system:

- Turbine performance following ingestion of two-phase flow
- Pump performance degradation
- Water carryover into the turbine

This Final Technical Report details the progress throughout the project duration and the accomplishments.

The technical approach to achieving the project goals was formulated into six technical tasks. Each of these tasks and associated accomplishments are summarized below.

#### Task 1: Critical evaluation of codes for RCIC System modeling

For system-level modeling, the leading severe accident codes in the US, MAAP and MELCOR, were found to not have any specialized components for RCIC System modeling. However both codes appear to have the capability for models to be incorporated via control functions or other code features. With respect to the RCIC turbine and RCIC pump, the multiphase phenomena expected to occur within the turbine's steam inlet nozzle, the Terry turbine and the pump are complicated and beyond the simulation capabilities of reactor safety codes. Computational Fluid Dynamics (CFD) codes are more appropriate for developing mechanistic models which can be simplified for incorporation into the systems-level codes. Gaps in the current modeling capabilities were identified and approaches were proposed for modeling within the context of CFD codes.

During the second year of the project, a Sandia National Laboratories report was published on system-level MELCOR models for the RCIC System and CFD analysis of the multiphase behavior inside the turbine wheel. This report was evaluated for relevance to the current project.

### Task 2: Code Selection

For CFD development of the Terry turbine and pump models, the STAR-CCM+ code was selected. The code has sufficient capabilities and user access to code models to enable completion of the turbomachinery model development. Further, the code's methods are similar to those of other

commercial codes, such as FLUENT or CFX. Thus any models developed in STAR-CCM+ are likely portable and adaptable to other codes.

During the first year of this project, the conclusion was reached that the CFD models could be simplified directly to the severe accident code level. Simplifying models to the thermal hydraulic code level, as described in the project proposal, and then further to the severe accident level would not bring any significant benefit to the project. Therefore, the decision was made to not develop models specifically for thermal hydraulic codes as originally planned.

MELCOR was chosen as the reference severe accident code for this project. The decision was based on past work to model the RCIC System within MELCOR, code availability and expertise of the investigators with the code.

#### Task 3: RCIC System Test Data Survey

Three types of validation data were found for the RCIC System turbine and pump models.

- First, several examples of CFD-to-experiment benchmarks for steam nozzle and steam turbine flow were identified. Test problems with the new turbine models were used to validate the models against these data as part of Task 6.
- Second, data for turbine model validation was acquired from the PI's experimental facility during the second and third year of this project. These experimental data were also used to validate the new CFD turbine models as part of Task 6.
- Third, very limited data from the Fukushima Dai-ichi accident are available for benchmarking RCIC System simulations. These data consist of boundary conditions such as Reactor Pressure Vessel water level, system pressures and times of RCIC System operation. These data were used to benchmark systems-level simulations as part of Task 6.

#### Task 4: Model Development and Implementation

Phenomenological models for RCIC System analysis were developed under this task. CFD models were developed first for the RCIC System turbine and pump, followed by models for systems-level severe accident codes.

For the CFD Terry turbine model development and implementation, several formulations were investigated in year 1 and, a quasi-two-fluid dispersed phase flow model was developed for implementation into STAR-CCM+. A condensing steam flow physics model was developed and successfully applied on a typical GS-1 Terry turbine pressure stage (steam nozzle) geometry with STAR-CCM+

Regarding the CFD RCIC pump modeling, after extensive searches for the pump geometry, proprietary RCIC pump diagrams were obtained that allowed for creation of a Solidworks model followed by a Computer Aided Design (CAD) model that is needed for CFD model development. A CFD model for a single-stage pump was created. This will serve as the starting point for generation of the more complicated multi-stage CFD model that can represent the RCIC pump.

On the system-level modeling with MELCOR, a homologous pump model was developed, coded and integrated into an up-to-date version of MELCOR, as was a systems-level steam nozzle (pressure stage) model based loosely on known analytical Wilson point solutions found in literature. Also, a turbo-shaft model (a torque inertia equation representing the shaft of a turbo-pump) was derived and implemented. To incorporate the pressure stage model into the existing MELCOR phasic velocity equation solution methodology, the time-independent flow path velocity function was co-opted by adding a special flag to the existing input structures. To couple the velocity stage model and the turbo-shaft torque-inertia equation with the semi-implicit

homologous pump model, some alterations were made to input structures and the format of the subroutine that handles pump calculations.

#### Task 5: Experimental Data Generation

The RCIC System facility in the Texas A&M University PI's laboratory was used to generate validation data for the models developed herein. The facility includes a steam generator, a suppression chamber, a very simple RCIC turbine analog, a RCIC pump and associated piping. Options were explored for installing a suitable RCIC turbine analog and for acquiring a smaller-scale ZS-1 Terry turbine for incorporation into the Texas A&M University RCIC System facility. The latter option proved to be feasible and more likely to generate data representative of RCIC System behavior.

In the first year of the project, a model ZS-1 Terry turbine was acquired. In the second year of the project, the turbine refurbishment was completed and the turbine was installed. It was set up in a once-through configuration, so that the exiting gases were not exhausted to the suppression pool. Instrumentation was upgraded to measure turbine performance, and the necessary structural modifications were applied to provide support to the turbine and its associated piping and equipment. The facility was equipped to inject compressed air or steam, along with a water component, into the inlet of the turbine. The turbine shaft work was measured by a water brake dynamometer.

Dry and wet mixes of air and of steam from 60 g/s to 0 g/s were injected into the turbine down to the lower limit of operability. Torque, shaft work, and isentropic efficiency were obtained for 1500, 2000, 2500, and 3000 shaft revolutions per minute.

## Task 6: Benchmarking against Fukushima data and test data

The limited data available from the Fukushima Dai-ichi accidents were reviewed and evaluated for utilization in the benchmarking effort. The MELCOR test problem used to examine the performance of the new Terry turbine systems-level models is a so-called "pseudo-Fukushima" calculation because it models a simplified 2000 MW<sub>th</sub> BWR system that employs boundary conditions (Suppression Chamber pressure) taken from known Fukushima Dai-ichi data points.

The new model predicts a turbine over-speed (turbine rotor speed exceeds the mechanical trip setpoint) in the seconds following loss of governor valve control. The calculation continued despite this occurrence. The predicted pressure curve matches the general trends of the recorded Fukushima Daiichi Unit 2 data, though the new models under-predict the data. This could indicate an over-estimation of RCIC system efficiency for the new models because RCIC system action keeps RPV pressure low relative to the data. There are several user inputs to examine for the new Terry turbine models before drawing more definite conclusions.

Development and validation of these RCIC System models is an important advancement with respect to both enhanced reactor safety and the state-of-the-art of severe accident modeling. Major outcomes of the project were:

- Increased knowledge of the RCIC System operational characteristics under accident conditions
- Technically-defensible models of the RCIC System

# **Table of Contents**

Ex	ecutive S	ummary	ii
Lis	st of Figu	res	vii
Lis	st of Tabl	es	X
Ac	ronyms .		xi
1.	Introduce 1.1 1.2 1.3	Description of the RCIC System Significance of RCIC System Multi-Phase Analysis Capabilities Project Goals and Objectives	1 8
2.	Technic 2.1 2.2	al Approach Overview of Technical Tasks Description of Existing Equipment in the NHTS Laboratory	10
3.	Task 1: 3.1 3.2 3.3	Critical Evaluation of Codes for RCIC System Modeling Summary of Current Code Capabilities Summary of Available Multi-phase Models for RCIC System Turbomachinery Identification of Gaps in Modeling Capabilities	14 15
4.	Task 2: 4.1 4.2 4.3	Code Selection CFD Thermal Hydraulic Code Severe Accident Code	19 19 20
5.	Task 3: 5.1 5.2	RCIC System Test Data Survey  Identification of Data Needed to Validate Models Developed Herein  Data Survey	22
6.	6.1 6.1.1 6.1.3 6.2 6.3 6.3.1 6.3.2 6.3.3 6.3.4 6.3.5	Model Development and Implementation Development of Computational Fluid Dynamics Code Models STAR-CCM+ Computational Fluid Dynamics Code Description Terry Turbine RCIC System Pump Development of Thermal-Hydraulics Code Models Development of Severe Accident Analysis Code Models MELCOR Severe Accident Code Description Homologous Pump Model Terry Turbine Velocity Stage Model Terry Turbine Pressure Stage Model Terry Turbine Shaft Model MELCOR Implementation and Aspects of Solution Methodology	24 33 65 77 78 78 82 100 104 118

7.	Task 5:	Experimental Data Generation	122
	7.1	Experimental Facility Description and Modifications	122
	7.2	Shakedown Testing and Facility Improvements	
	7.3	Test Description_	
	7.4	Air Test Results	
8.	Task 6:	Benchmarking against Fukushima data and test data	168
	8.1	Terry Turbine Model Comparison against Nuclear Heat Transfer	
		Labs Test Data	168
	8.2	Gyarmathy CFD Benchmark for Turbine Steam Nozzle (Pressure Model	e Stage)
	8.3	Pump Model Benchmarking	186
	8.4	Pseudo-Fukushima Reactor Core Isolation Cooling System Bench	hmark 199
9.	Compar	ison of Actual Accomplishments with the Project Goals and Objec	tives 203
10.	Conclus	ions	204
11.	Summar	ry of Project Activities	207
12.	Referen	ces	208
13.	Cost Sta	tus	213
14.	Schedul	e Status	214
15.	Changes	s during the Reporting Period in Project Approach	215
16.	Actual o	or Anticipated Problems or Delays	216
17.	Absence	e or Changes of Key Personnel	217
18.	Product	Produced or Technology Transfer Activities	218
19.	Proiect 1	Deliverables	219

# **List of Figures**

Figure 1	RCIC System Configuration for BWR/3/4 [GE, 2015]	3
Figure 2	Terry Turbine Drawing, Casing Lifted to Show Rotor and Milled Buckets	4
Figure 3	A typical Terry turbine helical steam flow path [Goudie, 1917]	5
Figure 4	Terry Turbine Cut-away [Leland, 1917]	5
Figure 5	Terry turbine coupled to a centrifugal pump [Leland, 1910]	6
Figure 6	Terry turbine nozzle geometry and dimensions (inches) [Ross et al., 2015]	
Figure 7	Pressure stage geometry used for CFD analyses [Ross et al., 2015]	
Figure 8	Terry turbine velocity stage geometry [Ross et al., 2015]	8
Figure 9	Simplified P&ID of Texas A&M RCIC System Facility [Solom 2016]	
Figure 10	NHTS Suppression Chamber Vessel Internal Thermocouple Layout	12
Figure 11	Geometry part tessellation (top) and surface triangulation (bottom)	29
Figure 12	Mixing plane illustration [CD-ADAPCO User's Guide, 2016]	31
Figure 13	Mixing plane, periodic interfaces, and moving reference frames	32
Figure 14	Condensation, evaporation, and net growth [McDonald, 1962b]	37
	Converging-Diverging nozzle flow at various back pressures	
	Qualitative h-s diagram for condensing steam flow in a nozzle	
Figure 17	Qualitative pressure plot for condensing steam flow	49
	Qualitative illustration of wetness and pressure along a steam nozzle	
Figure 19	IAPWS-IF97 regions, dependent/independent variables [IAPWS, 2007]	52
Figure 20	An axially split centrifugal multi-stage pump [Sulzer, 2014]	66
Figure 21	CAD model created for simulation of the RCIC pump	67
Figure 22	The rotation region that is set variable speeds in purple	68
Figure 23	Front view of CAD model with mesh apparent	69
Figure 24	Side view of the mesh opposite of outlet	69
Figure 25	The original mesh used through the duration of the simulation	75
Figure 26	The refined mesh used to verify the grid independence	76
Figure 27	MELCOR execution flow diagram [SNL, 2016a]	78
Figure 28	Semiscale single-phase head curve [Olson, 1974]	84
Figure 29	Polar homologous single-phase head curve, Semiscale	87
Figure 30	Universal correlation head function, each curve an x on $[0, \pi/2]$	89
	Universal correlation torque function, each curve an x value on $[0, \pi/2]$	_90
Figure 32	Control volume for angular momentum equation [Ross et al., 2015]	101
Figure 33	Qualitative h-s diagram, pressure/wetness plots for expansion	105
Figure 34	Simplified NHTS experimental facility diagram	123
Figure 35	Surplus turbines at Keene Turbomachinery Services	123
Figure 36	Turbine en route to be refurbished	124
	Turbine disassembly	
Figure 38	Trip Throttle Valve, with seized valve stem	126
Figure 39	Lower casing, with original nozzles and reversing chambers	126
	Lower casing, after sandblasting, with two nozzles removed	
Figure 41	"The Duchess"	128
Figure 42	Test platform, fabricated and painted	129
Figure 43	The Duchess, on platform, with instrumentation installed	

Figure 44	Shaft coupling	130
Figure 45	Turbine exhaust flange	131
Figure 46	Cartridge filter and resin tanks for deionization system	132
	Steam generator and blowdown drum	133
Figure 48	Feedwater storage tank and turbine	135
Figure 49		136
Figure 50	Data acquisition control station	138
Figure 51	LabVIEW graphical user interface	139
Figure 52		140
Figure 53	Air/steam injection control station	141
Figure 54	P&ID of steam generator with associated piping and components	142
	P&ID of feedwater storage tank with associated piping and components	143
_	P&ID of turbine with associated piping and components	
	Monarch ROLS-W Tachometer sensor	148
	Tachometer display	149
Figure 59	Dynamometer, with water supply tubing attached	150
Figure 60		151
Figure 61	Turbine, with dynamometer attached	152
	Turbine inlet pressure transmitter calibration certificate	155
_		156
	Tachometer calibration certificate	157
Figure 65		158
Figure 66	Representative air test data	162
Figure 67	Summary torque data point for 60 g/s dry air test	
	Summary power data point for 60 g/s dry air test	164
	High-flow air torque summary data	166
Figure 70	High-flow air power summary data	167
Figure 71	Full three-dimensional Terry turbine wedge	169
	Terry turbine wedge, rotor and reversing chamber	170
Figure 73	Cut-away view demonstrating mixing plane configuration	171
	Gyarmathy experimental nozzle 4B geometry [Gyarmathy, 2005]	173
Figure 75	Pressure [Pa] distribution along nozzle wall	176
Figure 76	Pressure [Pa] profile in nozzle	177
	Super-saturation [-] ratio in nozzle	
	Mach number [-] in nozzle	
	Velocity [m/s] vectors in nozzle	
Figure 80	Nucleation rate [drop/m³/s] in nozzle	181
	Condensation rate [m/s] in nozzle	
	Droplet two-zero (average) diameter [m] in nozzle	
Figure 83	Droplet number density [drop/m³] in nozzle	184
Figure 84	Droplet mass fraction [kg <sub>l</sub> /kg <sub>g</sub> ] in nozzle	185
Figure 85	Position of inlet (tan) and outlet (orange) pressure in pump model	187
	Outlet pressure from CFD pump simulation	
Figure 87	Inlet pressure from the same simulation seen in figure 86	188
Figure 88	The Wall-Y+ used to quantify the refinement of the mesh	189
	Pump model curve for performance as a function of rotational speed	

Figure 90	Pump curve for model with 90% water and 10% steam at variable speeds	191
Figure 91	Results from pump model simulations for with 80% water and 20% steam.	192
Figure 92	Pump curve for model with 70% water and 30% steam	193
Figure 93	All pump curves compared in a single figure	194
Figure 94	Pump normalized pressure increase for 90% water and 10% steam	195
Figure 95	Pump normalized pressure increase for 80% water and 20% steam	196
Figure 96	Pump normalized pressure increase for 70% water and 30% steam	197
Figure 97	Pump normalized pressure increase for all volume fractions simulated	198
Figure 98	Efficiency curve for pump model at normal operation and 30% water	199
Figure 99	Pseudo-Fukushima RCIC system model diagram	200
Figure 100	MELCOR test problem results comparison and benchmark to	
	Fukushima-2 data	201

# **List of Tables**

Table 1	RCIC Pump Test Simulation Conditions	70
Table 2	Grid Independence Study Results for RCIC Pump Simulations	76
Table 3	Possible Pump Operating Modes in MELCOR Simulations	83
Table 4	Octant Arrangement Under the Polar Homologous Representation	85
Table 5	Polynomial Fit Data for Curves in Figure 30	91
Table 6	Polynomial Fit Data for Curves in Figure 31	92
Table 7	NHTS RCIC Test Facility Instrumentation	145
Table 8	Calibration Profiles for NHTS RCIC Test Facility Instrumentation	153
Table 9	Load Cell Test Weights	153
Table 10	Target Control Variables in Terry Turbine Experiments	161
Table 11	NHTS Experimental Benchmark Conditions [Luthman, 2017]	171
Table 12	NHTS Experimental Torque/Power Comparison and Simulation Results	_172
Table 13	Gyarmathy Nozzle 4B Geometry Data (constant width 20 mm)	
	[Gyarmathy, 2005]	174
Table 14	Gyarmathy Experimental Benchmark, Nozzle 4B, Run 19A	175
Table 15	RCIC Pump Model Simulations for the Conditions of 100% Water	190
Table 16	RCIC Pump Model Simulations for 90% Water and 10% Steam	191
Table 17	RCIC Pump Model Simulations for 80% Water and 20% Steam	192
Table 18	RCIC Pump Model Simulations for 70% Water and 30% Steam	193
Table 19	Funding Expenditure Summary	213
Table 20	Project Milestones	214

## Acronyms

ANC Aerojet Nuclear Corporation

B&WBabcock & WilcoxBWRBoiling Water ReactorCADComputer Aided Design

CD Converging Diverging [nozzle]

CF Control Function (for the MELCOR code)

CFD Computational Fluid Dynamics
CST Condensate Storage Tank

CV Control Volume (for the MELCOR code)

DAQ Data Acquisition [System]

EPRI Electric Power Research Institute

EMP Eulerian multi-phase ESF Engineered Safety Feature

GPM Gallons Per Minute

HEM Homogeneous Equilibrium Model

LMP Lagrangian multi-phase LOCA Loss of Coolant Accident

Ma Mach [number]

MSIV Main Steam Isolation Valve

MSL Main Steam Line

NPSH Net Positive Suction Head

RCIC Reactor Core Isolation Cooling [System]

RPM Revolutions Per Minute RPV Reactor Pressure Vessel

SAMGs Severe Accident Management Guidelines

SRV Safety/Relief Valve
TTV Trip Throttle Valve
UPS Universal Power Supply
URV Upper Range Value

VI Virtual Instrument (for National Instruments LabView)

#### 1. Introduction

## 1.1 RCIC System Description

## 1.1.1 RCIC System Overview

The Reactor Core Isolation Cooling (RCIC) System is a safety-related system that provides makeup water for core cooling of some Boiling Water Reactors (BWRs) with a Mark I containment. As its name implies, the RCIC System is intended for isolation events, when the Main Steam Isolation Valves (MSIVs) are closed and the reactor is "isolated" from the turbines. The system may also be called to operate when the condensate and feedwater system is not available [GE, 2013]. It is functionally classified as a "safety related system" and is regarded for regulatory purposes as an Engineered Safety Feature (ESF) system [GE, 2013].

The RCIC System consists of a steam-driven turbine that powers a pump for providing water to the reactor pressure vessel (RPV). The turbine takes steam off of a main steam line and exhausts to the Suppression Pool. Initial pump suction alignment is from the Condensate Storage Tank (CST). Low CST level or operator action may realign pump suction to the Suppression Pool. Figure 1 shows the system configuration for a BWR/3/4 [figure 6.3-2 of GE, 2015].

The RCIC pump is a multi-stage centrifugal pump which is on the same shaft as the Terry turbine EPRI [2012]. The rated volumetric flow rate of the turbine-pump system is approximately equal to the reactor water boiloff rate 15 minutes after a reactor scram and isolation [GE, 2015]. The exact RCIC capacity varies with power level of a given BWR, but 400-800 gal/min of coolant delivery is typical. The RCIC system can operate across almost the entire range of possible system pressures from normal operating pressure (or 1135 psig) down to about 150 psig [GE, 2013]. The RCIC system is entirely independent of off-site AC power and needs no service air or cooling water.

The RCIC pump is initially aligned to take suction from the CST. It delivers coolant (from either the CST or the Suppression Pool) to a feed-water injection line and thereby to the RPV. The Terry turbine usually has both a mechanical over-speed trip and an electro-hydraulic control system with a governor to regulate steam flow. Note the governor may be manually operated (independent of the DC-powered flow controller).

RCIC system failure can result from:

- Some DC power supply issue causing the governor valve to fully open and leading abruptly to a turbine trip on over-speed
- High suppression pool temperature so that insufficient pump net positive suction head (NPSH) exists (unlikely if AC power allows suppression pool cooling by other systems)
- High containment pressure (and thus high turbine back-pressure)

With respect to RCIC System operational failure, the usual assumption is that, in the absence of AC power, operation ceases in the 4 to 12 hours required for on-site DC power to deplete. The failure mode in this case is a loss of governor control leading directly to an over-speed trip, perhaps after turbine ingestion of water due to pressure vessel over-fill and subsequent steam line flooding. This assumption discounts any and all ability of the Terry turbine to self-regulate (to maintain vessel inventory and pump NPSH requirements) without DC governor valve control.

#### 1.1.2 RCIC System Turbine

This project focuses on the RCIC System turbomachinery, in particular, the RCIC turbine and the RCIC pump. The RCIC turbine is a Terry solid-wheel turbine. The steam-driven turbine that

powers the RCIC system centrifugal pump is based on the early 20th century design of Edward Terry and the Terry Steam Turbine Company. Patents filed as early as 1903 detail a turbine that bears a strong resemblance to not only the GS-1 and GS-2 model turbines in BWR RCIC systems, but also to other smaller models (e.g. the Z-1) that find application in other industries. Terry turbines of all sizes could be classified as Pelton impulse type with multiple velocity stages [Moyer, 1917].

# Impulse-type turbines rely on:

- Conversion of steam enthalpy to kinetic energy via expansion in nozzles (expansion occurs in the so-called pressure stage of the turbine)
- Subsequent delivery of an impulse (force) to a turbine blade or bucket from high-velocity steam (occurs in the so-called velocity stage of the turbine)

The Terry turbine certainly conforms to this two-fold description. The single pressure stage consists of a series of converging/diverging nozzles that are circumferentially situated around the rotor. The nozzles are either all around the rotor or only around one half, depending on the specific Terry turbine model. Each nozzle receives steam that is first admitted through the up-stream turbine governor valve. Any given parcel of steam crosses a nozzle and expands only once, hence the single pressure stage. Note that an in-depth discussion of steam expansion and nozzle physics is deferred to a later section. Every nozzle discharges straight into one of the u-shaped buckets milled into the face of the solid rotor wheel.

Drawings of Terry turbine components are shown in Figure 2. Steam enters buckets and reverses direction (turning through 180°) before exiting at the opposite end. Paired with each nozzle is a series of reversing chambers (typically four per nozzle) affixed to the inside of the casing (visible in Figure 2). Reversing chambers constitute the velocity stages of the turbine because they return some portion of the steam flow to the rotor for secondary, tertiary, and quaternary impulse delivery. Each reversing chamber has a semi-circular or crescent-shaped hole in its top lateral surface that permits some expanded steam to vent. Otherwise, the flow passages would need to be progressively wider to accommodate the increased steam volume [Leland, 1917].

The typical steam flow path is shown in Figure 3. Note the nozzle plenum, the nozzle, and the rotor are shown with reversing chambers omitted. Note also the helical shape of the flow path which indicates the slightly slanted orientation of the reversing chambers with respect to the rotor buckets. Figure 4 cuts away the casing wall to show the nozzle, rotor, and four reversing chambers in their actual arrangement. In Figure 2, the large flanged pipe at the bottom of the turbine is the steam outlet. Steam exits from the casing here after it vents from a reversing chamber or traverses all four velocity stages. Steam travels through a turbine exhaust line to the suppression pool below the water level, thereby condensing the steam unless the pool is at or near saturation. The exhaust line is protected by vacuum breakers and a high turbine back-pressure trip capability.

To illustrate the turbo-pump concept, Figure 5 shows a Terry turbine (on the right) coupled to a centrifugal pump (on the left) via a torque shaft (spanning the space between). The RCIC system employs a similar turbo-pump concept to deliver make-up feed water to the RPV.

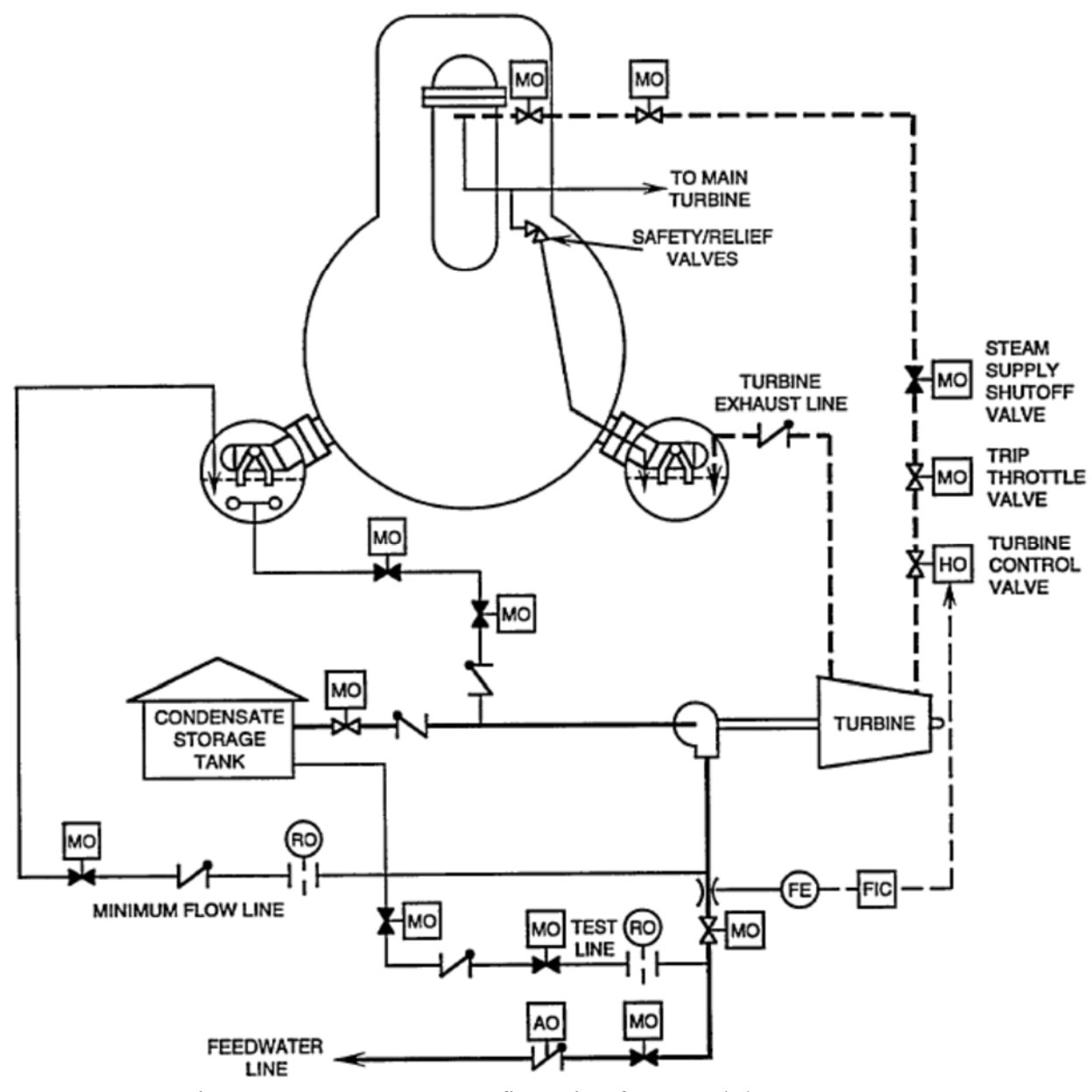


Figure 1 RCIC System Configuration for BWR/3/4 [GE, 2015]

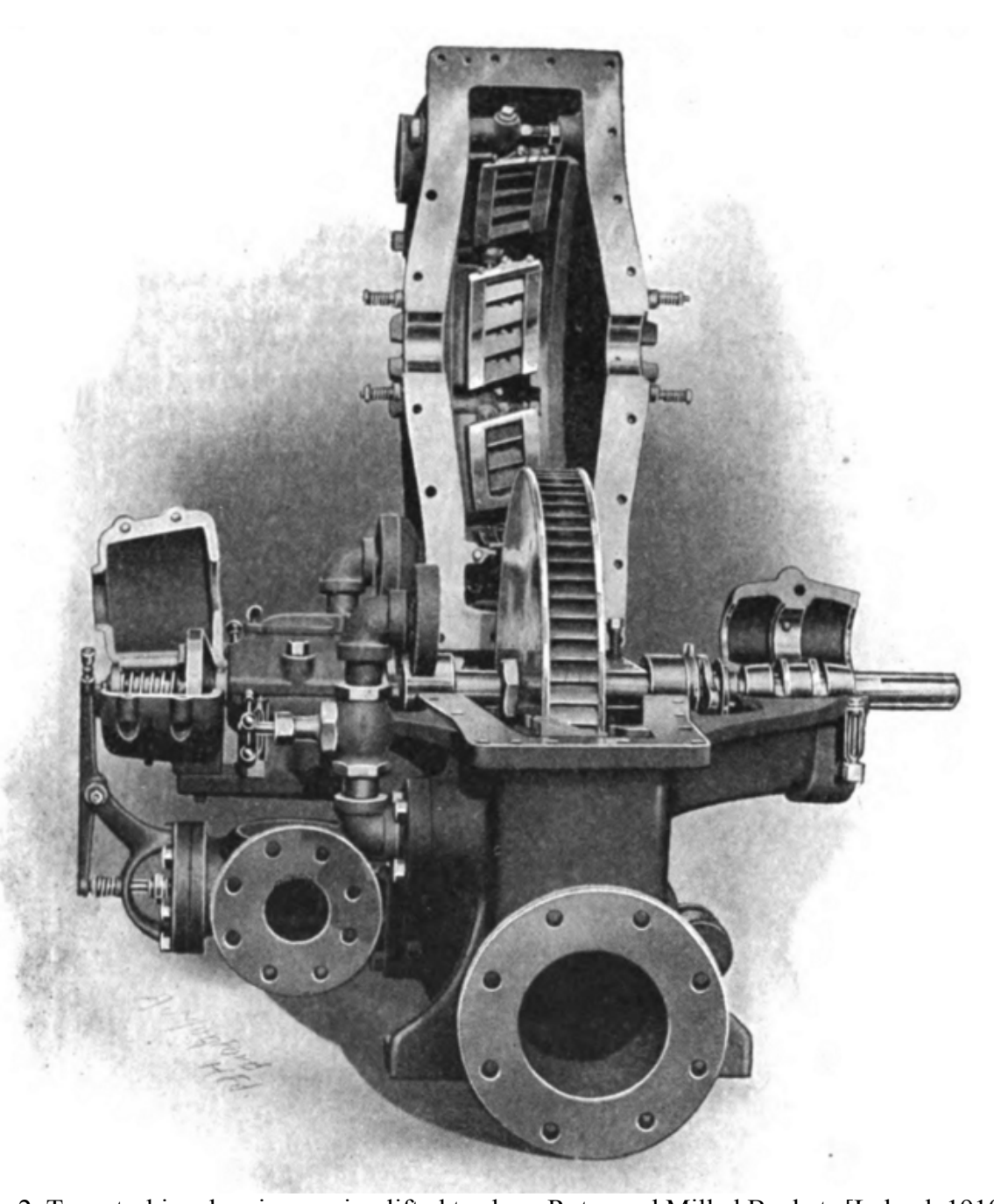


Figure 2 Terry turbine drawing, casing lifted to show Rotor and Milled Buckets [Leland, 1910]

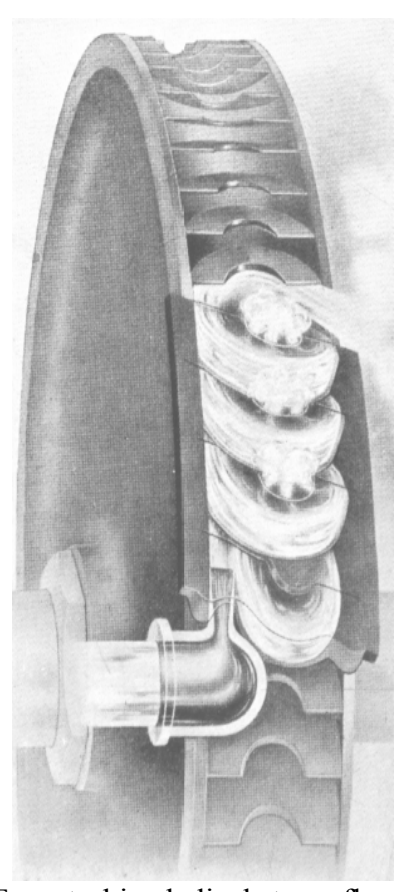


Figure 3 A typical Terry turbine helical steam flow path [Goudie, 1917]

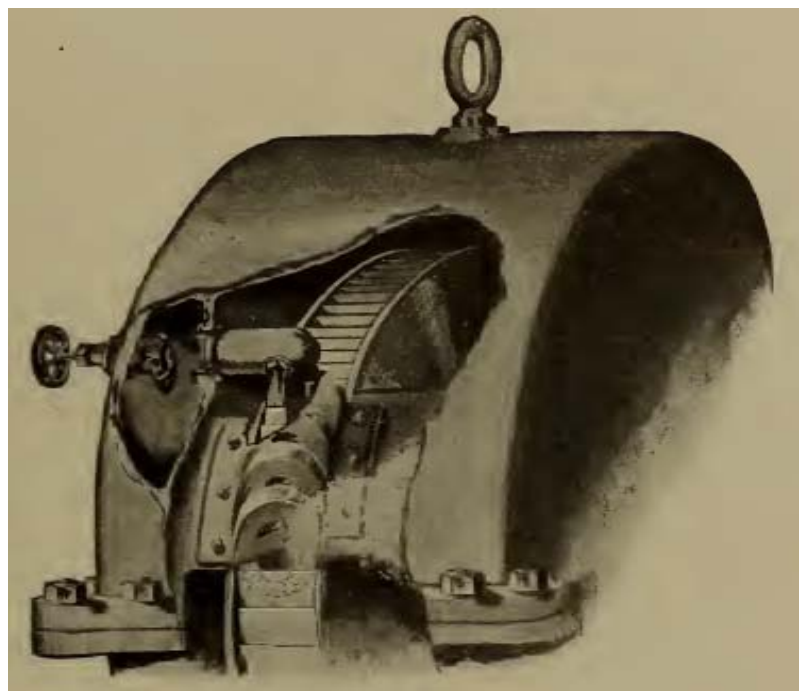


Figure 4 Terry Turbine Cut-away [Leland, 1917]

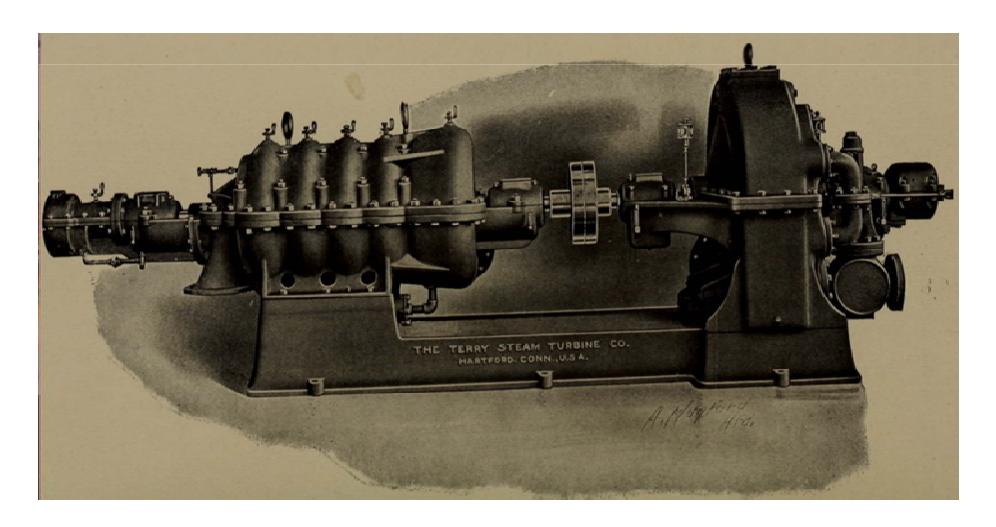


Figure 5 Terry turbine coupled to a centrifugal pump [Leland, 1910]

## 1.1.3 RCIC System Pump

As previously mentioned, the turbine-driven RCIC pump draws water from either the CST or the suppression pool. The CST suction line is physically lower in elevation relative to other system suction lines also found within the CST [GE, 2013]. Switch-over (CST to suppression pool) will occur upon indication of a low water level in the CST. The pump itself is horizontally-mounted, multi-stage, and centrifugal. The majority of water drawn in at suction is sent to the RPV, but a small fraction is conveyed to Terry turbine auxiliaries [GE, 2013]. To help preserve RCIC pump NPSH, the physical elevation of the pump is lower than any possible suction elevation [GE, 2013]. Note from Figure 1 that there are two motor-operated valves on the pump discharge line. Two flow paths (one for turbine auxiliaries and one for minimum flow) tap off upstream of the first discharge valve and another test line taps off just downstream of the first discharge valve [GE, 2013].

#### 1.1.4 RCIC Terry Turbine, Pressure Stage

The Terry turbine pressure stage is that part of the turbomachine within which a significant reduction in steam pressure occurs by virtue of rapid expansion in a converging-diverging nozzle. Typically, steam is superheated or high-quality saturated (if not totally dry) at the nozzle inlet after passing through the turbine governor. In accordance with the operating principles of an impulse-type turbine, a conversion of enthalpy to kinetic energy accompanies the steam expansion across the nozzle. This process allows for high-velocity steam to exit the nozzle. There are typically several nozzles in a Terry turbine, but these do not constitute multiple pressure stages because any given parcel of steam admitted through the governor valve expands only once in only one of the nozzles.

With respect to nozzle shape and geometry, dimensional estimates can be made from available sources including actual measurements of representative Terry turbine steam nozzles. **Error! Reference source not found.** depicts nozzle cross-sectional shape and dimensional estimates.

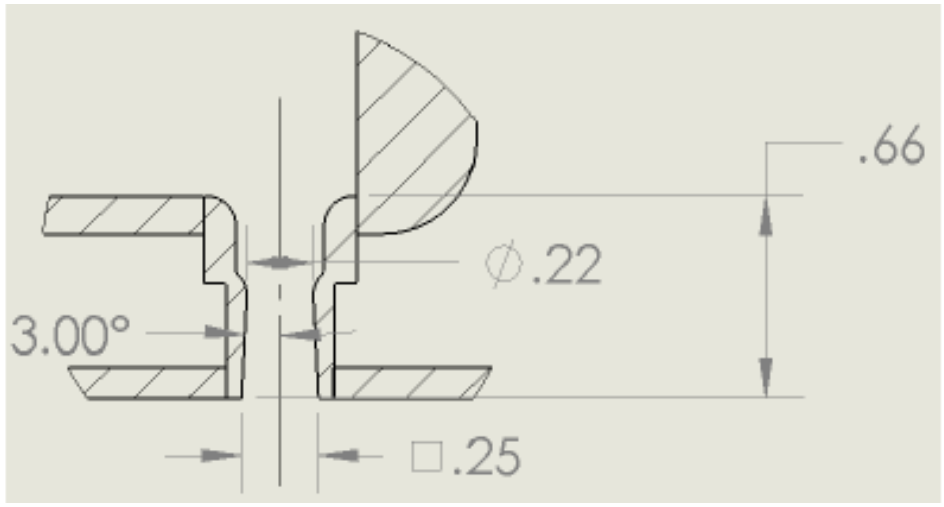


Figure 6 Terry turbine nozzle geometry and dimensions (inches) [Ross et al., 2015]

The nozzle cross-sectional shape and area both evolve along the direction of flow. In the converging section, the cross-section is circular and decreasing in area. At the throat (diameter of 0.22 in), the cross-section is still circular but begins transitioning to a square shape thereafter along the gradually diverging (3° angle) section. At the nozzle outlet, the cross-sectional shape is square with length and width of 0.25 in. The entire length of the nozzle is approximately 0.669 in (1.7 cm) so that the transition from circular to square cross-section occurs over a short length. Preceding dimensional estimates correspond to a typical BWR RCIC Terry turbine (GS-1 or GS-2). CAD renderings in Figure 7 show the geometry used for CFD analyses.

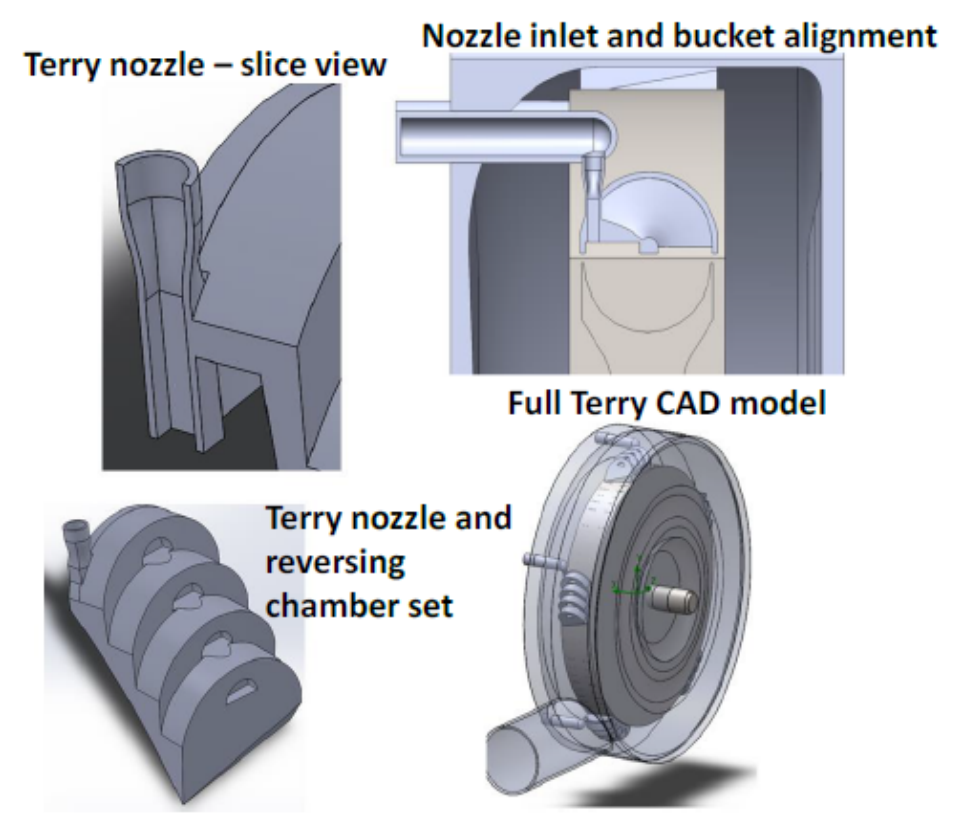


Figure 7 Pressure stage geometry used for CFD analyses [Ross et al., 2015]

## 1.1.5 RCIC Terry Turbine, Velocity Stage

The Terry turbine velocity stage consists of rotor buckets and reversing chambers and is characterized by a momentum exchange between impinging steam and the rotor. Because reversing chambers can return steam to the rotor after the first (or previous) impingement, the Terry turbine is technically a compound velocity stage machine. The first velocity stage involves a nozzle and the rotor whereas subsequent velocity stages involve reversing chambers and the rotor. In accordance with the operating principles of an impulse-type turbine, steam enters the rotor and delivers an impulse as it turns through a bucket. A force is generated in the local direction of bucket motion, acting with the leverage of a moment arm roughly equal in length to the turbine wheel radius. This creates a twisting moment, or torque, on the turbine shaft.

All Terry turbines found in domestic BWR RCIC systems have a wheel diameter of 24 in [Ross et al., 2015]. Anywhere between five and ten nozzles are situated circumferentially about the Terry turbine rotor. The turbine wheel/bucket width is estimated at 2.756 in (7 cm) and four reversing chambers per nozzle are assumed. About eighty-four buckets would fit around the perimeter of the rotor and there is a distance of about 0.59 in (1.5 cm) between the steam nozzle outlet and the rotor. Figure 8 shows oblique and side views of the full Terry turbine geometry.

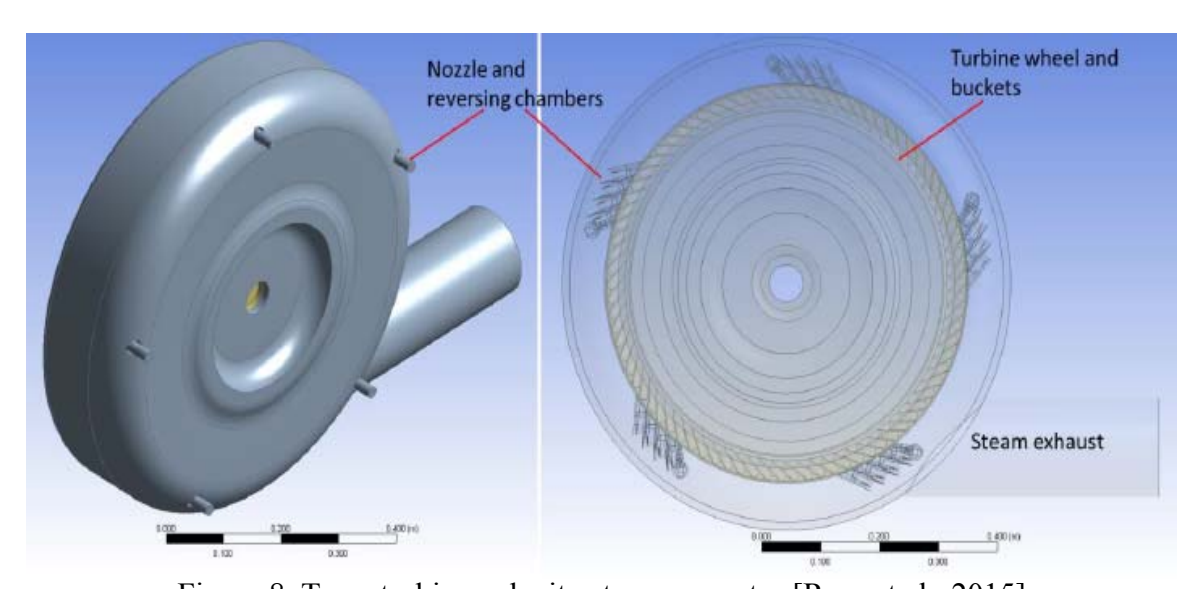


Figure 8 Terry turbine velocity stage geometry [Ross et al., 2015]

## 1.2 Significance of RCIC System Multi-Phase Analysis Capabilities

Although the RCIC System was designed for isolation events, the Fukushima Dai-ichi accidents demonstrated that the system can play an important role under accident conditions in removing core decay heat. The RCIC System is believed to have successfully removed decay heat for almost 70 hours in Unit 2. This duration greatly exceeds the 4 to 12-hour operation that the RCIC System is given credit for in US BWRs. The short credit time is based on the assumption that the RCIC System fails upon battery depletion because the turbine governor valve is controlled by an electro hydraulic system. Without power to regulate the turbine speed, the turbine is expected to trip on overspeed or to ingest water with steam to the extent that it loses functionality.

The unexpectedly sustained, good performance of the RCIC System in the Fukushima reactor demonstrates, firstly, that its capabilities are not well understood, and secondly, that the system has high potential for extended core cooling in accident scenarios. Better understanding of the

RCIC turbomachinery under multiphase conditions and analysis tools would allow for more options to cope with accident situations and to reduce the consequences.

A major significance of this project is, therefore, the general improvement of the state of knowledge of system performance under accident conditions. The events at Fukushima included significant uncertainty in the RCIC System operational conditions and supposed failure states. These same uncertainties were present in analyses of the RCIC System performance by the accident analysis community using state-of-the-art system codes [Gauntt, 2012 and Luxat et al., 2015]. The accident under investigation, a station blackout, is a significant contributor to the cumulative core damage frequency. Adequate predictive models of the RCIC system will enhance future probabilistic risk assessments performed by industry as well as the whole of the accident analysis community for loss of power accidents.

This project directly addresses the objectives described in Funding Opportunity Announcement's Technical Work Scope Identifier RC-7 (RCIC Performance under Severe Accident Conditions: Multi-Phase Analysis) by developing physics-based models of the RCIC System and incorporating them into a multi-phase code for validation. The project is tackling the current major challenges in RCIC System analysis to enable evaluation of the following two-phase thermodynamic aspects of the system:

- Turbine performance following ingestion of two-phase flow
- Pump performance degradation due to:
  - o Change in turbine performance
  - Suppression Pool heatup by turbine discharge
- Multi-dimensional temperature distribution in the Suppression Chamber
- Water carryover into the turbine

Some of the models currently are not available for reactor safety codes and their development will therefore be an important advancement with respect to both enhanced reactor safety and the state-of-the-art of severe accident modeling.

The outcome/impact of the project will be as below:

- Increased knowledge of the RCIC System operational characteristics under accident conditions
- Technically-defensible models of the RCIC System
- Potentially, suggestions for modification of Severe Accident Management Guidelines (SAMGs)
  - o Planning for extended pump operability under accident conditions
  - New options for operators to achieve recovery from near-accident conditions or to extend the timing to core damage and permit alternative injection alignment prior to core uncovery.

#### 1.3 Project Goals and Objectives

The overarching objective of this project is to provide analysis methods for evaluation of the RCIC System performance under severe accident conditions.

The technical approach involves integration of models for the key aspects of the RCIC System, some models which are being developed anew and others which will be adopted from existing techniques. The individual models will be validated against experimental data, some of which exists and some of which will be generated anew for the turbine model. Finally, the integrated analysis tool will be benchmarked against the Fukushima Dai-ichi Unit 2 reconstruction analysis that was performed with MELCOR [Gauntt et al., 2012].

#### 2. Technical Approach

#### 2.1 Overview of Technical Tasks

The technical approach of the project is as follows:

- Perform a critical evaluation of the present reactor safety codes and RCIC System models
  for severe accident and multiphase conditions and identify shortcomings/needs. A
  summary of the basic equations and closure equations, assumptions and any special models
  will be included. This task may include running the codes to determine whether particular
  capabilities are present.
- Select the multiphase code(s) to be used in this project;
- Survey available test data and plant data on RCIC System performance;
- Develop phenomenological models for selected multiphase code(s);
- Obtain data in the PI's facility to fulfill data gaps. The turbine analog will be manufactured and installed in the PI's facility. The instrumentation will be added in year 2 and testing conducted.
- Implement models into the selected code;
- Validate models against the new data produced in the PI's laboratory and published data and use Fukushima Dai-ichi Unit 2 data as the benchmark.

## 2.2 Description of Existing Equipment in the NHTS Laboratory

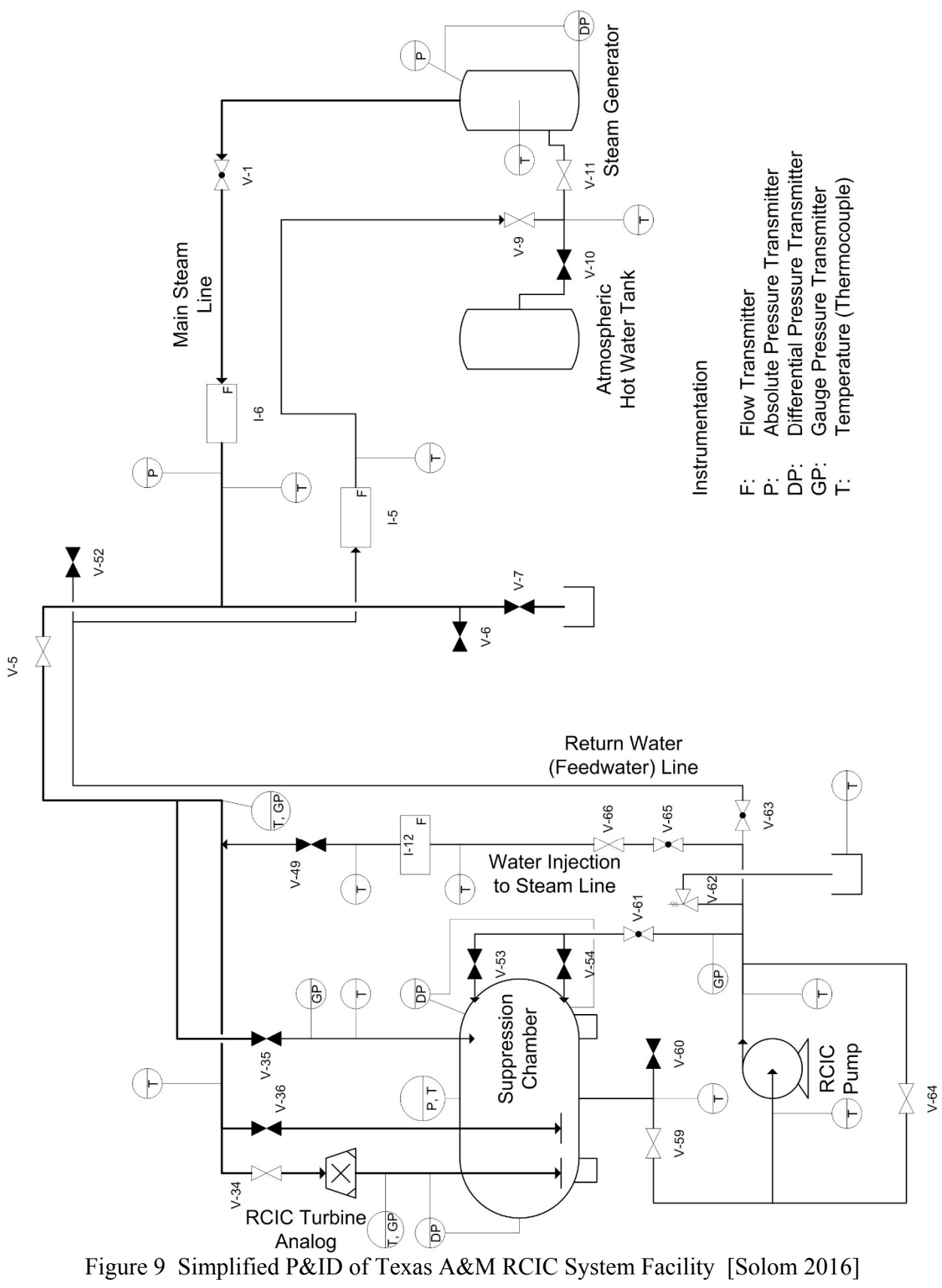
The experimental system existing in the PI's Nuclear Heat Transfer Systems Laboratory at Texas A&M University is applicable to RCIC Systems in use in BWR plants with a Mark I containment. The system description herein is largely taken from Solom et al. [2015] and Solom [2016].

Steam is supplied by the steam generator and directed to the Suppression Pool through one of two sparger systems. Water can be injected into the steam line upstream of the RCIC turbine analog to simulate reactor overfill scenarios. From the Suppression Chamber, typically filled halfway with water, a RCIC pump draws suction from the outlet at the bottom of the vessel. The pump suction is at the opposite end of the Suppression Chamber from the spargers. The water from the pump is directed to the steam generator, closing the loop, and into the steam line upstream of the RCIC turbine analog. The entirety of the system is well-insulated, thermally isolating it from the outside environment. Applicable flows, pressures, and temperatures are all monitored and recorded by the Data Acquisition (DAQ) system. A simplified P&ID is shown in Figure 9.

A semi-H2TS scaling analysis by Vierow [2015] gives this facility a volumetric scale of 1:1000, with some distortions. The Suppression Chamber is not toroidal, and may not reveal the full horizontal thermal profile of the Mark I Containment. The Suppression Chamber diameter scale is 1:5.6. For the steam and water flows, the high power limit scales to 1:375 when compared to a 400 GPM RCIC System. The steam flow through the RCIC sparger analog produces a maximum mass flux of 50.1 kg/m²s; this covers the lower range of mass fluxes in full systems. The Reynolds number, therefore, is not preserved. However, the mode of steam condensation in the water pool during extended operation is reproduced.

#### 2.2.1 Steam Supply

The steam supply in this facility is an electric steam generator. It is an ASME-rated pressure vessel with electric immersion heaters, and can supply up to 157 kW of heater power in increments as small as 2 kW. The outlet is connected to a moisture separator to dry the steam exiting the pressure vessel.



The steam generator is operated through a control panel that adjusts heater powers directly; they are not operated by a pressure regulator. Control of the heater power ensures better control of the steam flow, which is further regulated by a manually operated globe valve downstream of the separator.

## 2.2.2 Suppression Chamber and Suppression Pool

The Suppression Chamber is a 5,300 liter (1,400 gallon) horizontal cylindrical, ASME-rated pressure vessel. Its internal diameter is approximately 150 cm (59 in.), and has a peak internal length of nearly 310 cm (122 in.). The Suppression Pool is the pool of water within the Suppression Chamber.

An internal structure has been assembled inside the vessel to support both the spargers and the thermocouples placed throughout. It is intended to be minimally intrusive, but may display localized effects on the water mixing. Both the vessel and the internals are made of 304 stainless steel.

The thermocouples in the pool, shown in Figure 10, have been placed to provide insight into the 3-dimensional temperature profile. Nine thermocouples are located along the centerline of the vessel, 30.5 cm apart and 38 cm above the vessel bottom. At three axial locations, an additional four thermocouples have been added: an upper one (56 cm above vessel bottom, along the centerline, directly above the middle and lower thermocouples), a lower one (20 cm above the vessel bottom, and a left and right thermocouple (even with the middle one at 38 cm, but placed outward toward the side of the vessel by  $\pm 30.5$  cm from the centerline). In addition, two thermocouples sit in the airspace in the vessel, and another one reads the temperature at the vessel outlet near the front head at the bottom of the vessel. All thermocouples used are Omega Type T thermocouples with Special Limits of Error ( $\pm 0.5$  °C).

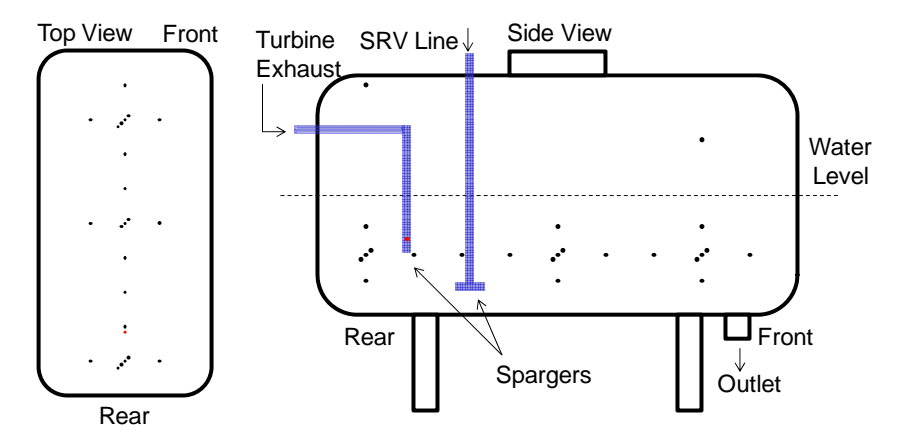


Figure 10 NHTS Suppression Chamber Vessel Internal Thermocouple Layout

#### 2.2.3 Turbine Analog

A scaled version of the Terry turbine used in BWR RCIC systems was not available for use prior to this project. The analog was an orifice plate, meant to provide a measure of similarity to the steam nozzles in the actual turbine. The bore size was 11 mm (7/16 in.), and there was a square loop of pipe immediately following the orifice. Such an assembly was deemed suitable for prior tests as the turbine employed in plant systems was of a very low thermodynamic efficiency and not of prime interest. For the project reported herein, a Terry turbine was procured, as described in Task 5.

## 2.2.4 **Pump**

The RCIC pump in a real system is a multistage centrifugal pump driven directly by the turbine [EPRI, 2012]. The analog used in this experiment is a multistage (five stage, closed-impellor) centrifugal pump driven by an electric motor.

#### 2.2.5 Spargers

Two steam spargers are installed in the analog to the Suppression Pool. One sparger, downstream of the RCIC turbine analog, is a vertical pipe (1.5-inch Schedule 40 NPS) open at the bottom. Its outlet is approximately 39 cm above the very bottom of the vessel, and is centered nearly 61 cm horizontally from the center of rear vessel head. A thermocouple is installed in the flow path shortly upstream (9 cm) of the outlet, and a shield on the bottom of the pressure vessel is installed directly below (38 cm from) the sparger outlet.

The second sparger, representing a Safety/Relief Valve (SRV) discharge line, is placed above the bottom centerline of the vessel approximately 95 cm horizontally from the center of the rear head. It consists of a 1-inch NPS tee with the outlets oriented along the centerline of the vessel toward either head. The outlets are nearly 18 cm apart, with the tee in the middle, and are open-ended 1-inch NPS Schedule 40 pipe. The center is 18 cm above the bottom of the vessel. It connects to the steam line at a branch-off point shortly upstream of the RCIC turbine analog. This sparger is similar to the old-style ramshead devices used on SRV lines before the advent of the T-quencher.

#### 2.2.6 Instrumentation and Data Acquisition

All temperatures in the system are measured using Omega Type T thermocouples with Special Limits of Error ( $\pm 0.5$  °C). In addition to the thermocouples in the Suppression Chamber, temperatures are measured in the steam generator, at the flow meters, upstream and downstream of the water injection point in the steam line, between the RCIC turbine analog and the spargers, on the inlet and outlet of the pump, and at the point where return water is injected into the steam generator.

Flow rates are measured on the steam line, on the water injection line to the steam line, and on the water injection line to the steam generator. Steam flow is measured with a Foxboro model 83 vortex flow meter with full pressure and temperature compensation. Water flows are measured with magnetic flow meters: a Yamatake MagneW 3000 PLUS on the water return line to the steam generator, and a Badger M2000 on the water injection line to the steam line.

Pressures are measured using Honeywell three STA940 absolute pressure transmitters and three Honeywell STD924 differential pressure transmitters. An additional set of Dwyer gauge pressure transmitters are used as monitors for the operator rather than as data instruments. Absolute pressures are measured on the steam generator, Suppression Chamber, and at the vortex flow meter on the steam line. Differential pressures are measured from the top to the bottom of both the steam generator and Suppression Chamber to estimate their water levels, and from the outlet of the RCIC turbine analog (upstream of the sparger) to the bulk Suppression Chamber vapor space to monitor the flow behavior through the sparger in conjunction with the line's thermocouples.

Signals from each thermocouple and 4-20 mA instrument are collected and recorded by the DAQ. DAQ consists of National Instruments (NI) SCXI hardware, including SCXI-1102/b/c modules and an NI data acquisition card in a PC. LabVIEW programs have been developed to collect and record the data gathered by the hardware, and all data are written to text files at 0.1 s intervals.

#### 3 Task 1: Critical Evaluation of Codes for RCIC System Modeling

# 3.1 Summary of Current Code Capabilities

The MELCOR and MAAP code capabilities were critically assessed in the first year of the project and were reported in the Year 1 annual progress report as below.

## 3.1.1 MELCOR Capabilities for RCIC System Modeling

At the time of project start, while there were no specialized code components for RCIC System modeling in MELCOR, several features of the flow path package were available that could be leveraged to represent the turbine-driven centrifugal pump and the turbine pressure stage (governor and nozzles). The control function utility could also be used to model Terry turbine rotor torque, e.g. with a simplified equation for conservation of angular momentum. An appropriate control volume, flow path, and heat structure nodalization could represent the remainder of the RCIC system (e.g. piping and valves). Once developed and tested with user-supplied boundary conditions, a RCIC system model could be integrated with a full plant deck e.g. the Fukushima-2 input that Sandia National Laboratories has used for its independent analyses.

The turbine pressure stage involves physics beyond the current scope of MELCOR thermal hydraulics modeling, i.e. compressible, supersonic condensing steam flow with non-equilibrium thermodynamics. As is typical of a systems-level severe accident code, MELCOR has no flow regime map and cannot presently account for homogeneous nucleation of a droplet phase or any continuous-to-dispersed phase mass/momentum/energy exchange thereafter. However, the code has high potential for modeling the RCIC System turbomachinery when simplified models that incorporate these physics are developed in conjunction with more rigorous CFD model development. The gas-space "atmosphere" in MELCOR is essentially treated with a homogeneous equilibrium approach where the pseudo-fluid includes vapor (steam plus noncondensibles) and "fog". Any CFD results and/or new systems code models informed by CFD should be adapted to fit this pseudo-fluid scheme.

The user has the option of activating a choking model for a given flow path, which would capture some of the Terry turbine nozzle physics. The flow path package flashing model, while not applicable for dispersed droplet flow, could be useful in modeling any liquid parcel flashing if water floods the main steam line and enters RCIC steam intake piping. Later chapters of this report document how CFD calculations are used within this project to inform new MELCOR models that were developed within this project. Specifically, CFD analysis was used to help develop methods within MELCOR to account for condensing steam nozzle phenomena, e.g. aerodynamic and condensation shocks, outlet wetness, nozzle jet behavior, etc. Certain aspects of the RCIC turbine upstream of the nozzles such as the governor and the trip-and-throttle valve can be modeled with typical flow path valves and associated control logic.

A MELCOR RCIC system model should utilize the new homologous pump capability – a feature of the flow path package – to represent the turbine-driven centrifugal pump. Known rated RCIC pump conditions could be input along with any known pump performance data (in conventional homologous form). An input motor torque (in this case a turbine torque as defined via control functions) would represent the turbine/pump coupling and would directly translate an impulse on the Terry turbine to a shaft torque that drives the RCIC pump. The homologous pump option in MELCOR offers the most realistic representation of steady-state and transient pump operation. It essentially represents the pump, for a specified flow path, as a momentum source dependent upon pump impeller speed and pump volumetric flow. There is an optional torque-inertia equation solver that predicts the evolution of pump impeller speed. Chapter 6 describes implementation of a homologous pump model into the MELCOR flow path.

During the second year of the project, Ross et al. [2015] published a description of system-level MELCOR models for the RCIC System and CFD analysis of the multiphase behavior inside the turbine wheel (downstream of the steam nozzle that the current project focused on).

## 3.1.2 MAAP Capabilities for RCIC System Modeling

The MAAP severe accident code has been used to evaluate the Fukushima Dai-ichi accidents. The most recent available descriptions of MAAP5 simulations in the US for Units 2 and 3 with the RCIC Systems suggest that the RCIC System was not explicitly modeled [Luxat et al., 2015]. Conditions appear to have been imposed on the simulation, such as time of RCIC System operation, RPV pressures and water and steam flow rates into the RCIC turbine.

Tokyo Electric Power Company has been using the MAAP code to simulate the accidents at Fukushima Dai-ichi Units 2 and 3. Their models for the RCIC System are not described in the available documents [TEPCO, 2013]. Therefore, no particular modeling capabilities that were developed for the RCIC System are known to the authors.

While no published models of the RCIC System within MAAP have been found, there is the possibility of incorporating new models into the code. The models developed in the current project are intended to be code-neutral and can be made available to the MAAP code developers.

## 3.2 Summary of Available Multi-phase Models for RCIC System Turbomachinery

Models for the Terry turbine and RCIC pump were reviewed in the first year of the project and reported in the Year 1 annual progress report as below.

# **3.2.1** Terry Turbine

The discussion of Terry turbine modeling begins at the CFD level because detailed treatment of the complicated multi-phase phenomena require capabilities beyond those of system-level codes. Without consideration to any specific CFD code, there are basically three approaches suitable to multi-phase flow modeling of the Terry turbine and its pressure stage in particular. These three types are the homogeneous equilibrium model (HEM), the Eulerian multi-phase (EMP) formulation, and the Lagrangian multi-phase (LMP) formulation.

- The HEM-type treatments consider a single fluid with averaged properties and could in some cases be classified as a pseudo two-fluid model because of certain "interphase" transfer terms and/or relaxed assumptions regarding phase equilibrium.
- The EMP formulation considers two distinct fluids (two phases of the same component in this case), each with its own set of conservation equations that may be cross-coupled via interphase transfer and/or source terms. Both sets of conservation equations are written from an Eulerian frame of reference, i.e. the frame of a stationary observer with respect to the flowing fluid.
- The LMP formulation considers two distinct fluids (again, two phases of the same component in this case), each with its own set of conservation equations that may be cross-coupled via interphase transfer and/or source terms. The continuous phase conservation equations are written from an Eulerian frame of reference while the dispersed phase conservation equations are written from a Lagrangian frame of reference, i.e. the frame of an observer moving with the fluid.

HEM approaches are the simplest of the three types mentioned above and are well-documented in the literature [Bakhtar et al., 1977, Campbell and Bakhtar, 1970, Dykas and Wroblewski, 2012]. Certain special interphase transfer terms are necessarily included so as to account for mass and energy exchange during homogeneous nucleation and subsequent condensation. Several

prescriptions from classical nucleation theory stand in as closures to describe droplet nucleation, critical nucleation size, and condensation growth rate. Extra transport equations that somehow account for the droplet phase are necessary. For example, a droplet mass fraction equation and a droplet number density equation are typically used. Alternatively, a collection of transport equations for droplet size distribution moments can be used. Common simplifying assumptions for the HEM approach include:

- Droplet phase is modeled with scalar transport equations describing either 1) the droplet number density and droplet size or 2) moments of the droplet size distribution
- The droplet volume fraction is negligibly small
- Mechanical equilibrium exists between the steam and any droplets no matter their size
- Droplet temperature is obtained from capillarity considerations rather than an energy equation
- Classical nucleation theory characterizes nucleation rate, critical droplet size, condensation, etc
- Process of steam/drop heat and mass exchange is somewhat simplified, e.g. no droplet energy storage or internal heat transfer
- Turbulence effects are often neglected, but not necessarily

The EMP approach is more complex than the HEM as it generally entails a full complement of conservation equations (mass, momentum, and energy) for both the continuous steam phase and the dispersed droplet phase. A few attempts at EMP modeling of high-pressure condensing steam flow are documented in the literature [Gerber and Kermani, 2004]. All the same interphase effects of nucleation and condensation are accounted for, again with closures from classical nucleation theory when necessary. However, because of the increased complexity of EMP vs. HEM, it is possible to assume mechanical non-equilibrium and account for interphase slip. The HEM assumption of negligible droplet volume fraction does not necessarily apply in the context of EMP models because the droplet phase has its own continuity equation. Furthermore, some CFD codes grant access to specialized continuous/dispersed and dispersed/dispersed phase interaction physics models when EMP is active. This could include dispersed phase coalescence and breakup, dispersed/film interactions, etc. The droplet size distribution is usually modeled via some kind of moment method and indeed some CFD codes have specialized dispersed phase size distribution models (e.g. the S-y model in STAR-CCM+). In the literature, a true droplet energy conservation equation is not usually solved. Rather, capillarity considerations determine the droplet temperature as a function of size. It should be noted that some CFD codes have several Eulerian dispersed phase treatments corresponding to different levels of modeling detail. STAR-CCM+ for example has a "multiphase segregated" model which entails the highest level of detail currently available. It also has a "dispersed multiphase" model for use when a simpler representation of dispersed phase physics is deemed adequate.

The LMP approach is similar to EMP in terms of continuous phase modeling. However, its dispersed phase modeling is decidedly more rigorous because droplets (or rather statistical parcels of droplets) are tracked in a Lagrangian frame of reference. There are motion, mass, momentum, and energy equations for the Lagrangian dispersed phase. A few attempts at LMP modeling of high-pressure condensing steam flow are documented in the literature [Gerber. 2002]. Compared to EMP, the same interphase transfers are modeled although the formulations look different due to the change in reference frame. LMP allows a more detailed modeling of droplet position and arguably of droplet size. Moment methods and scalar transport equations are not utilized, rather a droplet size for a statistical droplet parcel is deduced directly from a parcel mass equation. Greater fidelity in size distribution modeling comes at the cost of tracking more statistical parcels of identical droplets. Activating an LMP model in a CFD code usually permits the use of specialized continuous/dispersed and dispersed/dispersed interaction physics models. Some new wrinkles introduced by Lagrangian droplet tracking include the injection of droplets (e.g. from a user-defined injector in STAR-CCM+) and parcel statistics.

Desirable characteristics of a multiphase method include:

- Ability to model classical nucleation theory closures and condensation drop growth closures
- Ability to model passive scalars in the continuous steam phase according to user definition
- Ability to model user-defined volumetric source terms and interphase transfer terms
- Compatibility of the physics models with motion models (e.g. grid motion, surface motion)
- Ability to employ user-defined equations of state (e.g. for supersaturated steam phase)
- Ability to apply boundary conditions suitable for compressible flow
- Compatibility with conventional turbulence models
- Numerical method suitable to the physics, e.g. capable of capturing shocks

Some other considerations (not necessarily imperatives) include the ability to model fluid films, liquid flashing, and finer details like dispersed phase break-up, coalescence, impaction, and entrainment.

The problem at hand involves compressible flow with condensation shocks and, potentially, aerodynamic shocks. It might be helpful (if not necessary) for the selected modeling approach to be compatible with a coupled flow solution method rather than a segregated flow solution method. The coupled flow model solves conservation equations simultaneously while the segregated approach involves a SIMPLE-type algorithm that solves equations sequentially. Coupled flow methods in CFD codes often include certain other features like preconditioning and options for inviscid flux discretization. In general, coupled flow methods are more appropriate for compressible flows and shock-capturing. It may be that segregated flow methods are adequately robust for compressible steam flow, thus they should not be dismissed straightaway.

# 3.2.2 RCIC Pump

Several multi-phase models for pumps similar to the RCIC pump already exist. Therefore, rather than developing a new model as for the Terry turbine, the approach is to select an existing model suitable for detailed analysis with a CFD code. The model must be chosen carefully based on its parameters and its ability to model the key phenomena expected in the RCIC pump. Currently, the five most prevalent models are:

- the Aerojet Nuclear Corporation (ANC) Model
- the NASA Performance-Prediction Model
- the Babcock & Wilcox Pump-Performance Model
- the Westinghouse Equivalent-Density Model and
- the EPRI Mechanistic Model

The Aerojet Nuclear Corporation (ANC) Model was developed for RELAP to calculate thermal-hydraulic behavior under Loss of Coolant Accident (LOCA) conditions [Lane et al., 2008]. The model was developed from experimental data of the Semiscale project (conducted by ANC). In this project, four types of experiments were conducted: pump performance for steady state; single-phase subcooled water conditions; two-phase steam-water conditions; and transient two-phase conditions in a simulated LOCA scenario (1-1/2 loop Semiscale system and 1-1/2 loop Semiscale Mod-1 system). This empirical model presents the two-phase pump performance as a function of a single-phase pump performance and a fully degraded pump performance using a set of two-phase degradation multipliers, which are only a function of void fraction. ANC developed its own multipliers (steady-state two-phase, 1-1/2 loop Semiscale, 1-1/2 loop Semiscale mod-1).

The NASA Performance-Prediction Model [summarized in Lee et al, 1994] was originally for pumps handling liquid oxygen or liquid nitrogen. The model is based on compressible-flow

relationships and evaluations of heat transfer between the two phases. The model therefore requires a large number of inputs for the fluid properties and physics parameters. The NASA Performance-Prediction Model is found to be unsuitable for the current project because of the lack of knowledge about the liquid and gas going through the RCIC pump under severe accident conditions. The unknown nature of the two-phase flow in the RCIC System renders difficulty in identifying appropriate initial conditions for RCIC System studies.

The Babcock & Wilcox (B&W) Pump-Performance Model [summarized in Lee et al, 1994] is similar to the ANC but uses a different multiplier. The B&W multiplier was developed from data of a two-phase air-water test on scaled reactor-coolant pump. B&W Model does not consider the pump configuration, design, or the point of operation. Apart from this downside the model has the same outcome as the NASA performance Prediction Model with the skewing in the two-phase data. This skew can be caused from a number of things but most likely comes from the multiplier formulation. This skew shows the high uncertainty in the multiplier formulation.

In the Westinghouse Equivalent-Density Model [summarized in Lee et al, 1994], the two-phase head is obtained from the single-phase head through an equivalent density. The equivalent density provides an equivalent volumetric flow, which can be used with single-phase pump curves to find the two-phase pump head. This is similar to the two-phase multipliers in the ANC Model and the B&W model. Plots of the equivalent density against the inlet void fraction were found to deviate from experimental data when applying the model to the Semiscale data. Since this empirical model is not based on the physics and may not be applicable for RCIC System application, the Westinghouse Equivalent-Density Model was determined to not be the best choice for the current project.

The EPRI mechanistic model is a model developed by Electric Power Research Institute (EPRI) [summarized in Lee et al, 1994]. This mechanistic model is based on analysis that was developed as a result of EPRI's pump testing and analysis. The model is limited in its prediction capabilities of overall thermal hydraulic behavior of the reactor coolant system in a LOCA. The fact that it has limited prediction capabilities for LOCAs makes this very unappealing to the current project that is focusing on RCIC System operation.

#### 3.3 Identification of Gaps in Modeling Capabilities

The modeling gaps relevant to this project were discussed in the Year 1 annual progress report as below.

The modeling gaps identified within this project lie primarily within the realm of two-phase Terry turbine modeling. For the problem of condensing steam flow in converging-diverging nozzles, which can be important in the steam nozzles at the RCIC turbine inlet, there are experimentally-verified physical processes that do not have applicable models in CFD or systems codes. The primary issue is the phase non-equilibrium and the interphase transfer processes that correct the non-equilibrium. A brief exposition of these physical processes follows.

If saturated dry (or slightly wet) steam or superheated steam is expanded rapidly as in a converging-diverging nozzle, the process of phase change that normally begins at saturation may not be able to "keep up" with the rapid rate of expansion and hence may not maintain thermodynamic phase equilibrium. In particular, the decreasing pressure leaves the steam in a metastable, supersaturated (or subcooled) state, i.e. the steam pressure is less than the saturation pressure at its temperature. The only avenue for correction to equilibrium is phase change, i.e. homogeneous nucleation and subsequent condensation. However, there exists a thermodynamic barrier to formation of critically-sized liquid water droplets. This energetic barrier gets lower as steam supersaturation increases, and eventually the formation of critical droplets becomes probable. Once critically-sized droplets form, they can grow by steam condensation. This process

results in mass transfer from steam to droplet concurrent with sensible heat transfer from droplet to steam (equal in magnitude to the latent heat associated with the mass transfer). The resulting temperature rise (and entropy rise) of steam "shocks" the thermodynamic system towards phase equilibrium, a phenomenon called "condensation shock". The steam subcooling (i.e. supersaturation) is quickly relieved by such rapid condensation and a finely-dispersed droplet flow is established. Such processes within the Terry turbine pressure stage will surely impact turbine performance. Currently, CFD codes and systems codes do not generally have specialized physics models to account for this particular instance of interphase mass/momentum/energy transfer. With most commercial CFD codes however, users are given enough latitude via user-defined sources, interphase transfers, etc. to effectively build their own physics models from their own definitions and inputs.

Another issue that may become important to modeling off-normal RCIC conditions involves liquid flashing under influence of a pressure reduction. In off-normal operating conditions, liquid water can potentially flood the RCIC steam intake line, forcing the nozzles and the Terry turbine to "swallow" large liquid slugs. These parcels of liquid – given their larger size – might break up and/or flash under influence of the large pressure drop in the turbine pressure stage. Alternatively, flashing may occur just downstream of the nozzle jet. Predicting liquid flashing could be an important component of off-normal turbine performance modeling. It is not expected that liquid flashing is a concern for the fine droplets found in "fog flow" during normal RCIC operation. This is because small droplets are generally capable of adjusting (in temperature) to their pressure environment before voiding (which usually causes fragmentation) occurs in their interior.

Still other modeling issues may arise with the two-phase jets emanating from steam nozzle outlets. Three-dimensional expansion just outside the nozzle, shocks just outside the nozzle, and jet/bucket interaction are all important to RCIC turbine performance. Presumably, the selected CFD code and multiphase method could predict any jet expansion and any compression/rarefaction shocks should the nozzle flow be over-expanded or under-expanded, respectively.

#### 4. Task 2: Code Selection

#### 4.1 CFD

The STAR-CCM+ code from CD-ADAPCO [2016] was selected as the Computational Fluid Dynamics (CFD) code for this project. The discussion below is taken from the 1<sup>st</sup> year Annual Progress Report and remains current.

STAR-CCM+ is a commercial CFD/CMFD code from CD-ADAPCO [2016]. It has several of the previously mentioned features desirable for RCIC System modeling, e.g. diversity in its multiphase formulations and adequate flexibility in the way of user-defined functions, user-defined equations-of-state, and user-defined volumetric source and/or interphase transfer terms. Its methods are similar to those of other commercial codes, e.g. FLUENT or CFX. Thus any models developed in STAR-CCM+ are likely portable and adaptable to other codes. These are the primary reasons for selecting STAR-CCM+ for the CFD analyses.

As secondary reasons, STAR-CCM+ was chosen as the CFD code for this project because it has a number of conveniences. The Nuclear Heat Transfer Systems Laboratory at Texas A&M University has some previous user experience with STAR-CCM+. Student licenses that grant full access to all code features can be obtained at no cost. Additionally, a wealth of resources including publications, presentations, instructional articles, and tutorials may be accessed through CD-ADAPCO's online STEVE portal. There is also a reasonably complete user guide and theory manual for STAR-CCM+ that describes mathematical models, numerical methods, and best practices. STAR-CCM+ allows the user to import problem geometry and/or computational meshes (e.g. Computer Aided Design CAD files from Solidworks or mesh files from FLUENT) but also has robust CAD and meshing tools of its own. In terms of post-processing, STAR-CCM+ can create two or three-dimensional scalar/vector scenes, movies, and typical X/Y plots. If the user prefers another program for post-processing, STAR-CCM+ can export text files of tabular data.

A pseudo two-fluid HEM-like formulation can be configured in STAR-CCM+ using single-phase models (coupled or segregated solution approach) plus passive scalar transport equations and volumetric source terms. Two varieties of an EMP formulation can be configured in STAR-CCM+ by selecting either the dispersed multiphase model or the multiphase segregated model. The dispersed multiphase option is less detailed in general but allows the user to superimpose a dispersed phase (described in an Eulerian frame of reference) onto a background continuous phase (described in an Eulerian frame of reference) that uses either a coupled or segregated solution approach. Conversely, the multiphase segregated option uses a segregated solution approach for a full complement of conservation equations in all phases (described in an Eulerian frame of reference). An LMP formulation employing a statistical treatment of dispersed-phase parcels of particles is available in STAR-CCM+. The background continuous phase is treated with a coupled or segregated solution approach and an Eulerian frame of reference while the dispersed phase is tracked in a Lagrangian frame.

STAR-CCM+ has a field function utility with which the user may define scalar or vector fields for use with initial conditions, boundary conditions, and volumetric source and/or interphase transfer term definition. It is also possible to user-define look-up tables for equation-of-state relationships. This is a particularly useful feature for the problem at hand because commercial CFD codes do not typically have built-in state equations for supersaturated steam.

Given its user-flexibility, its diverse array of physics models and solution methods, its extensive user resources, its ready availability, its similarity to other commercial codes, and the researchers' prior experience, STAR-CCM+ was selected as the CFD code for RCIC Terry turbine analysis.

With respect to the two-phase pump modeling, STAR-CCM+ possesses the capability to model and mesh complicated pump geometry. The code has multi-phase models appropriate for pump applications, including the Volume of Fluid formulation and Rayleigh-Plesset cavitation. Finally, it has good flow visualization capabilities to assess pump performance.

# 4.2 Thermal Hydraulic Code

When the project proposal was written, it was expected that the new CFD models would need to be simplified in two stages, first to the thermal hydraulic code level (e.g. RELAP5-3D, TRACE) and then to the severe accident code level. During the first year of this project, further consideration led to the conclusion that the CFD models could be simplified directly to the severe accident code level. That is, the models developed within the project for the severe accident codes should also be applicable to the thermal hydraulic codes. Therefore, modeling specifically for a thermal hydraulic code is not necessary and will not be conducted as part of this project.

#### 4.3 Severe Accident Code

The MELCOR code, a best-estimate thermal hydraulics and severe accident code primarily used for light water reactor systems modeling, was selected as the demonstration code for this project. The discussion below is taken from the 1<sup>st</sup> year Annual Progress Report and remains current.

MELCOR is a best-estimate thermal hydraulics and severe accident code primarily used for light water reactor systems modeling. It is actively developed and maintained by Sandia National Laboratories for the Nuclear Regulatory Commission. It bears certain similarities to other thermal hydraulics codes such as RELAP5, TRACE, GOTHIC and MAAP (which is also used for severe accident modeling). Thus any RCIC system models developed in MELCOR are likely portable and adaptable to those codes. Sandia National Laboratories has previously performed several indepth analyses of the Fukushima accident and the RCIC system with MELCOR, thus TAMU and SNL investigators have a good idea as to how CFD could best inform a RCIC system model in MELCOR.

Efforts to incorporate a RCIC System model into MELCOR have been going on since the Fukushima Dai-ichi accident, under a separate funding mechanism. These are described under Task 4. These efforts are complementary to, not duplicative of, the current efforts in this project.

#### 5. Task 3: RCIC System Test Data Survey

# 5.1 Identification of Data Needed to Validate Models Developed Herein

Several examples of CFD-to-experiment benchmarks for steam nozzle and steam turbine flow are documented in the literature [e.g. Gyarmathy, 2005]. Typically, pressure and wetness measurements are taken from steam nozzle experiments and compared to code predictions. For example, a nozzle wall pressure distribution is often used to ascertain the physical location of the Wilson point (usually in the diverging section of the nozzle) while droplet concentration measurements (e.g. from light scattering techniques) are often used to ascertain dispersed droplet size distribution, number density, mass fraction, etc. Wilson point pressure, temperature, entropy, and enthalpy – whether measured directly or extrapolated – could be useful in judging the fidelity of an applied CFD method for steam nozzle modeling. Also, the flow conditions in turbine control valves (Governor Valve, trip-and-throttle valve, etc.) will undoubtedly effect turbine performance and would be a worthwhile subject for experimentation.

With respect to the Terry turbine velocity stage (i.e. the rotor bucket/reversing chamber pairs inside the turbine casing) an experiment would ideally characterize:

- Impulse (developed torque) on the rotor (stationary and rotating) by impinging steam and liquid,
- Velocities of steam and/or water jets as they traverse a turbine rotor bucket,
- Losses (e.g. windage) of turbine wheel (e.g. due to fluid drag by accumulated water),
- Efficacy and performance of reversing chambers under a range of conditions,
- Velocity, spreading, flashing, and dispersed phase dynamics in the nozzle outlet jet,
- Fluid state inside turbine casing,

Experimental measurements often represent area-averaged or volume-averaged quantities and hence do not directly compare to the two-dimensional or three-dimensional profiles predicted by CFD codes on a given computational mesh. However, STAR-CCM+ can produce reports with appropriately averaged quantities that would make for more accurate comparisons to experimental data.

During teleconferences between the PI and students at Texas A&M University and collaborators at Sandia National Laboratories, preliminary results given by Sandia's CFD models for Terry turbine flow were the basis for identifying parameters desired from the Texas A&M experiments for CFD model validation. Acquisition of an actual Terry turbine greatly improved the PI's ability to produce data useful for model validation. Variables discussed included the jet velocity from the steam nozzle and its dependence on pressure, spreading of the jet during entry and exit from buckets, and wet steam Mach number/pressure variations in the RCIC steam nozzles. Also discussed was the amount of action which happens in the first stage, especially after the startup process is complete. The amount of action refers to the amount of energy transferred from the incoming fluid to the turbine wheel.

These data points are all testable to some extent within the PI's laboratory. For the first stage, simply removing the reversing chamber would show the amount of action that happens in the first stage. Pressure can be directly measured and compared with shaft RPM.

The parameters that were actually used in the comparison of CFD model to NHTS experimental results were the turbine torque and power, as documented for Task 5 in this report.

#### 5.2 Data Survey

A CFD-to-experiment benchmark for steam nozzle and steam turbine flow [Gyarmathy, 2005] was used to validate the steam nozzle model under development for the Terry turbine.

The data from the Fukushima Dai-ichi plants remains extremely limited for the RCIC System turbomachinery. Times of operation are available, for example, but detailed information such as the flow rate through the turbine, or the pumped volumetric flow rate, are not known. Several important boundary conditions for a system simulation, as opposed to those needed at the validation on the turbine and pump component level, are available [Ross et al., 2013].

During the course of the project, the type or amount of available data did not increase to an appreciable extent. Insights into the RCIC system behavior were obtained through simulations, e.g. Ross et al., [2015]. An example is that in the second year of this project, Ross et al. [2015] presented an application of the RPV pressure time history from Fukushima Dai-ichi Unit 2 to MELCOR results. These insights were used to make educated guesses as to various boundary conditions and the like for MELCOR simulations reported herein.

#### **6** Task 4: Model Development and Implementation

Phenomenological models for RCIC System analysis were developed under this task. The Computational Fluid Dynamics (CFD) models are described first for the RCIC System turbine and pump, followed by models for systems-level severe accident codes.

#### 6.1 Development of Computational Fluid Dynamics Code Models

Aspects of the CFD code used for Terry turbine and pump analyses are discussed here. The code itself is introduced and certain features/capabilities relevant to RCIC system analysis are described in some detail. Model development as it pertains to RCIC system turbomachinery is discussed subsequently in separate sections for the turbine and pump.

### 6.1.1 STAR-CCM+ Computational Fluid Dynamics Code Description

#### 6.1.1.1 STAR-CCM+ Introduction

STAR-CCM+ is a computer code managed, maintained, and developed by CD-ADAPCO. It is capable of a wide variety of engineering physics simulations, but is used only as a CFD tool for purposes of this dissertation. The code employs an object-oriented architecture that readily lends itself to parallelization across multiple computing resources without extra effort from the user. The code itself is essentially a suite of integrated components, including [CD-ADAPCO User's Guide, 2016].

- A 3D CAD modeler with CAD imbedding
- Surface preparation tools
- Automated meshing technology
- Physics modeling (including turbulence)
- Post-processing tools and CAE integration

The 3D CAD modeler was not used extensively for the present work since the complicated geometry was imported from pre-existing Solidworks models [Ross et al., 2015]. Once the geometry was imported, surface preparation tools were used to condition for meshing. Several off-the-shelf physics models were applied as-is or were customized with user-defined functions and external tables. Physics models applied to the RCIC turbine include:

- Coupled flow and coupled energy model/solver with user-defined source terms and user-defined passive scalars
- Steady state time model/solver
- Turbulence model/solver
- User-defined equation of state model (ideal gas too)
- Mixing planes and a moving reference frame where applicable

A student license issued exclusively for research purposes was used for analyses in this dissertation. The configuration is convenient because any computer with STAR-CCM+ installed can launch one or more simulations via the CD-ADAPCO portable on-demand remote licensing server. The only requirement is an internet connection to communicate with the license server (to periodically verify connectivity). Computational speed is in no way dependent on internet connection quality.

#### 6.1.1.2 Code Mechanics

Some general concepts in STAR-CCM+ including simulations, parts, continua, models, regions, boundaries, interfaces, solvers, and reports, monitors, plots, and scenes are described in turn below.

A simulation holds the solution state and data for some given STAR-CCM+ analysis. The simulation is accessed and manipulated via the graphic user interface after a client has connected to a server. The simulation is fully described by an object tree through which the user may manipulate the simulation (e.g. define physics models, set boundary conditions, etc.).

Parts are components of a simulation that define its attributes. There are several subsets including geometry parts, model parts, and derived parts. Geometry parts represent the geometry of the simulation and have their own branch on the object tree. 3D CAD bodies must be converted into geometry parts before those parts can be used in a simulation. Geometry parts can be manipulated by operations (splitting, combining, etc.) that work on surfaces, curves, and contacts comprising the geometry part. Model parts are related to geometry parts and include regions, boundaries, and interfaces. Model parts represent portions of the geometry being analyzed and physics models are applied directly to model parts. Derived parts are typically used in the creation of analysis reports or flow visualization scenes (e.g. a plane derived part applied to a vector scene to show the solution velocity field on that plane). Derived parts are often inputs to other objects. A subsequent section discusses salient details of types of derived parts used in this study.

Continua are themselves STAR-CCM+ objects but are applied to one or more region objects. Continua have no associated geometry but instead consist of physics and/or meshing model objects that define a simulation as described below. A mesh continuum holds mesh model objects (e.g. surface mesher, volume meshers) that get applied to a region (which has geometry parts assigned to it, see description of regions below). A physics continuum holds physics model objects (solvers, time and motion models, etc.) that get applied to a region.

There are generally two types of models: mesh models (surface mesher, polyhedral mesher, prism layer mesher, etc.) and physics models (flow, time, motion). Mesh models control the creation of a computational domain (or rather the faces, cells, and vertices that comprise a computational domain) within a given region. Mesh models are not associated directly with any geometry parts but instead are indirectly linked with geometry parts through common affiliation with a region. Physics models characterize the problem that will ultimately be solved on a given computational domain. Physics models are also indirectly associated with geometry through a region. The mesh and physics models applied to a given region are not always independent of one another, e.g. certain kinds of turbulence physics models may require a sufficiently well-resolved near-wall mesh generated with the prism layer mesh model. Also, the geometry part assigned to a region might dictate certain features of the mesh model applied to that region, e.g. a finer volume mesh might be desired near certain geometric features (a sharp corner or the throat of a converging flow channel).

Regions are volume domains (for 3D simulations) or area domains (for 2D simulations) in space that are entirely enclosed by boundaries. Regions are discretized according to their assigned mesh models. Regions also have geometry parts assigned to them and thus they link the mesh models with problem geometry (the notion of boundaries also come from geometry part definition). Separate regions (with different mesh and physics models in general) can be joined with interfaces so that solution information may pass from region to region.

Boundaries are surfaces (for 3D simulations) or lines (for 2D simulations) that – alone or in combination with other boundaries - entirely surround a region. Regions do not share boundaries and so a given boundary belongs to only one region. Boundaries can come from the surfaces

defined in a geometry part upon assignment of that part to a region. Boundaries can also come from interfaces created between geometry parts or from other manipulations like splitting. Boundaries have associated properties that determine behavior (e.g. wall, stagnation inlet, pressure outlet, etc.)

Interfaces serve as connections between boundaries during the meshing and solution processes. Recall that each region has its own unique boundaries but that regions must be allowed to communicate. An interface facilitates that communication via its definition between two boundaries of two regions. When meshing, interfaces are necessary to generate a conformal mesh where two regions meet. When performing a solution on a volume mesh (computational domain), interfaces permit the flow of information (i.e. flow of mass, energy, other continuum properties) between regions. Interfaces have associated types that determine what is done with/to the information moving across it.

Solvers are activated once per solution iteration and control the progress of a solution. They are related to but distinct from physics models. Physics models often dictate the type of solver employed for a given simulation (e.g. the coupled flow model invokes the coupled solver) and some physics models have their own dedicated solvers. Solvers manage the algebraic multigrid procedure and control everything associated with the process of obtaining a converged solution.

Reports, monitors, plots, and scenes are all methods of conveying the progress and results of a simulation. Reports are often used to convey certain metrics from the solution data, e.g. a volume-averaged pressure or an area-averaged mass flow rate. Monitors are used to sample certain quantities (and perhaps plot them) as the solution progresses. Physical quantities (e.g. pressure) can be monitored but the most common use of monitors involves solver residuals. Reports can be used to create monitors. Plots show line graphs of solution data and monitors can be used to create plots. Scenes are used to visualize simulation properties like geometry, the mesh, or solution data. There are a few types of scenes including geometry, mesh, scalar, and vector. Geometry scenes are used to show geometry parts while mesh scenes will show surface or volume meshes from mesh models associated with regions. Scalar and vector scenes are used to display scalar or vector solution data. A pressure distribution might be shown in a solution scene, while a velocity field might be shown in a vector scene.

### 6.1.1.3 General Workflow

A comprehensive though simplified STAR-CCM+ simulation work-flow is [CD-ADAPCO User's Guide, 2016]:

- 1. Plan the regions layout
- 2. Prepare geometry (working with geometry-level objects)
- 3. Construct the regions layout (working with region-level objects)
- 4. Generate mesh after defining mesh continua (working with mesh objects)
- 5. Define physics, configure physics continua
- 6. Prepare for analysis (define boundary conditions)
- 7. Run the simulation(s) (tweak solver settings, boundary conditions as needed)
- 8. Analyze results

In step 1, the number of regions and their connectivity is determined. Several different factors may influence modeling decisions at this point including the physics of the problem, the number of materials, the type of boundary conditions on the problem, and any special region-wise interfacial requirements (mixing planes, etc.)

In step 2, 3D CAD is drawn up and translated into geometry parts. Alternatively, files from external CAD programs (e.g. Solidworks) can be read in as geometry parts. Then, surface repairs and part transformations/augmentations may be made as necessary. Generally, the modeler should configure geometry parts and underlying surfaces in such a way that boundary condition assignment is straightforward upon assigning parts to regions. Also, part contacts can be either automatically or manually defined.

In step 3, a "map" between the geometrical definition of a problem and the computational or physical definition of the problem is created [CD-ADAPCO User's Guide, 2016]. Region interfaces may be manufactured out of part contacts (which were defined in step 2) and region boundary conditions may be defined using part surfaces (likewise defined in step 2). Mesh models can run (step 4) only after valid regions with boundaries/interfaces are present, but physics models can be assigned to regions separate and apart from mesh models at this point.

Steps 4 through 8 above are often iterative in nature and one rarely proceeds directly from 4 to 8. In fact, each step could be an iterative process unto itself within the outer iterative loop over steps 4 to 8. For example, a solution might be poorly converged on a certain mesh, necessitating a return to 4 from 8. In the process of discovering that the solution needs a better mesh, step 7 might be performed over and over with different solver settings to assist the solution procedure on its way.

## 6.1.1.4 Selected Code Features and Concepts

A brief discussion of certain code features and concepts is useful at this point given their significance to the present analyses. These include the surface preparation tool, the surface mesher, the polyhedral mesher, the prism layer mesher, the coupled flow/energy model and solver, the passive scalar model and solver, the user-defined equation-of-state model, the user-defined scalar/vector field function utility, mixing planes, and moving reference frames. Any mathematical details or in-depth technical discussions of phenomenological models are deferred to later sections.

#### 6.1.1.4.1 Surface Preparation and Meshing

The surface preparation tool works on tessellated geometry parts to prepare their surfaces for meshing upon assignment to a region. Note that a tessellated surface is a surface discretized by small triangles so as to capture all features of its geometry. If imported, tessellated surfaces may have defects like improperly intersecting (i.e. pierced) faces, free edges, or non-manifold edges. These must be repaired before attempting to mesh the surface so as to avoid mesh generation errors. Launching the surface repair tool brings up a repair scene (for visualization) and a graphic user interface from which certain actions can be taken to remedy any defects. The surface repair tool is also useful for other applications like imprinting parts, performing Boolean operations on parts, and redefining surfaces/curves. A general surface repair workflow is as follows [CD-ADAPCO User's Guide, 2016]:

- 1. Launch the repair tool with one or more input surfaces
- 2. Perform repairs, run leak detection, or do merging, imprinting, and any surface Boolean operations
- 3. Run diagnostics, highlight problem areas, and graphically display them
- 4. Repair any remaining surface/feature errors

Surface preparation and repair was required for the present analyses. After importing three-dimensional RCIC turbine geometry into STAR-CCM+, several surfaces comprising different turbine parts were split out from the single initial surface. A few mating surfaces had pierced face errors and/or free-edge errors that required repair. Interfaces were needed between certain surface pairs to ensure a conformal volume mesh, a conformal periodic boundary condition, and mixing planes. With the surface preparation tool, part contacts for said interfaces were defined manually.

The surface mesher is a surface mesh model used to generate high-quality triangulated surfaces from either a geometry parts tessellation or the surface wrapper. A valid surface mesh is a prerequisite for volume meshing. The surface mesher is usually applied to a closed (i.e. watertight) geometry and as such is usually executed only after:

- The surface wrapper is used to close all holes in the geometry, or
- The surface preparation tool has been used to zip edges, fill holes, etc.

The user has control over target size for triangles created by the surface mesher, and the target value can apply globally or locally according to a volumetric control. Figure 11 below illustrates the difference between a geometry tessellation (e.g. for an imported part) and a triangulation from the surface mesher. A part of the RCIC turbine is shown, including a steam nozzle assembly, a set of reversing chambers, and a section of the rotor and its buckets. The triangles are much coarser in the geometry tessellation, but note all details of the geometry (curves, corners, etc.) are well resolved. The surface mesher triangulation shows darker clusters of triangles in places, a result of applying volumetric controls. The surface mesher triangulation gives a high-quality surface representation from which the volume mesh models may manufacture a fluid domain mesh.

The polyhedral mesher and the prism layer mesher are both volume mesh models typically applied to fluid domains. The polyhedral mesher forms a core mesh comprised of arbitrary polyhedral cells. The prism layer mesher works in tandem with a core mesher (e.g. tetrahedral or polyhedral) to form near-wall parallel layers of rectangular-shaped cells. The user has control over polyhedral mesh cell density (global parameters or local refinement by volumetric control) and may specify several parameters for the prism layer including total layer thickness, the number of constituent cells across the total layer, and the cell size distribution. The polyhedral mesher is a good choice for most meshing problems. The prism layer mesher has more specific applications, namely the resolution of near-wall (i.e. boundary layer) flows for purposes of turbulence modeling, conjugate heat transfer modeling, and reduction of numerical diffusion (increased accuracy) near the wall [CD-ADAPCO User's Guide, 2016]. For analyses in this dissertation, the prism layer mesher is used for turbulence modeling and for more accurate computation of fluid/surface interactions.

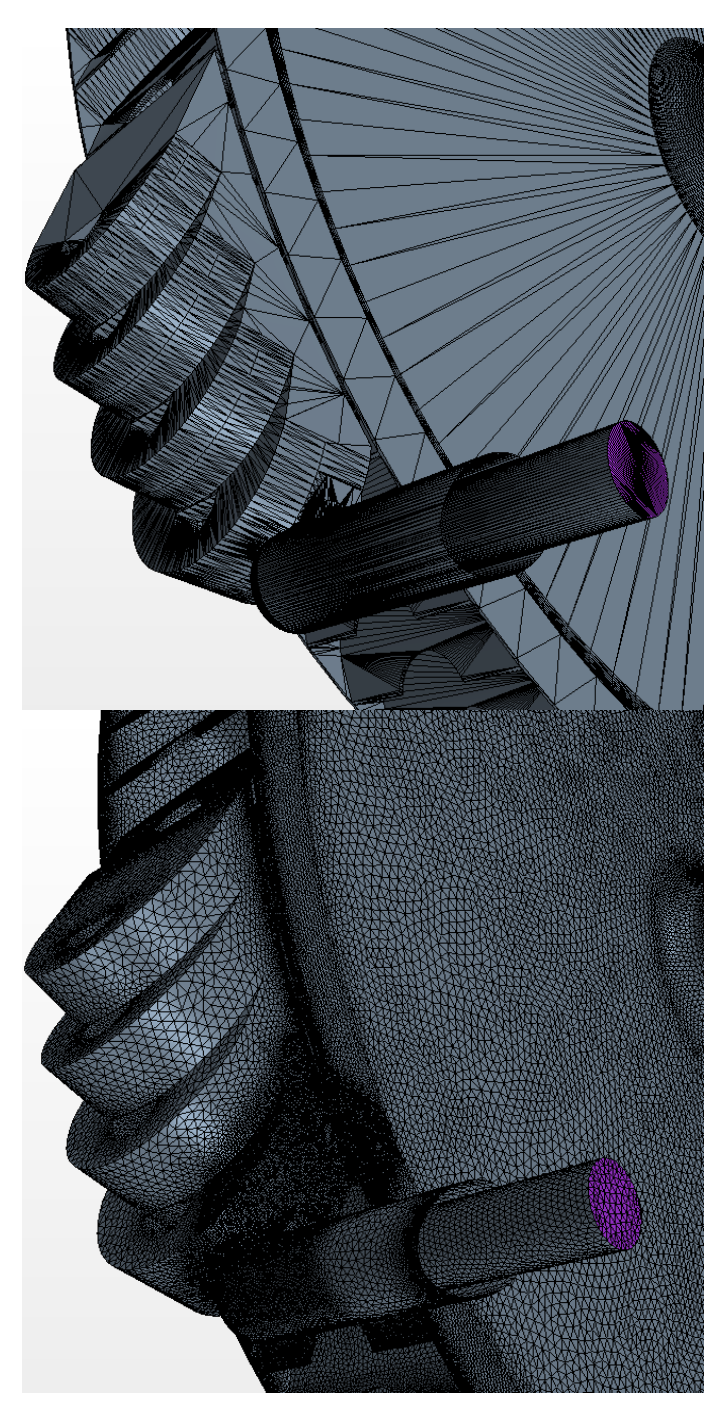


Figure 11 Geometry part tessellation (top) and surface triangulation (bottom)

6.1.1.4.2 Coupled Flow and Coupled Energy Models and Solvers
The coupled flow model is the best option available in STAR-CCM+ for compressible, trans/super-sonic flows in which aerodynamic shocks are expected [CD-ADAPCO User's Guide, 2016]. The coupled flow and energy approach is appropriate for the RCIC turbine because both aerodynamic and condensation shocks in compressible steam are possible. The shock-capturing capability of the coupled method - owing to its density-based solution approach - is beneficial for present analyses of compressible flow. Also, one aspect of the pseudo two-fluid model (described

more fully in a later section) is the incorporation of algebraically large mass, momentum, and energy sources. According to [CD-ADAPCO User's Guide, 2016], the coupled flow model is preferable to the segregated flow model when large energy sources are present in the simulation. The segregated flow model will not be described any further.

The coupled flow and coupled energy models collectively solve mass, momentum, and energy equations simultaneously rather than sequentially as might occur in a Semi-Implicit Method for Pressure-Linked Equations (SIMPLE) solution approach. Pseudo-time-marching is used for transient problems in tandem with either the explicit or implicit time model. For steady-state analyses, the unsteady forms of conservation equations are "driven" towards steadiness with the same pseudo-time marching scheme. The coupled flow model is compatible with several methods for finite volume face convective and diffusive flux computation, e.g. the second-order upwind method. Coupled flow also makes use of pre-conditioning for efficient solution of both compressible and incompressible flows at all speeds [CD-ADAPCO Theory Manual, 2016]. Additionally, inviscid flux discretization by Roe's scheme or Liou's AUSM+ scheme is employed.

The coupled solver manages the solution procedure for the coupled flow/energy models. The solver uses implicit spatial integration (or, alternatively, an explicit Runge-Kutta option) and algebraic multi-grid (AMG) methods to numerically solve discretized, finite-volume equations. There are several miscellaneous options available in the solver that may or may not be appropriate for a given application. Certain options pertain to solution initialization, e.g. expert initialization for grid sequencing. Other options are designed to assist the solution while running, e.g. convergence accelerators, and the expert solution driver.

### 6.1.1.4.3 Passive Scalar Model and Solver

The passive scalar model allows the user to simulate the convective/diffusive transport of some arbitrarily-valued scalar variable. With careful definition of source terms, passive scalars can be manipulated to model several phenomena. For the pseudo two-fluid condensing steam flow model of these analyses, passive scalars are used for a dispersed water droplet phase that evolves from and interacts with single-phase steam. Passive scalar transport generally consists of convection and diffusion (molecular and turbulent). The user can disable one or the other as appropriate.

### 6.1.1.4.4 User-defined Equation of State Model

The user-defined equation of state model allows the user to specify how the working fluid density depends on temperature and pressure. It also determines how other quantities are evaluated such as density derivatives, enthalpy, speed of sound (for compressible fluids), and certain transport properties like thermal conductivity, dynamic viscosity, and specific heat. While there are several built-in options available in STAR-CCM+, for certain fluids or certain states of a fluid (e.g. supersaturated state of steam), no data is available in the STAR-CCM+ database. In such situations, the user has the latitude to define (usually by tabular input) all equation of state data. For RCIC turbine modeling, steam is expected to exist in super-heated, saturated, and super-saturated states at various points in the simulation. Since STAR-CCM+ built-in steam/water data does not cover all the aforementioned thermodynamic states, user-defined data from International Association for the Properties of Water and Steam (IAPWS) Industrial Formulation-1997 (IF97) was used [IAPWS, 2007].

## 6.1.1.4.5 User-defined Sources via Field Function Utility

The user-defined scalar/vector field function utility is a means by which conservation equation source terms can be specified. A litany of field function arguments from the simulation are available for use. Field functions are updated on-the-fly as the solution progresses. Once defined a scalar/vector field function can be plotted, visualized in a scene, or used in the simulation directly (e.g. through source term definition).

# <u>6.1.1.4.6 Mixing Planes and Moving Reference Frames</u>

Mixing plane interfaces and moving reference frames play an important role in RCIC system turbine simulations of this dissertation. Both are used together in order to get time-averaged, steady-state solutions for turbo-machinery flows involving rigid-body rotational/translational motion which are inherently unsteady.

Mixing planes are implemented as interfaces across which circumferentially-averaged flow field data is transferred in a conservative manner between two rotationally periodic regions that share the same axis [CD-ADAPCO User's Guide, 2016]. The averaging of quantities (mass, momentum, energy, etc.) across a mixing plane occurs according to "bins" or uniformly-thick patches of area spanning the entire length and breadth of the boundary associated with the mixing plane interface. The transfer of information is such that identical, average quantities are used for each and every cell within a given bin. There are explicit and implicit options, the difference being the update strategy for circumferential averages. The user has limited control over mixing plane bin characteristics. At the geometry parts level, surface contacts can be designed so as to tailor a mixing plane interface to a limited area. Also, the so-called "bin coarsening factor" grants some control over the circumferential bin thickness. Figure 12 shows a mixing plane with two circumferential bins between two regions (a stator at left, a rotor at right). As the right-most region rotates or is subjected to a moving reference frame, the upstream flow quantities from the stator region are "mixed out" or averaged across mixing plane bins so that a time-averaged flow across the mixing plane is used.

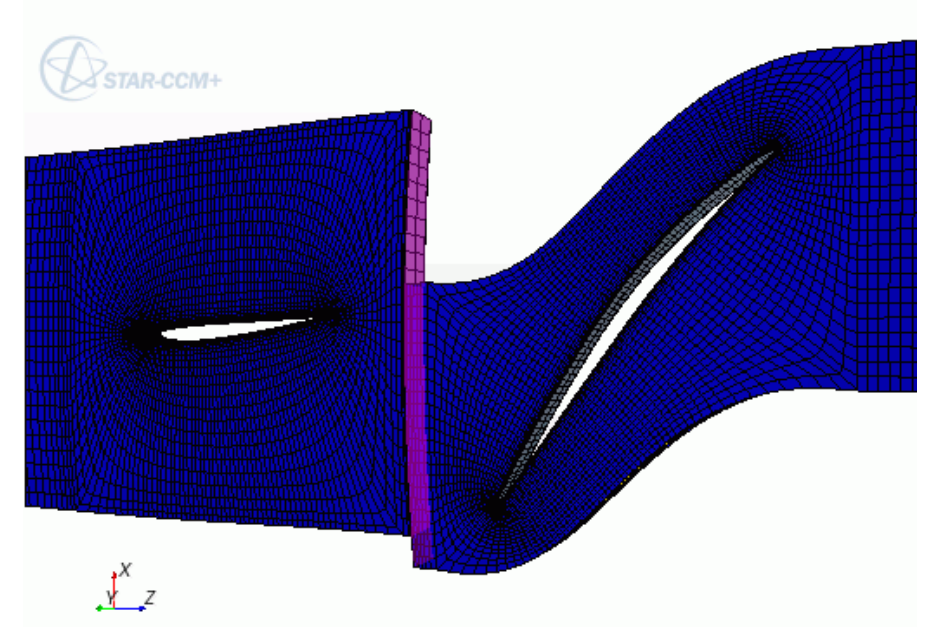


Figure 12 Mixing plane illustration (shown in purple) [CD-ADAPCO User's Guide, 2016]

With a moving reference frame, some effects of rotational and/or translational motion on a flow field can be captured without the heavy computational burden of a moving mesh. Similar to the mixing plane interface formulation, moving reference frames are appropriate in the context of steady-state analyses and can help provide a time-averaged depiction of turbo-machinery flows that are inherently unsteady. Applying a moving reference frame to a region, e.g. the right-most region of Figure 12 generates grid fluxes (new terms) in the conservation equations that approximate the effects that would be seen with true grid vertex motion [CD-ADAPCO User's Guide, 2016]. Figure 13 illustrates (in a two-dimensional view) the use of a mixing plane, periodic

interfaces, and a moving reference frame in the context of a turbo-machine which has a stator region (at left) and a rotor region (at right) containing the imposed moving reference frame.

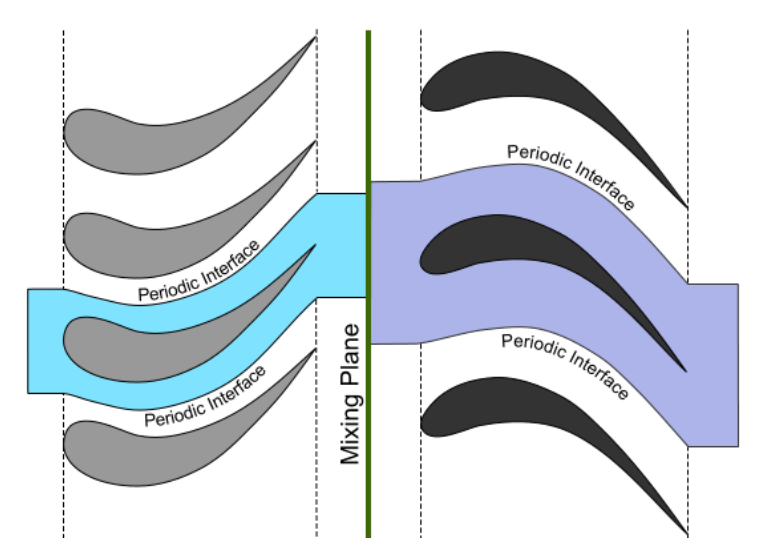


Figure 13 Mixing plane, periodic interfaces, and moving reference frames [CD-ADAPCO User's Guide, 2016]

#### 6.1.1.4.7 Derived Parts and Mesh Refinement via Volumetric Controls

Derived parts are one mechanism by which solution data may be accessed and/or manipulated (through certain operations like surface or volume averaging) in a STAR-CCM+ simulation. Essentially, the user has the capability to extract data for any part of the solution space without limit to defined regions, boundaries, cells, etc. [CD-ADAPCO User's Guide, 2016]. Derived parts can generally be described as user-defined parts based on other so-called "parent" parts (usually these are geometry parts). There are several types, but extensive use is made here of "implicit section" derived parts and, more specifically, planes and constrained planes. Implicit section parts are functions of coordinates and are useful for generating reports that tally solution quantities (e.g. mass flow rates and velocities) across certain user-defined surfaces of interest. For example, a user could insert a plane that spans the height and depth of a steam nozzle or that covers the exit area of a rotor bucket.

When properly coupled with a report, such use of derived parts can yield surface (plane) averaged solution quantities. For example, when a surface-average report is created using a plane derived part and the mass flow rate scalar field function, one can ascertain an average mass flow rate corresponding to the derived part. As explained in the results section, just such a calculation is done at the CFD level to ascertain factors entering into the systems-level Terry turbine velocity stage model.

Mesh refinement is sometimes necessary to better resolve the physics of certain regions of interest in a simulation. Two examples most important to this study are near-wall regions (where prism layers are constructed for turbulence modeling) and the nucleation/condensation zone of a steam nozzle. Volumetric controls apply to the mesh models utilized in a given simulation. With respect to this study, the polyhedral and prism layer mesh models are in play.

For the polyhedral mesh model, a control on target cell size can be set for a geometry part (a user-defined cylinder, sphere, box, cone, etc.) overlaid onto the problem geometry. Within the geometry part, the mesh is altered according to control target cell size. In areas where sharp gradients in

solution quantities are expected, the mesh may be refined for better resolution and presumably higher fidelity. An example that applies to steam nozzle analyses would be the diverging section downstream of the throat where nucleation and condensation is expected to occur over a short distance. Nucleation rate can change by an order of  $10^{20}$  or more, so a large number of small cells in the vicinity of the nucleation front would help with resolution.

For the prism layer mesh model, controls are available for the number of layers, their spacing, and their overall thickness. Across a steam nozzle along the direction of main flow, velocities can change by two or three orders of magnitude such that the nearest-wall prism layer thickness must decrease in order to keep y+ within range for whatever turbulence model is in use. This requirement could be met by increasing the number of prism layers along the nozzle flow direction or possibly by altering size distribution and/or total thickness.

### **6.1.2 Terry Turbine**

This section focuses largely on the physical and mathematical details of the pressure stage model developed for CMFD analyses of the RCIC turbine. The full formulations used for both pressure and velocity stage analyses of the turbomachine (with steam and air) are covered in this section. In the sequence of sub-sections below, a topic will be theoretically expounded and then described in sufficient (often simplified) physical and mathematical detail for CMFD analyses.

### 6.1.2.1 Physics of Condensing Steam Flow

The RCIC turbine pressure stage constitutes a complex thermodynamic system featuring non-equilibrium dispersed steam/water flow. Heat and mass transfer processes take place under super-saturated and saturated conditions and in continuum and free molecular regimes. In this section, the thermodynamics of phase change (droplet formation) in a mostly pure, homogeneous medium (steam) will be reviewed as will the process of drop-wise steam condensation. Both bear relevance to the problem at hand because the CMFD model incorporates conservation equation source terms to account for them. Compressible flow, turbulence in dispersed two-phase flow, and equation-of-state treatments for steam/water thermodynamic systems will be discussed also.

Thermodynamic aspects of steam-to-water phase change are covered in some detail here because a basic comprehension promotes understanding of the CMFD model and the fluid dynamics of a real-world RCIC turbine pressure stage. Across a steam nozzle in the RCIC turbine, incoming steam (dry superheated or high-quality saturated) is expanded such that enthalpy is converted into kinetic energy that may then be imparted to rotor buckets and converted into a torque on the pump shaft. The expansion occurs first in the converging section of the nozzle (while the flow is subsonic) and continues in the diverging section of the nozzle (while the flow is super-sonic). The steam pressure declines rapidly, and saturation conditions are reached somewhere at or slightly beyond the nozzle throat. From there, the assumption of thermodynamic equilibrium throughout the remainder of expansion has been shown [Mohsin et al., 2008] to yield under-predictions in steam mass flow at the nozzle discharge. More specifically, if non-equilibrium effects due to supersaturation are neglected, there is typically a 2-4% under-estimation in the steam mass inventory at nozzle discharge. The discrepancy is due to non-equilibrium effects, namely steam super-saturation and an attending delay in the onset of phase change (droplet formation and subsequent drop-wise condensation). The RCIC turbine relies primarily upon an impulse from impinging steam to turn the rotor, so an accurate prediction of steam discharge from the nozzles is crucial for accurate modeling. Thus, the CMFD model must account for non-equilibrium effects to some extent.

# 6.1.2.1.1 Homogeneous Nucleation

To understand the nature of the problem at hand, one must first distinguish between two mechanisms of water droplet formation from steam: homogeneous nucleation and heterogeneous nucleation. The term "nucleation" refers to the first formation of thermodynamically stable droplet embryos in the midst of saturated or super-saturated vapor. Nucleation occurs in a condensing vapor as a result of the tendency to minimize free energy in a thermodynamic system. Heterogeneous nucleation is of secondary importance here but refers to a situation in which some "nucleation site" in or adjacent to the condensing vapor – e.g. impurities, ions, or a rough wettable surface – aids the process of phase change. Nucleation sites effectively lower the Gibbs free energy barrier to nucleation (an explanation of which is given in the context of homogeneous nucleation below). Homogeneous nucleation is of primary interest here and refers to a situation in which a pure condensing vapor manufactures its own embryonic droplets without any assistance from nucleation sites in overcoming the Gibbs free energy barrier to nucleation. The following paragraphs include a detailed description of homogeneous nucleation as a thermodynamic, kinetic, and inherently probabilistic phenomenon. The excellent exposition put forth by McDonald [1962a, 1962b] serves well as a guide for discussion.

Considering pure, condensing steam (water vapor at the saturation pressure for its current temperature) and accepting without further evidence that the steam is inclined to minimize its free energy, the only way this minimization occurs is by phase change, i.e. the formation of small, embryonic droplets of water and subsequent growth by drop-wise condensation. When this happens, the bulk free energy of the steam decreases in an amount proportional to the mass (or volume) of the droplet formed. Therefore, the bulk free energy of the vapor decreases by an amount proportional to the cube of the drop embryo radius. The process actually unfolds in three parts:

- 1. isothermal decrease of vapor pressure to the saturation pressure,
- 2. conversion of vapor at saturation to liquid at saturation, and
- 3. isothermal increase of pressure to higher internal pressure of curved droplet

The first step is the most energetically consequential and the other two may be ignored for present purposes. Condensation would seem to move the system to a lower level of free energy except that along with droplet formation comes an increase in droplet surface area and an attending increase in system free energy. Thus, the system free energy increases as the square of the radius of the droplet formed. An equation for the change in free energy  $\Delta F$  accompanying drop formation then looks like:

$$\Delta F = 4\pi r^2 \sigma - \left(\frac{4}{3}\right) \pi r^3 \rho_{liq}(T_{stm}) RT_{stm} \ln(S)$$
 (1)

where:

r = radius of just-formed droplet [m] ;  $T_{stm}$  = steam temperature [K] R = gas constant of steam [J/mol/K] ;  $\rho_{liq}(T_{stm})$  = liquid density at  $T_{stm}$  [kg/m³]

 $S = P/P_{sat}$  = super-saturation ratio ;  $\sigma$  = Surface tension [N/cm]

There are dueling terms in the free energy equation. For small but positive r, the first term will mathematically dominate the second and keep the net free energy change of vapor condensation above zero, rendering the process of drop-wise condensation thermodynamically unfavorable. Condensation cannot move the system to a stable state of lower free energy and drop-wise condensation is no longer a spontaneous process. Phase change is delayed and the steam stays dry

in a metastable state called "super-saturated" or "super-cooled". The term "super-saturated" indicates a vapor pressure greater than the saturation pressure for the current vapor temperature, i.e. the super-saturation ratio exceeds unity. The term "super-cooled" indicates a vapor temperature lower than the saturation temperature for the current vapor pressure. Note from equation (1) that the bulk free energy term – which becomes larger in magnitude with increasing super-saturation ratio – ensures that  $\Delta F(r)$  has a maximum, i.e. an activation energy barrier, at some critical drop radius. Also, note that this critical drop radius decreases as super-saturation increases (since, approximately, the droplet forms isobarically and isothermally). The free energy barrier must be surmounted somehow for vapor condensation to become a spontaneous process and for the system to move towards thermodynamic equilibrium. Until the barrier is overcome, the steam stays in the metastable super-saturated state. Very small liquid embryos can still evolve from steam, but they cannot grow to critical size by steam condensation.

By differentiating equation (1) with respect to r (holding other variables constant) and setting the result equal to zero, the critical droplet radius  $r^*$  may be found as:

$$r^* = 2\sigma(T_{stm})/\rho_{liq}(T_{stm})RT_{stm}\ln(S)$$
 (2)

The maximum height of the energy barrier,  $\Delta F^*$ , corresponding to the critical droplet radius:

$$\Delta F^* = 16\pi\sigma (T_{stm})^3 / 3 \left(\rho_{liq}(T_{stm})RT_{stm}\ln(S)\right)^2$$
(3)

Note that equation (3) is simply Kelvin's equation describing the change in vapor pressure due to a curved liquid/vapor interface. The curvature of a critical embryo is such that it would raise the vapor pressure to the super-saturated pressure P from the saturation pressure  $P_{sat}$ . Equivalently, a droplet must reach the critical size in order to exist in metastable equilibrium with its super-saturated condensing vapor (which is itself a metastable state). A broad definition of metastability is given by Guggenheim [McDonald, 1962a] as:

"Any state which is stable with respect to all states differing only infinitesimally from the given state, but unstable with respect to some other state differing finitely from the given state"

The super-saturated condensing vapor satisfies Guggenheim's definition as does the critical droplet. If conditions change by some finite amount in either case, the super-saturated vapor can undergo reversion to thermodynamic equilibrium and the critically-sized droplet could either evaporate (if radius falls just below critical) or spontaneously grow (if radius climbs just above critical).

The question remains: how can critical droplets form and grow if embryonic droplet growth is disallowed by system thermodynamics? Since a droplet is merely a collection of water molecules, the question becomes: are there avenues other than condensation growth whereby water molecules may aggregate to possibly form a critical droplet? One may also ask if the free energy barrier could be lowered such that a critical droplet requires a smaller collection of water molecules. As already explained, the thermodynamic barrier  $\Delta F^*$  and the required critical radius  $r^*$  tend to decrease as steam super-saturation ratio S increases. So the longer the steam expands in a metastable state, the larger S grows and the smaller  $r^*$  becomes. Regardless of the manufacturing mechanism, critical droplets are more probably formed at higher steam super-saturation.

To identify the alternate means of critical droplet formation, McDonald [1962a] points out that super-heated (sub-saturated) or saturated steam (with S < 1) is not entirely free of liquid phase

embryos. Rather, embryos exist in a statistically-steady Boltzmann-like size distribution according to change in free energy for a given embryo size (size directly correlates to number of constituent water molecules). This distribution is supported by so-called "fluctuation phenomena" or random interactions of water molecules in vapor. As super-saturation increases, there is a general increase in embryo population across every point in the size distribution. Sufficient super-saturation ought to simultaneously lower the required  $r^*$  and increase the population of larger-sized embryos, thus making it more probable that collisions between larger embryos (fluctuation phenomena) could assemble a critical or supercritical embryo. Supercritical embryos have surmounted the free energy barrier such that their growth by vapor condensation is a thermodynamically-favorable, spontaneous process. Going back to equation (1), this means that the decrease in bulk free energy associated with droplet growth outmatches the increase in surface free energy accompanying that growth. Hence free energy is minimized by drop-wise condensation on supercritical embryos. Reversion to equilibrium from metastability coincides with spontaneous condensation growth of sufficiently many supercritical embryos.

Nucleation in the specific context of steam nozzle flow is discussed later, but it is important to note that phase change delay by steam super-saturation amounts to mere fractions of a millisecond assuming a super-heated or dry saturated nozzle inlet condition. Strictly speaking, the evolution of critical droplets is a kinetic process that unfolds over that small but finite period of time. However, as will be shown subsequently, critical droplet formation can be modeled as instantaneous with a steady-state critical droplet nucleation rate that depends on steam supersaturation and other parameters. The reader is referred to McDonald's overview of nucleation kinetics [McDonald, 1962b] for a complete discussion, but a few highlights of that discourse are included here.

Liquid droplet embryos evolved from steam are born sub-critical and at once are exposed to an environment in which, on average, evaporation (loss of water molecules) from the embryo exceeds condensation (gain of water molecules) on the embryo. Conversely, super-critical embryos have an excess of growth by condensation over decay by evaporation. A critically-sized embryo sees a balance in growth and decay of constituent water molecules. Dynamics of molecular exchange are illustrated by Figure 14 which shows evaporation, condensation, and net appearance rates as a function of embryo size (g being the number of water molecules). The condensation rate increases monotonically as embryo surface area increases with increasing g. The evaporation rate will eventually increase under action of increasing surface area but initially decreases due to a rapid rise in net work of escape (for an evaporating molecule) as the number of nearest-neighbors increases (g increases). This latter effect is considerable at first but becomes less consequential as g increases. The net loss rate curve shows a sub-critical region, a critical point, and a super-critical region. To develop a useful mathematical description of nucleation, the chaotic, statistical molecular interactions encapsulated by Figure 14 may be described by differential equations under simplifying assumptions. McDonald [1962b] gives valuable insight into embryo population dynamics.

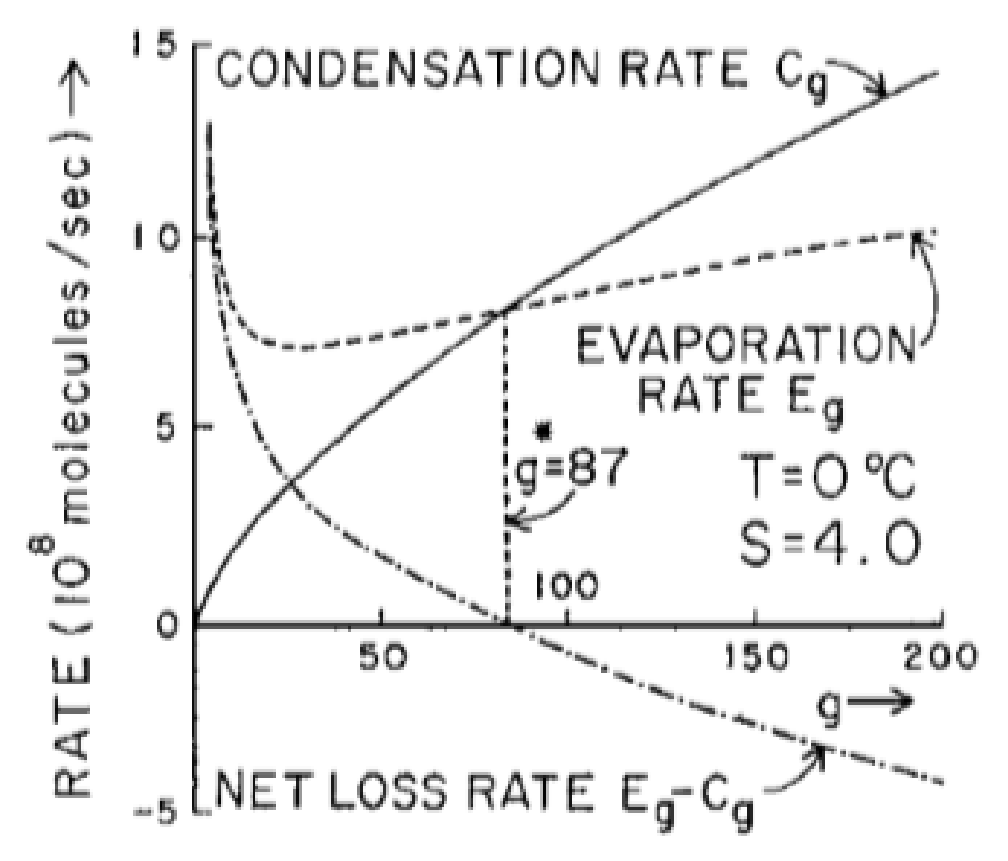


Figure 14 Condensation, evaporation, and net growth [McDonald, 1962b]

The stage of unbalanced, nonsteady-state embryo growth refers to a transient condition just after vapor has entered a super-saturated state (via isothermal compression or adiabatic expansion). The liquid embryo population (recall from above that a distribution exists before super-saturation) is at this point building up due to collisional processes. Condensation occurs when molecules collide with and stick to the embryo, and evaporation occurs when molecules escape. This stage can be described with a differential balance equation for concentration  $N_g$  of embryos containing g water molecules (g-mers):

$$\frac{\partial N_g}{\partial t} = I_{g-1} - I_g \tag{4}$$

where:

 $I_g = C_g N_g - E_{g+1} N_{g+1}$  = Current flowing between (g-1)-mers and g-mers  $C_g$  = Condensation rate for a g-mer ;  $E_g$  = Evaporation rate for a g-mer

When the current  $(I_g)$  equals zero for all g-mers and when the current equals some non-zero value for all g-mers, there exists a balanced and an unbalanced steady-state, respectively. In particular, the unbalanced steady-state case serves as the basis for a mathematically convenient and physically realistic predictor of the steady-state droplet embryo population. One simplifying assumption which is credible in light of the physical timescales involved is that the nucleation process may be divided into two distinct parts:

- 1) Short (tens of μs) transient build-up of an embryo population containing moderately large *g*-mers, and
- 2) Longer (tens to hundreds of ms) period of sustained supercritical embryo generation throughout the vapor

The latter period concludes when reversion to equilibrium commences. For a steam nozzle, this reversion is due to latent heat effects that relieve super-saturation.

Moving forward with this slightly simplified view of the nucleation process, the first and briefest period can be assumed instantaneous while the second and longest period can be approximated by the unbalanced steady-state idealization. For the unbalanced steady-state, the concentration of g-mer embryos, for all g in the embryo size distribution, does not evolve with time because the same nonzero current (for all g-mers) flows through the entire embryo chain. This is equivalent to saying that the same balance between condensation and evaporation is preserved between every (g-1)-mer and g-mer for all g in the embryo size distribution. A non-zero, positive current (where condensation dominates evaporation) between every neighboring g in the embryo size distribution is preserved by a statistical excess of condensational gain over evaporative loss. Note that this is true even when  $g < g^*$  where the loss rate of g-mers by evaporation outpaces the appearance rate of g-mers by condensation. Even though the loss rate exceeds the gain rate, total condensation can dominate total evaporation if the concentration of (g-1)-mers (any of which may grow to g-mers by condensation) sufficiently exceeds the concentration of g-mers (which may decay to smaller size by evaporation).

Another artifice is introduced along with the unbalanced steady-state approximation: at some size  $G >> g^*$ , let all molecules comprising G be reintroduced as monomers (single water molecules) at the "bottom" of the embryo chain. This is the so-called Szilard artifice [McDonald, 1962b] and its purpose is to maintain the steady state with a finite number of water molecules in the system. It also imposes a boundary condition on the nucleation problem, thus helping with the mathematical description of nucleation. Predictions from the eventual nucleation model are insensitive to the exact choice of G. Another boundary condition on the nucleation problem is needed. It is gotten from an observation of the balanced steady-state case: the concentration of g-mers for the unbalanced steady-state case and the balanced steady-state case are very nearly equal in the limit as g approaches unity [McDonald, 1962b].

An expression for the constant current may be derived by putting these pieces together and manipulating the mathematical description of the current. The result is that the current may be written in terms of known quantities (condensation rates, g-mer concentrations, the Szilard boundary condition, and the asymptotic boundary condition from the previous paragraph). The reader is referred to McDonald [1962b] for further mathematical details, but the end result is an expression for the generation rate of super-critical embryos. This expression has an exponential factor encapsulating the effects of super-saturation that tends to dominate the kinetics of the nucleation process.

The review given by McDonald [1962a, 1962b] comprises much of the so-called classical nucleation theory. Revisions outlined by Bakhtar and Young [2005] have been made to classical theory. The nucleation model employed in the CMFD studies here assumes classical nucleation theory and uses corrections posited by Courtney [1961] and Kantrowitz [1951] pertaining, respectively, to partial pressure of molecular clusters and the non-isothermal nature of nucleation. Courtney's correction amounts to a reduction in the nucleation rate by a factor equal to the supersaturation ratio, while Kantrowitz's correction amounts to a multiplicative factor on the classical nucleation rate. Finally, an expression for the nucleation rate (appearance of critically-sized embryos) is:

$$J = \left(\frac{1}{1+\nu}\right) \left(\frac{2\sigma(T_{stm})}{\pi m^3}\right)^{1/2} \left(\frac{\rho_{stm}^2}{\rho_{lig}(T_{stm})}\right) e^{\left(\frac{-4\pi r^{*2}\sigma(T_{stm})}{3KT_{stm}}\right)}$$
(5)

where:

J= Nucleation rate of droplets at  $r^*$  [drops/m³/s] ; m= Mass of water molecule [kg]  $\rho_{stm}=$  Steam density [kg/m³] ; K= Boltzmann constant = 1.380648\*10<sup>-23</sup> [J/K]  $\nu=2\left(\frac{\gamma-1}{\gamma+1}\right)\left(\frac{h_{fg}(P)}{RT_{stm}}\right)\left(\frac{h_{fg}(P)}{RT_{stm}}-0.5\right)=$  Kantrowitz isothermal correction factor  $\gamma=$  Specific heat ratio ;  $h_{fg}=$  Latent heat of vaporization [J/kg]

For modeling purposes, this nucleation rate is instantaneously evolved according to local conditions. Gyarmathy [1976] outlines a brief derivation of the nucleation time delay corresponding to typical steam nozzle conditions. By this estimate, the delay is approximately a nanosecond which is clearly negligible even with respect to the microsecond scale. This is some justification of the aforementioned assumption that steady-state nucleation is instantaneous.

One noteworthy source of uncertainty in classical and modified-classical nucleation theory regards the use of the bulk surface tension of a plane liquid interface despite the highly-curved surfaces of freshly-nucleated embryos. At present, no conclusions can be drawn as to the truly correct value for surface tension, but note that the choice of values may drastically influence nucleation theory predictions.

### 6.1.2.1.2 Drop-wise Condensation

Once the steam super-saturation lowers the thermodynamic barrier to condensation, critical droplets appear at a high volumetric rate throughout the vapor. Drop-wise vapor condensation on critical embryos is a spontaneous process that quickly relieves super-saturation by the phenomenon of condensation shock. The underlying heat and mass exchanges, which strongly depend on droplet size, must be mathematically modeled because they contribute to inter-phase terms in the CMFD formulation.

Drop-wise condensation heat/mass transfer cannot be considered a continuum phenomenon for all embryo sizes, particularly sizes on the order of  $r^*$ . Rather, heat/mass transfer must initially be considered from a free-molecular perspective and, as an embryo grows by condensation through a broad transition regime, the continuum approximation becomes valid [Gyarmathy, 1976]. The pertinent measure for size regime is the Knudsen number:

$$Kn = \frac{\ell}{2r} \tag{6}$$

where:

 $\ell$  = Mean free path of steam molecule [m]

The mean free path can be computed from one of several prescriptions using, for example, steam properties at saturation conditions. It represents the average distance of free travel by steam molecules before collision or interaction. A large Knudsen number implies the steam mean free path exceeds the droplet size, so the droplet "sees" individual molecules streaming around the vapor space. A small Knudsen number implies the droplet is much larger than the steam mean free path, so the droplet "sees" a continuous medium instead. Typically, Knudsen number less than or equal to 0.01 indicates continuum flow whereas Knudsen number greater than or equal to 4.5 indicates free-molecular flow [23].

Regardless of Knudsen number, the process of condensation is governed by latent heat removal from droplet to vapor via conduction heat transfer. Upon condensation, mass moves from vapor to droplet with an attending latent heat release to the droplet (as condensation is an exothermal process). In actuality some small fraction of latent heat is stored in the droplet while the remainder transfers back to vapor. To good approximation however, the entirety of the latent heat transfers back to vapor. This is the energy balance maintained throughout the process of drop-wise condensation, with the final result being sensible heat transfer through a finite temperature difference from droplet to vapor. Size regime is important when choosing a conduction heat transfer coefficient to characterize drop/vapor heat transfer so that:

$$h_{fg}(P)\frac{dm}{dt} = h_{fg}(P)4\pi r^{2}\rho_{liq}(T_{stm})\frac{dr}{dt} = 4\pi r^{2}\alpha_{r}(T_{r} - T_{stm})$$

$$= 4\pi r^{2}\alpha_{r}(T_{sat}|_{P} - T_{stm})\left(1 - \frac{r^{*}}{r}\right)$$
(7)

where:

 $\alpha_r = \text{Droplet/vapor heat transfer coefficient } [\text{W/m}^2/\text{K}]$ ;

 $T_r$  = Droplet temperature [K]

 $T_{sat}|_{P}$  = Saturation temperature at system pressure [K]

The drop-to-vapor heat transfer constitutes an increase in steam entropy and raises steam pressure rapidly, giving rise to the condensation shock phenomenon that corrects the system to equilibrium. Note the temperature change that characterizes the heat transfer is the difference between the droplet and the vapor, but a capillarity relation [23] may be used to eliminate droplet temperature as an unknown. The capillarity relationship says that the steam sub-cooling multiplied by a geometric factor approximates the difference between droplet temperature and steam temperature.

In the free molecular regime, kinetic theory is often employed to predict heat and mass transfer to droplets, e.g. by taking the difference between condensation and evaporation rates [Hill, 1966]. Under the assumptions of negligible droplet slip velocity, uniform steam temperature, and negligible temperature variations within the small droplets, Hill [1966], Young [1982], and Zori and Kelecy [2005] suggest a free-molecular condensation rate:

$$\frac{dr}{dt} = \left(\frac{\gamma+1}{2\gamma}\right) C_{p,stm} (T_{sat}|_{P} - T_{stm}) \left(\frac{P}{\rho_{liq}(T_{stm})h_{fg}(P)} (2\pi RT_{stm})^{-1/2}\right)$$
(8)

where:

 $C_{p,stm}$  = Specific heat capacity at constant pressure of steam [J/kg/K]

In the continuum regime, the typical approach is to employ a theoretically-developed and empirically-tuned heat transfer coefficient. Gyarmathy [1976] proposes a heat transfer coefficient of the form:

$$\alpha_r = \begin{cases} \frac{k_{stm}}{r} \left( 1 + \left( \frac{2\sqrt{8\pi}}{1.5 * Pr_{stm}} \right) \left( \frac{\gamma}{\gamma + 1} \right) \left( \frac{Kn}{a_{th}} \right) \right)^{-1} & , free molecular \\ 0.357 \left( \frac{k_{stm}}{r} \right) \sqrt{Re_r Pr_{stm} + 7.96} & , continuum \end{cases}$$
(9)

where:

 $k_{stm}$  = Thermal conductivity of steam [W/m/K] ;

 $Pr_{stm}$  = Steam Prandtl Number

 $a_{th}$  = Thermal accommodation coefficient;  $Re_r$  = Droplet Reynolds Number

with a droplet growth law given by:

$$\frac{dr}{dt} = \left(\frac{k_{stm}}{\rho_{liq}(T_{stm})h_{fg}(P)}\right) \left(\frac{1 - \frac{r^*}{r}}{1 + \left(\frac{2\sqrt{8\pi}}{1.5 * Pr_{stm}}\right)\left(\frac{\gamma}{\gamma + 1}\right)\left(\frac{Kn}{a_{th}}\right)}\right) \left(\frac{(T_{sat}|_P - T_{stm})}{r}\right) \tag{10}$$

Or, more approximately:

$$\frac{dr}{dt} = \left(\frac{k_{stm}}{\rho_{liq}(T_{stm})h_{fg}(P)}\right) \left(\frac{1 - \frac{r^*}{r}}{r + 1.59\ell}\right) \left((T_{sat}|_{P} - T_{stm})\right)$$
(11)

where the following values are assumed:

$$Pr_{stm} = 1.3, \gamma = 1.2, a_{th} = 1$$

Note the thermal accommodation coefficient [Hill, 1966] essentially quantifies the amount of energy carried away by molecules that, upon colliding with a droplet surface, reflect from it rather than condense (and stick) to it. The very concept of a thermal accommodation coefficient assumes a condensation coefficient less than unity. Hill [1966] describes the condensation coefficient as the fraction of collided molecules that condense rather than reflect from a droplet surface. Both the thermal accommodation coefficient and the condensation coefficient factor into growth law formulations.

### 6.1.2.2 Dispersed-Phase Size Distribution Modeling

# 6.1.2.2.1 Polydisperse Droplet Size Distribution by Moment Method

Consider some general droplet population evolved from super-saturated steam. The phenomena of nucleation and condensation both drastically alter the size distribution of that population. Nucleation rapidly generates new droplets at the critical size while condensation quickly grows existing droplets to larger sizes. Since heat and mass transfer between vapor and droplets depends on droplet number density, size, and surface area, it is important to model the dispersed-phase size distribution in fair fidelity. The assumption of mono-dispersity at a suitably averaged droplet size has been used in the literature with some success. However, a more appealing alternative is put forth by Giordano [2008]. Polydispersity is captured by solving scalar transport equations for the first few statistical moments of a size distribution. A brief synopsis follows.

Assume a continuous droplet size distribution in radius r with number density function f such that the product f \* dr is the number of drops per unit mass of steam falling within the size range (r, r + dr). Also assume a four-dimensional phase space consisting of three spatial dimensions x, y, z and a droplet size (radius) dimension r. In a volume V' of this phase space, there is a total droplet population  $N_V$ :

$$N_V = \int_{V'} \rho_{stm} f dV' \tag{12}$$

The trajectories of droplets in the four-dimensional phase space are described by the usual components of velocity plus a droplet growth rate which could be interpreted as a droplet growth velocity:

$$\overrightarrow{u'} = \left[\frac{dx}{dt}, \frac{dy}{dt}, \frac{dz}{dt}, \frac{dr}{dt}\right] = \left[u_x, u_y, u_z, G\right]$$
(13)

Note that if zero phase slip is assumed (appropriate for sufficiently small droplets) the velocity components in the vector u' are those of steam. A conservation equation may be written for droplet number in an elemental volume of the phase space under the assumption that only nucleation and condensation affect the population (to the exclusion of coagulation/coalescence and break-up, which is a good approximation). Droplets appear in the phase space volume by nucleation (rate J) and stream through the phase space volume control surface S' under the influence of the velocity vector u'. Note that by the definition of the phase space and of u', the "control surface" must also consist of boundaries on droplet size. Droplets enter/exit the phase space volume by streaming across x, y, or z boundaries but also by condensation growth across r boundaries with "velocity" G. The droplet conservation equation is:

$$\frac{\partial}{\partial t} \int_{V'} \rho_{stm} f dV' + \int_{S'} \rho_{stm} f \left( \overrightarrow{u'} * d\overrightarrow{S'} \right) = \int_{V'} \rho_{stm} J dV'$$
 (14)

Applying Gauss' divergence theorem to the last term on the left-hand side, one obtains a differential balance equation for the droplet population in an Eulerian frame of reference that includes a transient term, two flux terms, and a volumetric source term:

$$\frac{\partial}{\partial t}(\rho_{stm}f) + \overrightarrow{\nabla} * (\rho_{stm}f\overrightarrow{u}) + \frac{\partial}{\partial r}(\rho_{stm}fG) = \rho_{stm}J$$
(15)

Note that the one flux term resulting from application of the divergence theorem is split into two: one for the usual convective flux involving flow velocity  $\vec{u} = [u_x, u_y, u_z]$  and one for the convective flux involving drop growth velocity G.

Now, consider the definition of the  $j^{th}$  moment of size distribution f:

$$\mu_j = \int_0^\infty r^j f dr \tag{16}$$

Here, the statistically-distributed radius r is raised to the  $j^{th}$  power and multiplied into the distribution function. The result is then integrated over all possible r. Given that r has units of length and the distribution function has units of inverse length times inverse mass, one could discern from dimensional considerations that the  $0^{th}$  moment is related to droplet number [drop/kg], the  $1^{st}$  moment is related to droplet size [m\*drop/kg], the  $2^{nd}$  moment is related to droplet surface area  $[m^2*drop/kg]$ , and the  $3^{rd}$  moment is related to droplet volume  $[m^3*drop/kg]$ . These first four moments may be used in conservation equation inter-phase heat/mass transfer source terms so as to capture the poly-disperse nature of the droplet population. Such an approach is more detailed than the mono-disperse treatment and simpler to implement than a discretized size binning approach. Each of the moments is a passive scalar quantity transported by the flow field. A general transport equation for the moments is still required.

Taking the product of  $r^j$  with the differential droplet balance equation, moving  $r^j$  across differential operators where possible, and integrating over all radii:

$$\int_{0}^{\infty} \left[ \frac{\partial}{\partial t} (\rho_{stm} r^{j} f) + \overrightarrow{\nabla} * (\rho_{stm} r^{j} f \overrightarrow{u}) + r^{j} \frac{\partial}{\partial r} (\rho_{stm} f G) = \rho_{stm} J r^{j} \right] dr$$
(17)

The first and second terms are straightforward. The term on the right-hand side is evaluated by allowing the nucleation rate to be represented as a step function since the source term produces droplets of one radius only (the critical radius). The third term on the left-hand side requires integration by parts:

$$\int_{0}^{\infty} \left[ r^{j} \frac{\partial}{\partial r} (\rho_{stm} f G) \right] dr = (r^{j} \rho_{stm} f G)_{0}^{\infty} - \int_{0}^{\infty} j r^{j-1} \rho_{stm} f G dr =$$

$$-j \rho_{stm} \int_{0}^{\infty} r^{j-1} f G dr$$
(18)

where:

$$\left(r^{j}\rho_{stm}fG\right)_{0}^{\infty}=0$$

 $\int_0^\infty r^{j-1} f G dr$  , requires knowledge about G(r) before it can be evaluated

Finally, the general moment transport equation is:

$$\frac{\partial}{\partial t} (\rho_{stm} \, \mu_j) + \overrightarrow{\nabla} * (\rho_{stm} \, \mu_j \overrightarrow{u}) = j \rho_{stm} \int_0^\infty r^{j-1} f G dr + \rho_{stm} J_* r^{*j}$$
(19)

where:

$$J_*$$
 = Nucleation rate  $\left[\frac{drop}{kg*s}\right]$  of droplets, size  $r^*$ , from integration of  $J_*\delta(r-r^*)$ 

A further closure describing the condensation growth (G = dr/dt) dependence on r is required to evaluate the integral in the moment transport equation. Considering the possible definitions of droplet growth laws from above, G(r) could be a constant. Even if G depends on r somehow, the dependence might be approximated as a constant by using a certain definition of r, e.g. the "two-zero" diameter as proposed by Giordano [2008]. Other measurements of significance could also be used, e.g. the "three-two" diameter also known as the Sauter mean diameter. In any case, the droplet growth rate G comes outside the integral on r and the definition of the size distribution moment is applied, i.e:

$$\int_0^\infty r^{j-1} f dr = \mu_{j-1} \tag{20}$$

In writing out the four moment equations, it is readily apparent that they are coupled through the condensation growth term:

$$\frac{\partial}{\partial t}(\rho_{stm}\,\mu_0) + \overrightarrow{\nabla} * (\rho_{stm}\,\mu_0\overrightarrow{u}) = \rho_{stm}\,J_* \tag{21}$$

$$\frac{\partial}{\partial t}(\rho_{stm}\,\mu_1) + \overrightarrow{\nabla} * (\rho_{stm}\,\mu_1\overrightarrow{u}) = \rho_{stm}(G\,\mu_0 + J_*r^*)$$
(22)

$$\frac{\partial}{\partial t}(\rho_{stm}\,\mu_2) + \overrightarrow{\nabla} * (\rho_{stm}\,\mu_2\overrightarrow{u}) = \rho_{stm}(2G\,\mu_1 + J_*r^{*2})$$
(23)

$$\frac{\partial}{\partial t}(\rho_{stm}\,\mu_3) + \overrightarrow{\nabla} * (\rho_{stm}\,\mu_3\overrightarrow{u}) = \rho_{stm}(3G\,\mu_2 + J_*r^{*3})$$
(24)

Notice that the 0<sup>th</sup> moment (proportional to total droplet number) has no condensation source term, only a nucleation source term. The 0<sup>th</sup> moment equation accounts for the effects of nucleation on total droplet number. The 2<sup>nd</sup> moment equation accounts for the effects of both condensation and nucleation on droplet surface area distribution. The 3<sup>rd</sup> moment equation accounts for the effects of both condensation and nucleation on droplet volume and/or wetness fraction. Some useful droplet population measures are related to size distribution moments:

$$n\left[\frac{drop}{m_{stm}^3}\right] = \rho_{stm} \,\mu_0$$
, Droplet number density (25)

$$d_{32}[m] = \frac{\mu_3}{\mu_2}$$
 = Sauter mean diameter (26)

$$\overline{r}[m] = \frac{d_{32}}{2}$$
 = Droplet average radius (27)

$$\beta \left[ \frac{kg_l}{kg_{stm}} \right] = \rho_{liq}(T_{stm}) \mu_0 \frac{4}{3} \pi \left( \frac{\mu_3}{2\mu_2} \right)^3 = \text{Droplet mass (wetness) fraction}$$
 (28)

$$\alpha \left[ \frac{m_l^3}{m_{stm}^3} \right] = \beta \left( \frac{\rho_{stm}}{\rho_{lig}(T_{stm})} \right) = \text{Droplet volume fraction}$$
 (29)

$$\overline{m} \left[ \frac{kg_l}{drop} \right] = \frac{\beta}{\mu_0} = \text{Mass of average}$$
 (30)

$$\rho_{stm}^{l} \left[ \frac{kg_{l}}{m_{stm}^{3}} \right] = \beta \rho_{stm} = \text{Droplet density in vapor}$$
(31)

$$\overline{A} \left[ \frac{m_l^2}{drop} \right] = 4\pi \overline{r}^2 = \text{Surface area of average droplet}$$
 (32)

$$a\left[\frac{m_l^2}{m_{stm}^3}\right] = \overline{A}n = \text{Droplet areal density}$$
 (33)

Note from the formulae above that mass, length, area, and volume units sometimes have subscripts indicating a phase (l for liquid, stm for vapor/steam). This is helpful in clarifying the physical meaning of certain droplet parameters.

### 6.1.2.2.2 Size Distribution Moments as Passive Scalars

As an interesting side note, the formulation above bears some resemblance to the S- $\gamma$  model for dispersed-phase size distribution modeling in STAR-CCM+ [CD-ADAPCO User's Guide, 2016]. Since the S- $\gamma$  model is compatible only with certain two-phase flow formulations (e.g. multiphase segregated Eulerian/Eulerian) that are not being exercised in CMFD analyses here, the S- $\gamma$  model cannot be used directly. Instead, the four size distribution transport equations can be cast as passive scalar transport equations which assume the form [CD-ADAPCO User's Guide, 2016]:

$$\frac{\partial}{\partial t} \int_{V} (\rho \, \phi_{j}) dV + \oint_{A} (\rho \, \phi_{j} \overline{u}) * dA = \oint_{A} J_{j} * dA + \int_{V} S_{\phi_{j}} dV$$
 (34)

where:

 $\phi_i$  is a passive scalar component

 $J_j$  a diffusion flux ;  $S_{\phi_j}$  is a source term for the passive scalar component

Comparing equation (34) to equations (21) through (24) it is readily apparent that the moments of the droplet size distribution are passive scalars that experience convective transport only (zeroed diffusion flux) and that have source terms equal to the right hand sides of equations (21) through (24).

### 6.1.2.3 Compressible Flow and Steam Nozzles

Nucleation and drop-wise condensation have already been discussed as stand-alone phenomena. It is useful to now consider them in the context of compressible, condensing steam flow in a converging-diverging nozzle as may be found in the pressure stage of the RCIC turbine.

## 6.1.2.3.1 Generic Converging-Diverging Nozzle Flow

A quick overview of compressible converging-diverging (CD) nozzle flow is in order. The discussion provided by Cengel and Boles [2008] is an excellent review of some basic concepts of compressible flow in nozzles. It is devoid of any two-phase non-equilibrium flow considerations, but the same concepts of choking and aerodynamic shock are important in condensing steam nozzle flow. Figure 15 shows the various possibilities for nozzle flow with stagnation inlet pressure  $P_0$ , back pressure  $P_b$ , and exit plane pressure  $P_e$ . There are several cases of back pressure (A through G) shown graphically in terms of pressure and Mach number. They run the gamut from no flow to choked flow with/without aerodynamic shocks inside/outside the nozzle.

For flow to occur at all, the back pressure must be less than the inlet pressure (case A shows no flow, no pressure drop). As the back pressure is reduced below the inlet pressure but held above  $P_C = P^*$ , flow along the nozzle commences and there is a pressure drop until the throat is reached (maximum velocity, mass flow rate, and Mach number). Since  $P_b$  is above critical pressure of the working fluid (the lowest pressure attainable at the throat regardless of back pressure), the Mach number at the throat is less than one and flow never reaches sonic speed. As such, the diverging section of the nozzle behaves like a diffuser and increases fluid pressure at the expense of decreasing velocity. Flow is sub-sonic throughout the nozzle and no aerodynamic shocks occur.

When the back pressure is lowered to just equal the critical pressure, flow goes sonic at the throat (Ma=1) but slows to sub-sonic in the diverging section of the nozzle. The maximum mass flow rate through the nozzle is just established at the throat where sonic flow prevails. Because of the choked condition at the nozzle throat, further drop in back pressure will not influence flow in the converging section. Therefore, the throat velocity and mass flow rate will not increase beyond their values for back pressure  $P_b$  equal to critical pressure  $P^*$ .

As back pressure is lowered below critical, flow at the throat remains choked but flow in the diverging section accelerates to super-sonic velocity since the diverging cross-section now behaves like a nozzle. A standing, compressive, normal shock occurs inside the diverging section of the nozzle while  $P_b > P_E$ . Since in this illustration  $P_E$  is the back pressure at which flow is approximately isentropic across the nozzle, if back pressure is higher an introduction of entropy is required. The shock is highly irreversible (non-isentropic) and suddenly decelerates the flow to sub-sonic while raising pressure. The rest of the diverging section acts as a diffuser, decelerating the flow and raising the pressure.

Reducing the back pressure towards  $P_E$  will effectively lengthen the region of super-sonic flow in the diverging section and push the location of the normal shock down the nozzle. Ultimately the normal shock is pushed to the nozzle exit plane when  $P_b = P_E$ . Flow across the nozzle is approximately isentropic and super-sonic conditions prevail beyond the throat until the shock at/near the exit plane. The shock leads to an emanating jet that is sub-sonic.

Decreasing the back pressure still further below  $P_E$  leads to expansion to pressure  $P_F$  (approximately isentropic) at the exit plane regardless of the value of  $P_b$ . The relative values of back pressure and  $P_F$  determine what happens just beyond the exit plane. If  $P_b > P_F$ , the flow is over-expanded because back pressure exceeds the exit plane pressure. This causes the standing shock at the exit plane to bow outward and leads to a mixed sub/super-sonic jet emanating from the nozzle. The shock is still compressive and there is also some degree of jet contraction because

the shock is not perpendicular to the nozzle wall. If  $P_b = P_F$ , there will be no shocks inside or beyond the nozzle. If  $P_b < P_F$ , the flow is under-expanded because exit plane pressure exceeds back pressure. This causes a complex pattern of oblique, expansive shocks (tending to lower pressure) to appear outside the nozzle, leading to a slightly expanded jet. These considerations underscore the need for a strong shock-capturing CMFD solution.

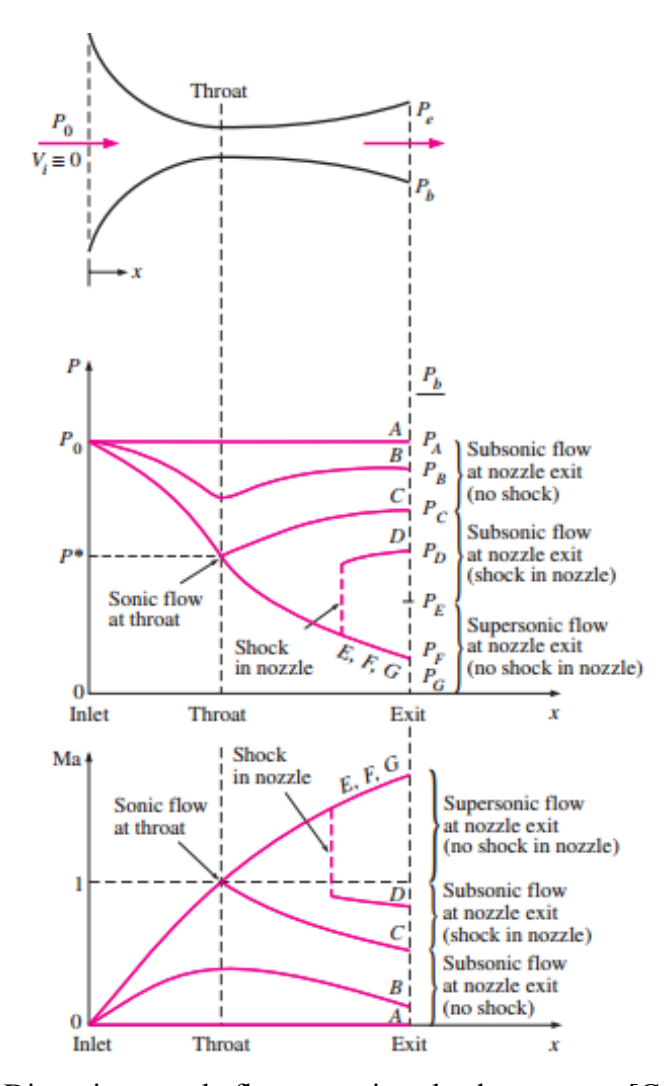


Figure 15 Converging-Diverging nozzle flow at various back pressures [Cengel and Boles [2008]

### 6.1.2.3.2 Condensing Steam Nozzle Flow

When super-heated or saturated steam expands in a converging-diverging nozzle, the steam pressure and temperature both decrease, eventually crossing into the saturation region. At this point, the steam temperature equals the saturation temperature for the steam pressure and one might expect phase change to commence. As discussed previously however, homogeneous condensation is often the only route for phase change and some short but finite amount of time is required to surmount the Gibbs free energy barrier. In the interim, steam exists in the usual saturation region but remains dry in a sub-cooled or, equivalently, a super-saturated state of thermodynamic non-equilibrium. Condensation becomes a thermodynamically-favorable (spontaneous) process when some sufficient degree of sub-cooling or super-saturation is

established. The point at which this happens (inside the saturation dome) is called the Wilson point and, for different nozzle inlet conditions, the locus of Wilson points forms the Wilson line. Typically, the Wilson line falls around the 4-5 % wetness curve in the saturation region and is often approximated as the 4% moisture line [Cengel and Boles [2008]. Thus, super-saturated steam will not begin condensing until its saturation conditions would dictate roughly a 96% quality.

The thermodynamics of steam nozzle flow are illustrated in an h-s diagram in Figure 16 [Hasini and Norhazwani, 2012]. The numbers on the diagram correspond to the pressure plot along the steam nozzle as shown in Figure 17. Super-heated inlet conditions are assumed at (1), and expansion to saturation at (3) and then to the Wilson line at (4) is shown.

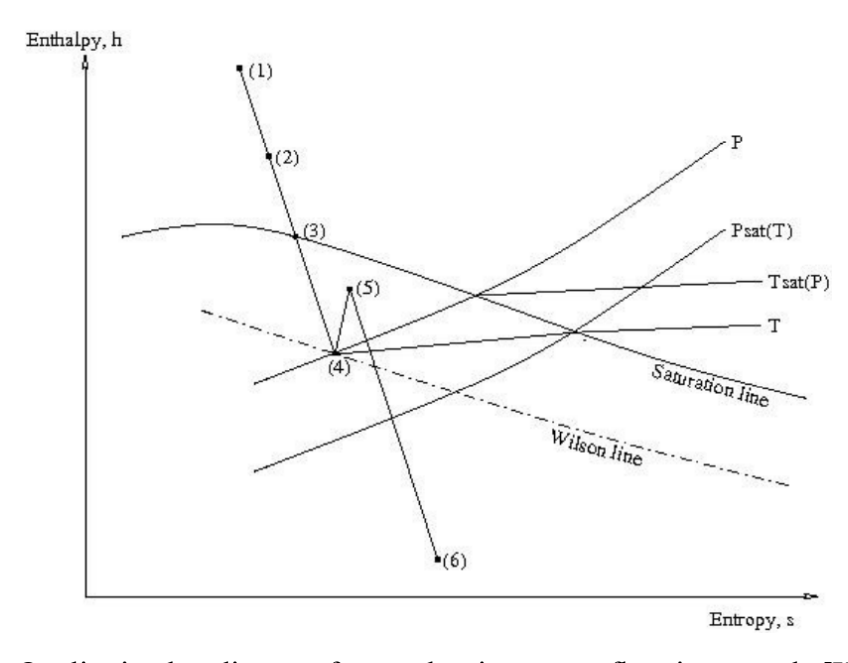


Figure 16 Qualitative h-s diagram for condensing steam flow in a nozzle [Hasini and Norhazwani, 2012]

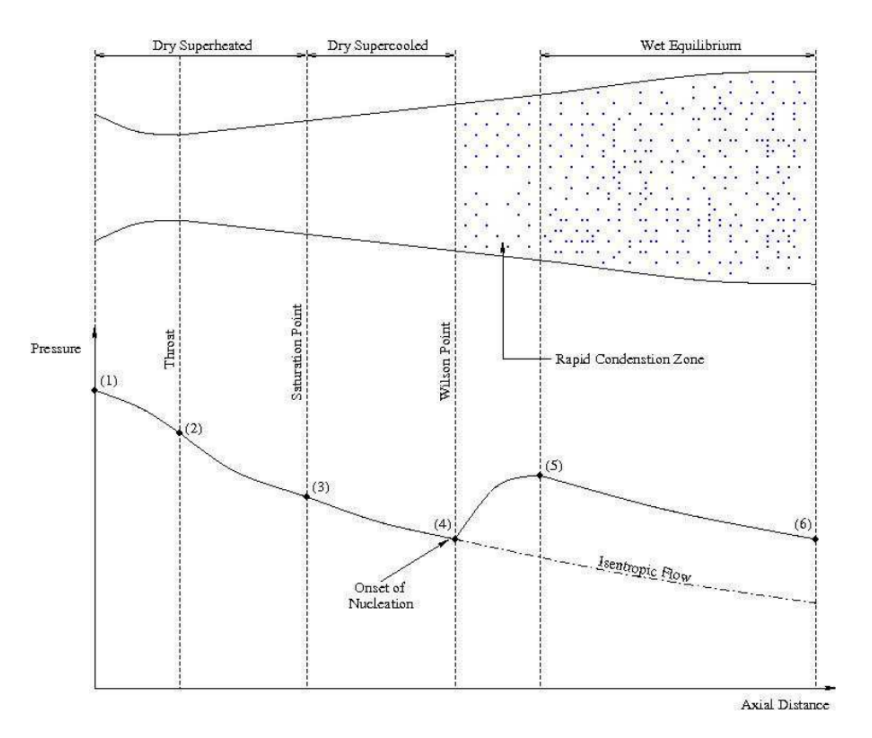


Figure 17 Qualitative pressure plot for condensing steam flow [Hasini and Norhazwani, 2012]

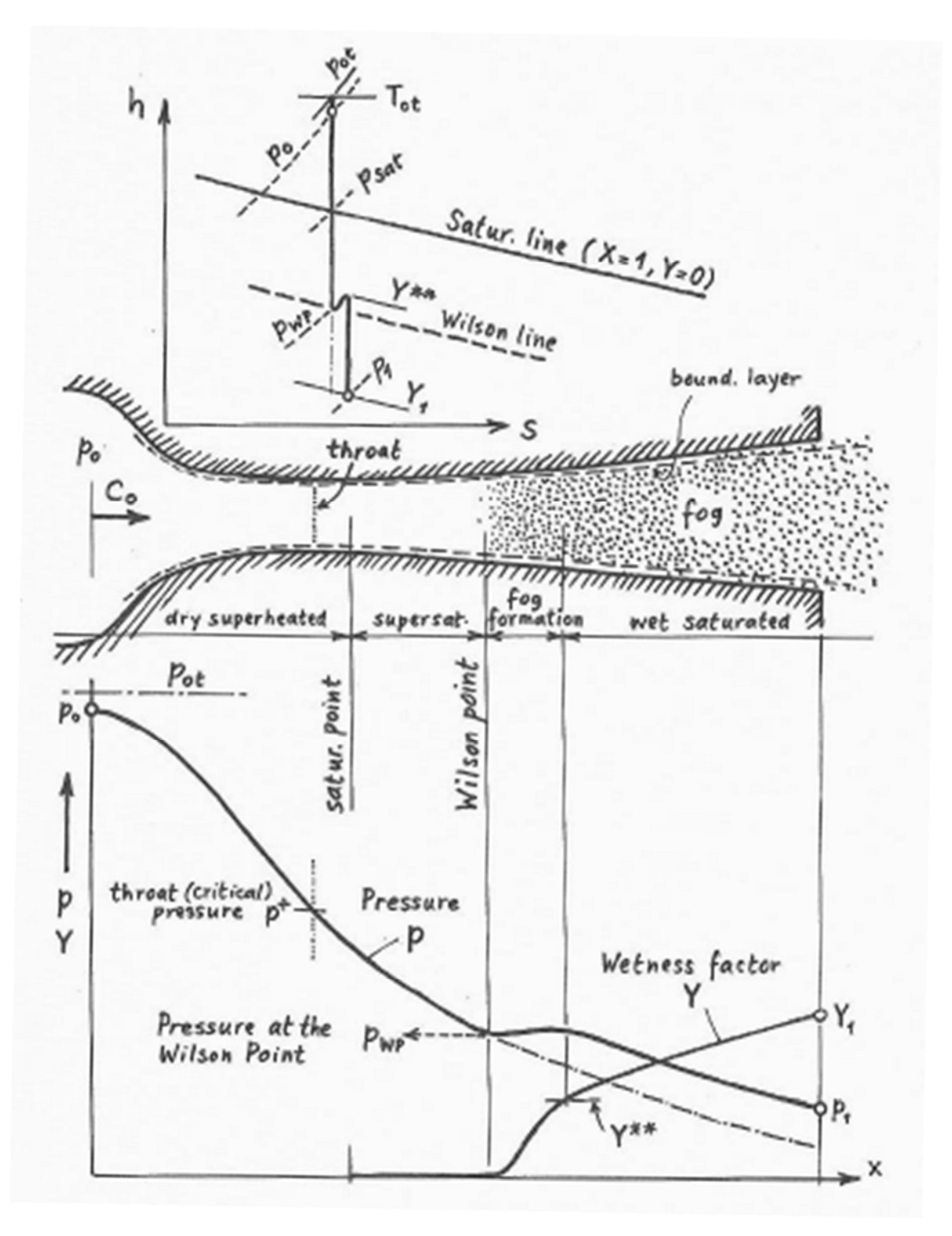


Figure 18 Qualitative illustration of wetness and pressure along a steam nozzle [Gyarmathy, 1976]

The region between (3) and (4) is the "nucleation zone" where dry sub-cooled (super-saturated) steam exists. The nucleation zone eventually terminates at the Wilson point (point of maximum sub-cooling and super-saturation) as nucleation furnishes a large number density of critically-sized droplets on which steam may condense unhindered by a thermodynamic barrier. The "condensation zone" begins at the Wilson point and terminates when condensation shock (pressure bump between (4) and (5)) has corrected the two-phase system back to thermodynamic equilibrium. The point of equilibrium at (5) is somewhere between the Wilson line and the top of the saturation dome. As seen from the wetness curve in Figure 18, the condensation delay (zero wetness after saturation point until Wilson point) and shock (rapid condensation) leads to different nozzle outlet conditions (pressure, wetness) relative to an approximately isentropic expansion predicted by steam tables or a Mollier diagram. A few special considerations for steam nozzle flow:

- Two-dimensional effects cause asymmetric or v-shaped condensation fronts
- Latent heat release during condensation lowers Mach number so that a super-sonic flow can be made super-sonic (lower Ma) or sub-sonic with transient, pulsating patterns possible
- Pre-existing wetness or foreign nuclei (impurities in steam) could lead to some amount of condensation soon after saturation conditions are reached
- Droplet flashing (cavitation boiling and subsequent fragmentation due to a sudden expansion pressure drop) within or just outside the nozzle is something is unlikely for sufficiently small droplets
- Flashing of larger liquid parcels in the nozzle or jet is more probable.

#### 6.1.2.4 Miscellaneous Considerations

With respect to latent heat release and its effects on super-sonic nozzle flow, an interesting transient phenomenon can potentially occur if latent heat release (condensation shock) is sufficient to decelerate the flow to sonic velocity. This could occur if condensation takes place close enough to the throat where the Mach number is only slightly larger than unity. When condensation shock does not cause reversion to sonic flow, condensation is referred to as sub-critical and there is no "thermal choking". In this case, a steady-state flow can be established. When condensation shock is sufficiently strong to cause reversion to sonic flow, condensation is referred to as super-critical and there is thermal choking. An adiabatic shock sets up inside the diverging section of the nozzle. The shock moves upstream towards the nozzle throat if it cannot establish a position downstream at which flow remains super-sonic upon crossing it [White and Young, 1993]. If the shock moves far enough upstream, it will inhibit nucleation by virtue of the attending steam temperature increase across the shock. This disrupts the very phenomenon that leads to condensation and, in turn, the shock disappears. Nucleation within super-sonic flow is re-established downstream of the throat, condensation begins again, and the strong condensation shock re-appears. This oscillatory pattern repeats itself with some frequency due to the self-sustaining nature of the phenomenon [White and Young, 1993]. Should this occur in the pressure stage of a RCIC turbine, it could lead to more thermodynamic losses, and an altered droplet size distribution (fewer droplets that are larger in size).

With respect to modeling heterogeneous nucleation sites, the same drop-wise condensation source terms can be applied and a special set of size distribution equations could be utilized. The effect of any nucleation sites or inlet wetness is to decrease the steam super-saturation that would otherwise occur because steam can readily condense out on heterogeneous sites without appreciable hindrance from a thermodynamic barrier. If inlet moisture is excessive or if impurities exist in large concentrations, condensation shock might not occur in the nozzle or might be much less pronounced.

With respect to modeling droplet flashing/cavitation, Gyarmathy [1976] briefly describes the physics. Droplet flashing (by cavitation) can only proceed if a rapid pressure decrease (expansion) occurs in ambient steam and internal droplet temperature cannot quickly adjust (cool by heat transfer) to the new pressure environment. In this scenario, the whole droplet "feels" the lower pressure instantly and thus the liquid droplet has new saturation conditions immediately. However, the internal droplet temperature can only decrease by heat transfer with the drop surface and the surrounding steam. If internal droplet temperature cannot decrease quickly enough, cavitation boiling (flashing) could occur. This would cause the droplet to fragment as some liquid vaporizes. Gyarmathy [1976] proposes an equation for the maximum droplet size that escapes flashing as a function of the pressure drop and the time interval of expansion. Most droplets evolved from condensing steam flow are likely small enough to avoid flashing under normal conditions.

## 6.1.2.5 Equation-of-State for Super-Saturated Steam

### 6.1.2.5.1 IAPWS-IF97 Background

STAR-CCM+ has certain built-in data for water as a working fluid, be it in the liquid or vapor state. It even incorporates a few of the five IAPWS-IF97 regions as show in Figure 19 below [IAPWS, 2007].

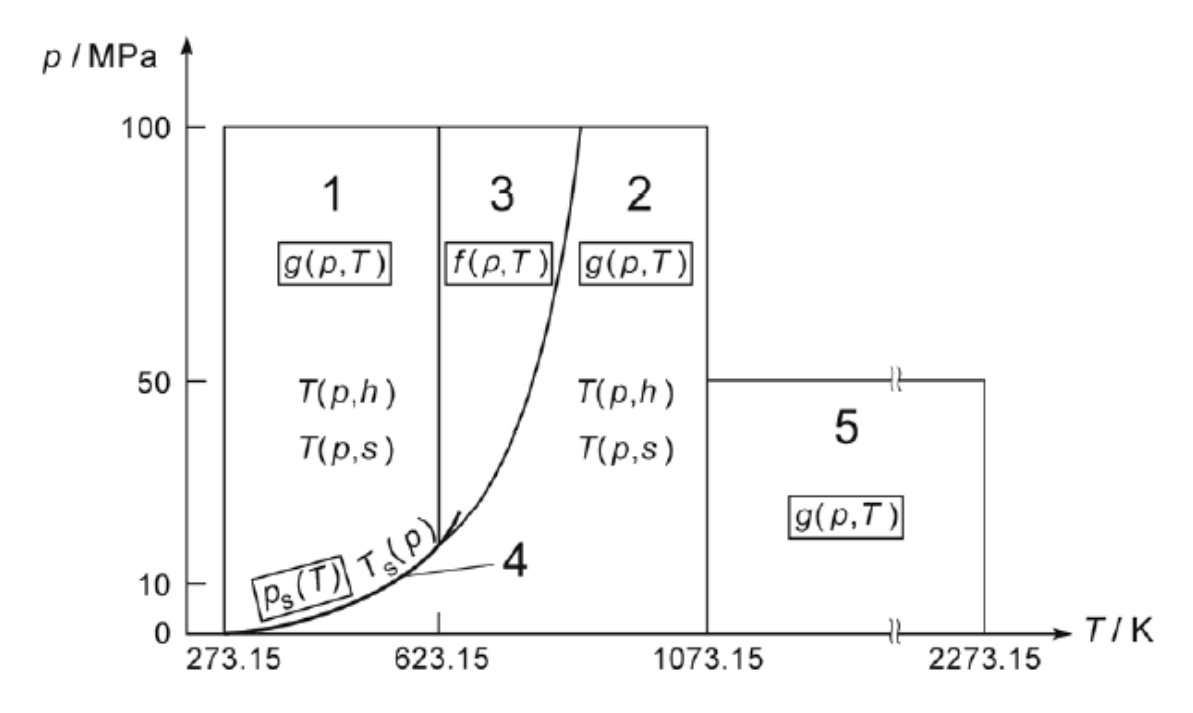


Figure 19 IAPWS-IF97 regions, dependent/independent variables [IAPWS, 2007]

The STAR-CCM+ material database does not contain equation-of-state data for saturated and super-saturated steam, two states of water that must be modeled in a CMFD calculation of condensing steam flow in particular and steam turbines in general. The code does, however, allow a user to totally define equation-of-state closures for compressible fluids via external data tables. IAPWS-IF97 provides the requisite data (by furnishing the necessary equations, constants, exponents, etc.) for saturated, super-saturated, and super-heated steam as well as saturated and sub-cooled water. Regions 2 and 2m from Figure 19 (2m not explicitly marked in the diagram)

represent super-heated and super-saturated steam, respectively. Region 4 (actually just a curve) represents saturated steam/water. Region 1 represents sub-cooled (or compressed) water.

IAPWS-IF97 provides region-wise equations and tables of fitting exponents and constants which are derived empirically or – in the case of metastable super-saturated steam – from special extrapolations of experimental data. Using, for example, a suitably-written MATLAB script or EXCEL spreadsheet, one can borrow from IAPWS-IF97 as needed and compile whatever water data tables are required for a given application. In this case, tables of data are needed for thermodynamic and transport properties of steam in the super-heated, saturated, and super-saturated states as well as for water in the saturated and sub-cooled states. The following properties as functions of both temperature and pressure (excluding saturation where temperature and pressure are dependent) were required:

- Density
- Specific enthalpy
- Dynamic (absolute) viscosity
- Thermal conductivity
- Speed of sound

Certain other properties like isobaric and isochoric specific heat and certain required property derivatives are obtained from numerical differentiation or integration in STAR-CCM+. With data tables input, all requisite equation-of-state closures for compressible steam and incompressible water are known. Furthermore, interpolating field functions can be written to retrieve steam and water properties for use in other instances like conservation equation source terms.

# 6.1.2.5.2 IAPWS-IF97 Data Table Extraction

The IAPWS-IF97 methodology for predicting steam and meta-stable steam properties is described subsequently. Then, an outline is given for a short MATLAB script that produces data tables for import into STAR-CCM+. Though IAPWS-IF97 was employed for the present condensing steam CMFD analyses, note that other alternatives are viable and have been used in the literature. One popular method employs the Vukalovich virial equation of state [Bakhtar and Piran, 1979] which is expected to give reasonable results when extrapolated into the super-saturated region.

For regions 2 and 2m of Figure 19, IAPWS-IF97 proposes a fundamental equation for specific Gibbs free energy as a function of pressure and temperature - g(P,T) - consisting of a sum of two parts: 1) an "ideal gas" part  $\gamma^0$ , and 2) a "residual" part  $\gamma^r$ :

$$\frac{g(P,T)}{RT} = \gamma \left( \pi = \frac{P}{P^*}, \tau = \frac{T^*}{T} \right) = \gamma^0(\pi, \tau) + \gamma^r(\pi, \tau)$$
(35)

where:

P = Steam pressure; T = Steam temperature;  $P^* = \text{Reducing pressure} = 1 \text{ MPa}$ 

 $T^*$  = Reducing temperature = 540 K ;  $\pi$  = Dimensionless pressure

 $\tau$  = Dimensionless temperature

The ideal-gas and residual terms consist of equations in dimensionless pressure and temperature including a litany of empirical coefficients and exponents. For super-heated and super-saturated steam, the ideal-gas part is identical in form, uses slightly different empirical coefficients  $n^0$ , and uses identical empirical exponents  $J^0$ :

$$\gamma^{0}(\pi,\tau) = \ln(\pi) + \sum_{i=1}^{9} n_{i}^{0} \tau^{J_{i}^{0}}$$
(36)

The residual part differs in form for super-heated and super-saturated steam. For super-heated steam, the expression for the residual part is:

$$\gamma^{r}(\pi,\tau) = \sum_{i=1}^{43} n_i \pi^{I_i} (\tau - 0.5)^{J_i}$$
(37)

For super-saturated steam, the expression for the residual part is:

$$\gamma^{r}(\pi,\tau) = \sum_{i=1}^{13} n_{i} \pi^{l_{i}} (\tau - 0.5)^{l_{i}}$$
(38)

Thermodynamic properties – specific volume (density), specific internal energy, specific entropy, specific enthalpy, specific heat capacity (isobaric), specific heat capacity (isochoric), and speed of sound – are all expressed as functions of specific Gibbs free energy and derivatives thereof. These can be found in [IAPWS, 2007].along with all empirical coefficients and exponents. Since Gibbs free energy is written as a sum of two terms, all thermodynamic properties may be written as functions of the ideal-gas term (and derivatives thereof) and the residual term (and derivatives thereof).

To compute desired steam properties one must select a temperature and pressure (or rather a matrix of those independent variables) inside the range of validity for a region in question, compute all the ideal-gas and residual terms (including the various derivatives), and then compute thermodynamic variables of interest. This is the rather simple approach followed for equilibrium states of steam and water, i.e. super-heated steam, saturated steam/water, and sub-cooled water. For metastable super-saturated steam, the floor on the range of validity is the 5% equilibrium moisture line (95% quality) [IAPWS, 2007]. To compile super-saturated steam property tables – where independent variables are temperature and pressure - the minimum valid steam sub-cooled temperature for a given pressure was recovered from a Newton's method solution (for temperature T) of:

$$h = g(P, T) - T \left(\frac{\partial g}{\partial T}\right)_{P} = RT\tau(\gamma_{\tau}^{0} + \gamma_{\tau}^{r})$$
(39)

where:

$$h = h_{95} = h_{f,sat} + 0.95 * (h_{g,sat} - h_{f,sat})$$

For each pressure the range of validity on super-saturated steam temperature is  $\left(T_{stm_{h_{95}}}, T_{sat}\right)$  with  $T_{stm_{h_{95}}}$  coming from the Newton's method solution. Thermodynamic properties of super-saturated Steam follow from IAPWS-IF97 prescriptions. There are special IAPWS-IF97 documents for thermal conductivity [IAPWS, 2011], viscosity [IAPWS, 2008], and surface tension [IAPWS, 2014].

A MATLAB function file IAPWS\_IF97.m [Mikofski, 2012] was called from a specially-developed script to compute steam and water properties. The super-saturated region 2m

computations and the Newton's method solution for steam sub-cooling were coded around IAPWS IF97 function calls as necessary. Generally, the script proceeds as:

- Define pressure *P* array (logarithmically spaced between 0.01 100 MPa)
- Get a saturation temperature  $T_{sat}$  array, a value for each member of the P array Define a  $T_{stm}$  matrix, 500 points for each P between  $T_{sat}(P)$  to 1073.0 K Get  $h_{f,sat}$ ,  $h_{g,sat}$ , and  $h_{95}$  for each member of the P array

- Initialize/zero arrays for  $h_{stm}$ ,  $\rho_{stm}$ ,  $C_{stm}$ ,  $\mu_{stm}$ ,  $k_{stm}$ Specify arrays of IAPWS-IF97 data (coefficients, exponents)
- Newton's method for array of  $T_{stm,min}$ , the maximum sub-cooling for each P
- Use region 2m formulae for  $h_{stm}$ ,  $\rho_{stm}$ ,  $\rho_{stm}$ ,  $\ell_{stm}$ ,  $k_{stm}$  Use region 2 formulae for  $h_{stm}$ ,  $\rho_{stm}$ ,  $\ell_{stm}$ ,  $\ell_{stm}$ ,  $\ell_{stm}$  of super-heated steam
- Compute saturated steam/liquid properties
- Print all data to text files in tabular format, condition for STAR-CCM+ import

#### 6.1.2.6 Turbulence

In trans-sonic condensing steam flow, turbulence could conceivably impact the process of spontaneous condensatio n and affect both inter-phase mass/momentum/energy transfer and condensation shock formation. There are two general mechanisms by which turbulence could impact the condensation process [Avetissian et al., 2008], though one is negligible with respect to the other:

- The impact of turbulent transfers on the hydrodynamic pattern of flow
- The impact of statistical, turbulent fluctuations on nucleation and condensation

The former is thought more consequential than the latter [Avetissian et al., 2008], thus much of the research in this area has focused on how turbulence affects a condensing steam flow field rather than how statistical fluctuations of, say, steam pressure and temperature might secondarily impact nucleation and condensation. Turbulence modeling for condensing steam flow is usually limited to a two-equation approach, typically a modified k-\varepsilon formulation which retains special source/sink terms for dispersed phase effects. A third equation for dispersed phase turbulence kinetic energy is sometimes added [Ma et al., 2009] if inter-phase slip (dispersed phase velocity) is not neglected. Some basic concepts of two-equation turbulence modeling are reviewed below as are the special modifications necessary for application to compressible condensing steam flow. The realizable kε two-layer all y+ model as it applies in STAR-CCM+ will be presented in a subsequent section.

### <u>6.1.2.6.1 Two-Equation $k-\epsilon$ Turbulence Modeling Concepts</u>

A detailed discussion of fundamental turbulence concepts is omitted here, but the reader is referred to textbooks such as [Tennekes and Lumley, 1972], [Wilcox, 1994] and [Bradshaw, 1971] for proper introductions to turbulence theory. Every type of k-\varepsilon formulation seeks to address the closure problem of turbulence introduced upon Reynolds averaging of the non-linear Navier-Stokes equations. To solve for the mean turbulent flow, one requires a set of closures for Reynolds stresses that arise because of turbulent velocity fluctuations. These closures should describe how Reynolds stresses relate to mean flow strain (mean flow velocity gradients or the mean flow strain rate tensor). The k-\varepsilon formulations use the Boussinesq eddy viscosity approximation to correlate Reynolds stresses and mean flow velocity gradients. Thus, the turbulent stresses assume the mathematical form of a molecular stress.

An expression is required for the turbulent viscosity which is the constant of proportionality between the Reynolds stress tensor and the strain rate tensor (consisting of mean flow velocity gradients). The k- $\epsilon$  approach follows Prandtl's proposal of connecting the turbulent viscosity to a characteristic velocity scale of turbulence via the specific turbulence kinetic energy. This obviates

the need for a mixing length approximation but assumes some method to compute turbulence kinetic energy is available. The trace of the Reynolds stress tensor is proportional to specific turbulence kinetic energy [Wilcox, 1994]. A transport equation for the Reynolds stress can be obtained – see [Wilcox, 1994] for a walk-through – by averaging the moment equation formed upon multiplying the Navier-Stokes equation component-wise by turbulent velocity fluctuations. Taking the trace of the Reynolds stress transport equation leads to a scalar equation for turbulence kinetic energy.

A by-product of that operation is a turbulence kinetic energy sink (loss) term that is known as the turbulence energy dissipation. It measures the loss of turbulence kinetic energy (its dissipation into thermal energy) by action of viscosity. It too requires a closure of some kind. Certain so-called one-equation models make assumptions that follow purely from dimensional arguments, algebraically correlating the dissipation to turbulence kinetic energy, length scales, and fluid properties. The k-ε model instead proposes a scalar transport equation for the turbulence dissipation which follows from averaging of a certain moment of the Navier-Stokes equation [Wilcox, 1994].

The two scalar transport equations for turbulence kinetic energy and turbulence energy dissipation require further closures before they can be solved. The gradient transport hypothesis provides one closure and posits that turbulent Reynolds stress is proportional to mean flow velocity gradients. Another gradient transport closure is enforced on the so-called turbulent transport and pressure diffusion terms, thus defining:

- a triple correlation among fluctuating velocity components, and
- a correlation between fluctuating pressure and fluctuating velocity

Further closures involve approximations to certain terms in the kinetic energy and dissipation equations that include tuning constants. Thus, the model must be calibrated via experiments or with some other strategy.

There are actually eight different types of k-\$\varepsilon\$ model available in STAR-CCM+ including a few varieties of the so-called standard k-\$\varepsilon\$ formulation. It is left to the user to decide which form is most appropriate for a given application, but there are general guidelines [CD-ADAPCO User's Guide, 2016] that aid the user in weighing the various trade-offs. One particularly attractive alternative is the so-called "realizable, two-layer k-\$\varepsilon\$" model which can be combined with an all-y+ wall treatment. Subsequent paragraphs expound on the three aspects of this particular turbulence model: realizable, two-layer, and all-y+. These explanations are drawn from the STAR-CCM+ users' guide [CD-ADAPCO User's Guide, 2016] which has references to original papers.

The term "realizable" indicates certain augmentations to the standard model that make the mathematics more consistent with empirically-observed physics of turbulence. Specifically, a different turbulence energy dissipation equation is employed. Also, one particular model coefficient assumed constant in the standard model is instead made a function of mean flow and turbulence properties.

The term "two-layer" refers to a scheme that makes the k-ɛ model applicable in the viscous sublayer of a turbulent boundary layer (near a wall). A wall function approach to near-wall modeling is rendered unnecessary because, in the computational cell nearest the wall, both the dissipation and turbulent viscosity assume a functional dependence on wall distance while the normal transport equation for turbulence kinetic energy is solved. In computational cells farther from the wall, the full complement of k-ɛ transport equations is solved. There is then a blending between the near-wall layer and the outer layers. There are different prescriptions for near-wall dissipation and turbulent viscosity as well as for the blending method. With respect to two-layer models, STAR-CCM+ has two slightly different shear-driven flow formulations and one buoyancy-driven flow formulation.

The term "all-y+" refers to a hybrid treatment that compromises between low-y+ (the mesh is fine enough to resolve the near-wall viscous sublayer) and high-y+ (the mesh is coarse and wall laws are used to represent near-wall regions). All y+ treatment attempts to duplicate low-y+ results when the mesh is fine and high-y+ results when the mesh is coarse. It also gives reasonable results when the mesh is somewhere between low and high y+. The all-y+ model provides an expression for u\* (friction velocity) near the wall and also affects the turbulence kinetic energy production term in the near-wall layer. Furthermore, when combined with the two-layer scheme a special algebraic prescription for near-wall dissipation is used.

### 6.1.2.6.2 Turbulent, Compressible, Condensing Steam Flow

Modifications have been proposed to a certain term in the turbulence kinetic energy transport equation that increases its predictive accuracy for compressible flows. Wilcox notes [Wilcox, 1994], for example, that the stand-alone k-ε model without compressibility modifications cannot predict the experimentally-observed decrease in spreading rate for a compressible mixing layer. The turbulence kinetic energy sink (dissipation) term proposed by Sarkar is targeted at correcting just this defect. While it is demonstrably imperfect in some respects [Wilcox, 1994], the Sarkar compressibility modification is adopted in STAR-CCM+ for purposes of computing the so-called dilation dissipation term in the turbulence kinetic energy equation. This term comes from an expansion of the turbulence kinetic energy dissipation term into two parts: solenoidal dissipation related to fluctuating vorticity and dilation dissipation related to divergence of fluctuating vorticity. The dilation part, nonzero only for compressible flows, is taken as proportional to the turbulent Mach number and the solenoidal dissipation. The equality is substituted into the turbulence kinetic energy equation, completing the compressibility treatment in either the standard or the realizable k-ε model.

The dispersed droplet phase present in condensing steam flow will influence continuous phase turbulence kinetic energy and dissipation. In the literature (e.g. [Avetissian et al., 2008]. [Ma et al., 2009]) the influence of droplets and nucleation is treated via source terms. The turbulence kinetic energy source/sink term accounts for:

- Turbulence modulation due to the presence of droplets, and
- Loss of steam phase turbulence kinetic energy due to nucleation.

The turbulence energy dissipation source/sink term is typically assumed proportional to the kinetic energy source/sink term according to time scaling arguments [Crowe et al., 2012]. Turbulence modulation refers to any effect a dispersed particle/droplet phase has on the turbulence of its carrier phase. Several categories of such effects have been observed empirically [Crowe et al., 2012]:

- Surface effects
- Loading effects (dispersed phase concentration including fluid displacement)
- Inertial effects (related to the relative Reynolds number of drops/particles)
- Response effects (droplet response/relaxation time, Stokes number, etc.)
- Interaction effects (particle-particle and/or particle-wall effects)
- Enhanced turbulence dissipation due to drop/particle presence
- Extra turbulence kinetic energy transfer due to drop/particle presence
- Effects due to wakes of moving drops/particles

Experimentally, such effects manifest themselves in the turbulence statistics of the continuous phase, as they are altered relative to the case of single-phase flow. For the dilute, dispersed two-phase condensing steam flow, some of the effects listed above are in play. Namely, the steam turbulence kinetic energy is modulated by additional dissipation due to droplet presence. Also, nucleation and condensation (essentially a mass transfer from steam phase to droplet phase) will cost the steam turbulence some of its specific kinetic energy and some of its dissipation.

Turbulence modulation due to droplet presence is not modeled in these studies, though they possibly could be following the example in [Avetissian et al., 2008]. Here, the authors appeal to a Lagrangian stochastic model of turbulent dispersion to characterize a coefficient of droplet response to turbulent steam velocity fluctuations. Sawford's Lagrangian stochastic model [Sawford, 1991] considers Lagrangian position, velocity, and acceleration to be collectively Markovian. More specifically, memory effects are neglected at the 0<sup>th</sup> order but encapsulated by two time-scales at the 1<sup>st</sup> and 2<sup>nd</sup> order. The 1<sup>st</sup> order time scale characterizes the energy-containing scales and the 2<sup>nd</sup> order time scale is the familiar Kolmogorov time scale which characterizes the dissipative scales. To fully understand the methods [Sawford, 1991], a working knowledge of turbulence statistics, e.g. as presented in [Tennekes and Lumley, 1972] is required. Results from [Sawford, 1991] are borrowed [Avetissian et al., 2008] to formulate a steam turbulence kinetic energy dissipation term (appearing in the turbulence kinetic energy equation as a source term) which describes a modulation effect – more specifically a response effect – of the condensed droplets. The dispersed droplets impact steam turbulence kinetic energy dissipation but are themselves impacted by steam turbulent dispersion. Such effects are accounted for by this method, and it would be particularly attractive for RCIC turbine CMFD modeling because it does not require computation of phase slip as other methods do, e.g. the k-ε-k<sub>p</sub> model from [Ma et al., 2009]. Instead, the only turbulence kinetic energy and turbulence dissipation source terms in this study are those corresponding to phase change.

## 6.1.2.7 Full Pseudo Two-Fluid Formulation for Condensing Steam Flow

## 6.1.2.7.1 Coupled Flow Model

Conservation equations for the steam phase are solved via the coupled flow model in STAR-CCM+. These equations in their general integro-differential form are first presented. Then, the particular equations for the condensing steam flow problem at hand are reviewed. ons to the coupled flow model such as the passive scalar model and user-defined sources were discussed previously.

The general coupled flow conservation equations for an infinitesimal control volume dV with differential surface area dA in integro-differential operator form are:

$$\frac{\partial}{\partial t} \int_{V} \overrightarrow{W} dV + \oint_{A} (\overrightarrow{F} - \overrightarrow{G}) * (d\overrightarrow{A}) = \int_{V} \overrightarrow{H} dV$$
 (40)

where:

$$\vec{W} = \begin{cases} \rho \\ \rho \vec{u} \\ \rho E \end{cases}$$
 a vector of dependent variables (density and flux variables)

$$\vec{F} = \begin{cases} \rho(\vec{u} - \vec{u}_{grid}) \\ (\rho(\vec{u} - \vec{u}_{grid}) X \vec{u}) + P\bar{l} \end{cases} \text{ a vector of convective fluxes and pressure terms} \\ (\rho(\vec{u} - \vec{u}_{grid}) H) + P\vec{u} \end{cases}$$

$$\vec{G} = \begin{cases} 0\\ \bar{T}\\ \bar{T} * \vec{u} + \vec{q''} \end{cases}$$
 a vector of molecular fluxes

$$\vec{H} = \begin{cases} S_m \\ \vec{f_r} + \vec{f_g} + \vec{f_p} + \vec{f_u} + \vec{f_\omega} + \vec{f_L} & \text{a vector of various source terms} \\ S_e \end{cases}$$

E = total specific energy [J/kg]; P = pressure [Pa];  $\bar{I} = \text{Identity tensor}$ 

$$H = E + \frac{P}{\rho_{stm}} = h + \frac{|\vec{u}|^2}{2} = C_p T + \frac{|\vec{u}|^2}{2} = \text{Total specific enthalpy [J/kg]}$$

 $\overline{\overline{T}}$  = viscous stress tensor [Pa] ;  $\overline{q''} = -k\overline{V}\overline{T}$  = Heat flux vector [W/m<sup>2</sup>]

 $S_m = \text{Mass source term}$ ;  $S_e = \text{Energy source term}$ 

 $\vec{f}_x$ , x = r, g, p, u, w, L are various momentum source terms

The major assumptions of the physics model presented here are:

- Droplet phase is represented by passive scalar transport equations
- The droplet volume fraction is negligibly small
- Mechanical equilibrium (no slip) between the steam and any droplets evolved
- Droplet temperature follows from capillarity considerations (Gyarmathy [1976])
- Classical nucleation theory (with corrections) applies
- Process of steam/droplet heat and mass exchange is simplified, e.g. no droplet energy storage or internal heat transfer
- Two-layer, all y+, realizable k-epsilon turbulence model

The specialized continuity, momentum, and energy equations in integro-differential form for the continuous steam phase in the RCIC turbine CMFD model are:

$$\frac{\partial}{\partial t} \int_{V} \rho_{stm} dV + \oint_{A} \rho_{stm} (\vec{u} * d\vec{A}) = \int_{V} S_{m} dV$$
 (41)

$$\frac{\partial}{\partial t} \int_{V} \rho_{stm} \vec{u} dV + \oint_{A} \left[ \rho_{g}(\vec{u} \times \vec{u}) + P \overline{I} - \overline{T} \right] * d\vec{A} = \int_{V} \overrightarrow{S_{u}} dV$$
 (42)

$$\frac{\partial}{\partial t} \int_{V} \rho_{stm} \left( h_{stm} + \frac{|\vec{u}|^{2}}{2} - \frac{P}{\rho_{stm}} \right) dV + \tag{43}$$

$$\oint_{A} \left[ \rho_{stm} \overrightarrow{u} \left( h_{stm} + \frac{|\overrightarrow{u}|^{2}}{2} \right) - \left( \overline{T} * \overrightarrow{u} \right) + \overrightarrow{q''} \right] * d\overrightarrow{A}$$

$$= \int_{V} S_{e} dV$$

The droplet phase equations (reproduced below) are:

$$\frac{\partial}{\partial t}(\rho_{stm}\,\mu_0) + \overrightarrow{V} * (\rho_{stm}\,\mu_0\overrightarrow{u}) = \rho_{stm}\,J_* \tag{44}$$

$$\frac{\partial}{\partial t}(\rho_{stm}\,\mu_1) + \overrightarrow{\nabla} * (\rho_{stm}\,\mu_1\overrightarrow{u}) = \rho_{stm}(G\,\mu_0 + J_*r^*)$$
(45)

$$\frac{\partial}{\partial t}(\rho_{stm}\,\mu_2) + \overrightarrow{\nabla} * (\rho_{stm}\,\mu_2\overrightarrow{u}) = \rho_{stm}(2G\,\mu_1 + J_*r^{*2})$$
(46)

$$\frac{\partial}{\partial t}(\rho_{stm}\,\mu_3) + \overrightarrow{\nabla} * (\rho_{stm}\,\mu_3\overrightarrow{u}) = \rho_{stm}(3G\,\mu_2 + J_*r^{*3})$$
(47)

Interphase transfer terms G,  $S_m$ ,  $\overrightarrow{S_u}$ ,  $S_e$  remain to be specified. Note also that  $\rho_{stm} J_*$  equals  $J_*$ . One possible expression for a constant condensation growth rate was already presented and is reproduced here:

$$\frac{dr}{dt} = G = \left(\frac{k_{stm}}{\rho_{liq}(T_{stm})h_{fg}(P)}\right) \left(\frac{1 - \frac{r^*}{r}}{r + 1.59\ell}\right) \left((T_{sat}|_{P} - T_{stm})\right)$$
(48)

The mass, momentum, and energy source terms will contain nucleation and condensation parts in general. The steam mass source term is negative when nucleation and condensation occur and can be written as:

$$S_{m} = -\frac{4}{3}\pi r^{*3} \rho_{liq}|_{T_{stm}} J - 4\pi \left(\frac{D_{32}}{2}\right)^{2} \rho_{liq}|_{T_{stm}} NG$$
(49)

The steam momentum source is negative when nucleation and condensation occur and can be written as:

$$\overrightarrow{S_u} = (\overrightarrow{u}S_m) + (\overrightarrow{v}S_m) + (\overrightarrow{k}S_m) \tag{50}$$

where:

 $\vec{u}, \vec{v}, \vec{k}$  are Cartesian components of the steam velocity vector

The steam energy source is negative when nucleation and condensation occur:

$$(S_e = -S_m h_{fg}(P) \tag{51}$$

where:

 $h_{fg}(P)$  is latent heat of vaporization at steam pressure P

Combining equations (41) through (51) with the turbulence model presented in the next section completes the coupled flow, pseudo two-fluid formulation.

## 6.1.2.7.2 Realizable k-€ Two-Layer All-y+

The full set of realizable k-\varepsilon two-layer all-y+ equations with terms for compressibility effects and dispersed-phase effects is presented below in integro-differential form. The transport equations are taken directly from [CD-ADAPCO User's Guide, 2016] and the turbulence modulation source terms are taken from [Avetissian et al., 2008] and [Ma et al., 2009]. Note the transport equations are for turbulence kinetic energy and dissipation in the steam phase exclusively. There is no modeling of dispersed phase turbulence parameters. The steam turbulence kinetic energy transport equation is:

$$\frac{\partial}{\partial t} \int_{V} \rho_{stm} k dV + \oint_{A} \rho_{stm} k \left( \left( \overrightarrow{u} - \overrightarrow{u}_{grid} \right) * d\overrightarrow{A} \right) =$$

$$\oint_{A} \left( \mu_{stm} + \frac{\mu_{t}}{\sigma_{k}} \right) \left( \overrightarrow{V} \overrightarrow{k} * d\overrightarrow{A} \right) +$$

$$\int_{V} \left( f_{c} G_{k} + G_{b} - \rho_{stm} \left( (\epsilon - \epsilon_{0}) + Y_{M} \right) + S_{k} \right) dV$$
(52)

where:

k = Turbulent kinetic energy [J/kg];  $\vec{u}_{grid} = \text{Grid velocity [m/s]}$ 

 $\mu_t$  = Turbulent viscosity [Pa\*s];  $\sigma_k$  = Turbulent Prantl number

 $f_c$  = Curvature factor ;  $G_k$  = Production source term for k

 $G_b$  = Buoyancy production source term for k

 $\epsilon$  = Turbulence dissipation rate [J/kg/s] ;  $\epsilon_0$  = Ambient turbulence value

 $Y_M = \text{Dilation dissipation}$ ;  $S_k = \text{Miscellaneous source term for } k$ 

The steam turbulence dissipation rate transport equation is:

$$\frac{\partial}{\partial t} \int_{V} \rho_{stm} \epsilon dV + \oint_{A} \rho_{stm} \epsilon \left( \left( \overrightarrow{u} - \overrightarrow{u}_{grid} \right) * d\overrightarrow{A} \right) =$$
 (53)

$$\oint_{A} \left( \mu_{stm} + \frac{\mu_{t}}{\sigma_{\varepsilon}} \right) \left( \overrightarrow{V} \overrightarrow{\epsilon} * d\overrightarrow{A} \right) +$$

$$\int_{V} \left( f_{c} C_{\epsilon 1} S_{\epsilon} + \frac{\epsilon}{k} \left( C_{\epsilon 1} C_{\epsilon 3} G_{b} \right) - \left( \frac{\epsilon}{k + \sqrt{\nu_{stm} \epsilon}} \right) \left( C_{\epsilon 2} \rho_{stm} (\epsilon - \epsilon_{0}) + S_{\epsilon} \right) \right) dV$$

where:

 $S_{\epsilon}$  = Miscellaneous source term for  $\epsilon$  ;  $v_{stm} = \frac{\mu_{stm}}{\rho_{stm}}$ 

 $\sigma_{\varepsilon}$ ,  $C_{\epsilon 1}$ ,  $C_{\epsilon 3}$ ,  $C_{\epsilon 2}$  are model coefficients

The various closures needed for the two transport equations include the turbulence production term, the buoyancy production term, the dilation dissipation (compressibility modification) term, and the turbulent viscosity expression. The model closure coefficients must also be specified. All closures are discussed in turn. The turbulence production term representing the rate at which kinetic energy is transferred to the turbulence from mean flow (an interaction between mean flow strain rate and turbulent stresses) is:

$$G_k = \mu_t S^2 - \frac{2}{3} \rho_{stm} k(\nabla * \overrightarrow{u}) - \frac{2}{3} \mu_t (\nabla * \overrightarrow{u})^2$$
(54)

where:

$$S = |\bar{S}| = \sqrt{2\bar{S}:\bar{S}}$$
;  $\bar{S} = \frac{1}{2}(\nabla \vec{u} + \nabla \vec{u}^T)$ , for S the strain rate tensor

The buoyancy production term is:

$$G_b = \beta \frac{\mu_t}{\sigma_t} (\nabla T * \overrightarrow{g}) \tag{55}$$

where:

 $\beta$  = thermal expansion coefficient

The dilation dissipation term proposed by Sarkar [Wilcox, 1994] is:

$$\Upsilon_{M} = \frac{2k\epsilon}{c^{2}} \tag{56}$$

where:

c is the speed of sound in steam (from equation-of-state prescription)

The turbulent viscosity assumes the form of:

$$\mu_t = \rho_{stm} C_\mu \frac{k^2}{\epsilon} \tag{57}$$

where:

$$\begin{split} &C_{\mu}=1/A_{0}+A_{s}U^{(*)}\frac{k}{\epsilon} \ ; \ U^{(*)}=\sqrt{\bar{S}}:\bar{\bar{S}}+\bar{\bar{W}}:\bar{\bar{W}} \ ; \ \bar{\bar{W}}=\frac{1}{2}(\nabla \vec{u}-\nabla \vec{u}^{T}) \\ &\bar{\bar{W}} \ \text{is the rotation rate tensor} \ ; \ A_{0}=4.0 \ ; \ A_{s}=\sqrt{6}cos(\phi) \\ &\phi=\frac{1}{3}arccos(\sqrt{6}W) \ ; \ W=\frac{s_{ij}s_{jk}s_{ki}}{(\sqrt{s_{ij}s_{ij}})^{3}} \text{ and } S=|\bar{\bar{S}}| \\ &C_{\epsilon 1}=max\left(0.43,\frac{\eta}{5+\eta}\right) \ ; \ \eta=\frac{sk}{\epsilon} \ ; \ C_{\epsilon 2}=1.9 \ ; \ \sigma_{k}=1.0 \ ; \ \sigma_{\epsilon}=1.2 \end{split}$$

The turbulence kinetic energy equation is solved everywhere in the two-layer approach. However, the near-wall layer has special prescriptions for turbulent viscosity, dissipation, and turbulence kinetic energy production. The two-layer approach coupled with an all-y+ wall treatment aims to blend the one-equation near-wall layer treatment with the normal two-equation treatment elsewhere. Blending is done for the dissipation and turbulence kinetic energy production. The turbulent viscosity depends on a length scale function and a wall proximity indicator. Also, the near-wall layer dissipation depends on the length scale function.

The length scale function and turbulent viscosity ratio in general look like:

$$l_{\epsilon} = f(y, Re_{\nu}) \tag{58}$$

$$\frac{\mu_t}{\mu_{stm}} = f(Re_y) \tag{59}$$

There are different prescriptions for the length scale function and the turbulent viscosity ratio, but all correlations are written in terms of a wall-distance (y) Reynolds number:

$$Re_{y} = \frac{\sqrt{ky}}{v_{stm}} \tag{60}$$

Additionally, all correlations have the same algebraic dissipation equation:

$$\epsilon = \frac{k^{3/2}}{l_c} \tag{61}$$

For all correlations of length scale function and turbulent viscosity ratio, the layer blending depends on a wall proximity indicator:

$$\lambda = \frac{1}{2} \left[ 1 + \tanh \left( \frac{Re_y - Re_y^*}{A} \right) \right] \tag{62}$$

where:

$$Re_{\nu}^* = 60$$
 ;  $A = |\Delta Re_{\nu}| / \text{atanh}(0.98)$  ;  $\Delta Re_{\nu} = 10$ 

Such that the blended turbulent viscosity is expressed as:

$$\mu_t = \lambda \mu_{t_{k-\epsilon}} + (1 - \lambda) \mu \left(\frac{\mu_t}{\mu}\right)_{2-layer}$$
(63)

where:

$$\mu_{t_{k-\epsilon}}$$
 = Realizable k- $\epsilon$  turbulent viscosity

The remainder of the two-layer model formulation depends on the choice of either the Norris-Reynolds or the Wolfstein models. Neither is clearly preferable over the other [CD-ADAPCO User's Guide, 2016]. Norris-Reynolds length scale function and turbulent viscosity is:

$$l_{\epsilon}(Re_{y}, y) = \frac{c_{l}Re_{y}y}{Re_{y} + C_{\epsilon}}$$
(64)

where:

$$C_{\epsilon} = 5.3$$
 ;  $C_{l} = kC_{\mu}^{-3/4}$  ;  $k = 0.42$ 

$$\frac{\mu_t}{\mu} (Re_y) = Re_y k C_\mu^{1/4} \left[ 1 - exp \left( \frac{-Re_y}{A_\mu} \right) \right]$$
 (65)

where:

$$A_{u} = 50.5$$

As for the kinetic energy production blending and the dissipation blending, it is accomplished via a blending function:

$$g = exp\left(\frac{-Re_y}{11}\right) \tag{66}$$

Then, the friction velocity  $(u^*)$ , near-wall cell turbulence energy production  $(G_k)$ , and near-wall cell dissipation  $(\epsilon)$ , can be expressed in terms of the blending function:

$$u^* = \sqrt{\frac{g\nu_{stm}u}{y} + (1 - g)C_{\mu}^{1/2}k}$$
 (67)

$$G_{k} = g\mu_{t}S^{2} + (1 - g)\frac{1}{\mu_{stm}} \left(\rho u^{*} \frac{u}{u^{+}}\right)^{2} \frac{\partial u^{+}}{\partial y^{+}}$$
(68)

$$\epsilon = g \frac{2\nu_{stm}k}{\nu^2} + \frac{k^{3/2}}{l_{\epsilon}} \tag{69}$$

where:

 $u^+$  is wall-parallel velocity, non-dimensionalized with  $u^*$ 

 $y^+$  is non-dimensional wall distance (from near-wall cell centroid)

# 6.1.2.7.3 Ideal Gas Formulation

For certain simulations, air is used as a working fluid. The ideal gas approximation applies as the equation of state describing density, temperature, and pressure:

$$\rho = P_{abs}/RT \tag{70}$$

where:

 $P_{abs}$  = Absolute pressure [Pa] ; T = Absolute temperature [K] ;  $R = R_u/M$  $R_u = 8.3144621$  [J/mol/K] ; M = Molecular weight [g/mol]

### 6.1.3 RCIC System Pump

### 6.1.3.1 Modeled Pump Characteristics

In Figure 20, the cutaway of a pump used in nuclear safety related systems around the globe is shown. This pump is similar to the one that will be modelled. The pump that will be modelled with have the following:

- Optimal flow rate of 425 GPM
- Four stage impellers (Single Stage is used in CFD under assumption of equal head applied from each impeller)
- Variable Pump Speed from 2000 RPM- 3500 RPM
- Turbine Driven (Terry Turbine)
- Impeller diameter is 9 inches



Figure 20 An axially split centrifugal multi-stage pump [Sulzer, 2014]

The CAD model of a RCIC pump was created using the CAD modelling software Solidworks. The CAD model was created in likeness to the pump seen above in Figure 20. The exact specifications of the RCIC pump modelled cannot be detailed in this thesis due to the proprietary nature of the pump. The CAD Model of the impeller can be seen in Figure 21 below.



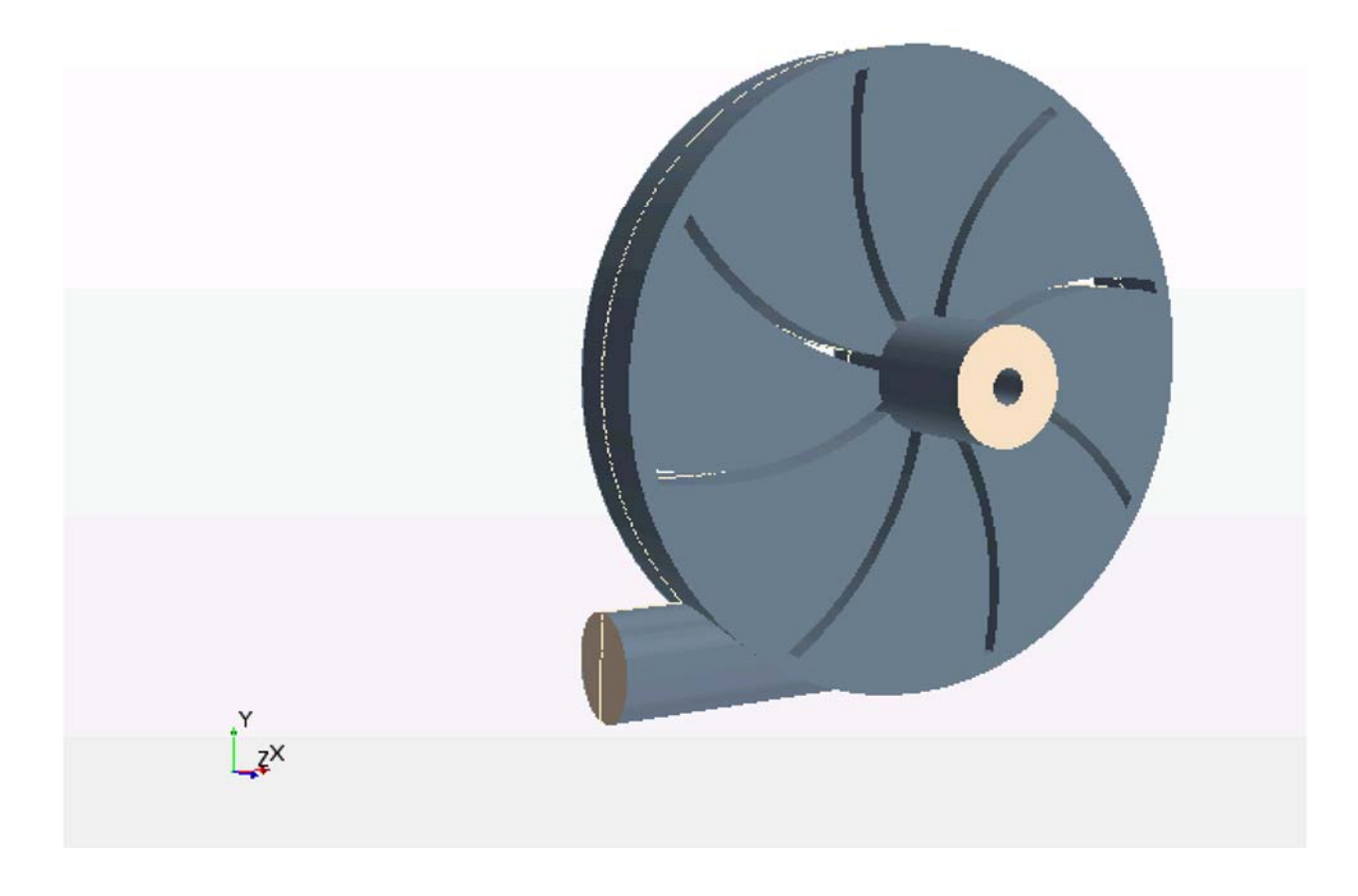


Figure 21 CAD model created for simulation of the RCIC pump

The CAD model was created by creating a volume extraction from the pump casing and impellers. This provided a solid the area where fluid would actually be flowing. This allows STAR-CCM+ to mesh only the areas of interest to help decrease computation time. In Figure 21, seen above, the front of the model is the inlet while the side to the left is set as the outlet. There were two different regions specified in the model: the impeller and the casing. The casing was set to the regular reference frame while a special reference frame was created specifically for the impeller. The reference frame had to be created to capture the motion of the impeller. Within the reference frame, there is a setting for the user to dictate the direction and the rotational speed of the reference frame. Figure 22 depicts the reference frame that was set to rotate.



Figure 22 The rotation region that is set variable speeds in purple

There were many specified boundary conditions input into the new model to help with computation. The two most important boundary conditions are set to the inlet and outlet. The inlet boundary condition was set as a mass flow rate inlet boundary condition to help stability of the simulation. The flow rate was specified as being perpendicular to the inlet face, meaning the flow was entering into the impeller. The outlet was set as a pressure outlet boundary condition. The boundary conditions for all of the walls were set as no slip walls. There was also an interface boundary condition set between the two regions to transfer information between them.

The mesh was created in STAR-CCM+ using the automated mesh capabilities of the program. The meshing selections that were made include: polyhedral mesh, surface remesher, automatic surface repair, and prism layer mesh. The polyhedral and prism layer mesh were used to create the volume mesh while the surface remesher and automatic surface repair were used to create the surface mesh. There was also an increased mesh in the blades and edges of the wall. The base size, or target size for each cell, for the automated mesh was set to 0.02m. The number of prism layers was set to 12. The total prism layer thickness was set to 10% of the base. The high number of prism layers was used because of the turbulent nature of fluid in the pump, especially near the wall. This allows for greater accuracy of the solver in the near-wall region because of the no slip boundary condition set. Two figures below (Figures 23 and 24) are images of the mesh created in STAR-CCM+. The total number of nodes created in the mesh exceeded 22 million cells for both the casing and impeller combined.

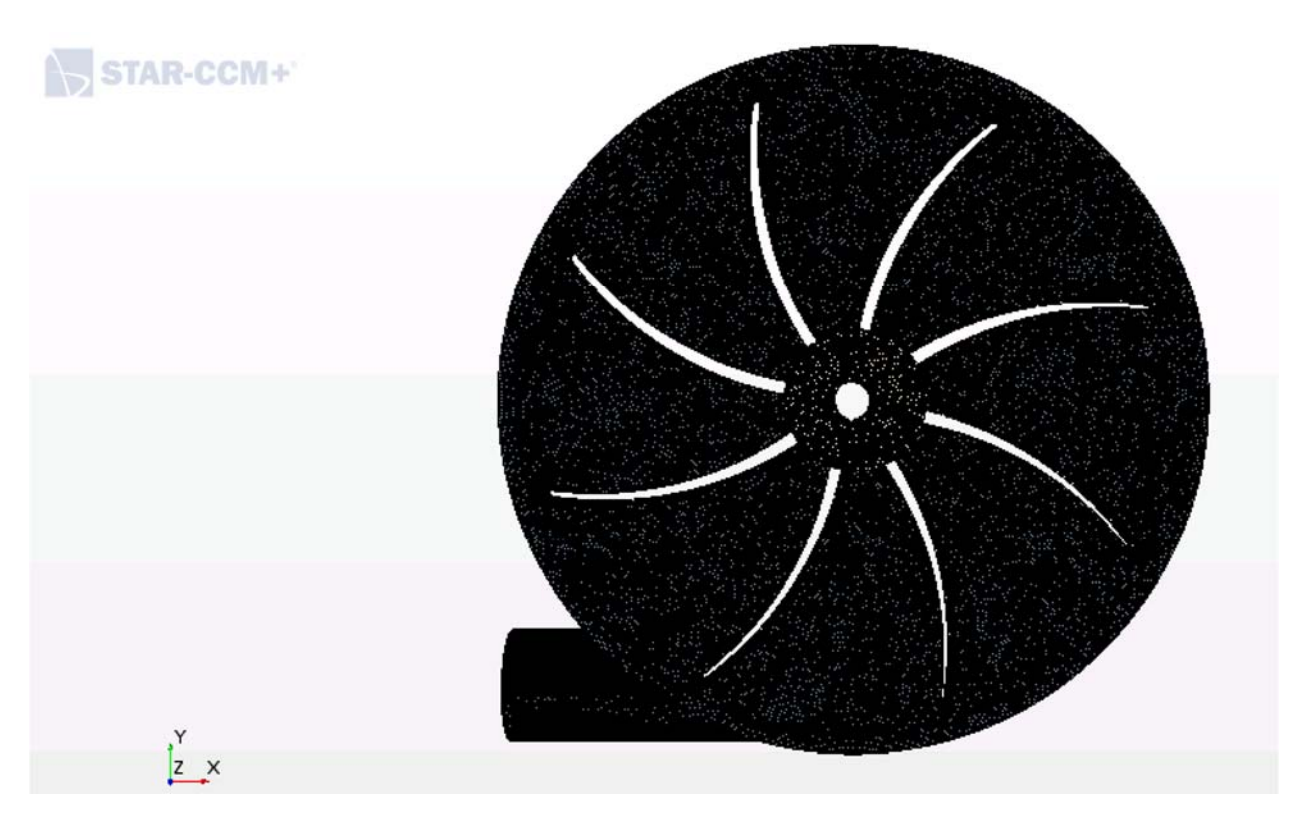


Figure 23 Front view of CAD model with mesh apparent

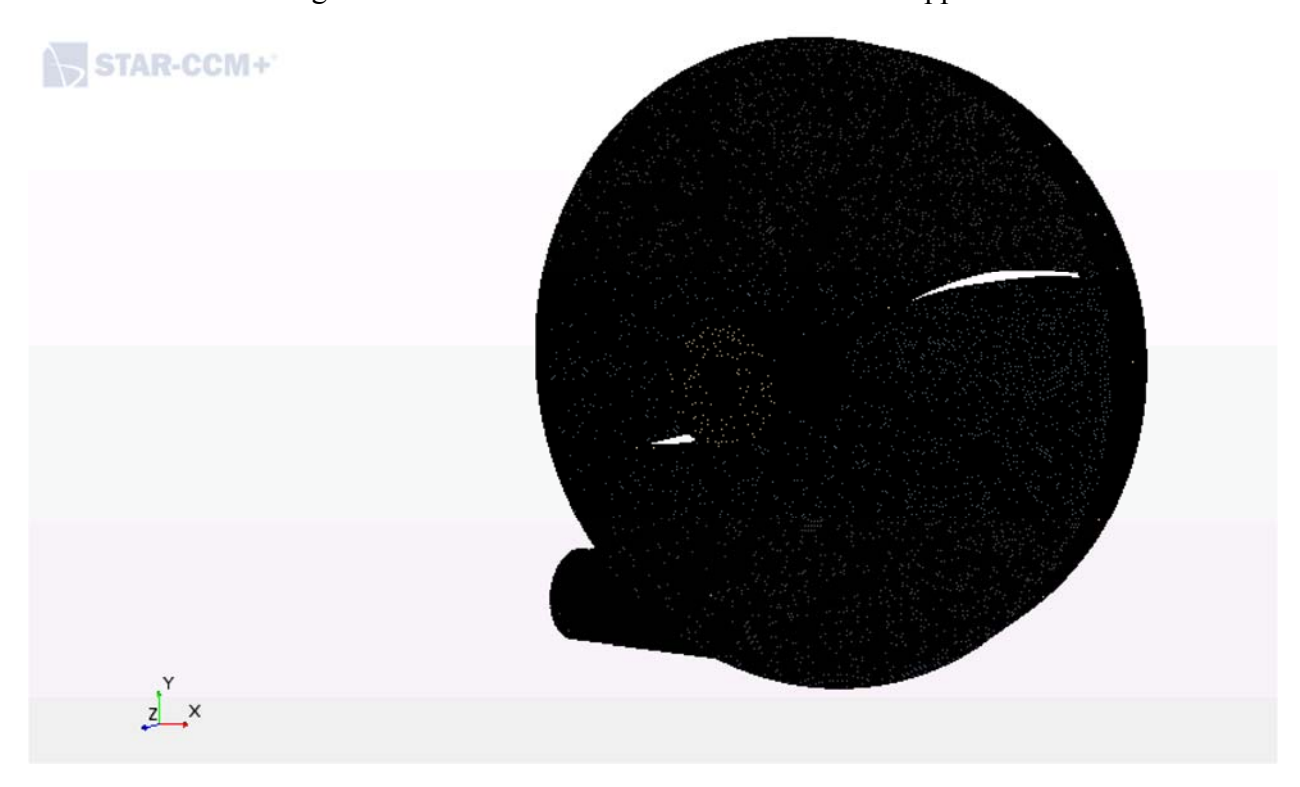


Figure 24 Side view of the mesh opposite of outlet

#### 6.1.3.2 Simulation Setup

#### 6.1.3.2.1 Model Variations

Multiple parameters were varied to assess various aspects of the RCIC pump performance over a range of suppression pool accident conditions. The longer the postulated accident continues to progress, the higher the Suppression Pool saturation temperature can become due to RCIC turbine exhaust into the pool and the greater the probability is for steam to enter the RCIC pump suction. The increased saturation temperature could also cause vapor formation within the pump, further degrading the performance of the pump. In order to simulate the effects that pressure and temperature have on the RCIC pump, pump suction void fraction will be changed.

As with input conditions in the model, the volume fractions of gas and fluid are supplied by the code user. Within the simulation, the density and viscosity of the fluid and gas are required inputs. In order to calculate the density and viscosity of the fluid and gas, a Matlab script was written to calculate the density of water and steam at the saturation temperature of the operating pressure of the RCIC system [Strater, 2017]. The volume fraction affects how the pump will perform as pressure and temperature change. Table 1 lists the differences in simulations completed during this study.

Rotational	Speed	Volume Fraction	Flow Rate
(RPM)			(GPM)
2000		0.0	425
3000		0.0	425
3500		0.0	425
2000		0.1	425
3000		0.1	425
3500		0.1	425
2000		0.2	425
3000		0.2	425
3500		0.2	425
2000		0.3	425
3000		0.3	425
3500		0.3	425

Table 1 RCIC Pump Test Simulation Conditions

#### 6.1.3.2.2 Physics Models

The flow in the pump is turbulent due to the high flow rate and the small eye inlet of the pump. The pump also imparts extra force causing greater amounts of turbulence within the pump. A detailed description of turbulence fundamentals can be found in [Bradshaw, 1971].

STAR-CCM+ has eight different types of k-ε models available. The user must know what the optimal form of the model is applicable for the required application. In modelling, I selected the realizable two-layer k-ε model. This was coupled with an all-y+ wall treatment. The specifics of these turbulence models will be found in the following paragraphs. The explanations in the following paragraphs are drawn from the STAR-CCM+ users guide [CD ADAPCO, 2016a].

The term "realizable" means that changes will be made to the standard k- $\varepsilon$  model that align more correctly with empirical evidence from physics. Specifically, the way the dissipation equation is

employed. One coefficient from the standard model is varied to be a function of mean flow. Realizable k-ɛ model was used to help produce results that would closer mimic that of empirical evidence. The purpose of this study is to examine real pump performance in accident conditions and the closer to physics the more applicable this study will be.

The term "two-layer" refers to the application of the k-ɛ model to the viscous sub-layer of the turbulent boundary layer. This turbulent boundary layer occurs at near wall locations. To do this a wall function approach is not needed because the dissipation and turbulent viscosity are dependent on the wall distance. The normal transport equation for turbulent kinetic energy (TKE) is solved, however. In the bulk flow cells (farther from wall) all the k-ɛ equations are solved. The two different layers (near-wall and bulk flow) are then blended. This model was selected due to the high Reynold's number of the simulated flow. Wall function approach is needed for low Reynold's number simulations and do not apply well to Reynold's number simulations.

The term "all-y+" refers to the combination of low-y+ and high y+ wall treatment. The low-y+ signifies that the mesh is fine enough to resolve the near-wall viscous sublayer. The high-y+ signifies that the mesh is coarse and wall laws are used to represent near-wall regions. How the all-y+ treatment works is attempts to duplicate the low-y+ results when the mesh is fine enough and the high-y+ when the mesh is coarse. The all-y+ model provides a friction velocity near the wall and affects the TKE production term near the wall. The all-y+ model was selected as to reduce the mesh size required for the simulation. The blending approach helps to decrease the number of cells needed in the viscous sub-layer by combining the two solving techniques.

The turbulence kinetic energy transport equation is:

$$\frac{\partial}{\partial t} \int_{V} \rho_{avg} k dV + \oint_{A} \rho_{avg} k ((\vec{u} - \vec{u}_{grid}) * d\vec{A}) = \oint_{A} \left( \mu_{avg} + \frac{\mu_{t}}{\sigma_{k}} \right) (\vec{\nabla k} * d\vec{A}) +$$

$$\int_{V} \left( f_{c} G_{k} + G_{b} - \rho_{avg} \left( (\epsilon - \epsilon_{0}) + Y_{m} \right) + S_{k} \right) dV$$
(71)

where:

k = Turbulent kinetic energy [J/kg] ;  $\vec{u}_{grid}$  = Grid velocity [m/s]

 $\mu_t$  = Turbulent viscosity [Pa\*s] ;  $\sigma_k$  = Turbulent Prantl number

 $f_c$  = Curvature factor ;  $G_k$  = Production source term for k

 $G_b$  = Buoyancy production source term for k

 $\epsilon$  = Turbulence dissipation rate [J/kg/s]

 $\epsilon_0$  = Ambient turbulence value ;  $Y_m$  = Dilation dissipation

 $S_k$  = Miscellaneous source term for k

The turbulence dissipation rate equation is:

$$\frac{\partial}{\partial t} \int_{V} \rho_{avg} \epsilon dV + \oint_{A} \rho_{avg} \epsilon ((\vec{u} - \vec{u}_{grid}) * d\vec{A}) = \oint_{A} \left( \mu_{avg} + \frac{\mu_{t}}{\sigma_{\epsilon}} \right) (\vec{\nabla} \vec{\epsilon} * d\vec{A}) + \int_{V} \left( f_{c} C_{\epsilon 1} S_{\epsilon} + \frac{\epsilon}{k} (C_{\epsilon 2} C_{\epsilon 3} G_{b}) - \left( \frac{\epsilon}{k + \sqrt{\nu_{avg} \epsilon}} \right) \left( C_{\epsilon 2} \rho_{avg} (\epsilon - \epsilon_{0}) \right) + S_{\epsilon} \right) dV \tag{72}$$

where:

$$S_{\epsilon}$$
 = Miscellaneous source term for  $\epsilon$  ;  $v_{avg} = \frac{\mu_{avg}}{\rho_{avg}}$ 

 $\sigma_{\epsilon}$ ,  $C_{\epsilon 1}$ ,  $C_{\epsilon 2}$ ,  $C_{\epsilon 3}$  are model coefficients

The closures that are need for the transport equations include: Turbulence production term, buoyancy production term, dilation dissipation term, and the turbulent viscosity term. The model coefficients closure must be specified as well. Turbulence is increased by interactions between the mean flow strain and turbulent stresses. The turbulence production term is representative of the rate that turbulence is introduced to the flow is defined by equation (73):

$$G_k = \mu_t S^2 - \frac{2}{3} \rho_{avg} k(\nabla * \overrightarrow{u}) - \frac{2}{3} \mu_t (\nabla * \overrightarrow{u})^2$$
(73)

where:

$$S = |\overline{S}| = \sqrt{2\overline{S}:S}$$
;  $\overline{S} = \frac{1}{2}(\nabla \vec{u} + \nabla \vec{u}^T)$ , for S the strain rate tensor

The Buoyance production term is defined by equation (74)

$$G_k = \beta \frac{\mu_t}{\sigma_t} (\nabla T * \overrightarrow{g}) \tag{74}$$

where:

 $\beta$  = Thermal expansion coefficient

The dilation dissipation term defined in STAR-CCM+ is:

$$Y_m = \frac{2k\epsilon}{c^2} \tag{75}$$

where:

c is the speed of sound

The turbulent viscosity takes the following form:

$$\mu_t = \rho_{avg} C_{\mu} \frac{k^2}{\epsilon} \tag{76}$$

where:

$$C_{\mu} = \frac{1}{A_0} + A_S U^{(*)} \frac{k}{\epsilon} \; ; \qquad U^{(*)} = \sqrt{\overline{S} : \overline{S} + \overline{W} : \overline{W}} \; ; \qquad \overline{W} = \frac{1}{2} \left( \overline{\nabla \overrightarrow{u} + \nabla \overrightarrow{u}^T} \right)$$

$$\overline{\overline{W}}$$
 is the rotation rate tensor;  $A_0 = 4.0$  ;  $A_s = \sqrt{6}\cos(\phi)$ 

$$\phi = \frac{1}{3} \arccos(\sqrt{6}W)$$
 ;  $W = \frac{S_{ij}S_{jk}S_{ki}}{(\sqrt{S_{ij}S_{ij}})^3}$  and  $S = |\bar{S}|$ 

The turbulence kinetic energy equation is solved in all cells of the mesh in the two-layer approach. In the viscous sublayer, however, special treatments are used for the turbulent viscosity, turbulent dissipation, and turbulent kinetic energy production. The two-layer approach coupled with an all-y+ treatment blends the wall function (single equation) near-wall layer treatment with the two-equation treatment in the bulk flow. Blending is done on the turbulent dissipation rate and the turbulent kinetic energy production. The turbulent viscosity isn't blended due to its dependence on a length scale function. The length scale function takes the form seen in equation (77). Equation (78) depicts the turbulent viscosity ratio.

$$l_{\epsilon} = f(y, Re_{\nu}) \tag{77}$$

$$\frac{\mu_t}{\mu_{ang}} = f(Re_y) \tag{78}$$

There are different ways to treat the length scale function and the turbulent viscosity ratio, however, all treatments are written as a function of the wall-distance (y) Reynolds number, seen in equation (79).

$$Re_y = \frac{\sqrt{ky}}{v_{avg}} \tag{79}$$

All of the correlations use the same dissipation seen in equation (80).

$$\epsilon = \frac{k^{3/2}}{l_{\epsilon}} \tag{80}$$

For all equations using the length scale function and the turbulent viscosity ratio, the layer blending is dependent on a wall proximity indicator defined as:

$$\lambda = \frac{1}{2} \left[ 1 + \tanh \left( \frac{Re_y - Re_y^*}{A} \right) \right] \tag{81}$$

where:

$$Re_y^* = 60$$
 ;  $A = \frac{|\Delta Re_y|}{\text{atanh 0.98}}$  ;  $\Delta Re_y = 10$ 

Such that the blended turbulent viscosity is defined as:

$$\mu_t = \lambda \mu_{t_{k-\epsilon}} + (1 - \lambda) \mu \left(\frac{\mu_t}{\mu}\right)_{2-layer}$$
(82)

where:

 $\mu_{t_{k-\epsilon}} = \textit{Realizable } k - \epsilon \; \textit{turbulent viscosity}$ 

# 6.1.3.3 Uncertainty Quantification

A grid independence study was performed to investigate the impact of the variation in the base size, or number of cells in the mesh. Two different sized meshes with variations in the total number of cells were created to see if a finer mesh would vary the results of the model. The total number of nodes in the primary mesh contained 23 million cells while the refined mesh contained 28 million cells. Figures 25 and 26 depict the comparison of the original mesh and the refined mesh. The mesh was refined uniformly throughout the model.



Figure 25 The original mesh used through the duration of the simulation



Figure 26 The refined mesh used to verify the grid independence

In Table 2 the results of both models can be seen. In the final results, the pressure rise between the two stages is very similar. The pressure rise of the single stage changes merely 0.06%. This study verifies that changing the size of the mesh makes the change in simulation results negligible. This proves that the original grid is independent of the number of cells. The original grid was used for the remaining CFD simulations.

 Table 2 Grid Independence Study Results for RCIC Pump Simulations

	Original	Refined
	Mesh	Mesh
Cells	22907590	28400285
Pressure rise (Pa)	1137562	1144387
Ft. Head	1522.297142	1531.430925

# **6.2** Development of Thermal-Hydraulics Code Models

When the project proposal was written, it was expected that the new CFD models would need to be simplified in two stages, first to the thermal hydraulic code level (e.g. RELAP5-3D, TRACE) and then to the severe accident code level. During the first year of this project, further consideration led to the conclusion that the CFD models could be simplified directly to the severe accident code level. That is, the models developed within the project for the severe accident codes should also be applicable to the thermal hydraulic codes. Therefore, modeling specifically for a thermal hydraulic code was not necessary and was not conducted as part of this project.

#### **6.3** Development of Severe Accident Analysis Code Models

# **6.3.1 MELCOR Severe Accident Code Description**

Created by SNL for the Nuclear Regulatory Commission (NRC), MELCOR was originally conceived as a flexible, fast-running probabilistic risk assessment tool that has since evolved in to a best-estimate, systems-level severe accident analysis code primarily for light water reactors. MELCOR development began in 1982 - a few years after the events at TMI unit 2 - and has continued to the present day. MELCOR is capable of tracking severe accident progression up to source term generation. It can be employed in alternate capacities to study various thermal hydraulic, heat transfer, and aerosol transport phenomena. This is due in large part to the lumped parameter control volume/flow path modeling approach that is quite general and adaptable. MELCOR is under active development and maintenance by the reactor modeling and analysis division at SNL.

#### 6.3.1.1 Code Mechanics

MELCOR is comprised of a suite of packages that each fit in to one of three categories: basic physical phenomena, reactor-specific phenomena, or support functions [SNL, 2009]. Program execution involves two steps, MELGEN and MELCOR, as shown in Figure 27. All code packages used for a given problem communicate with one another as directed by an overseeing executive package. User input is processed by MELGEN, checked against code requirements, initialized, and used to write a restart file before running MELCOR. Calculation advancement through a specified problem time is performed by MELCOR. Text output and plot data are written to certain output files with a user-prescribed frequency. Certain code packages important to systems-level BWR and RCIC system modeling are described below.

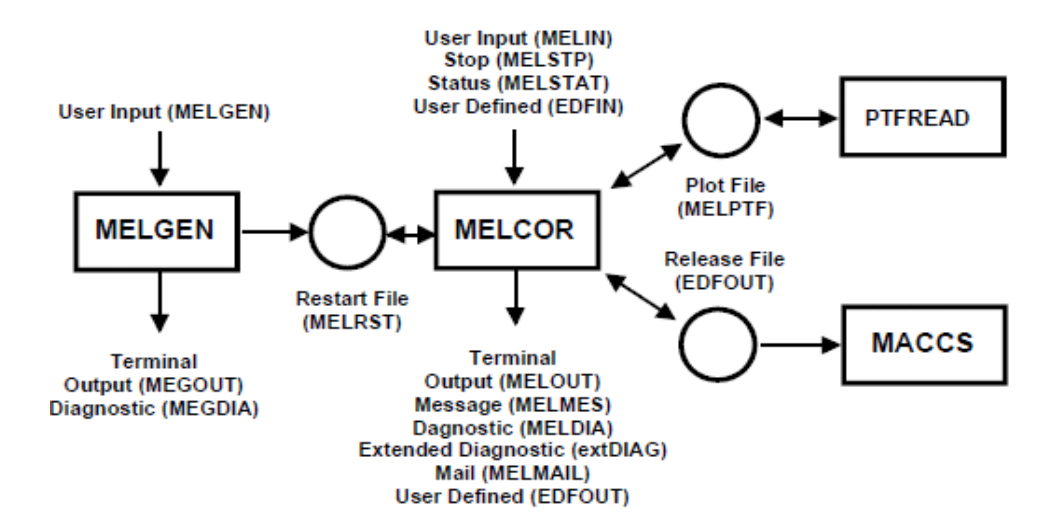


Figure 27 MELCOR execution flow diagram [SNL, 2016a]

The executive (EXEC) package is a support functions module responsible for overall execution control when running MELGEN or MELCOR. It essentially coordinates processing tasks for all other packages. It performs file handling functions, input and output processing, sensitivity coefficient modifications, time-step selection, problem time advancement, and calculation termination [SNL, 2016a].

The Control Volume Hydrodynamics (CVH) package is a basic physical phenomena module. It models, in part, the thermal-hydraulic behavior of all hydrodynamic materials that are assigned to control volumes in a calculation. Control volume altitudes (relative to some chosen reference) as well as material volumes are specified by CVH input. The initial thermodynamic states of all control volumes are defined by CVH input as are any energy or material sources/sinks. As part of this dissertation, the CVH package was modified to include a Terry turbine velocity stage model that is capable of interfacing with a Terry turbine pressure stage model (via the new "steam nozzle" type flow path). This development with the CVH package directly benefits current and future RCIC system (or TDAFW system) modeling. Much more technical detail on this new development is included in a subsequent section.

The Flow Path (FL) package is a basic physical phenomena module that works in tandem with the CVH package to predict thermal-hydraulic response. The FL input defines all characteristics of the control volume connections through which hydrodynamic material can relocate. However, no material can physically reside within a flow path in any given time-step. Instead, the FL package is concerned with momentum and heat transport of single or two phase material as it moves from one control volume to another. Friction losses (e.g. to pipe walls), form losses, flow blockages, valves, and momentum sources (e.g. pumps) are defined through the FL package. As part of this dissertation, the FL package was modified (new user input and new physics models in MELCOR source code) to include a homologous pump model so that a more mechanistic treatment of centrifugal pumps is available. Also, the FL package was modified to include a Terry turbine pressure stage (steam nozzle expansion) model that co-opts some features of the "time-independent" flow path. A turbo-shaft model capable of interfacing with homologous pumps and the new Terry turbine models was also integrated into the FL package as part of this dissertation. Obviously, these developments benefit RCIC system modeling directly, and further technical details are included in subsequent sections.

The Heat Structure (HS) package is another basic physical phenomena module that calculates onedimensional heat conduction within any so-called heat structures. The structures are intact, solid, and comprised of some material with some definite geometry. The HS package also models energy transfer at a heat structure surface. This might include convection heat transfer to hydrodynamic material of an adjacent control volume or radiation heat transfer to separate heat structures.

The core (COR) package is a reactor-specific phenomena module because the physics models employed generally depend on reactor type. It predicts the thermal response of the core and lower plenum. It frequently communicates with CVH, FL, and HS packages as fission power ultimately goes to hydrodynamic material or heat structures.

The Material Properties (MP) package is a support functions module that acts as a repository for material properties data. Apart from the NCG package that treats noncondensable gases, the MP package is the sole reference for all thermo-physical data of materials. There are built-in properties for certain materials (most of which are common to LWR's), but the user may optionally overwrite those defaults or create new materials entirely. Density, thermal conductivity, specific heat capacity, and enthalpy/melt point can be defined as functions of material temperature.

The Noncondensable Gases (NCG) package is a basic physical phenomena module in that it predicts noncondensable gas properties via the ideal gas law. Similar to the MP package, it acts in a support functions capacity because it passes requisite materials data to other physics packages for use. In the NCG package, a gas is characterized by its molecular weight, energy of formation, and specific heat capacity at constant volume which is assumed to be an analytic function of the gas temperature [SNL, 2016a]. There are over a dozen built-in noncondensable gases. As with the MP package, the user may overwrite any default properties or create entirely new materials.

The Decay Heat (DCH) package is a basic physical phenomena module. It can be deployed in "whole-core" mode so that the power at all times subsequent to reactor scram is computed using a version of the ANS standard decay curve.

The Control Function (CF) package is a support functions module. It can be leveraged to create real or logical functions for use by the physics packages. Real-valued control functions return a real value (i.e. floating point value), while logical control functions return one of two integer values that are interpreted as either "true" or "false". Most mathematical and logical functions available in FORTRAN are available for use in the CF package. A real-valued control function might be used to compute the density of some user-defined material via a user-defined function of material temperature. A logical-valued control function might be used to signal the start of a reactor scram or to close a user-defined valve in some flow path. Physics packages often reference control functions for required information. Control functions can also be helpful when a user is interested in calculating or plotting some variable that MELCOR does not compute by default.

The Tabular Function (TF) package is a support functions module. Tabular functions are utilized when definition of some dependent variable (e.g. decay heat) is required as a tabular function of some independent variable (usually time or temperature). As an example, the MP package often references tabular functions to retrieve material property values as a function of temperature. The user retains the option to define many input variables as either tabular or control functions. There are situations wherein a tabular function is more appropriate (e.g. material property data is known only at certain values of temperature), and there are cases in which a control function is more useful (e.g. material property data is approximated by an analytic function of temperature).

### 6.3.1.2 Modeling Concepts

Since the MELCOR development efforts undertaken for this work deal primarily with the CVH package and the FL package - and because the new RCIC system physics models must fit within pre-existing MELCOR paradigms - a more detailed overview of control volumes and flow paths is in order. The intent is to support subsequent mathematical descriptions of the new RCIC system models.

#### 6.3.1.3 Control Volumes

The MELCOR CVH/FL approach to model building is abstract and flexible relative to methods of other thermal-hydraulics codes. There are no pre-defined reactor components or structures. The user has the latitude to create pipes, vessels, ducts, core coolant channels, etc. using control volumes, flow paths, and heat structures in whatever manner deemed appropriate. Control volumes contain hydrodynamic material mass and associated energy consisting of internal energy and flow work (or just enthalpy, by definition). These materials can be liquids, vapors, and noncondensable gases so that in general all control volumes contain a "pool" of liquid and an "atmosphere" of vapor or gas. Control volume geometry specification is required, as the user must give an altitude and describe, indirectly, a control volume shape by specifying the available hydrodynamic volume between control volume elevations. Thermodynamic conditions of the pool and atmosphere are initially set by the user and may evolve with time (subject to solution of the governing equations) or not. Thermodynamic states of active control volumes are advanced by solving linearizedimplicit finite difference equations for mass, momentum, and energy [SNL, 2016a]. These equations are not reproduced here (see [SNL, 2016b]), but note that the control volume mass and energy equations contain source terms that could be leveraged by new RCIC system models to account for the evolution of a dispersed droplet (or fog) field upon condensation or the effects of a turbine as it extracts work from a control volume atmosphere.

#### 6.3.1.4 Flow Paths

Flow paths are code constructs that model the flow and momentum transport of hydrodynamic material between control volumes. As mentioned before, hydrodynamic material has no residence time in a flow path across any time-step. The tacit assumption is that any amount of hydrodynamic material that would occupy the physical volume of the flow path connection is negligibly small compared to hydrodynamic volume of the connected control volumes [SNL, 2016a]. The flow path package does account for friction losses, form losses, and inter-phase momentum/heat transport that would be associated with actual flow between connected volumes. Any single flow path connects only two control volumes, but there are no restrictions on the number of flow paths attached to any given control volume. Flow paths may be vertical or horizontal with several versions of each (e.g. atmosphere-first, pool-first, etc.)

The user must designate a "from", or "donor", control volume and a "to", or "acceptor", control volume, as well as several geometric parameters like from/to elevations, junction opening heights, flow path area, flow path length, and open fraction. Junction heights and from/to elevations have implications for any gravitational head terms appearing in the flow equations. The flow path length is related to the distance over which inter-phase momentum transport occurs. The importance is diminished in cases of single phase flow, and normally this length is assumed to be the center-to-center distance between connected control volumes. Flow paths may be fully open, partially open, or completely closed.

Regarding momentum transport, all dissipative pressure drops related to wall friction and form losses are accounted for in FL package input. The user must specify any and all form loss coefficients directly, as there are no predictive models for these values. Conversely, wall friction is handled by treating the flow path as one or more segments (in series along the flow direction), calculating an appropriate mixture Reynolds number based on a segment velocity, and deriving a Fanning friction factor that is used to compute a pressure drop in each segment [SNL, 2016a]. All that is needed from the user are segment geometric parameters such as area, length, and hydraulic diameter.

#### 6.3.1.5 Flow Paths and Steam Nozzle Expansion

Much like control volumes, flow paths can be "active" or "time-independent" with the distinction being that phasic velocity equations are solved to predict evolution of flow conditions in the former. For the latter, user input instead dictates phasic velocities. For purposes of RCIC system turbine pressure stage modeling, this "time independent" flow path functionality can be co-opted to implement a new steam nozzle expansion model. Essentially, the usual phasic velocity equations can be bypassed (in source code) for specially-flagged steam nozzle flow paths. These special flow paths would be treated as time-independent up until the point where look-ups for user-specified velocities would normally be performed. At that point, new steam nozzle physics subroutines could be called to compute, among other things, the phasic velocities (for atmosphere and/or fog). The results from these phasic velocity calculations could be used in a CVH package Terry turbine velocity stage model. Details of the new turbine pressure stage (steam nozzle physics) models are deferred to a subsequent section.

#### 6.3.1.6 Flow Paths and the Homologous Pump Formulation

The phasic velocity equations used to "solve" flow paths contain an explicit pressure head term reserved for momentum sources from influences external to the flow, e.g. a pump impeller. There are also semi-implicit terms in the phasic velocity equations that accounting for various other physics but not for pump head. Before homologous pump model development, CF-specified pumps were allowed in MELCOR but only a numerically explicit treatment of their effects was possible. As will be demonstrated in a subsequent section, the pre-existing explicit pump head term and the in-place semi-implicit terms of the general phasic velocity equation can be

manipulated to create a numerically semi-implicit pump head term treatment. The homologous pump performance model can be coded in MELCOR source and interfaced to both sides (implicit and explicit) of the phasic velocity equation pressure head term. Details of this new homologous pump model are deferred to a subsequent section.

# 6.3.1.7 Proposed Enhancements for RCIC System Modeling

As a quick recapitulation of the proposed enhancements to MELCOR source code for purposes of RCIC system modeling:

- Build a new centrifugal pump performance model (homologous pump model) and integrate it into the current CVH/FL solution framework with "semi-implicitness"
- Conceptualize a Terry turbine pressure stage (steam nozzle expansion) model and integrate it into the current CVH/FL framework using a strategy similar to that of "time-independent" flow paths
- Conceptualize a Terry turbine velocity stage model and integrate it into the current CVH/FL framework
- Conceptualize a turbo-shaft model capable of interfacing with the homologous pump model and the Terry turbine velocity stage model, integrate it into the current CVH/FL framework

A great deal of extra coding comes along with these models, namely the provisions for user input processing and text/plot output.

# **6.3.2** Homologous Pump Model

A homologous pump model was integrated into the MELCOR flow path (FL) package to predict the attending fluid momentum source (pressure head) of a centrifugal pump as a function of the pump impeller speed and the pump capacity (volumetric flow). This addition to MELCOR increases light water reactor modeling capability in general and RCIC system modeling in specific as a more mechanistic model of pump performance is available. The model also computes hydraulic torque (indicative of the brake power), pump friction torque, pump inertia, and pump energy dissipation (and thus efficiency). The homologous pump performance model therefore predicts the "brake power" (proportional to hydraulic torque) and the "hydraulic power" (proportional to the product of head and flow), with the difference between the two being the pump dissipation energy. Pump inefficiencies are "baked-in" to the pump performance model, but user input of rated conditions can account for extra inefficiencies if necessary.

The new MELCOR homologous pump model is similar to that of RELAP [INL, 2005] but with some distinguishing features including a polar homologous pump curve representation and a "universal correlation" as discussed in a later section. Several new MELGEN input records have been added that, in general, allow the user to fully specify:

- 1. Rated pump conditions,
- 2. Single/two-phase pump performance via homologous curve input,
- 3. Pump friction torque as a polynomial in pump speed  $\omega$ , or rather the non-dimensional ratio  $|\omega/\omega_R|$  with  $\omega_R$  the rated pump speed,
- 4. Pump inertia as a polynomial in the quantity  $|\omega/\omega_R|$ ,
- 5. Pump speed and motor torque controls,
- 6. Pump trips,
- 7. Pump numerical treatment options

Additionally, pump data from both the Semiscale [Olson, 1974] and Loft [Reeder, 1978] experiments are available as "built-in" performance modeling options. A "universal correlation" [Lahssuny and Jedral. 2004] is included. These features are described below.

6.3.2.1 Conventional Homologous Pump Representation

The essential goal of the homologous pump model is to characterize centrifugal pump performance by predicting the pressure head  $(\Delta P)$  and the hydraulic torque  $(\tau_H)$  given inputs of impeller speed (i.e. pump speed)  $\omega$  and pump capacity (volumetric flow rate) Q. Empirical homologous curves are one way of compactly summarizing pump performance in response to given conditions  $\omega$ , Q. In this representation, non-dimensional ratios  $\alpha$  and  $\nu$  are formed as:

$$\alpha = \frac{\omega}{\omega_R} \tag{81}$$

$$\nu = \frac{Q}{Q_R} \tag{82}$$

where:

 $\omega_R$ ,  $Q_R$  are rated pump impeller speed and rated pump capacity (volumetric flow)

Homologous ratios  $\alpha/\nu$  and  $\nu/\alpha$  are formed from the non-dimensional ratios. The entire domain of pump operation (4 modes) is covered by an independent variable space:

- | π/α | ≤ 1, then in the "α range" of the independent variable space
   | α/ν | < 1, then in the "ν range" of the independent variable space</li>

These homologous ratios become the independent variables for the homologous curve dependent variables which include single-phase pump head, single-phase hydraulic torque, fullydegraded pump head, and fully-degraded hydraulic torque. For each dependent variable, a plot can be created that traces out 4 possible operating mode curves, each with 2 pieces (called octants): the  $\alpha$  range piece and the v range piece. Thus, a homologous curve for a given dependent variable consists of 8 octants each representing different combinations of pump speed ( $\ge 0$  or < 0) and capacity (>= 0 or < 0). When  $\omega$  and Q are such that  $|\nu/\alpha|$  is less than or equal to 1, this indicates pump operation in the v range of the current mode, and as soon as v grows large enough that  $|\nu/\alpha|$ would exceed 1, the independent variable is changed to  $|\alpha/\nu|$  such that pump operation enters the α range of the current mode. Therefore, the magnitude of the independent variable is never greater than I and is bounded by [-1, 1]. Note that  $\alpha$  and  $\nu$  ranges deal exclusively with non-dimensional pump speed/capacity magnitudes and their ratios. The pump modes account for the 4 possible combinations of negative/positive speed and negative/positive capacity. The modes are summarized in Table 3 below.

Table 3 Possible Pump Operating Modes in MELCOR Simulations

Plot Quadrant	Non-dimensional Speed/Capacity	<b>Mode Identifier</b>
1 <sup>st</sup> (upper right)	$\alpha \ge 0$ and $\nu \ge 0$	Normal (N)
2 <sup>nd</sup> (Upper Left)	$\alpha > 0$ and $\nu < 0$	Dissipation (D)
3 <sup>rd</sup> (Lower Left)	$\alpha \le 0$ and $\nu \le 0$	Turbine (T)
4 <sup>th</sup> (Lower Right)	$\alpha < 0$ and $\nu > 0$	Reversal (R)

Note that the possibility of negative speed and negative capacity requires the independent variable to cross the zero value. The dependent variable also changes depending on the range  $(\alpha \text{ or } \nu)$  in question. In the homologous formulation, non-dimensional values for pump head and hydraulic torque are:

$$\boldsymbol{h} = \frac{H}{H_R} \tag{83}$$

$$t = \frac{\tau_H}{\tau_{H,R}} \tag{84}$$

where:

 $H_R$ ,  $\tau_{H,R}$  are rated head and rated hydraulic torque

Furthermore, these quantities are divided by either  $\alpha^2$  or  $\nu^2$  depending upon the range ( $\alpha$  or  $\nu$ ). An example of the final form for a homologous curve is shown in Figure 28. Note that Appendix A of Beeny [2017] contains all Semiscale [Olson, 1974] and Loft [Reeder, 1978] homologous pump curves.

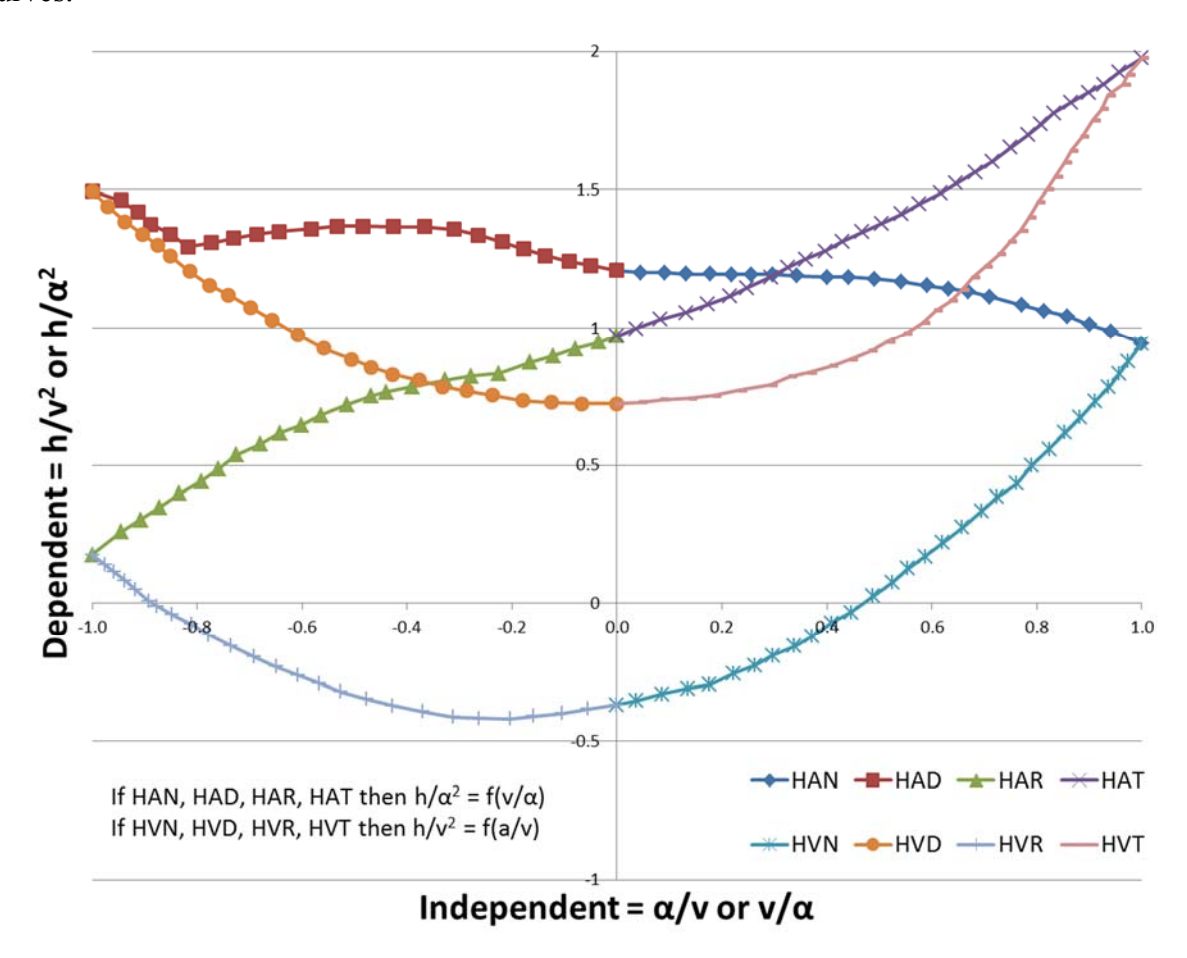


Figure 28 Semiscale single-phase head curve [Olson, 1974]

Note that a system of three-letter octant identifiers is used. Each octant identifier indicates at once the dependent variable, the independent variable, and the pump mode. The general identifier is [H/B][A/V][N/D/T/R], where the first [ ] denotes head (H)/torque (B), the second [ ] denotes  $\alpha$  range (A) or  $\nu$  range (V), and the third [ ] denotes normal (N)/dissipation (D)/turbine (T)/reversal (R).

# 6.3.2.2 Polar Homologous Pump Representation

For several reasons related to programming convenience, MELCOR internally employs the so-called polar homologous representation ([Narabayashi, 1986], [Kazimi and Todreas, 2001]) of pump performance. It bears some resemblance to the conventional homologous method, but uses different variable definitions such that the independent variable is always positive and bounded on  $[0, 2\pi]$ . The variable transformation allows all octants to be ordered in monotonically-increasing fashion with respect to a single independent variable. This obviously simplifies data interpolation logic, since with the homologous data representation a total of 8 separate data tables (one per octant) are used. Essentially, the polar homologous variable transformation results in one independent variable and one dependent variable.

The polar homologous representation is identical to the homologous representation until the point where independent and dependent variables are chosen. The new independent variable is:

$$x = C + \tan^{-1}\left(\frac{\alpha}{\nu}\right) \tag{85}$$

where:

 $\alpha$ ,  $\nu$  are defined as before for the conventional homologous pump representation

The constant C assumes different values depending upon the mode of pump operation. Regardless of the negative/positive sign of speed or capacity, the argument of the inverse tangent function does not change. Some useful properties of the inverse tangent function:

- Defined for an argument equal to zero
- Bounded ( $\pm \pi/2$ ) as its argument goes to infinity on either side of zero

One could foresee a problem if capacity and hence  $\nu$  equals zero, but in fact the division by zero can simply be treated as a case of the argument  $\alpha/\nu$  approaching  $+/-\infty$ . The homologous octants, under this definition of x, are arranged in a predictable way on  $[0,2\pi]$  as summarized in **Error!** Reference source not found.

Table 4 Octant Arrangement Under the Polar Homologous Representation

Octant Identifier (C Value)	Portion of Domain on $[0,2\pi]$
[H/B]VN (0)	$[0,\pi/4]$
[H/B]AN (0)	$[\pi/4,\pi/2]$
[H/B]AD (π)	$[\pi/2, 3\pi/4]$
[H/B]VD (π)	$[3\pi/4,\pi]$

[H/B]VT (π)	$[\pi, 5\pi/4]$
[H/B]AT (π)	$[5\pi/4, 3\pi/2]$
[H/B]AR (2π)	$[3\pi/2,7\pi/4]$
[H/B]VR (2π)	$[7\pi/4,2\pi]$

The dependent variables (head and torque functions, WH and WT) are:

$$WH = \left(\frac{h}{\alpha^2} \left| \frac{h}{\nu^2} \right) \middle/ \left( 1 + \left( \left( \frac{\nu}{\alpha} \right)^2 \right| \left( \frac{\alpha}{\nu} \right)^2 \right) \right)$$
 (86)

$$WT = \left(\frac{t}{\alpha^2} \left| \frac{t}{v^2} \right) \middle/ \left( 1 + \left( \left( \frac{v}{\alpha} \right)^2 \left| \left( \frac{\alpha}{v} \right)^2 \right) \right) \right)$$
 (87)

where:

 $h, t, \alpha, \nu$  are defined as before

( | ) a decision where left and right correspond to  $\alpha$  range and  $\nu$  range, respectively

One observes that WH, for example, is readily obtained from data pairs corresponding to any given octant, e.g. HAN where the homologous data pairs are  $(v/\alpha, h/\alpha^2)$ . Thus, there is no need for extra programming logic as the data pairs of each octant can be substituted into the WH and WT equations directly. After converting independent and dependent variables into polar homologous form, new plots (encapsulating the very same information) can be created. An example is shown in Figure 29 and may be compared to Figure 28. Clearly Figure 29 is more convenient for lookups and interpolation. Appendix A of Beeny [2017] contains all polar homologous plots for Semiscale and Loft data.

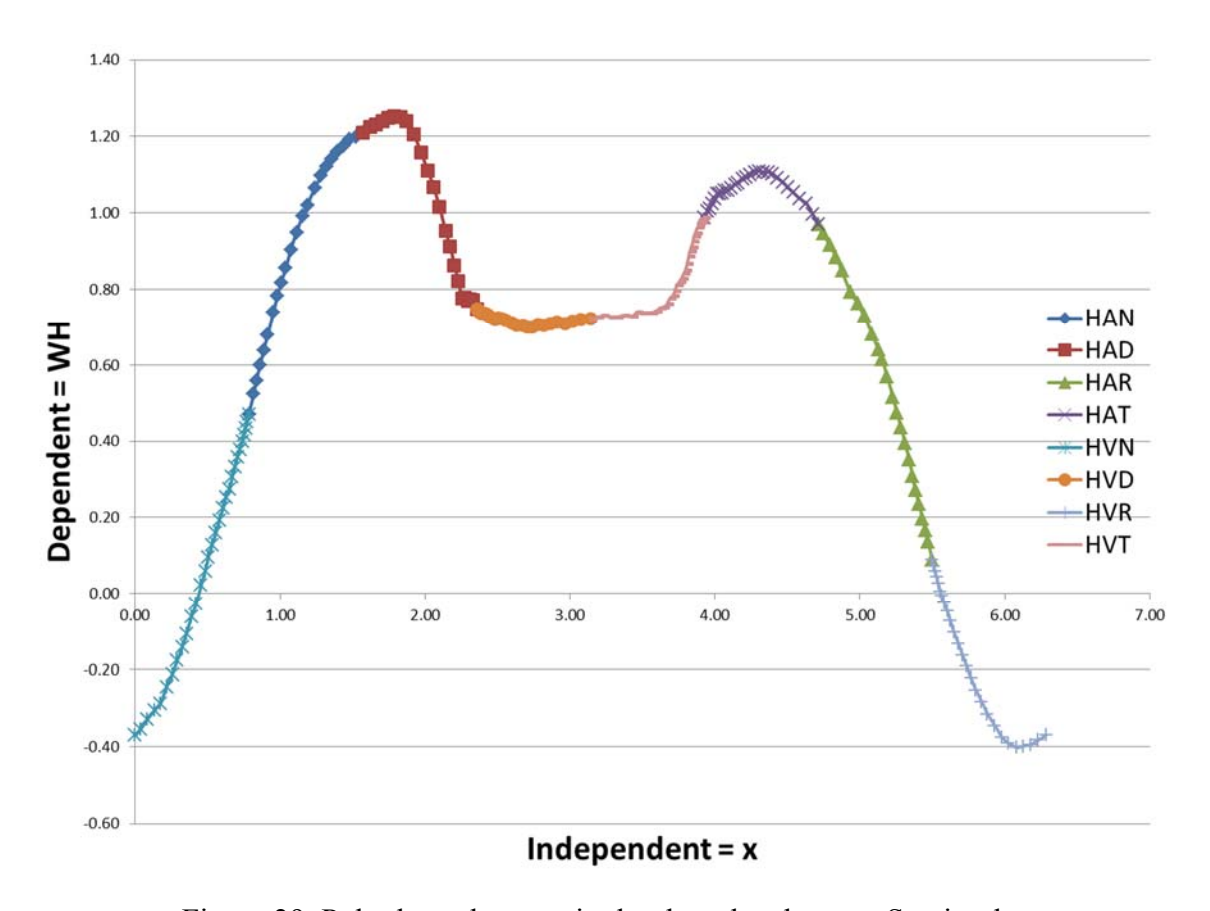


Figure 29 Polar homologous single-phase head curve, Semiscale

#### 6.3.2.3 Universal Pump Correlation Alternative

If inadequate information is known about a given centrifugal pump to furnish a full set of performance data for the homologous pump model, an alternative "universal correlation" is available that requires only the specific pump speed as an input. Based upon several data sets, head and hydraulic torque functions were derived as a function of pump specific speed for a given set of pump conditions  $x(\omega,Q)$  [Lahssuny and Jedral. 2004]. These functions are only valid in the normal pump operating mode (x on  $[0,\pi/2]$ ). Pump specific speed is defined, in this context, as a dimensional quantity:

$$N_s = \frac{\omega_R \sqrt{Q_R}}{{H_R}^{3/4}} \tag{88}$$

where:

 $\omega_R$ ,  $Q_R$ ,  $H_R$  are rated pump impeller speed, rated capacity, and rated head

Given specific speed and given pump conditions ω and Q, a double interpolation may be performed on independent variable x and dependent variable WH (WT) to recover an estimate of WH (WT) from which a dimensional head (hydraulic torque) can be recovered. Outside the normal mode and/or for two-phase considerations, the universal correlation cannot apply. The actual MELCOR

implementation follows the method in [Lahssuny and Jedral. 2004] so that each curve of Figure 30 and Figure 31 is fitted with a  $3^{\rm rd}$  order polynomial  $f(N_s)$ . Interpolation is done with fits rather than with raw tabular pump data. Arrays of curve fit data are included in Tables 5 and 6. The constants A through D represent polynomial coefficients:

$$(WH|WT) = A + BN_s + CN_s^2 + DN_s^3$$
(89)

A user with knowledge only of rated conditions for a given pump may predict its performance for the normal operating mode. Semiscale and LOFT data are included in the universal correlation data set.

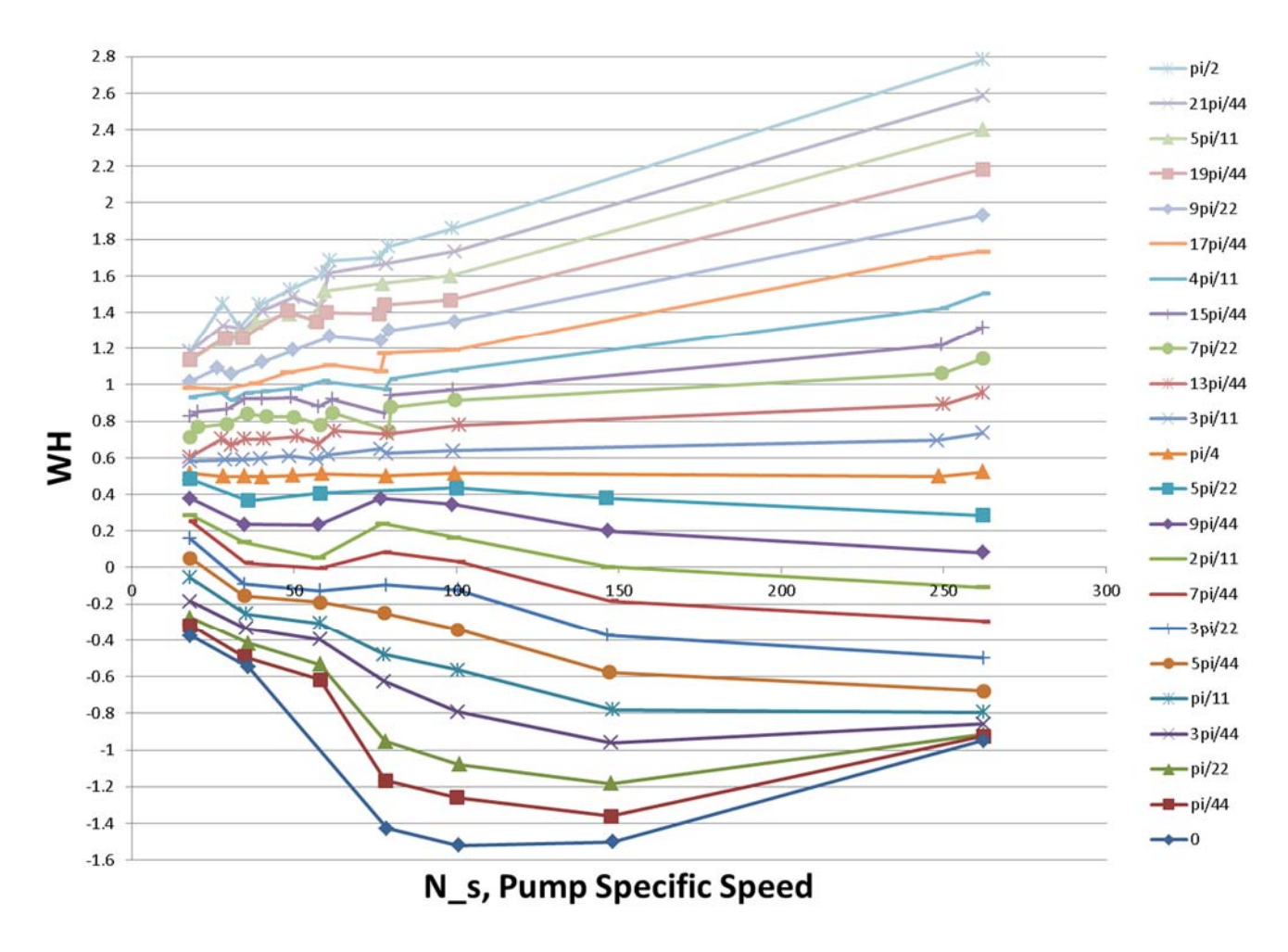


Figure 30 Universal correlation head function, each curve an x on  $[0, \pi/2]$  [Lahssuny and Jedral. 2004]

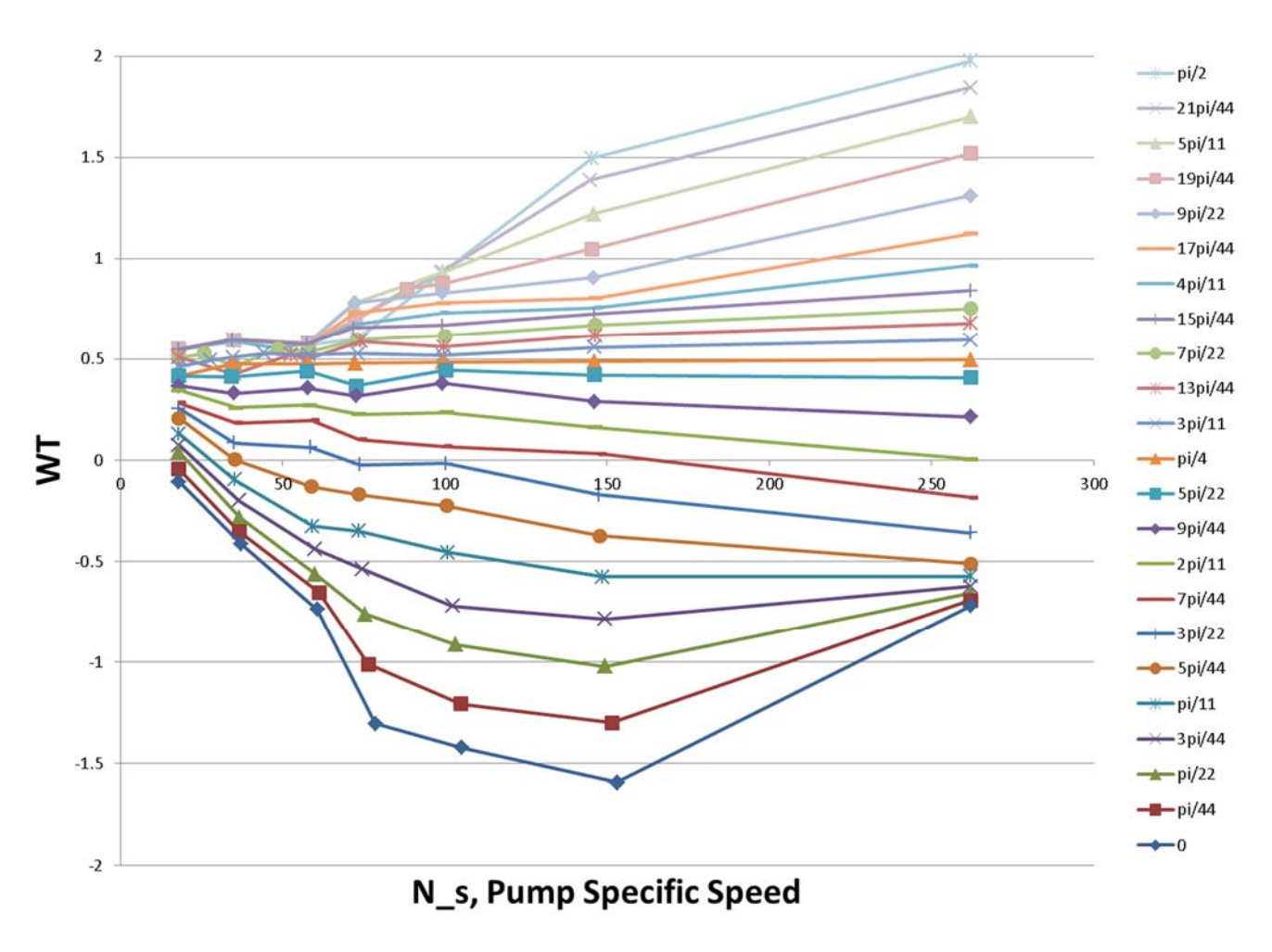


Figure 31 Universal correlation torque function, each curve an x value on  $[0, \pi/2]$  [Lahssuny and Jedral. 2004]

Table 5 Polynomial fit data for curves in Figure 30

X	A	В	C	D	X	A	В	C	D
$\pi/2$	1.0946	0.0088	-9.5600E-06	0.00	$5\pi/22$	0.4515	-0.0062	0.0000E+00	0.0000E+00
$21\pi/44$	1.0855	0.0077	-8.2443E-06	0.00	$9\pi/44$	0.3630	-0.0010	0.0000E+00	0.0000E+00
5π/11	1.0813	0.0063	-5.3857E-06	0.00	$2\pi/11$	0.2595	-0.0021	7.1163E-06	-1.7401E-08
19π/44	1.0486	0.0049	-2.6536E-06	0.00	$7\pi/44$	0.2138	-0.0025	-5.8728E-07	1.0494E-08
$9\pi/22$	0.9948	0.0038	-1.0063E-06	0.00	$3\pi/22$	0.1375	-0.0038	2.6036E-06	9.2164E-09
17π/44	0.9508	0.0021	2.7905E-06	0.00	$5\pi/44$	0.1218	-0.0063	1.2390E-05	0.0000E+00
$4\pi/11$	0.9048	0.0011	4.1812E-06	0.00	π/11	0.0200	-0.0065	-2.8421E-07	4.9910E-08
$15\pi/44$	0.8508	0.0007	3.4325E-06	0.00	$3\pi/44$	-0.1975	0.0022	-1.7558E-04	1.1621E-06
$7\pi/22$	0.7454	0.0012	7.6247E-07	0.00	$\pi/22$	0.0130	-0.0143	3.8180E-05	1.0995E-08
$13\pi/44$	0.6240	0.0017	-2.1960E-06	0.00	$\pi/44$	0.0541	-0.0184	5.7827E-05	-8.7150E-09
$3\pi/11$	0.5494	0.0012	-1.9922E-06	0.00	0	0.2704	-0.0346	2.0041E-04	-3.2951E-07
$\pi/4$	0.5000	0.0000	0.0000E+00	0.00		0.2704	0.05 10	2.001112 04	3.273111 07

Table 6 Polynomial Fit Data for Curves in Figure 31

X	A	В	С	D	X	A	В	С	D
π/2	0.3014	0.0068	-1.00E-06	0.00E+00	$5\pi/22$	0.4089	0.0002	-6.00E-07	0.00E+00
$21\pi/44$	0.3385	0.0065	-3.00E-06	0.00E+00	$9\pi/44$	0.3540	0.0000	-2.00E-06	0.00E+00
$5\pi/11$	0.3909	0.0056	-2.00E-06	0.00E+00	$2\pi/11$	0.3371	-0.0012	-3.00E-07	0.00E+00
$19\pi/44$	0.4370	0.0041	2.00E-07	0.00E+00	$7\pi/44$	0.3522	-0.0048	3.00E-05	-6.00E-08
$9\pi/22$	0.4532	0.0044	-1.00E-05	3.00E-08	$3\pi/22$	0.2704	-0.0039	6.00E-06	0.00E+00
$17\pi/44$	0.4577	0.0044	-2.00E-05	5.00E-08	$5\pi/44$	0.3547	-0.0108	6.00E-05	-1.00E-07
$4\pi/11$	0.4992	0.0021	-1.00E-06	0.00E+00	$\pi/11$	0.3614	-0.0153	8.00E-05	-1.00E-07
$15\pi/44$	0.5235	0.0016	-1.00E-06	0.00E+00	$3\pi/44$	0.3814	-0.0190	1.00E-04	-1.00E-07
$7\pi/22$	0.4573	0.0018	-3.00E-06	0.00E+00	$\pi/22$	0.4123	-0.0227	1.00E-04	-1.00E-07
$13\pi/44$	0.4382	0.0016	-3.00E-06	0.00E+00	$\pi/44$	0.3134	-0.0210	7.00E-05	0.00E+00
$3\pi/11$	0.4750	0.0007	-1.00E-06	0.00E+00	0	0.3756	-0.0257	8.00E-05	0.00E+00
$\pi/4$	0.4294	0.0008	-2.00E-06	0.00E+00	,	0.5760	0.0207	0.002 00	0.002

### 6.3.2.4 Head and Hydraulic Torque

Speed and flow are used to deduce a value of the polar homologous independent variable x which can then be used to interpolate the polar homologous functions WH and WT. In general, two-phase effects must also be accounted for and x may be used to interpolate WH2 and WT2. Note WH2 and WT2 are the two-phase (fully-degraded) head and torque functions obtained from empirical data. The void fraction (or in the case of a MELCOR flow path, the atmosphere area fraction) can be used to interpolate the so-called head and torque degradation multipliers MH and MT. These functions of void fraction are included in Appendix A of Beeny [2017]. Note that the LOFT report [Reeder, 1978] provides degradation multipliers as well. This information is used to compute overall head and torque functions:

$$WH_{overall} = WH - MH * (WH - WH2)$$

$$(90)$$

$$WT_{overall} = WT - MT * (WT - WT2)$$
(91)

Using definitions already presented, the non-dimensional head and hydraulic torque are obtained from these overall functions. The dimensional head and hydraulic torque is then:

$$H = hH_R \tag{92}$$

$$\tau_H = t\tau_{H,R} \tag{93}$$

If the user chooses an explicit numerical formulation, the pump pressure head is included as a momentum source term in the flow path phasic velocity equations (like FANA and QUICK-CF pump types in the MELCOR FL package [SNL, 2016b]). The user may also request a semi-implicit numerical formulation for which pump head is expanded into implicit and explicit terms such that new-time phasic velocities do depend on new-time pump head terms. The details of this implementation are included in a subsequent section.

#### 6.3.2.5 Miscellaneous Pump Model Features

#### 6.3.2.5.1 Pump Friction Torque

The frictional torque associated with a pump is modeled as in RELAP [INL, 2005] with a polynomial in the quantity  $|\omega/\omega_R|$ , according to:

$$\tau_{fr} = \begin{cases} \tau_{frn}, \left| \frac{\omega}{\omega_R} \right| < S_{PF} \\ \tau_{fr0} + \tau_{fr1} \left| \frac{\omega}{\omega_R} \right|^{x1} + \tau_{fr2} \left| \frac{\omega}{\omega_R} \right|^{x2} + \tau_{fr3} \left| \frac{\omega}{\omega_R} \right|^{x3}, \left| \frac{\omega}{\omega_R} \right| \ge S_{PF} \end{cases}$$

$$(94)$$

The user specifies each of the constants and exponents in the above equations as well as the critical speed ratio  $S_{PF}$  below which the frictional torque is constant. The sign convention is that frictional torque is negative for a positive pump speed but positive for a negative pump speed. The exponents x1, x2, and x3 cannot equal 0 but there are no restrictions on the torque coefficients.

# 6.3.2.5.2 Pump Moment of Inertia

The pump inertia may be variable in certain situations, so a model similar to that of frictional torque is applied. A 3<sup>rd</sup> order polynomial is written as:

$$I_{p} = \begin{cases} I_{pn}, for \left| \frac{\omega}{\omega_{R}} \right| < S_{PI} \\ I_{P0} + I_{P1} \left| \frac{\omega}{\omega_{R}} \right| + I_{P2} \left| \frac{\omega}{\omega_{R}} \right|^{2} + I_{P3} \left| \frac{\omega}{\omega_{R}} \right|^{3}, for \left| \frac{\omega}{\omega_{R}} \right| \ge S_{PI} \end{cases}$$

$$(95)$$

The user may specify each polynomial coefficient but not the exponents. The pump inertia is a positive nonzero quantity and, as with friction torque, may be held constant for pump speed below a threshold.

# 6.3.2.5.3 Pump Controls: Speed, Motor Torque, Trips

Pump speed is controlled either by the user via CF or TF or by the code via solution of a torque-inertia equation. The user has three options for speed control:

- 1. Always specified by CF/TF,
- 2. Always obtained by torque-inertia equation solution, or
- 3. CF/TF specified until a trip indicates switchover to torque-inertia equation

Option 1 would be appropriate if, for example, some externally-imposed CF model was dictating pump speed. Option 3 would be appropriate for modeling a pump coast-down during off-normal operating conditions after some time of normal pump operation. Option 2 allows the net torque (motor torque less the sum of hydraulic and friction torque) to determine whether pump speed increases (net positive torque), decreases (net negative torque), or stays constant (net zero torque, motor balances friction and hydraulic torques).

To model a scenario in which the pump speed can ramp up and coast down repeatedly, option 2 would allow for finer control over motor torque and hence net torque so as to drive pump speed in the desired direction. The convention for a pump motor under MELCOR TRIP CF (see [SNL, 2016a] for a description) control is: if the TRIP CF is ON-FORWARD, motor torque is zero and if TRIP CF is ON-REVERSE motor torque is given by CF/TF. Given the motor torque/trip convention, virtually any pump shut off and restart sequence can be modeled. The torque-inertia equation is:

$$I_{p} \frac{d\omega}{dt} = \tau_{net} = \tau_{motor} - (\tau_{H} + \tau_{fr})$$
(96)

In general, the net torque has three components shown above (motor, hydraulic, friction), but the motor torque is only nonzero if:

- the pump trip has not occurred or
- a pump trip CF is in an ON-REVERSE state

The assumptions are that an ON-FORWARD trip CF state signifies a pump disconnection from its driving motor while an ON-REVERSE trip CF state allows pump connection to its driving motor. Equation (96) above is treated either:

- explicitly in time via a forward Euler technique with all terms being functions of old-time pump speed, or
- implicitly in time via a backward Euler technique and fixed-point iteration such that all terms depend on new-time pump speed

For the forward Euler method, the difference equation for pump speed update is:

$$\boldsymbol{\omega}^{n} = \boldsymbol{\omega}^{n-1} + \frac{\tau_{net}(\boldsymbol{\omega}^{n-1})}{I_{p}(\boldsymbol{\omega}^{n-1})} \Delta t \tag{97}$$

where:

n = current time level; n - 1 = old time level;  $\Delta t = \text{time-step}$ 

For the backward Euler method, the fixed-point iteration scheme is:

$$\begin{cases}
\boldsymbol{\omega}^{n}_{[0]} = \boldsymbol{\omega}^{n-1} \\
\boldsymbol{\omega}^{n}_{[i+1]} = \boldsymbol{\omega}^{n-1} + \frac{\tau_{net}(\boldsymbol{\omega}^{n}_{[i]})}{I_{p}(\boldsymbol{\omega}^{n}_{[i]})} \Delta t, for i = 1 \dots i_{lim}
\end{cases}$$
(98)

The fixed-point iteration scheme starts with the guess that pump speed at time level n is that of time level n-l. Then, an iterative solution proceeds wherein the net torque and pump inertia are evaluated at the latest-iterate pump speed to approximate the next-iterate value. Eventually, the next-iterate pump speed matches the last-iterate pump speed within some convergence tolerance. This solution method incorporates n-level information into the solution of the n-level pump speed and ought to improve code performance when the torque-inertia equation is being solved.

# 6.3.2.5.4 Pump Energy Dissipation and Efficiency

The total power imparted to a pumped fluid by an impeller rotating at a given speed is equal to the product of that speed and the delivered hydraulic torque. This quantity is also known as "brake power" or "brake horsepower". In reality, not all the power delivered to the fluid is manifest as a pressure (head) increase (and therefore as "hydraulic power") because some fraction is lost to dissipation, appearing as thermal energy added to the fluid. If the brake power is known and the hydraulic power can be calculated, the energy dissipation DISS is:

DISS = 
$$(brake\ power) - (hydraulic\ power) =$$
 (99)
$$\tau_H \omega \frac{2\pi}{60} - gH\left((1 - \alpha_g)\rho_f V_f + \alpha_g \rho_g V_g\right) Af$$

This suggests one measure of pump efficiency EFF:

$$EFF = \frac{gH((1-\alpha_g)\rho_f V_f + \alpha_g \rho_g V_g)Af}{\tau_H \omega_{60}^{2\pi}}$$
(100)

By this definition, efficiency is the quotient of hydraulic power (i.e. used for pumping) and brake power (the sum of useful and lost power).

The dissipated energy heats up the pumped fluid and cannot, in general, be neglected. A simple way to account for dissipation energy addition is to assume that both the pool and the atmosphere (if both are present) receive amounts of thermal energy that would lead to identical increases in their respective phasic temperatures [INL, 2005]. Therefore, if the pool and atmosphere were in thermal equilibrium before the dissipation energy addition, they remain so afterwards. Accordingly, a phasic split fraction is computed as:

$$f_{P,DISS} = \frac{\left( (1 - \alpha_g) \rho_f C_{p,f} \right)}{\left( (1 - \alpha_g) \rho_f C_{p,f} + \alpha_g \rho_g C_{p,g} \right)} \tag{101}$$

Then, the rate of dissipation energy addition to the pool is:

$$DISS_P = DISS * f_{P,DISS} =$$

$$\left(\tau_{H}\omega\frac{2\pi}{60} - gH\left(\left(1 - \alpha_{g}\right)\rho_{f}V_{f} + \alpha_{g}\rho_{g}V_{g}\right)Af\right)\left(\frac{\left(\left(1 - \alpha_{g}\right)\rho_{f}C_{p,f}\right)}{\left(\left(1 - \alpha_{g}\right)\rho_{f}C_{p,f} + \alpha_{g}\rho_{g}C_{p,g}\right)}\right)$$
(102)

While the rate of dissipation energy addition to the atmosphere is:

$$DISS_A = DISS * (1 - f_{P,DISS}) =$$
(103)

$$\left(\tau_H \omega \frac{2\pi}{60} - gH\left((1 - \alpha_g)\rho_f V_f + \alpha_g \rho_g V_g\right) Af\right) \left(\frac{(\alpha_g \rho_g C_{p,g})}{(1 - \alpha_g)\rho_f C_{p,f} + \alpha_g \rho_g C_{p,g}}\right)$$

Note that the dissipation energy source is essentially equivalent, in MELCOR terms, to two external sources (one AE-type and one PE-type, see [SNL, 2016a]) with a RATE interpretation. The dissipation energy is effectively treated as such when the user chooses to model dissipation energy addition

# 6.3.2.6 Semi-Implicitness and Integration with MELCOR Solution Scheme

6.3.2.6.1 MELCOR Phasic Velocity Equation

The general set of linearized phasic velocity equations MELCOR solves [SNL, 2016b] is included below as equation (104). The left-hand side includes new-time phase  $\varphi$  velocities for the  $j^{th}$  flow path  $(V_{j,\varphi}^n)$  and  $V_{j,\varphi}^n$  as well as terms for other flow paths interfaced to the same from/to CVs with which flow path j communicates. The right- hand side includes old-time information, i.e. velocity equation terms that are treated explicitly. Currently, the term  $\Delta P_j$  appears on the right-hand side of the  $j^{th}$  flow path velocity equation and is treated as an explicit source term.

$$\left(1 + \frac{K_{j,\varphi}^{*} \Delta t}{2L_{j}} \left| V_{j,\varphi}^{n-} + V_{j,\varphi}' \right| + \frac{\alpha_{j,-\varphi} f_{2,j} L_{2,j} \Delta t}{\rho_{j,\varphi} L_{j}} \right) V_{j,\varphi}^{n} - \frac{\alpha_{j,-\varphi} f_{2,j} L_{2,j} \Delta t}{\rho_{j,\varphi} L_{j}} V_{j,-\varphi}^{n} + \sum_{s,\psi} C(j,\varphi:s,\psi) V_{s,\psi}^{n} \tag{104}$$

$$= V_{j,\varphi}^{o+} + \frac{K_{j,\varphi}^{*} \Delta t}{2L_{j}} \Big| V_{j,\varphi}^{\prime} \Big| V_{j,\varphi}^{n-} + \frac{\Delta t}{\rho_{j,\varphi} L_{j}} \Big( \hat{P}_{i} + \Delta P_{j} - \hat{P}_{k} \Big)$$

$$+ \Big( \rho \ g \Delta z \Big)_{j,\varphi}^{o} + \frac{\partial (\rho \ g \Delta z)_{j,\varphi}}{\partial M_{i,P}} \Big( \hat{M}_{i,P}^{o} - M_{i,P}^{o+} \Big)$$

$$+ \frac{\partial (\rho \ g \Delta z)_{j,\varphi}}{\partial M_{k,P}} \Big( \hat{M}_{k,P}^{o} - M_{k,P}^{o+} \Big) \Big]$$

It is through  $\Delta P_i$  that any type of pump must deliver a pressure head (momentum source) to its assigned flow path. For the newly-implemented homologous pump model to be semi-implicit such that phasic velocity calculations do not totally treat pump head as an "old-time" quantity, then:

- ΔP<sub>j</sub> must be expanded into implicit and explicit terms, and
   Equation (104) above must be rearranged such that:
- - o Terms multiplying  $V_{j,\varphi}^n$  and  $V_{j,-\varphi}^n$  on the left account for the implicit part of  $\Delta P_j$
  - The explicit part of  $\Delta P_i$  is retained on the right-hand side

#### 6.3.2.6.2 Expansion of $\Delta P_i$

The new pump model predicts, among other things, the pump performance in terms of delivered pressure head H as a result of pumping the fluid. The pressure head is computed as a function of pump speed, ω, and pump capacity (volumetric flow rate), Q. The pump capacity is a function of phasic velocities and is computed, for flow path j, as:

$$Q_j = Af(V_{j,P} + V_{j,A}) \tag{105}$$

where:

$$Q_j$$
 = Volumetric flow rate, flow path j [m<sup>3</sup>/s]; A = Flow path j area [m<sup>2</sup>]  
 $f$  = Flow path j open fraction;  $V_{j,X}$  = Velocity,  $X$  = P (pool),  $X$  = A (atmosphere)

Note Af is the product of flow path area and flow path open fraction. Thus  $Q_j$  depends on phasic velocities so that pump head can be expressed as a function of phasic velocities. Neglecting the dependence of head on pump speed (i.e. assuming pump speed is constant) and expanding via a two-term Taylor series about  $Q_j^{n-}$  for n- the latest-iterate value (computed with n- velocities during the inner velocity iteration) one recovers:

$$H_j^n = H_j^{n-1} + \left(\frac{dH}{dQ}\right)^{n-1} \left(Q_j^n - Q_j^{n-1}\right)$$
(106)

Alternatively, expanding  $\Delta P_i$  with respect to Q:

$$\Delta P_j = \Delta P_j^{n-1} + \left(\frac{d\Delta P}{dQ}\right)^{n-1} \left(Q_j^n - Q_j^{n-1}\right)$$
(107)

where:

$$\Delta P_j^{n-1} = \rho_m g H_j^{n-1}$$
, relating pressure [Pa] to head [m] 
$$\left(\frac{d\Delta P}{dQ}\right)^{n-1} = \rho_m g \left(\frac{dH}{dQ}\right)^{n-1}$$
, relating derivatives

Substituting from equation (105):

$$\Delta P_{j} = \rho_{m}gH_{j}^{n-1} +$$

$$\rho_{m}gAf\left(\frac{dH}{dQ}\right)^{n-1}\left(V_{j,P}^{n} + V_{j,A}^{n}\right) - \rho_{m}gAf\left(\frac{dH}{dQ}\right)^{n-1}\left(V_{j,P}^{n-} + V_{j,A}^{n-}\right)$$

$$(108)$$

Separating out the terms further:

$$\Delta P_{j} = \rho_{m} g H_{j}^{n-1} - \rho_{m} g A f \left(\frac{dH}{dQ}\right)^{n-1} \left(V_{j,P}^{n-}\right) -$$

$$\rho_{m} g A f \left(\frac{dH}{dQ}\right)^{n-1} \left(V_{j,A}^{n-}\right) + \rho_{m} g A f \left(\frac{dH}{dQ}\right)^{n-1} \left(V_{j,P}^{n}\right) +$$

$$98$$

$$(109)$$

$$\rho_m g A f \left(\frac{dH}{dQ}\right)^{n-1} \left(V_{j,A}^n\right)$$

<u>6.3.2.6.3 Modified Velocity Equation</u> This expression for  $\Delta P_j$  can be substituted back into equation (104). Also, the new-time information can be moved to the left side while the old-time information can be kept on the right

$$V_{j,\varphi}^{n}\left(1+\left(\frac{K_{j,\varphi}^{*}\Delta t}{2L_{j}}\right)\left|V_{j,\varphi}^{n-}+V_{j,\varphi}^{\prime}\right|+\left(\frac{\alpha_{j,-\varphi}f_{2,j}L_{2,j}\Delta t}{\rho_{j,\varphi}L_{j}}\right)-\zeta\left(\frac{\Delta t}{\rho_{j,\varphi}L_{j}}\right)\rho_{m}gAf\left(\frac{dH}{dQ}\right)^{n-1}\right)- (110)$$

$$V_{j,-\varphi}^{n}\left(\frac{\alpha_{j,-\varphi}f_{2,j}L_{2,j}\Delta t}{\rho_{j,\varphi}L_{j}}+\zeta\left(\frac{\Delta t}{\rho_{j,\varphi}L_{j}}\right)\rho_{m}gAf\left(\frac{dH}{dQ}\right)^{n-1}\right)+\sum_{S,\psi}\left[C(j,\varphi;S,\psi)V_{S,\psi}^{n}\right]=$$

$$V_{j,\varphi}^{o+}+\left(\frac{K_{j,\varphi}^{*}\Delta t}{2L_{j}}\right)\left(\left|V_{j,\varphi}^{\prime}\right|V_{j,\varphi}^{n-}\right)+$$

$$\left(\frac{\Delta t}{\rho_{j,\varphi}L_{j}}\right)\left(\hat{P}_{i}+\left(\rho_{m}gH_{j}^{n-}-\zeta\rho_{m}gAf\left(\frac{dH}{dQ}\right)^{n-1}\left(V_{j,\varphi}^{n-}+V_{j,-\varphi}^{n-}\right)\right)-\hat{P}_{k}\right)$$

$$+\left(\rho g\Delta z\right)_{j,\varphi}^{o}+\frac{\partial(\rho g\Delta z)_{j,\varphi}}{\partial M_{i,P}}\left(\hat{M}_{i,P}^{o}-M_{i,P}^{o+}\right)+\frac{\partial(\rho g\Delta z)_{j,\varphi}}{\partial M_{k,P}}\left(\hat{M}_{k,P}^{o}-M_{k,P}^{o+}\right)$$

Thus linearizing  $\Delta P_i$  leads to:

- New terms in coefficient multipliers of  $V_{j,\phi}^n$  and  $V_{j,-\phi}^n$  for implicit part of  $\Delta P_j$  a modified explicit term for  $\Delta P_j$

The new terms are written in bold text in equation (110). Note the factor  $\zeta$  is positioned so that if set to 1 the semi-implicit formulation can be used while if set to 0, the solution reverts to a fully explicit treatment for  $\Delta P_j$  ( $\Delta P_j = \rho_m g H_j^{n-}$ ). Note the "old-time" information is denoted (n-1) while the "latest-iterate" information is denoted n-, the distinction being that n-1 quantities are set before the level n velocity iteration loop is entered while n- quantities change with each level n velocity iteration.

Within the doubly-iterative MELCOR solution (an outer pressure iteration, an inner velocity iteration), the evaluation of pump semi-implicit terms happens within the innermost phasic velocity solution. Changes in provisional flow path phasic velocities impact flow path volumetric flow rates and thus new  $\frac{dH}{dQ}$  values and new explicit and semi-implicit terms are evaluated with each velocity iteration.

# 6.3.2.6.4 Derivative Computation, (dH/dQ)<sup>n-1</sup>

The change in pump head with respect to flow (at constant speed) must be evaluated at level n-1 conditions (speed and flow). This derivative describes how the pump head (generally a function of single and two-phase pump performance) varies with capacity in the neighborhood of  $Q_i^{n-1}$ . A cubic spline interpolation method is used to evaluate the derivative. An outline of the method is as follows:

- Use cubic spline fit formula to approximate user-specified single-phase head  $H_{1\varphi}$  data and two-phase head  $H_{2\varphi}$  data as a function of the polar homologous independent variable  $x = C + atan\left(\frac{\omega Q_R}{\omega_R Q}\right)$
- Compute  $\frac{dH_{1\phi}}{dx}$  and  $\frac{dH_{2\phi}}{dx}$  from cubic spline prescriptions for the first derivative of a spline-fitted function (involves function values and 2<sup>nd</sup> derivatives)

An approach outlined in [Press et al., 1986] was followed to obtain cubic spline fits of the functions  $H_{1\varphi}$  and  $H_{2\varphi}$  in addition to their respective derivatives  $\frac{dH_{1\varphi}}{dx}$  and  $\frac{dH_{2\varphi}}{dx}$ . A "natural cubic spline" was assumed, i.e. the 2<sup>nd</sup> derivatives at both boundaries of the function were set to zero. The procedure amounts to solving a tridiagonal system of equations for second derivatives of the function in question and then substituting those values into formulae for interpolated values of the function and its first derivative. The total head derivative is:

$$\frac{dH}{dQ} = \frac{dH_{1\varphi}}{dQ}_{x(Q)} + \frac{dH_{2\varphi}}{dQ}_{x(Q)} = \frac{dx}{dQ}_{Q} \left( \frac{dH_{1\varphi}}{dx}_{x(Q)} + \frac{dH_{2\varphi}}{dx}_{x(Q)} \right)$$
(111)

where:

$$\frac{dx}{dQ_O} = -\omega Q_R \omega_R / (\omega_R^2 Q^2 + \omega^2 Q_R^2) \text{ since } x = C + a \tan\left(\frac{\omega Q_R}{\omega_R Q}\right)$$

#### 6.3.3 Terry Turbine Velocity Stage Model

The Terry turbine compound velocity stage model is a somewhat more generalized version of a single control-volume angular momentum balance approach originally proposed for Pelton turbine analysis [Shames, 1982]. It is the method proposed for a CF model in a pre-existing RCIC system MELCOR deck [Ross et al., 2015], but with explicit accounting for:

- Several separate nozzles and their jets of steam/water
- Each bucket/reversing chamber pair (i.e. each velocity stage)
- A general number 'n' of reversing chambers allotted per steam nozzle, with the proposed capability to model any user-requested number of steam nozzles that may be circumferentially-situated about the rotor wheel

For a given Terry turbine wheel with x steam nozzles around its perimeter and with y reversing chambers per nozzle, this model could be applied in all x instances with different steam nozzle jet effluents for every instance. The steam jets would be predicted by separate applications of a Terry turbine pressure stage model as described in a subsequent section.

The mathematical model of the velocity stage of a Terry turbine is based on a control volume (CV) formulation for conservation of angular momentum [Ross et al., 2015]. A simpler form of the model presented in this section has already been applied in MELCOR via user-defined control functions with some success.

The quantity of interest in a velocity stage model of an impulse-type turbine is the momentum flux delivered to the rotor because the attending force ultimately turns the rotor and exerts a "positive" torque on a coupled shaft. For a compounded velocity stage, the total momentum flux and/or force integrated over all velocity stages is of interest. The velocity stage model developed hereafter predicts a turbine torque that is intended to factor into a shaft torque/inertia (angular speed) equation which dictates pump impeller speed and hence turbo-pump performance.

Conceptually, the CV used for analysis resembles the sketch in Figure 32. Note the CV is drawn around a Terry turbine rotor in such a way that the turbo-pump shaft is cut by the control surface. Rotor buckets reside within the cylindrical CV while steam nozzles and any reversing chambers in the turbine casing interior are outside the CV.

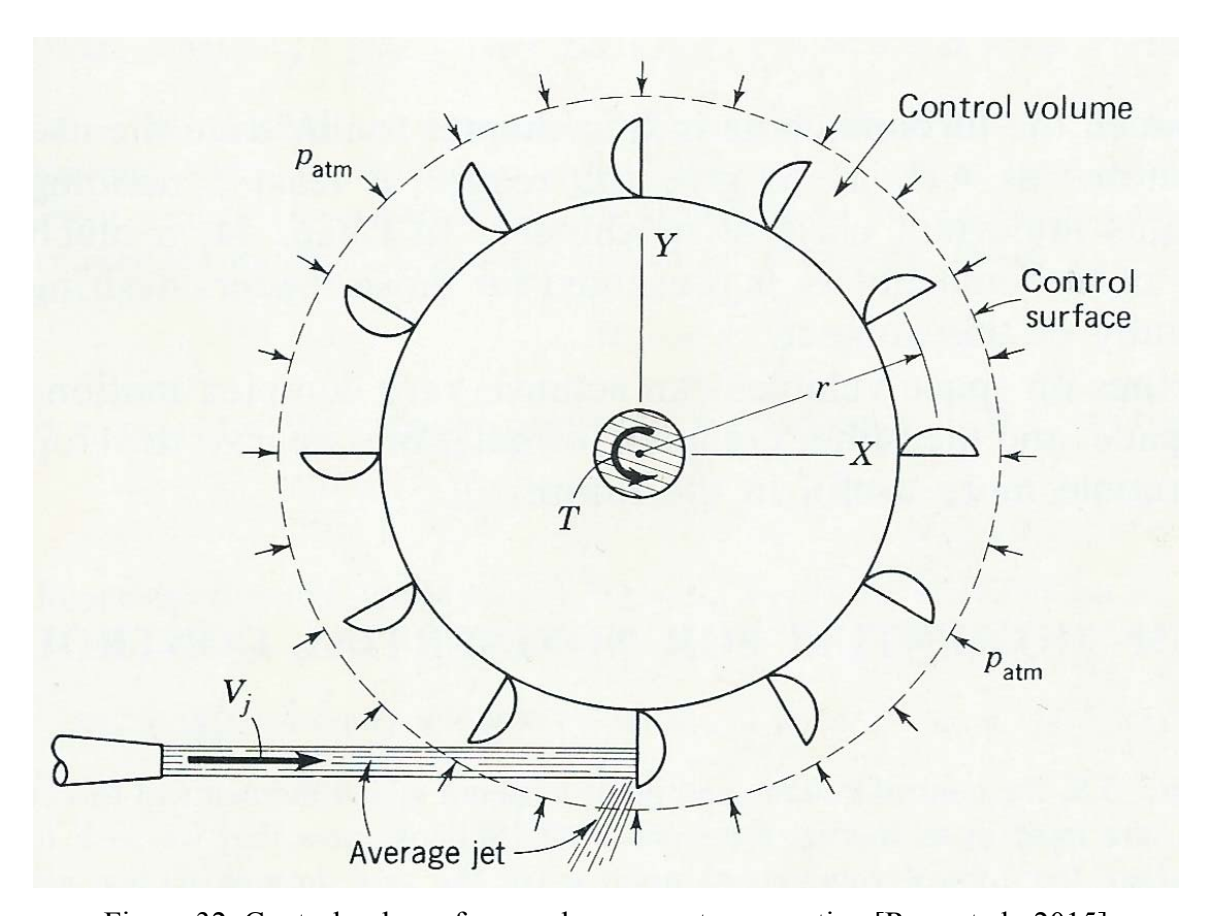


Figure 32 Control volume for angular momentum equation [Ross et al., 2015]

Figure 32 shows how the steam jet emanating from a nozzle crosses the CV boundaries. Presumably, the fluid jet would cross the control surface several more times (steam enters, exits the CV while passing through rotor bucket and reversing chambers) in a compound velocity stage though this is not explicitly shown. Working in cylindrical coordinates, the  $\theta$  component of angular momentum has a scalar equation written as:

where:

 $\vec{u}$  is the fluid velocity vector incoming to a rotor bucket

 $u_{\theta}$  is the tangential component of the fluid velocity vector exiting a rotor bucket

r is the turbine rotor radius

The first term in equation (112) accounts for any torques crossing the control surface. In this case, only the shaft crosses the boundary. The second term accounts for body forces and may be neglected. The third term accounts for net moment of momentum flux delivered by any fluid flow crossing the control surface. This term may be expanded so that compound velocity stages (multiple entries/exits of a fluid stream across the control surface) may be taken into account. The fourth term is a transient term that is shown in Appendix B of Beeny [2017] to contain the moment of inertia and time derivative of rotor angular speed.

The net moment of momentum flux term may be written for the CV as:

Details behind the evaluation of this term for a compound velocity stage turbine are included in Appendix B of Beeny [2017] which resembles the derivations in [Ross et al., 2015]. The OUT sum consists of n+1 distinct fluid streams exiting n+1 distinct rotor buckets, where n is the number of reversing chambers per steam nozzle. The IN sum consists of one fluid stream emanating from a nozzle and n distinct fluid streams entering n distinct buckets after exiting from one of n reversing chambers. Velocity triangles (a typical analysis tool for Pelton-type turbines) can be leveraged to describe the IN summation in terms of bucket loss coefficients and angles between the bucket velocity vector and fluid inlet/outlet velocity vectors (details in Appendix B of Beeny [2017]). The OUT summation can be written in terms of the tangential component of fluid velocity exiting the bucket. Thus:

$$\sum_{OUT} \left[ \left| \overrightarrow{R} \times \overrightarrow{u} \right|_{out} \dot{m}_{out} \right] = \sum_{i=1}^{n+1} \left[ r u_{\theta,i} \dot{m}_{out,i} \right]$$
(114)

$$\sum_{IN} \left[ \left| \overrightarrow{R} x \overrightarrow{u} \right|_{in} \dot{m}_{in} \right] = \sum_{i=1}^{n+1} \left[ rV_{j,i} \cos(\beta_i) \dot{m}_{in,i} \right]$$
(115)

Employing relationships from velocity triangles (Appendix B of Beeny [2017]), the moment of momentum flux term looks like:

$$\sum_{i=1}^{n+1} \left[ r^2 \omega \dot{m}_{in,i} \left( 1 + C_{B,i} (\cos(\beta_i)) \right) - r V_{j,i} (\cos(\beta_i)) \left( C_{B,i} + 1 \right) \dot{m}_{in,i} \right]$$

Furthermore, there are relationships between terms in the above equation (Appendix B of Beeny [2017]):

$$\dot{m}_{in.i} = \gamma_{RC.i-1} \xi_{i-1} \dot{m}_{in.i-1} \tag{117}$$

$$V_{j,i} = u_{\theta,i-1}C_{RC,n} = C_{RC,i-1} \left( r\omega - C_{B,i-1} \left( V_{j,i-1} - r\omega \right) (\cos(\beta_{i-1})) \right)$$
(118)

These essentially capture the effects of reversing chambers. Reversing chamber crescent holes can vent some steam mass to the casing, hence the factor  $\gamma_{RC}$ . Also, they can cause some decrease in steam velocity, hence the factor  $C_{RC}$  analogous to  $C_B$  for a rotor bucket.

Turning now to the transient term, it can be shown (Appendix B of Beeny [2017]) through use of velocity triangle relationships and with some mathematical manipulations that:

$$\frac{\partial}{\partial t} \iiint \rho r u_{\theta} dV = \sum_{i=1}^{n+1} \left[ \frac{\partial}{\partial t} \iiint \rho r u_{\theta,i} dV \right] = I_T \frac{\partial \omega}{\partial t} \left( 1 + C_{B,i} (\cos(\beta_i)) \right)$$
(119)

Assembling all pieces and accounting for multiple nozzles, the torque-inertia equation is:

$$-\tau_{shaft} = -\tau_{pump} = I_{T} \frac{\partial \omega}{\partial t} \sum_{k=1}^{m} \left[ \sum_{i=1}^{n+1} \left[ 1 + C_{B,i}(\cos(\beta_{i})) \right] \right] +$$

$$\sum_{k=1}^{m} \left[ \sum_{i=1}^{n+1} \left[ \left[ r^{2} \omega \dot{m}_{in,i} \left( 1 + C_{B,i}(\cos(\beta_{i})) \right) \right] - \left[ rV_{j,i}(\cos(\beta_{i})) \left( C_{B,i} + 1 \right) \dot{m}_{in,i} \right] \right] \right]$$
(120)

$$\dot{m}_{in,i} = \begin{cases} \dot{m}_{jet} & i = 1\\ \gamma_{RC,i-1} \xi_{i-1} \dot{m}_{in,i-1} & i > 1 \end{cases}$$
 (121)

$$V_{j,i} = \begin{cases} V_{jet} & i = 1 \\ C_{RC,i-1} \left( r\omega - C_{B,i-1} \left( V_{j,i-1} - r\omega \right) (\cos(\beta_{i-1})) \right) & i > 1 \end{cases}$$
 (122)

where:

 $\dot{m}_{in,i} = \dot{m}_{out,i}$ , for i > 1, mass into bucket equals mass out of bucket

n = number of reversing chambers in  $k^{th}$  nozzle; m = number of nozzles in turbine

Therefore, the turbine torque can be calculated in terms of the nozzle jet conditions and a set of bucket loss coefficients  $C_{B,i}$ , steam exit angles  $\beta_i$ , steam carry-over fractions  $\xi_{i-1}$ , reversing chamber loss coefficients  $C_{RC,i}$ , and reversing chamber leakage coefficients  $\gamma_{RC,i}$ . These various coefficients will be left for the user to specify or, as described in a subsequent section, CMFD results could furnish a "built in" data set. Note also that in Equation (120), the pump moment of inertia and any friction torques can be added in to round out the full torque-inertia equation for the entire RCIC turbo-pump.

#### **6.3.4 Terry Turbine Pressure Stage Model**

The pressure stage model treats the flow of steam (dry saturated or superheated) through a converging/diverging nozzle as a sequence of expansion processes:

- An isentropic expansion from the nozzle inlet through the throat and to a point where condensation heat release begins to introduce entropy
- A Rayleigh flow process between the end of the last isentropic expansion and the Wilson point (point of maximum nucleation, maximum steam super-saturation)
- A Rayleigh flow process between the Wilson point and the point of full reversion from thermodynamic non-equilibrium (re-establishment of saturation)
- An isentropic expansion between the end of the last Rayleigh flow process and the nozzle outlet with provision for standing normal shocks
- A standing normal shock (over-expanded flow with respect to back-pressure) or a jet expansion (if under-expanded flow with respect to back-pressure)

Implementation in MELCOR follows the example of a time-independent, user-specified flow path (see [SNL, 2016a], [SNL, 2016b]) except an expansion model is applied for phasic velocities in a steam nozzle.

The expansion process without any consideration of aerodynamic shocks is shown in Figure 33 below. The states included on the h-s diagram are:

- 01, representing inlet stagnation conditions
- 2, representing the point where expanding steam crosses the saturation line
- m, representing the point where condensation starts to release latent heat to the steam such that significant entropy is introduced
- $\mathbf{n}$ , representing the Wilson point (point of maximum nucleation and maximum super-saturation), reached at a time  $t_n$  after point 2 is reached
- **a**, representing the state that expanding steam would have reached if it expanded on an isentropic line for a time  $t_n$  after point 2 is reached
- 3, representing the point where thermodynamic phase equilibrium is re-established
- 4, representing the nozzle exit state (on an isentropic line with state 3, no shocks)

The only distinguishing feature from conventional isentropic compressible flow theory is the latent heat release between states m and 3. This process can be modeled by a Rayleigh flow process which assumes:

- One dimensional flow through a constant cross-sectional area duct
- Steady flow
- Frictionless flow

#### • Heat addition (non-adiabatic flow)

In the present case, thermal energy is added to flowing steam as a consequence of latent heat release. Heat addition in this case equals the product of latent heat and wetness fraction. Thus, the heat addition is proportional to evolved wetness which can be obtained by evaluation of the so-called nucleation-growth integrals [Dobbins, 1983] as will be discussed below. The Rayleigh flow relationships ([Cengel and Boles [2008], [Dobbins, 1983], [Ding et al., 2013]) are such that a downstream state (e.g. state 'n') can be determined from an upstream state (idealized state 'a' in this case) and a known heat addition between states.

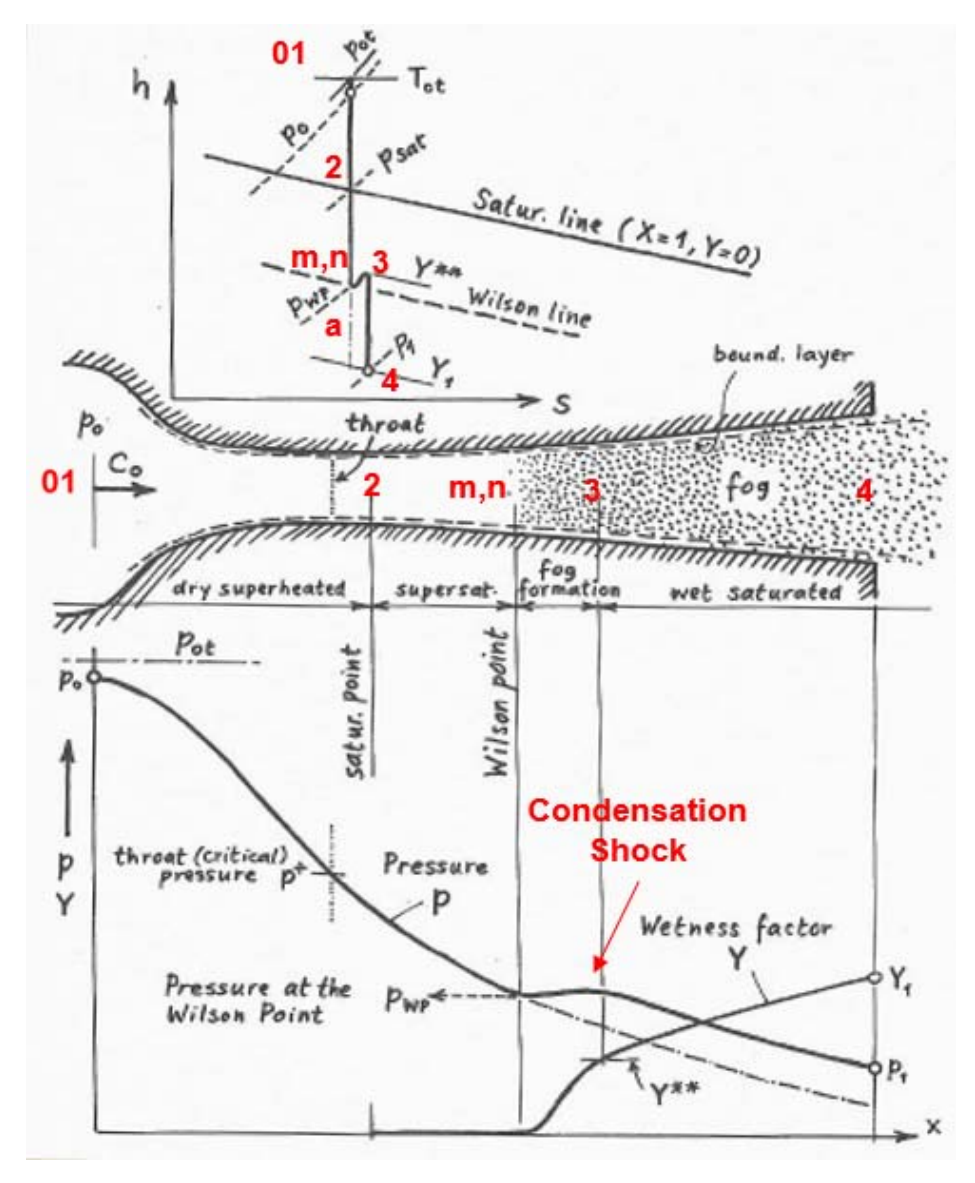


Figure 33 Qualitative h-s diagram, pressure/wetness plots for expansion

An ideal gas equation-of-state relationship is typically chosen for analytical Wilson point solutions, and this assumption has been shown to compare well with more rigorous computations

and experiments. The error is certainly low enough to justify the assumption in light of the considerable complexity in implementing more complicated equations of state.

Note that a user input option for purely isentropic steam expansion (to the neglect of any and all steam phase metastability) is included. This particular formulation is discussed in turn below.

#### 6.3.4.1 Ideal Gas Isentropic Flow

Isentropic flow in this case implies one-dimensional, steady, frictionless, adiabatic flow such that stagnation enthalpy and entropy both remain constant during the expansion process. Isentropic flow property relations that connect any downstream location 2 to the inlet stagnation state 01 are [Cengel and Boles [2008]:

$$\frac{T_2}{T_{01}} = \left(1 + \left(\frac{\gamma - 1}{2}\right) M_2^2\right)^{-1}$$
 Temperature Ratio (123)

$$\frac{P_2}{P_{01}} = \left(1 + \left(\frac{\gamma - 1}{2}\right) M_2^2\right)^{-\gamma/\gamma - 1}$$
 Pressure Ratio (124)

$$\frac{\rho_2}{\rho_{01}} = \left(1 + \left(\frac{\gamma - 1}{2}\right) M_2^2\right)^{-1/\gamma - 1} \quad \text{Density Ratio}$$
 (125)

Relating entropy and enthalpy:

$$T * ds = du + P * dv = dh - v * dP$$
(126)

Using specific heat definitions (isochoric and isobaric):

$$c_v = \frac{\partial u}{\partial T_v}$$
;  $c_p = \frac{\partial h}{\partial T_p}$  (127)

Thus, for an isentropic process and using static temperatures and pressures:

$$R * \ln\left(\frac{P_2}{P_1}\right) = \int_{T_1}^{T_2} c_p(T) * \left(\frac{dT}{T}\right)$$
 (128)

Rearranging leads to a pressure ratio equation:

$$\frac{P_2}{P_1} = exp\left[-\frac{1}{R} * \int_{T_2}^{T_1} c_p(T) * \left(\frac{dT}{T}\right)\right]$$

$$\tag{129}$$

Additionally, a Mach number relationship can be derived from the fact that stagnation enthalpy remains constant across the expansion (pressure and kinetic energy trade-off):

$$M_2^2 = \frac{2}{KRT_2} \int_{T_2}^{T_1} c_p(T) * dT$$
 (130)

Note that with the above isentropic flow relations, the state 2 pressure and Mach number may be evaluated from known state 2 temperature (or from a guessed value in an iterative procedure). In a computational procedure, constant specific heats may be assumed if appropriate or a Gaussian quadrature approach could be applied (see Appendix C of Beeny [2017]).

#### 6.3.4.2 Ideal Gas Rayleigh Flow

Rayleigh flow implies one-dimensional, steady, compressible, frictionless flow through a constant-area duct. It is an idealized representation of steam nozzle flow locally at/around the Wilson point and rapid condensation zone. Conservation equations between two states 1 and 2 are [Cengel and Boles [2008]:

$$\rho_1 v_1 = \rho_2 v_2 \quad \text{Continuity} \tag{131}$$

$$P_1 + \rho_1 v_1^2 = P_2 + \rho_2 v_2^2$$
 Momentum (132)

$$q + h_1 + \frac{{v_1}^2}{2} = h_2 + \frac{{v_2}^2}{2}$$
 Energy (133)

Thus:

$$q = c_p(T_2 - T_1) + \frac{v_1^2 - v_2^2}{2} = h_{02} - h_{01} = c_p(T_{02} - T_{01})$$
(134)

Giving rise to property relations in terms of Mach number *Ma* for a Rayleigh process [Cengel and Boles [2008]:

$$\frac{P_2}{P_1} = \frac{\left(1 + \gamma M_1^2\right)}{\left(1 + \gamma M_2^2\right)}$$
 Pressure Ratio (135)

$$\frac{T_2}{T_1} = \frac{\left(M_2^2 (1 + \gamma M_1^2)^2\right)}{\left(M_1^2 (1 + \gamma M_2^2)^2\right)} \text{ Temperature Ratio}$$

$$\frac{\rho_2}{\rho_1} = \frac{v_1}{v_2} = \frac{\left(M_1^2 (1 + \gamma M_2^2)\right)}{\left(M_2^2 (1 + \gamma M_1^2)\right)} \text{ Density Ratio}$$
(136)

$$\frac{\rho_2}{\rho_1} = \frac{v_1}{v_2} = \frac{(M_1^2 (1 + \gamma M_2^2))}{(M_2^2 (1 + \gamma M_1^2))}$$
 Density Ratio (137)

Additionally, there are stagnation property relations not reproduced here. It should be mentioned however that during a Rayleigh flow process with heat addition, the stagnation enthalpy (and hence the stagnation temperature) changes as a result of heat addition [Cengel and Boles [2008]:

$$\frac{h_{02} - h_{01}}{c_p} = (T_{02} - T_{01}) = \frac{q}{c_p} = \frac{h_{fg} Y_2}{c_p}$$
(138)

where:

Y = Wetness fraction

The dimensionless entropy change can be written as [Cengel and Boles [2008].:

$$\frac{s_2 - s_1}{c_p} = \ln \left[ \left( \frac{M_2^2}{M_1^2} \right) \left( \frac{1 + \gamma M_1^2}{1 + \gamma M_2^2} \right)^{\gamma + 1/\gamma} \right]$$
 (139)

The wetness fraction Y must come from nucleation-growth integral evaluation across the Rayleigh process (discussed subsequently), and it will be shown how these relationships can be employed in an iterative solution process to deduce Wilson point conditions and to predict flow properties at the point of reversion from non-equilibrium.

#### 6.3.4.3 Nucleation-Growth Integrals

The nucleation-growth integral assists with determining wetness evolved from super-saturated steam. The wetness fraction (mass of liquid water per unit mass of steam) is predicted at a downstream state 2 from an upstream state 1 by integrating the effects of nucleation and condensation growth between states. Gyarmathy [1976] and Dobbins [1983] present two slightly different takes on the nucleation-growth integral. Both will be presented here because both help to solidify the concept.

Gyarmathy's discussion [1976] of the nucleation growth integral begins with the definition of a spatial variable x and a spatial variable of integration  $\xi$  defined between  $x_s$  (the spatial location of state 2 where saturation line is first crossed by expanding steam) and x. Then, the wetness fraction is:

$$Y(x) = \frac{4\pi}{3} \rho_l \int_{x_s}^{x} r(x,\xi)^3 v(\xi) d\xi$$
 (140)

where:

 $r(x, \xi)$  = Radius of droplet at x assuming droplet born at upstream location  $\xi$ 

 $v(\xi)d\xi$  = Drop number per mass of steam, born between  $x = \xi$  and  $x = \xi + d\xi$ 

This wetness fraction expression can be differentiated to yield:

$$Y'(x) = \frac{4\pi}{3} \rho_l \left[ \frac{d}{dx} \left( \int_{x_s}^x r(x,\xi)^3 v(\xi) d\xi \right) + \int_{x_s}^x \frac{d}{dx} (r(x,\xi)^3 v(\xi) d\xi) \right]$$
(141)

$$=\frac{4\pi}{3}\rho_{l}\left[\frac{d}{dx}\left(\int_{x_{s}}^{x}r(x,\xi)^{3}v(\xi)d\xi\right)+\int_{x_{s}}^{x}3\left(r(x,\xi)^{2}\frac{\partial r(x,\xi)}{\partial x}v(\xi)d\xi\right)\right]$$

Furthermore:

$$r(x,\xi) = r^*(\xi) + \int_{\xi}^{x} \frac{\partial r(x',\xi)}{\partial x'} dx', \text{ for } x' \text{ between } \xi \text{ and } x$$
 (142)

$$\dot{r} = \frac{\partial r(x,\xi)}{\partial t}$$
, expressing condensation growth rate of droplet radius (143)

$$v(x) = \frac{I(x)}{v(x)} = \frac{\text{Nucleation rate } \left[\frac{\text{drop}}{\text{kg}_{/s}}\right]}{\text{velocity } [m/s]}$$
(144)

$$Y'(x) = \frac{4\pi}{3} \rho_l r^*(x) \frac{I(x)}{v(x)} + \frac{4\pi \rho_l}{v(x)} \int_{x_s}^{x} \left[ r^*(\xi) + \int_{\xi}^{x} \frac{\dot{r}}{v(x)} dx' \right]^2 \dot{r} \frac{I(\xi)}{v(\xi)} d\xi$$
 (145)

Dobbins [1983] proposes a slightly different formulation in which spatial variables are converted into time variables. Beginning with a similar definition of wetness fraction:

$$Y(x)\dot{m} = \int_{-\infty}^{x} m(x_1, x) J(x_1) A_c(x_1) dx_1$$
 (146)

where:

 $m(x_1, x) = \text{Mass of a droplet at } x$ , born at location  $x_1$ 

 $A_c(x_1)dx_1$  = Local volume element

 $J(x_1)$  = Embryo formation rate per unit volume per time

Dividing through by  $\dot{m} = \rho_q vA$  leads to a conversion from space to time coordinates:

$$Y = \int_0^t \frac{4\pi}{3} \rho_l r(t_1, t)^3 \left( \frac{J(x_1)}{\rho_g} \right) \left( \frac{dx_1}{v} \right) = \int_0^t \frac{4\pi}{3} \rho_l r(t_1, t)^3 I(t_1) dt_1$$
 (147)

Differentiating with respect to time:

$$Y' = 4\pi\rho_l \int_0^t r(t_1, t)^2 I(t_1) \frac{\partial r(t_1, t)}{\partial t_1} dt_1 + \frac{4\pi\rho_l}{3} I(t) r^{*3}$$
(148)

The nucleation-growth integrals for wetness fraction and its time derivative are now defined with respect to time, and certain other assumptions can be used to evaluate the integrals between two states, i.e. between two times.

Firstly, elements of classical nucleation theory may be assumed so that the following relationships hold for nucleation rate and condensation growth rate:

$$I = Ae^{-B\eta}$$
 Nucleation Rate (149)

where:

$$\eta = \frac{1}{T^3(\ln(S))^2}$$

$$A = \frac{\rho_g}{\rho_l} \left( \frac{2\sigma}{\pi m_v^3} \right)^{1/2}$$

$$B = \frac{16\pi\sigma^3}{K(\rho_l R)^2}$$

$$\frac{\partial r}{\partial t} = \dot{r} = \left(\frac{\lambda_g \Delta T}{\rho_l h_{fg}}\right) \frac{1 - r^*/r}{1 + 1.59 \bar{\lambda}/r} \quad \text{Condensation Rate}$$
 (150)

The critical radius (size of freshly-nucleated drops) comes from a thermodynamic relation:

$$r^* = \frac{2\sigma}{\rho_l RT \ln(S)} \tag{151}$$

Assuming an approximately constant condensation growth rate and assuming a definition of vapor molecule mean free path leads to a simplified droplet growth rate equation:

$$\frac{\partial r}{\partial t} = \dot{r} = c_g = \frac{\rho_g c_p \Delta T}{2.4 \rho_l h_{fg} P r_g} \sqrt{RT}$$
(152)

Both integrals (for Y and Y' as in Equations (147) and (148) or Equations (140) and (141) can be evaluated (Laplace method, see Appendix C of Beeny [2017]) to ascertain wetness at the Wilson point. Note the integration is from time zero at state '2' to time  $t_n$  at Wilson point. However, the problem is not quite so straightforward, and several auxiliary relationships are derived based on a mixture of assumptions and physical observations about the Wilson point (Appendix C of Beeny [2017]). The entire set of nucleation/growth closures can be used along with Rayleigh flow property relationships (and isentropic flow relationships for upstream states) in an iterative approach to resolve a self-consistent set of Wilson point conditions.

#### 6.3.4.4 Normal Shocks and Aerodynamic Back Pressure Effects

Converging-diverging nozzle flow of an ideal gas is largely governed by back pressure. Choked flow at the throat will only occur if the ratio of inlet to back pressure reaches a sufficiently low value. When treating steam as an ideal gas, this critical pressure ratio is approximately 0.546 or 0.576 depending upon whether the steam is superheated or saturated, respectively. As the back pressure is lowered and the inlet-to-back pressure ratio falls further below the critical value, certain quantities remain unchanged:

- The throat Mach number reaches a maximum (unity, sonic flow),
- The flow velocity reaches a maximum (speed of sound of the medium),
- The pressure reaches a minimum, and
- The mass flow rate reaches a maximum

However, the decreasing back pressure will affect the flow beyond (downstream of) the throat as discussed previously. One outcome of that review was that nozzle back pressure, at certain values, can lead to standing normal shocks within or just outside the diverging section. Across a shock plane, pressure increases and velocity decreases in an approximately step-wise fashion such that the flow becomes subsonic.

To account for aerodynamic effects in a systems-level, control volume oriented solution approach, some simplifications must be made. Most importantly, the physical location of the shock inside the diverging section cannot be resolved. If the known back pressure indicates it, the flow may be assumed to pass through a standing normal shock at the nozzle exit plane. There are conservation equations that must be satisfied upstream (1) and downstream (2) of the shock [Cengel and Boles [2008]:

$$\rho_1 v_1 A_1 = \rho_2 v_2 A_2 \quad \text{Continuity} \tag{153}$$

$$A(P_1 - P_2) = \dot{m}(v_2 - v_1) \quad \text{Momentum}$$
 (154)

$$h_1 + \frac{{v_1}^2}{2} = h_2 + \frac{{v_2}^2}{2}$$
, or  $h_{02} = h_{01}$  Energy (155)

Note there is an attending increase in entropy such that  $s_2 > s_1$ . Thus, for a one-dimensional ideal gas flow across a normal shock, these property relations hold [Cengel and Boles [2008]:

$$M_2 = \left[ \frac{M_1^2(\gamma - 1) + 2}{2\gamma M_1^2 - \gamma + 1} \right]^{1/2}$$
 Mach Number (156)

$$\frac{P_2}{P_1} = \frac{1 + \gamma M_1^2}{1 + \gamma M_2^2} = \frac{2\gamma M_1^2 - \gamma + 1}{\gamma + 1} \text{ Pressure Ratio}$$
 (157)

$$\frac{\rho_2}{\rho_1} = \frac{P_2/p_1}{T_2/T_1} = \frac{(\gamma+1)M_1^2}{2+(\gamma-1)M_1^2} = \frac{V_1}{V_2} \text{ Density Ratio}$$
 (158)

$$\frac{T_2}{T_1} = \frac{2 + M_1^2(\gamma - 1)}{2 + M_2^2(\gamma - 1)}$$
 Temperature Ratio (159)

Stagnation pressure relationships [Cengel and Boles [2008]:

$$\frac{P_{02}}{P_{01}} = \left(\frac{M_1}{M_2}\right) \left[\frac{1 + M_2^2 \left(\frac{\gamma - 1}{2}\right)}{1 + M_1^2 \left(\frac{\gamma - 1}{2}\right)}\right]^{(\gamma + 1)/(2\gamma - 2)} \tag{160}$$

$$\frac{P_{02}}{P_1} = \frac{(1+\gamma M_1^2)\left(1+M_2^2\left(\frac{\gamma-1}{2}\right)\right)^{\gamma/\gamma-1}}{1+\gamma M_2^2} \tag{161}$$

Normal shock effects can be at least partially captured by application of these shock relations at the nozzle exit plane if back pressure suggests a standing normal shock should exist. Several aspects of shock physics (multi-dimensional effects, impact on condensation, boundary layer separation, etc.) are beyond the scope of a simple systems-level control volume formulation.

#### 6.3.4.5 Saturation Line Equation

A saturation line equation which expresses the inter-dependence of pressure and temperature for saturated steam is used for purposes of fixing thermodynamic states along the steam expansion. The saturation equation is [1983]:

$$\ln(P_{sat}) = A_0 - \frac{A_1}{T_{sat}} - \frac{A_2}{T_{sat}^2}$$
(162)

where:

$$A_0 = 23.24348$$
 ;  $A_1 = 3757.8699$  ;  $A_2 = 229190.7$ 

#### 6.3.4.6 Steam Nozzle Expansion Model

A strategy for "marching" through the one-dimensional, steady, frictionless ideal gas converging-diverging nozzle steam flow is proposed here. Concepts of isentropic flow and Rayleigh flow are applied for different segments of the nozzle. Reference is made to Figure 33 as its state points (01, 2, m, n, a, 3, 4) are treated as "expansion waypoints" that guide the expansion model calculation. The process is outlined in subsequent paragraphs for each step to computing steam nozzle expansion.

#### 6.3.4.6.1 First Step

First, a stagnation state **01** ( $T_{01}$ ,  $P_{01}$ ) is fixed from known CV conditions upstream of the nozzle FL and from assumed specific heat ratio  $\gamma = 1.3$  or 1.14 for superheated or saturated steam, respectively. The relationships are purely algebraic and need no iteration:

$$T_{01} = T_1 + \frac{v_{CV}^2}{2c_n(T_1)} \tag{163}$$

$$P_{01} = P_1 \left(\frac{T_{01}}{T_1}\right)^{\gamma/\gamma - 1} \tag{164}$$

#### 6.3.4.6.2 Second Step

Second, the saturated state **2** (T<sub>2</sub>, P<sub>2</sub>) is fixed using known conditions at **01**, isentropic flow relations, and a saturation line equation. A system of two equations are solved with a Newton iteration scheme as generally outlined in Appendix C of Beeny [2017]:

$$R * \ln\left(\frac{P_2}{P_1}\right) = \int_{T_1}^{T_2} c_p(T) * \left(\frac{dT}{T}\right)$$
 (165)

$$\ln(P_2) = A_0 - \frac{A_1}{T_2} - \frac{A_2}{T_2^2} \tag{166}$$

Note that if no solution is found for a given set of nozzle inlet conditions, an isentropic expansion of steam (superheated throughout expansion) is assumed through the nozzle.

# 6.3.4.6.3 Third Step

Third, states **a** and **n** are solved (T<sub>a</sub>, P<sub>a</sub>, M<sub>a</sub>, T<sub>n</sub>, P<sub>n</sub>, M<sub>n</sub>, Y<sub>n</sub>, Y'<sub>n</sub>) with an iterative technique. This "wetness iteration" attempts to arrive at a self-consistent set of conditions for the isentropic reference state **a** and the Wilson point **n** according to a highly non-linear set of equations that encapsulate all applicable isentropic flow, Rayleigh flow, and nucleation/growth relationships. The process is more completely outlined in Appendix C of Beeny [2017], but some important property relations that must hold are:

$$\frac{P_a}{P_{01}} = exp\left[\left(\frac{-1}{R}\right)\int_{T_a}^{T_{01}} c_p(T) * \left(\frac{dT}{T}\right)\right]$$
 (Isentropic flow, 01 to a) (167)

$$M_a^2 = \frac{2}{\gamma R T_a} \int_{T_a}^{T_{01}} c_p(T) * dT \qquad \text{(Isenthalpic (stagnation) flow, 01 to a)}$$
 (168)

$$\frac{T_n}{T_a} = \mathbf{1} + \left(\frac{\gamma M a^2 - 1}{M a^2 - 1}\right) \left(\frac{h_{fg} Y}{T_a c_{ng}}\right)$$
 (Rayleigh flow, a to n, simplified) (169)

$$\frac{P_n}{P_a} = \mathbf{1} + \left(\frac{\gamma M a^2}{M a^2 - 1}\right) \left(\frac{h_{fg} Y}{T_a c_{p,a}}\right)$$
 (Rayleigh flow, a to n, simplified) (170)

Wilson point wetness:

$$Y_n = \frac{2\pi}{3} \rho_l I_n \alpha^4 c_{gn}^3 \left( 1 + \frac{3\sqrt{\pi}}{2} \left( \frac{r_n^*}{c_{gn}\alpha} \right) + 3 \left( \frac{r_n^*}{c_{gn}\alpha} \right)^2 + \sqrt{\pi} \left( \frac{r_n^*}{c_{gn}\alpha} \right)^3 \right)$$
(171)

$$Y'_{n} = \pi^{3/2} \rho_{l} I_{n} \alpha^{3} c_{gn}^{3} \left( 1 + \frac{4}{\sqrt{\pi}} \left( \frac{r_{n}^{*}}{c_{gn} \alpha} \right) + 2 \left( \frac{r_{n}^{*}}{c_{gn} \alpha} \right)^{2} + \frac{4}{3\sqrt{\pi}} \left( \frac{r_{n}^{*}}{c_{gn} \alpha} \right)^{3} \right)$$
(172)

The solution procedure involves a Regula-Falsi search for a Wilson point temperature that leads to convergence of nucleation pulse half-width as predicted by two separate prescriptions (outlined in Appendix C of Beeny [2017]). The converged nucleation pulse half-width yields Wilson point wetness directly and thereby all state **a** and **n** properties. At the end of each wetness iteration, the updated state properties at **a** and **n** including wetness are checked with equations (167) through (172), among others, to judge "convergence". Iteration-to-iteration changes in quantities are also tracked.

If the searching algorithm and regula-falsi solution method cannot establish a Wilson point temperature leading to sufficiently converged nucleation pulse half-width, metastability is discounted and an isentropic steam expansion from state 2 to state 4 is assumed. Note this expansion occurs upon user request too. The solution process is:

- Using the assumed critical pressure ratio, get nozzle throat conditions
- Compute the state **4** properties from throat properties and user-input area fraction (nozzle exit to nozzle throat) using an iterative bisection approach with Y<sub>4</sub> the variable and an entropy equation the function
- Compute a normal shock or jet expansion depending on back pressure

Some important aspects of the 2-to-4 isentropic steam expansion:

• The critical pressure ratio is

$$P^*/P_{01} = \left(\frac{2}{\gamma+1}\right)^{\gamma/\gamma-1}$$
 (173)

- Saturation conditions are assumed at the throat and stagnation enthalpy is constant between state 2 and the throat
- The Mach number relation used in the throat-to-4 bisection scheme:

$$M_4 = \frac{A_t}{A_e} \left[ \left( \frac{2}{\gamma + 1} \right) \left( 1 + \left( \frac{\gamma - 1}{2} \right) M_4^2 \right) \right]^{\gamma + 1/2(\gamma - 1)}$$
(174)

• The entropy relation used in the bisection scheme is:

$$\overline{C}_{p,4} \ln \left( \frac{T_4}{T_t} \right) = R \ln \left( \frac{P_4}{P_t} \right), \overline{C}_{p,4} = \left( \frac{1}{1 + Y_4} \right) \left( C_{pg,t} + Y_4 C_{pl,t} \right)$$
(175)

• The calculation of velocity at 4 uses  $\bar{C}_{p,4}$ 

#### 6.3.4.6.4 Fourth Step

Fourth, a Rayleigh flow process is followed from the Wilson point  $\mathbf{n}$  to the reversion point  $\mathbf{3}$  (solving for P<sub>3</sub>, M<sub>3</sub>, Y<sub>3</sub>) which is the point where saturation conditions are re-established. Four equations are involved (recall  $\mathbf{M}_n = \mathbf{M}_a$ ):

$$\frac{P_3}{P_n} = \frac{\left(1 + \gamma M_n^2\right)}{\left(1 + \gamma M_3^2\right)} \tag{176}$$

$$\frac{T_3}{T_n} = \frac{\left(M_3^2 (1 + \gamma M_n^2)^2\right)}{\left(M_n^2 (1 + \gamma M_3^2)^2\right)}$$
(177)

$$P_3 = exp\left(A_0 - \frac{A_1}{T_3} - \frac{A_2}{T_3^2}\right) \tag{178}$$

$$\frac{\Delta s_{3n}}{c_p} = \frac{\Delta y_{3n} h_{fg}}{c_p} = \ln \left[ \left( \frac{M_3}{M_n} \right)^2 \left( \frac{1 + \gamma M_n^2}{1 + \gamma M_3^2} \right)^{1 + \gamma/\gamma} \right]$$
 (179)

Also, wetness relates to flow quality as:

$$Y_3 = \frac{1 - X_3}{X_3} \tag{180}$$

Newton's method is used to solve a two-equation system consisting of equation (176) and (177) for T<sub>3</sub> and M<sub>3</sub>. Saturation pressure P<sub>3</sub> follows immediately from T<sub>3</sub> according to equation (178). Equations (179) and (180) yield wetness and flow quality. Then, state **3** entropy and enthalpy can be calculated using flow quality and saturated liquid/vapor entropy and enthalpy.

If no solution is found during the Newton's method system solve, an assumption of thermally-choked flow is applied. In this case, the latent heat released during reversion from the Wilson point is sufficient to either:

- Lower the Mach number to unity if M<sub>n</sub> was larger than unity, or
- Raise the Mach number to unity if M<sub>n</sub> was smaller than unity

This behavior is consistent with the nature of the "Rayleigh line" which the Rayleigh flow process follows from **n** to **3** [Cengel and Boles [2008]. The choked Rayleigh flow property relations and an entropy equation similar to (179) may be applied in this case where M<sub>3</sub> is unity:

$$T_3 = T_n \left( \frac{1 + \gamma M_n^2}{M_n (1 + \gamma)} \right)^2 \tag{181}$$

$$P_3 = P_n \left( \frac{1 + \gamma M_n^2}{1 + \gamma} \right) \tag{182}$$

$$\frac{\Delta s_{3n}}{c_p} = \frac{\Delta y_{3n} h_{fg}}{c_p} = \ln \left[ \left( \frac{1}{M_n} \right)^2 \left( \frac{1 + \gamma M_n^2}{1 + \gamma} \right)^{1 + \gamma/\gamma} \right]$$
(183)

#### 6.3.4.6.5 Fifth Step

In the fifth step, a specialized homogeneous-equilibrium two-phase flow model is employed to model the expansion of saturated steam between states 3 and 4. As suggested in [Wallis, 1969], a two-phase mixture of an ideal gas and a dilute, dispersed secondary phase may be treated with the conventional HEM plus augmented specific heats depending on the mass fraction of the dispersed phase. Details are expounded in Appendix F of Beeny [2017]. This approach holds under the assumption of thermal equilibrium between the continuous gas phase and dilute liquid phase (as would occur under saturation conditions) Thus, the pseudo-gas is treated as ideal but with modified specific heat and specific heat ratio. To get to state 4:

- A Newton's method solution to an ideal gas expansion law and the saturation line equation is done to recover P<sub>4</sub> and T<sub>4</sub>
- A Newton's method solution to a stagnation pressure relation is used to get M<sub>4</sub>
- A Newton's method solution to a stagnation enthalpy relation is used to get Y<sub>4</sub>

### 6.3.4.6.6 Sixth Step

Sixth, if an oblique shock ought to exist according to turbine back pressure (i.e. if over-expansion occurs such that P4 is lower than the back pressure), the effects of such a phenomenon are approximated by those of a standing normal shock and are imposed on the nozzle outlet state 4. In this case, expansion state 4p is computed with:

$$M_{4p} = \left[ \left( M_4^2 (\gamma - 1) + 2 \right) / \left( 2\gamma M_4^2 - \gamma + 1 \right) \right]^{1/2}$$
 (184)

$${P_{4p}/p_4} = {1 + \gamma M_4^2 \choose 1 + \gamma M_{4p}^2} = (2\gamma M_4^2 - \gamma + 1)/(\gamma + 1)$$
 (185)

$$T_{4p}/T_4 = (2 + M_4^2(\gamma - 1))/(2 + M_{4p}^2(\gamma - 1))$$
 (186)

If instead the flow at 4 is under-expanded (i.e. if P4 is higher than the back pressure), an algebraic formulation proposed by Idaho National Laboratories (INL) [Zhao, 2016] is used to predict the jet expansion that occurs between the nozzle outlet plane and the rotor bucket inlet. The model is summarized in Appendix G of Beeny [2017] and is based on the "virtual nozzle" concept. Three sequentially-solved algebraic equations are used to predict:

- Velocity and Mach number at end of virtual nozzle
- Temperature at end of virtual nozzle (pressure is known turbine back pressure)
- Density at end of virtual nozzle

Because the jet expands further beyond the nozzle exit plane, the velocity at the end of the virtual nozzle will be higher and the pressure lower. The equations for 4p in this case are:

$$V_{4P} = \frac{P_4 - P_B + \rho_4 V_4^2}{\rho_4 V_4} \tag{187}$$

$$T_{4P} = T_4 + \frac{V_4^2 - V_{4P}^2}{2 \cdot C_{p4}} \tag{188}$$

$$\rho_{4P} = \left(\frac{\rho_4 T_4}{\rho_4}\right) \left(\frac{\rho_{4P}}{T_{4P}}\right) \tag{189}$$

The nozzle outlet conditions feed into the Terry turbine compound velocity stage model so that impulses delivered by steam on the turbine can be calculated. One pressure stage FL (representing one steam nozzle) feeds one "set" of rotor buckets and reversing chambers. Several steam nozzles are typically situated around the rotor circumferentially and there is no need to assume all nozzles have the same flow conditions. However, the capability to model multiple, identical nozzles with a sole flow path is included via a so-called steam nozzle multiplicity factor.

# 6.3.5 Terry Turbine Shaft Model

The shaft torque-inertia equation represents the rigid coupling between the driving steam turbine rotor on one end and the following/resisting centrifugal pump impeller on the other. Shaft speed is computed as a function of torques exerted on the shaft by the turbine (typically in a "positive" direction via steam impinging on the rotor buckets) and on the shaft by the pump (typically in a "negative" direction via hydraulic resistance of the pumped fluid against the impeller). The resistance of the pumped fluid is "felt" immediately on the turbine side via the rigid shaft. Additional terms for turbine and pump friction torque ought to be included. Additionally, some extra user-defined torque ought to be allowed. The shaft speed equation can be written as:

$$(I_T + I_P)\frac{\partial \omega}{\partial t} = \tau_T - \tau_P - \tau_{fr,T} - \tau_{fr,P} - \tau_{user}$$
(190)

where:

T denotes "turbine"; P denotes "pump"; fr denotes "friction"

Note that the moments of inertia and the friction torques are user-defined quantities. The turbine moment of inertia and friction torque are formulated just as they are for the pump model. The turbine and pump torques come from the new Terry turbine compound velocity stage (and pressure stage) model and the homologous pump model, respectively. Note in the above equation that  $\tau_T$  must consider all pressure stage nozzles (each associated with a set of reversing chambers) circumferentially-situated about a rotor

The numerical solution method for the shaft speed equation will resemble that of the homologous pump model torque-inertia equation. Thus, an explicit (forward Euler) or a fully implicit (backward Euler with fixed-point iteration) numerical solution technique will be employed.

#### 6.3.6 MELCOR Implementation and Aspects of Solution Methodology

Below, user input provisions are described and some discussion of MELCOR solution strategy is included. Each aspect of the Terry turbine model is taken in turn.

#### 6.3.6.1 Velocity Stage Model

With respect to user input in MELCOR, provisions were added to the CVH block input structure. For any CV, a Terry turbine rotor may be defined by (see Appendix D of Beeny [2017]):

- CV\_ROT card for rotor name and number, number of reversing chambers per nozzle for all nozzles in the rotor, and rotor radius
- CV RIN for turbine moment-of-inertia calculations
- CV RFR for turbine friction torque calculations
- CV\_RBE for bucket steam exit angles, CF or constant, one per each bucket associated with steam nozzles
- CV\_RCB for bucket loss coefficients, CF or constant, one per each bucket associated with steam nozzles
- CV\_RGR for reversing chamber leakage coefficients, CF or constant, one per each reversing chamber associated with steam nozzles
- CV\_RCR for reversing chamber loss coefficients, CF or constant, one per each reversing chamber associated with steam nozzles
- CV\_RXZI for steam carry-over fractions, CF or constant, one per each reversing chamber associated with steam nozzles
- CV NFP to identify all steam nozzle FLs associated with rotor

In terms of actually solving for the Terry turbine velocity stage, the pertinent Terry turbine code is triggered when a homologous pump is being used and when that pump is specified as coupled to a turbine (FL\_TSH, see Appendix D of Beeny [2017]). The Terry turbine calculations (moment-of-inertia, friction torque, total turbine torque due to steam impingement on rotor) are called from within the inner velocity iteration that solves for phasic velocities.

Due to observed numerical wiggles in time, a temporal relaxation was added to the homologous pump model when it is used in tandem with the new RCIC turbine-side physics models. The temporal relaxation is applied to the pump flow path volumetric flow rate because this quantity is a function of phasic velocities following from the MELCOR phasic velocity equation system solution. The formulation is:

$$\dot{Q}_{relax} = \omega * \dot{Q}_{new-time} + (1 - \omega) * \dot{Q}_{old-time}$$
(191)

The factor  $\omega$  is the temporal relaxation factor, defined with a time-scale T as:

$$\omega = MIN(1, \Delta t/T) \tag{192}$$

The temporal relaxation factor is a user input and essentially defines the allowable time-scale on which the pump volumetric flow rate is allowed to change. If the current problem time-step  $\Delta t$  is smaller than the prescribed time-scale, the change in pump volumetric flow is limited via a blending between old and new quantities. This approach helps to eliminate oscillations of model parameters in time that naturally arise due to the application of steady-state models to a transient.

### 6.3.6.2 Pressure Stage Model

With respect to user input in MELCOR, new FL tabular input records were added. For any given FL, a steam nozzle may be defined via FL\_VTM and a pump object may be associated with a rotor object via FL\_TSH. Further details are in Appendix D of Beeny [2017].

In terms of actually solving for the Terry turbine pressure stage, the pertinent steam nozzle code is triggered when user-specified flow path is found and furthermore when that flow path is both:

- Flagged with a special keyword as a steam nozzle
- Associated with a rotor object in some CV

#### 6.3.6.3 Turboshaft Model

No special user input provisions exist exclusively for the turboshaft. A turboshaft is implied when an association is made between a pump object and a rotor object (FL\_TSH, see Appendix D of Beeny [2017]). When this occurs, a torque-inertia equation is solved subject to torques from the turbine and pump. The shaft speed equals the pump impeller speed which in turn equals the turbine rotor speed due to the assumed rigidity of the shaft.

To actually solve for the turbo-shaft speed, a subroutine is called just after all of the following occur:

- A pump associated with a turbine is found
- The turbine torques are resolved and turbine moment-of-inertia is computed
- The pump torques are resolved and pump moment-of-inertia is computed

The calculation itself resembles that of a stand-alone homologous pump with impeller speed coming from a torque-inertia equation solution.

# 6.3.6.4 CFD-informed Systems Level Model Parameters

The systems-level RCIC Terry turbine formulations have parameters that account for effects beyond the scope of systems-level modeling. Generally, these parameters must be supplied by the MELCOR user but some CFD studies undertaken in this dissertation can furnish a "built-in" data set. The parameters will be discussed briefly in turn below. Appendix D of Beeny [2017] gives an idea as to required user input in MELCOR for these new parameters.

#### <u>6.3.6.4.1 Velocity Stage Model Parameters</u>

Referring back to equations (120) through (122), there are several factors in the velocity stage model formulation that require user specification:

- Bucket loss coefficients  $C_B$ ,
- Steam exit angles  $\beta$ ,
- Carry-over fractions  $\xi$ ,
- Reversing chamber loss coefficients  $C_{RC}$ , and
- Reversing chamber leakage coefficients  $\gamma_{RC}$

Physical insights as to the significance of these terms may be gleaned from Appendix B of Beeny [2017]. To quickly recapitulate:

- Bucket loss coefficients capture the attending decrease in flow velocity when steam traverses a given rotor bucket
- Steam exit angles figure into moment-of-momentum computations and bear significance to the torque exerted by steam on a bucket
- Steam carry-over fractions account for the mismatch in steam flow exiting a given bucket and entering the downstream reversing chamber
- Reversing chamber loss coefficients capture the attending decrease in flow velocity when steam traverses a given reversing chamber

• Reversing chamber leakage coefficients account for loss of steam mass through the crescent hole in a given reversing chamber

These factors are specified by steam nozzle for all steam nozzles in a rotor object. There is some user-defined number of buckets and reversing chambers per steam nozzle and user input for all factors are organized as such.

<u>6.3.6.4.2 Pressure Stage Model Parameters</u>
The only pressure stage model parameter required of the user that must be informed by CFD or by experiments is the steam nozzle expansion rate  $(\dot{P})$ . This parameter factors into the nucleation/growth closures. The expansion rate is essentially an externally-imposed feature of nozzle geometry with units of inverse time. Mathematically, it is [1983]:

$$\dot{P} = \frac{1}{P} \frac{dP}{dt} = \frac{1}{P} \left( u \frac{dP}{dx} \right) \tag{193}$$

# 7 Task 5: Experimental Data Generation

A unique part of this project is the ability to generate code validation data. The PI had a RCIC System facility for investigating long-term mixing in the Suppression Pool prior to commencement of this project. Also available in the PI's lab were all of the components necessary for integral RCIC system simulation except a turbine. A Terry turbine was acquired for this project to produce validation data.

The turbine is a refurbished Terry turbine, model ZS-1. The Z indicates the wheel diameter (pitch) is 18 inches. The S stands for stainless steel. The 1 indicates that there are steam inlet nozzles in only the lower half of the casing. For this project, the ZS-1 model is a valid representation of a Terry turbine used in a nuclear plant. The turbines in the plants are model GS-1 or GS-2, which vary in volumetric flow rate of the coupled RCIC pump. GS-2 Terry turbines have steam inlet nozzles in both the upper and lower halves of the turbine casing. The ZS-1 and the GS-series all have the solid wheel construction of bucket design and the reversing chambers. Steam flow paths are therefore analogous. Design differences that may exist, such as in the lubrication system, the governor valve and controls, are not important for validation of the models developed in this project.

Data obtained from air injection tests were used as part of the validation of the Terry turbine CFD models described under Task 4. The facility was modified to also perform steam injection tests and these data may be used for code validation in the future. Experimentally measured parameters that were compared against CFD model predictions included turbine torque and power. These complemented the local-scale parameters that were obtained from previously published experiments on nozzles. As such, the experimental data generation was an important part of this project.

# 7.1 Experimental Facility Description and Modifications

# 7.1.1 Experimental Facility Layout

The major equipment of the facility are the steam generator, the water injection pump, the turbine, the turbine, exhaust volume, and connecting piping. A simplified diagram is provided in **Error! Reference source not found.**4. Gas is directed from the steam generator to an injection point where water may be added, and then the mix is directed to the turbine inlet. The gas may be steam or air. Both the gas and water are metered.

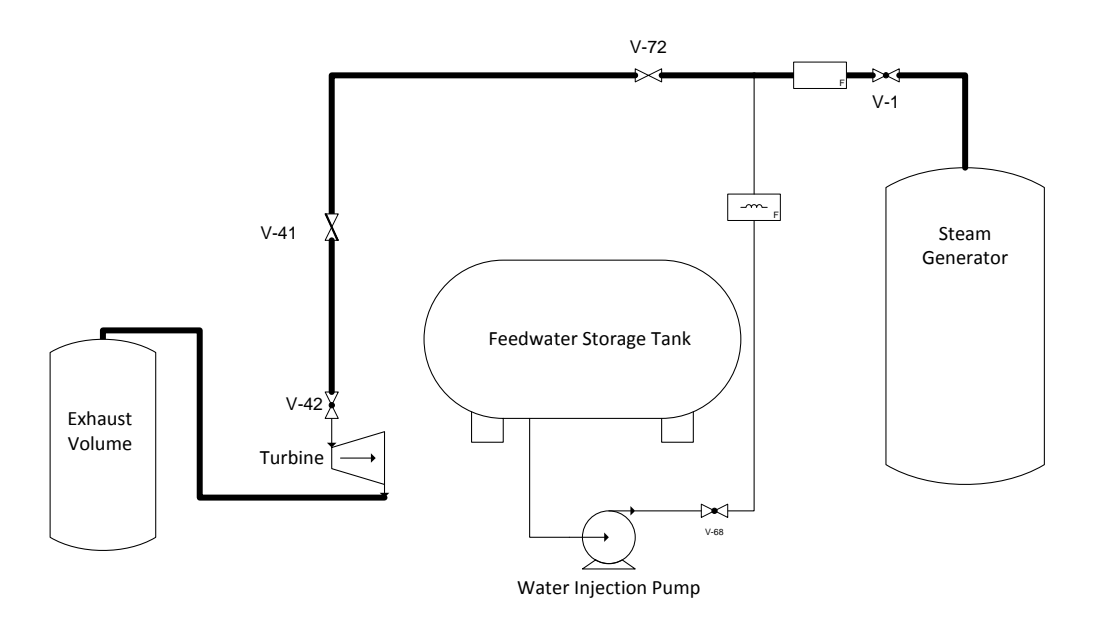


Figure 34 Simplified NHTS experimental facility diagram

# 7.1.2 Experimental Equipment

# 7.1.2.1 Turbine

A suitable turbine for this test series was identified in a storage area of a Houston area turbomachinery service provider, Keene Turbomachinery Services. A portion of the storage area can be seen in 35. Mr. Keene graciously agreed to loan the turbine to Texas A&M University for testing.



Figure 35 Surplus turbines at Keene Turbomachinery Services

Before testing, a refurbishment was necessary. The turbine was transported to TW Revak, for a thorough refurbishment (Figure ).



Figure 36 Turbine en route to be refurbished

The turbine was disassembled. The upper casing and bearing covers were removed, and the rotor and shaft were lifted out. A photo with component labels just before shaft removal is given in Figure .

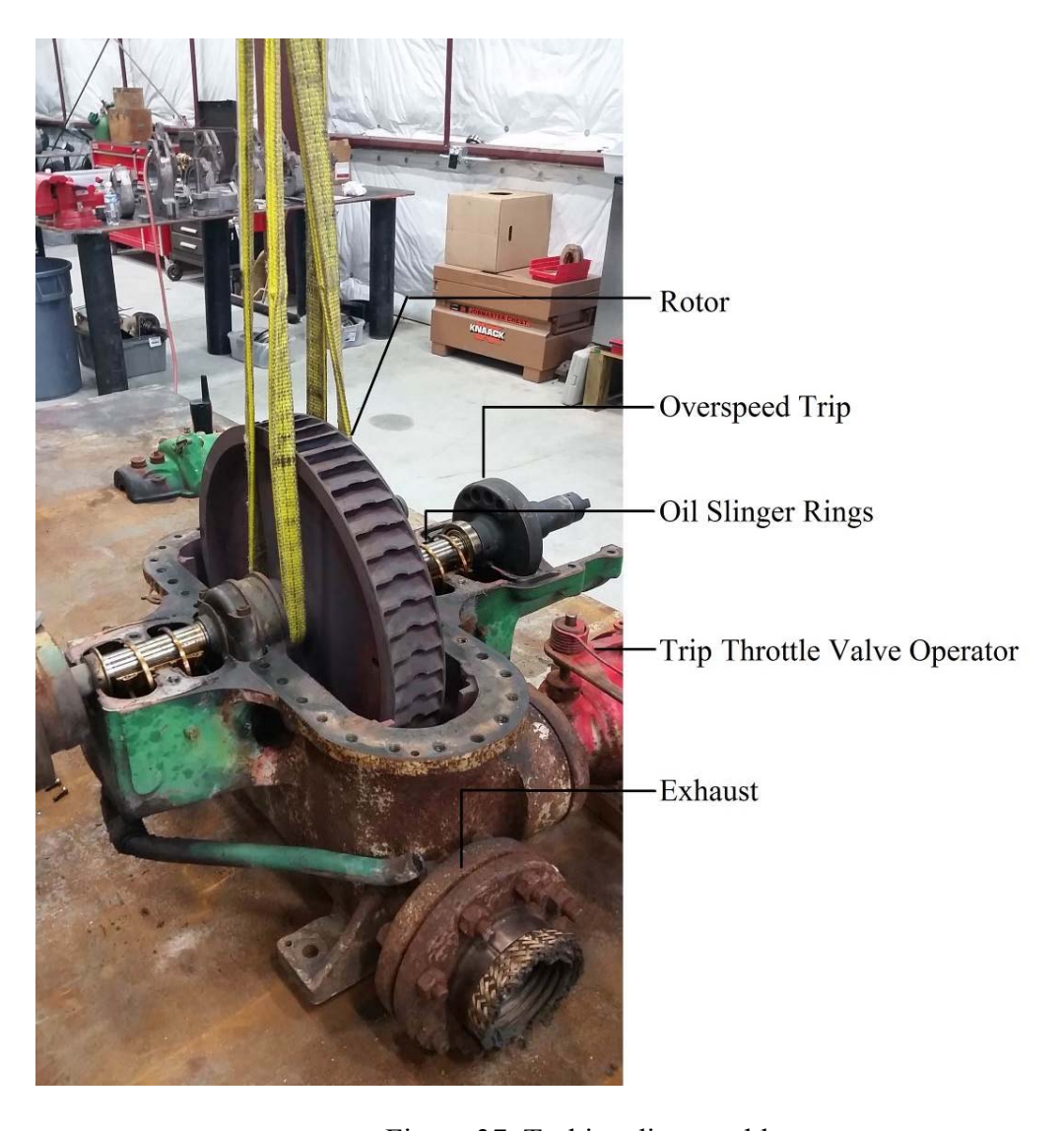


Figure 37 Turbine disassembly

The Trip Throttle Valve (TTV), shown in Figure , was found to be seized in the open position. The TTV is a butterfly valve which is designed to shut in the event of an overspeed condition. The old valve stem was hammered out and replaced, and the valve was returned to service.



Figure 38 Trip Throttle Valve, with seized valve stem

The turbine came equipped with three steam nozzles, pictured in 39. Two of these nozzles were removed, and their installation ports plugged to adapt the turbine to the flowrates expected during testing. The throat of each pre-existing nozzle was 0.380 inches in diameter.



Figure 39 Lower casing, with original nozzles and reversing chambers



Figure 40 Lower casing, after sandblasting, with two nozzles removed

The turbine was then sandblasted, reassembled, painted, and returned to service as "The Duchess," an experimental test turbine (Figure ). The lower half of the casing is shown after sandblasting in Figure .



Figure 41 "The Duchess"

The Duchess is a Terry Solid-Wheel ZS-1 model. The Z indicates the wheel diameter (pitch) is 18 inches. The S stands for steel. The 1 indicates that there are nozzles in only the lower half of the casing. The shaft is 1 3/8-inch in diameter, with a keyway in the drive end for coupling fitup. The bearings are beryllium bronze.

The casing allows for installation of four nozzles, but only one nozzle was used for this experiment. Each nozzle port is equipped with a set of reversing chambers to redirect steam into the turbine wheel. The shaft seals consist of three carbon rings on each side of the wheel. Leakoff piping is supplied between the second and third rings on each side of the shaft.

The casing is equipped to accommodate a Woodward TG-13 governor valve. This governor valve was removed for this test series. Speed was controlled by hand-operated valves. Also included is a mechanical overspeed trip. A spring-loaded mechanism is attached to the rotor. Upon reaching the overspeed setpoint, the spring pressure is overcome, and the mechanism contacts a linkage which shuts the TTV. The TTV is a butterfly valve just upstream of the inlet plenum. The steam inlet nozzle has a nominal 0.380-inch throat diameter. This inlet nozzle has a converging-diverging flow path which is designed to enable the gas flow to reach supersonic speed, and directs this flow into the turbine buckets.

The turbines in use at Fukushima Daiichi Unit 2 and Unit 3 were model GS-1 or GS-2. These share many characteristics with the ZS-1 used in this experiment. They employ a tangential flow path, and have a solid milled turbine rotor with reversing chambers. Their wheel pitch is 24 inches. This is a larger size than the ZS-1 wheel pitch of 18 inches, but for the purpose of investigating the effects of water ingestion, the ZS-1 was determined to be an acceptable choice.

The turbine is supported by a test platform. The test platform, shown in Figure , consists of a large stainless steel base and supports made from mild carbon steel angle iron and C-beams. The test platform was fabricated locally. The test platform is not bolted to the floor. Instead, it is placed on rubber sheeting to absorb vibrations. This is a requirement of the dynamometer. Figure shows the turbine installed on the test platform with instrumentation installed.

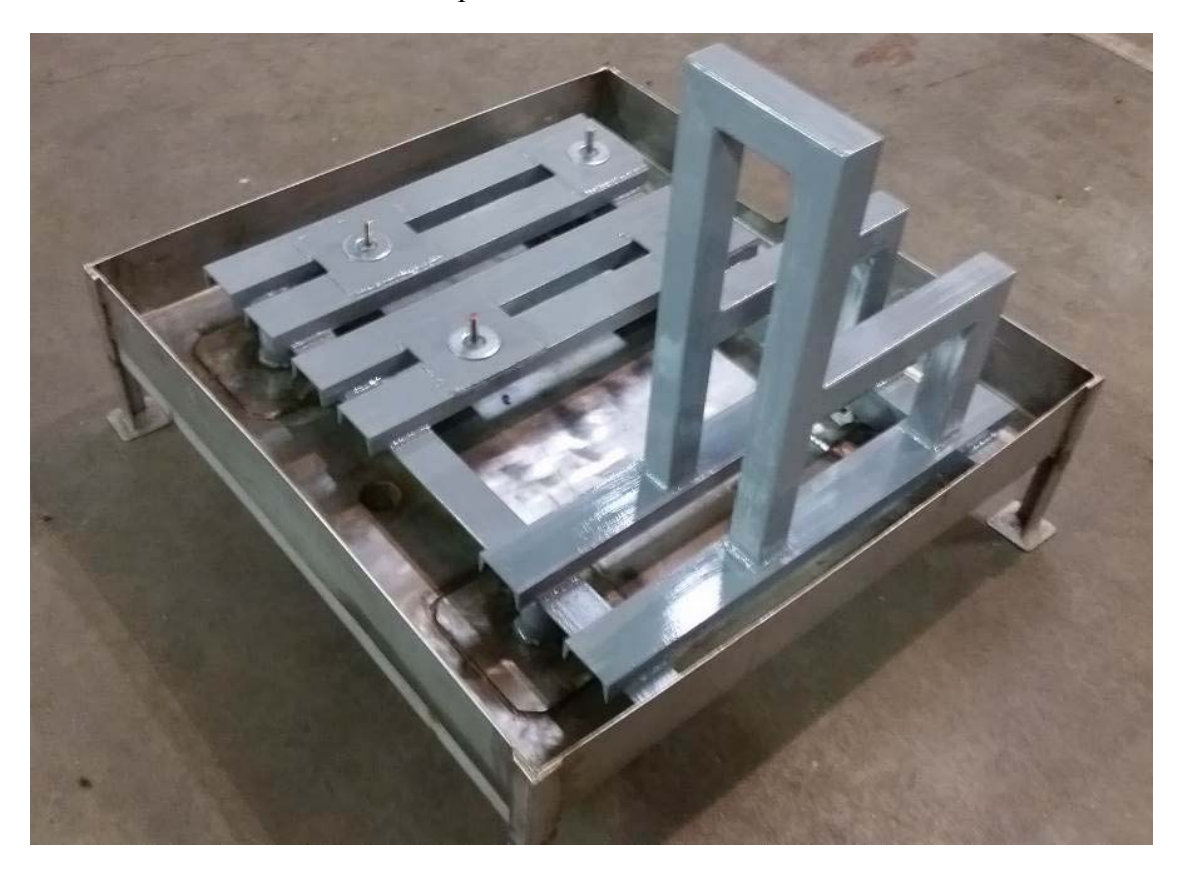


Figure 42 Test platform, fabricated and painted

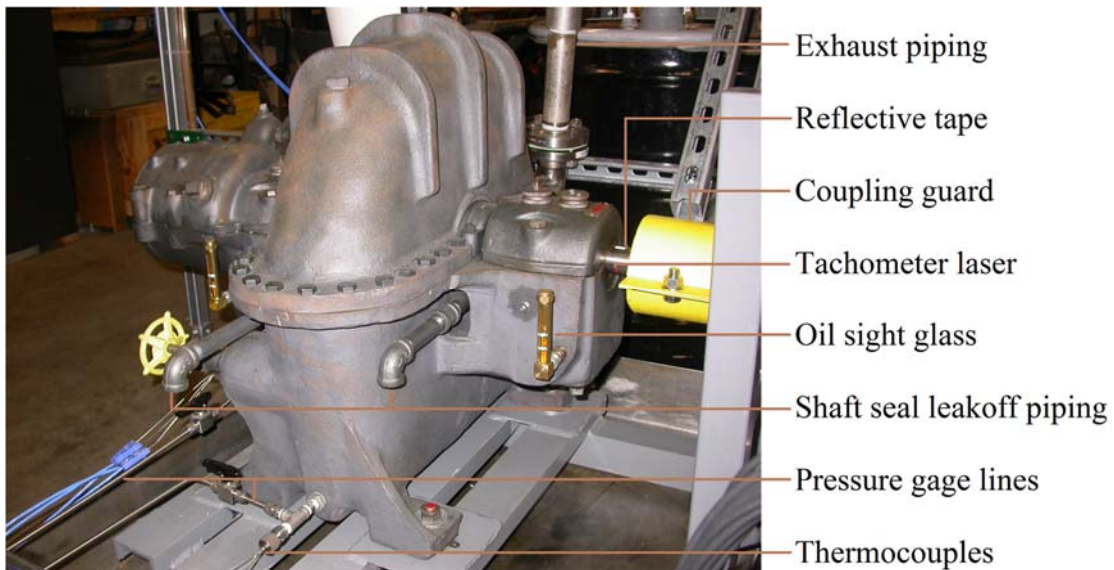


Figure 43 The Duchess, on platform, with instrumentation installed

The turbine drives a Lovejoy L110 rubber spider coupling (Figure ), which is coupled to the dynamometer shaft. A coupling guard is installed during operations.



Figure 44 Shaft coupling

The inlet piping is 1.5-inch NPS piping that branches from the Main Steam line and includes a 9-inch stainless steel braided corrugated segment to minimize stresses to piping due to operational

stresses, as well as to simplify alignment during installation. The piping includes two thermal sensing ports with thermocouples. These were included to characterize the heat losses of the piping upstream of the turbine.

Exhaust piping is directed to a 55-gallon drum. Like the inlet piping, the exhaust piping includes a steel corrugated hose segment to minimize piping stresses (Figure ). The exhaust pipe protrudes 18 inches into the drum. For steam testing, water level is maintained greater than 20 inches from the bottom so that the quench volume of water within the drum can condense the steam. For air tests, the drum is drained.



Figure 45 Turbine exhaust flange

#### 7.1.2.2 Water Deionization System

To minimize fouling and scaling, deionized water was used for all tests that required water. The water was passed through a Culligan mixed bed system, shown in Figure . In this system, the water passes through several components in series: an activated charcoal filter, a cartridge filter, two mixed bed resin tanks, and another cartridge filter. An automatic monitoring device indicates when the resin must be regenerated. Regeneration is required after approximately 350 gallons are purified because relatively high levels of total dissolved solids are in the water supply. This system was installed in the facility prior to the start of the ZS-1 experiment ([Solom, 2016] and [Solom and Kirkland, 2016]).



Figure 46 Cartridge filter and resin tanks for deionization system

#### 7.1.2.3 Pump

A five-stage centrifugal pump is used to feed the Steam Generator and inject liquid flow into the Main Steam line is. The model is Dayton 5UXF5, and it was installed prior to the ZS-1 research. It is driven by a 0.75 HP, 115VAC electric motor. Maximum boost pressure is 93 psi. The inlet and outlet are 0.75-inch NPT connections. The nominal speed is 3450 RPM. This speed is not user controlled, so flow adjustments are performed by throttling system valves [Solom, 2016].

#### 7.1.2.4 Steam Generator

For this experiment, a steam generator manufactured by Kennedy Tank and Manufacturing Co. was used. The steam generator was a part of the facility prior to the ZS-1 experiment. Its capacity of 130-135 gallons. The tank was hydrostatically tested to 180 psig. During operations, pressure was limited to 135 psig, and maximum temperature is 350°F. It is of a vertically-mounted cylinderical shape; diameter is 24 inches, and height is 60 inches. Total height is approximately 72 inches if the curved heads are accounted for. It is supported by four legs at the base, and additional piping, relief valves and moisture separaters are built above the unit. It is fabricated from schedule 10 stainless steel 304 pipe. The assembly is enclosed in two-inch thick rigid fiberglass insulation. A photo of the steam generator pressure vessel and associated equipment is shown in Figure [Solom, 2016].



Figure 47 Steam generator and blowdown drum

The steam generator uses six electric immersion heaters. The heaters operate using 3-phase 480 VAC. Total nominal heat capacity is 157 kW. The heaters are submerged below the water surface. The sizes of the heaters differ: two are two kW capacity screw-in heaters, one is a three kW screw-in type, and the remainder are fifty-kW heaters of 8-inch flange type. Two of the fifty-kW heaters can be powered in 25-kW intervals. The third has 6.25 kW intervals. The total

nominal heat input can be divided to supply a total of 2, 3, 4, 5, 6.25, 7, 8.25, 9.25, 10.25, 12.5, 13.25, and so on up to a maximum of 157 kW. The heaters and control system were produced by Watlow Process Systems [Solom, 2016].

A small moisture separator is attached to the Main Steam Line, between the Steam Generator and the Steam Line Isolation Valves. The moisture separator was manufactured by Clark Reliance. Both the Steam Generator and the moisture separator are ASME-code rated. A saturated steam/water mix from the steam generator enters the moisture separator through a 1.5-inch line. Moisture is separated out and directed back to the Steam Generator, while dry saturated steam can flow down the Main Steam Line [Solom, 2016].

The steam generator includes instrumentation. Bulk temperature is measured by four thermocouples at different vertical placements penetrating the vessel. These thermocouples supply temperature information to the DAQ for different elevations within the Steam Generator. There are also two pressure transducers in the Steam Generator. There are a differential pressure transmitter which provides level indication based on reference leg and variable leg water column heights, and an absolute pressure detector to indicate Steam Generator pressure [Solom, 2016].

There are locally-readable indications of Steam Generator pressure and level as well. The level indicator uses a magnetic float to provide level indication. Pressure indication is a bourdon tube pressure gage on top of the pressure vessel. The level indicator includes a reed switch, which provides heater interlock functionality. When a thermal overload is detected at the heaters or when the level float lowers below a certain level, power to the heaters is interrupted [Solom, 2016].

The steam generator is connected to the main steam line, the feed line, two Kunkle pressure relief valves, a vent line, a vacuum breaker line, a drain line, an air connection which includes a quick-disconnect fitting [Solom, 2016].

The relief valves are ASME-code rated. Both are set to lift at 115 psig. The discharges are directed to a blowdown drum which is partly filled with water to provide condensing action. The vent line is directed outside the laboratory space [Solom, 2016].

The vacuum breaker is included to prevent drawing a vacuum inside the steam generator as the water cools and steam condenses. It comprises a ball valve, a check valve, and an air filter. The ball valve is shut while the system is in operation, to preclude leakage through the check valve. When the system is in a shutdown condition, the vacuum breaker ball valve should be open. The air filter prevents dust from entering the system and causing contamination [Solom, 2016].

### 7.1.2.5 Feedwater Storage Tank

The Feedwater Storage Tank, shown in Figure , provides makeup water for the Steam Generator, and it also is the source of water injection into the steam line. It was installed in the facility prior to the start of the ZS-1 research. It is a horizontal cylinder with approximately 1,400 gallon volume. It was originally produced in 1952 by Wyatt Metal & Boiler Works. It is constructed of 304 Stainless Steel. The stamped ASME-API pressure rating is 88 psig; maximum temperature rating is 400°F. The inner diameter is 59 inches, and total length from end to end is approximately 122 inches. The vessel legs support the vessel approximately 18 inches above the surface beneath. The face with the ASME-API stamped plate will be referred to as the front face; the side to the right when facing toward the front head from the rear head will be referred to as the right side. Vessel penetrations include a 6-inch NPS flange beneath the front end where the pump takes suction, a 20-inch manhole at the top for personnel access, and a 4-inch NPS flange near the back end of the top [Solom, 2016].



Figure 48 Feedwater storage tank and turbine

## 7.1.2.6 Vessel Connections

The 1.5-inch flange atop the front end of the vessel provides connections for pressure relief, vacuum breaker, vent, and generic main steam line functions. A 1.5-inch pipe splits into separate lines for these features. The top line is connected to the main steam line. This can be used to pressurize the vapor space or to drain water from the main steam line. Relief valves branch from the tee as well. The two pressure reliefs are 0.5-inch Kunkle valves set to 88 psig. They are ASME-rated. They discharge to an atmospheric blowdown drum. This drum, like the Steam Generator blowdown drum, is partially filled with water to condense steam. A manual vent is also piped to the drum. A third relief valve is also directed to the drum. This is the pump discharge relief, set to 150 psig. The vacuum breaker for the Feedwater Storage Tank is larger than that of the Steam Generator, and it does not have an isolation valve. It is equipped with an air filter as well. The vacuum breaker is designed to prevent the Feedwater Storage Tank from drawing a vacuum. In the event that the pump discharge was directed to the vapor space while steam is present, steam bubble collapse could conceivably draw a rapid vacuum, resulting in damage to the pressure vessel. For this reason, the vacuum breaker should in no case be isolated, and so no isolation valve is provided [Solom, 2016].

### 7.1.2.7 Air Compressor

For air tests, compressed air is supplied by a QT-15 reciprocating air compressor from Quincy compressor. A photo of the compressor is given in Figure . The compressor was installed before the start of the ZS-1 experiment. The compressor operates in two stages. It is air cooled, and splash lubricated. The compressor is driven by a belt coupled to the electrical motor. Air is

sucked into the intake valve into the first stage cylinder where it is compressed to about 125 psig. The low pressure air then exits through the discharge valve and is routed to the second compression stage. The heat that is generated in the first compression cycle is dissipated through an intercooler of finned copper tubing. The flywheel includes fan blades to direct airflow toward the intercooler and compressor cylinders to remove heat. The low pressure air enters the second compression stage, where it is compressed to 175 psig. The high pressure air is then directed to an air cooled aftercooler. The aftercooler allows the water vapor contained in the air to condense to liquid phase. This condensate is removed by a moisture separator. The air is directed to a 120-gallon receiver tank. One revolution of the crankshaft facilitates one complete compression cycle. A dipper connected to the connecting rod splash lubricates the internals with oil. The V configuration of the compressor head is designed to operate as a balanced unit with a total of four cylinders. Rated output is 51 CFM at 175 psig [Wynne, 2015].



Figure 49 Facility air compressor

The compressor is belt driven by a 15 HP Baldor electric motor. The motor is driven by a 3-phase 460 VAC power supply. The magnetic starter containing the EATON contactor and an overload relay is situated on the front of the unit. Power is supplied through a 30-A three-pole breaker. A pressure switch causes the compressor to start when the receiver pressure is less than 125 psig and to stop when the pressure reaches 175 psig. After the compressor stops, an unloader valve vents air from the pistons. This allows for easier subsequent startups [Wynne, 2015].

The compressor unit is secured to the floor with 0.5-inch diameter wedge anchors. The nylock nuts were installed loosely to prevent stresses to the compressor and concrete floor due to the

vibrations occurring in normal operation. Rubber and cork insulation pads were installed under the compressor feet to dampen vibrational stresses to the piping and building foundation [Wynne, 2015].

During operation, large amounts of moisture condense inside the receiver tank. A solenoid operated drain valve was installed to automatically drain this condensate at 45-minute intervals. The outlet of the valve is 0.5-inch black iron piping. It directs the condensate outside the building [Wynne, 2015].

The compressor intake is equipped with two 10-micron inlet air filters and silencers to remove large particulates. A 5-micron particulate filter and a 0.01 micron coalescing oil filter are installed downstream of the receiver tank. The filter housings are both aluminum, with 1.5-inch NPT threaded connections. The filters feature automatic condensate drain valve and indicators to display when filter changeout is needed. This filter combination provides a clean and relatively oil-free air supply for the experimental facility [Wynne, 2015].

Following the filters, the air travels through a refrigerated air dryer. The Quincy QPNC-100 dryer lowers the temperature of the compressed air to 39°F, resulting in condensation of entrained moisture. This moisture is piped to outside of the laboratory space. Operation of the dryer is completely automatic; it maintains a dew point of 39°F which results in an estimated relative humidity of 20%. The dryer inlet and outlet are 1.5-inch NPT connections. Electrical power is 115VAC with a 20-A plug [Wynne, 2015].

Downstream of the air dryer, air pressure is regulated by a 1.5-inch Speedaire relieving type pressure regulator. After the regulator, the air supply line branches into hose connections and the main line, which connects to the steam generator. For air tests, the regulated air pressure is directed to the steam generator. For these tests, the Steam Generator was drained of all water to maximize the air volume available for testing [Wynne, 2015].

## 7.1.3 Data Acquisition System

The Data Acquisition System comprises both the hardware and software that interpret and record data that is produced in an experiment. This includes thermocouple, pressure transmitter, flowmeter, load cell, and turbine speed data. The Data Acquisition System was installed before the ZS-1 experiment began. However, the PC was upgraded at the start of this testing, and the software was modified to accommodate newly installed instruments [Solom, 2016].

## 7.1.3.1 *Hardware*

Instrument signals are received by a National Instruments SCXI system connected to a PC. The SCXI, PC, and converter equipment are shown in Figure . The SCXI consists of an SCXI-1000 chassis with four installed modules: two SCXI-1102 module, one SCXI-1102B module, and one SCXI-1102C module. These models are differentiated by their respective lowpass filters. The 1102 bandwidth is 2 Hz, the 1102B bandwidth is 200 Hz, and the 1102C bandwidth is 10 kHz. Each of these modules has 32 voltage/thermocouple inputs, and a cold junction sensor input from the terminal block. Each channel has an independent amplifier and filter. Each module connects to its instruments using an SCXI-1303 terminal block and the necessary wiring [Solom, 2016].



Figure 50 Data acquisition control station

The PC connects to the SCXI-1000 chassis through a shielded cable. The cable connects from the back of one of the SCXI-1102 modules to an NI PCIe-6341 card in the PC. The analog input signals are multiplexed into a single channel between the chassis and the PC. Most of the multiplexing is handled using the LabVIEW software with DAQmx drivers, and is transparent to the user. However, configuration can be optimized to prevent unexpected phenomena such as extra settling time due to channel-to-channel gain transitions. Best practice is to group like signals together (e.g. avoid putting a small signal on channel 0, a large signal on channel 1, a small signal on channel 2, etc.) [Solom, 2016].

The current hardware permits thermocouple wire to be connected directly to the terminal blocks. However, current loops cannot. Instruments that use 4-20 mA analog outputs require intermediate treatment. This is performed by placing a 249-Ohm resistor in the current loop. Normally, a 250-Ohm resistor would be used to produce a 1-5V signal. A 249-Ohm resistor was used here instead to allow more margin for offscale high signals. Additionally, a 249-Ohm resistor would be used internally in the 1102 module to make it a 4-20 mA channel. The current from each instrument is passed through its connected resistor; the voltage drop is measured by the SCXI system by connecting both ends of the resistor to the input terminals for that specific channel [Solom, 2016].

## 7.1.3.2 *Software*

The Data Acquisition system runs LabVIEW 2015 32-bit under 64-bit Microsoft Windows 7 Professional with SP1. The DAQmx drivers are version 15. The LabVIEW Virtual Instrument

(VI) was designed to be frugal with CPU resources while retaining the required functionality. Figure shows the graphical user interface for the data acquisition system [Solom, 2016].

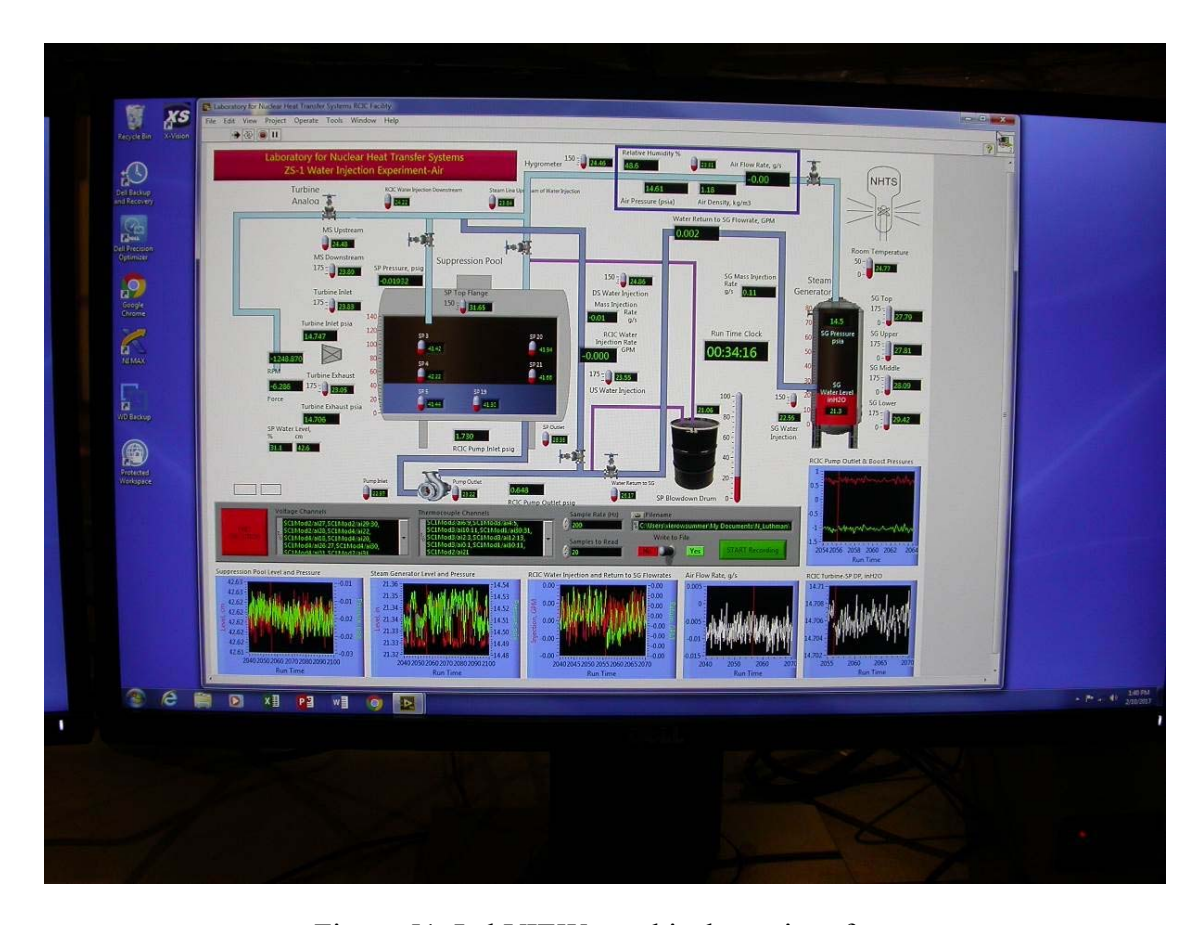


Figure 51 LabVIEW graphical user interface

The LabVIEW VI for this experiment was based on those used for previous experiments performed in the Laboratory for Nuclear Heat Transfer Systems, primarily the RCIC Suppression Chamber Stratification experiments. Similar conventions are used in the interface and data logging. It also incorporates data averaging for each channel, along with standard deviation of each sample set. This assists in determining uncertainty as well as characterizing the amount of rapid fluctuations occurring in a channel on very short time spans [Solom, 2016].

For each channel, a collection of samples is obtained and averaged. Over a span of one second, 200 samples are collected and averaged over 20 groups. This yields 10 records per second. The averaging function reports both the mean and the standard deviation. These will be in units of temperature for thermocouples, and units of voltage for all other instruments. The mean and standard deviation are recorded, and then the mean value is passed to a code block containing the calibration profile for that particular channel. The raw voltage is converted to a fraction from 0 to 1 of the full scale for the instrument. A signal of 4 mA corresponds to 0, and a signal of 20 mA corresponds to 1. Then, the obtained value is passed to a code block transforming it with the set range of the instrument. This reports the value in units appropriate to the instrument, i.e. 20 psia, 1.0 gpm, etc. Thermocouples do not require this processing, because DAQmx implements all processing internally. Additional processing may be needed for some instruments. One example

would be a transformation of differential pressure readings into vessel water levels. Additionally, some unit conversions may be necessary, especially if the value of one instrument depend upon a reading from another instrument. In all cases, the final computed value before motivation each instrument is recorded [Solom, 2016].

Steam flow values from vortex flowmeter are an example of a data point which is dependent upon other values. The instrument incorporates pressure and temperature compensations, and steam density is computed using a dll from the X Steam Tables. For this instrument, some intermediate values are recorded as well [Solom, 2016].

Aside from logging data, the LabVIEW VI displays a large amount of operational data to the user in the form of numerical indicators and charts. These indicators are superimposed on a graphic of the ZS-1 Turbine Experiment. This allows the user view the live data, and also provides information that can assist in determining valve positions and other manual controls. The VI can be seen at remote operating stations. The two remote operating stations are the water injection control station, Figure , and the air/steam injection control station, Figure [Solom, 2016].



Figure 52 Water injection control station



Figure 53 Air/steam injection control station

# 7.1.4 Instrumentation

# 7.1.4.1 General

Instruments near the steam generator are shown in Figure . The instruments in vicinity of the feedwater storage tank are featured in Figure . Instrumentation on or near the turbine are in Figure . A list of instrumentation is given in Table 7.

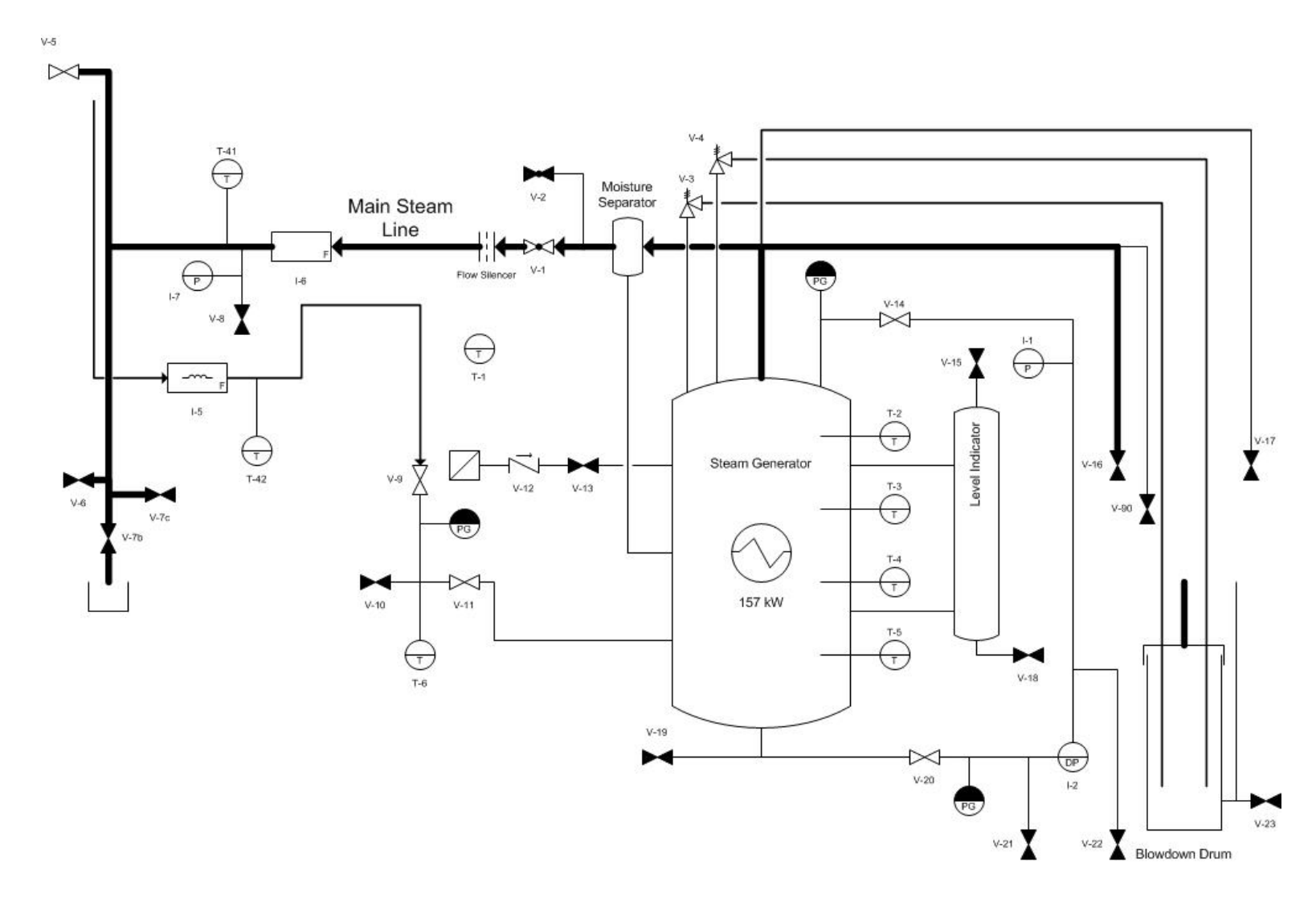


Figure 54 P&ID of steam generator with associated piping and components

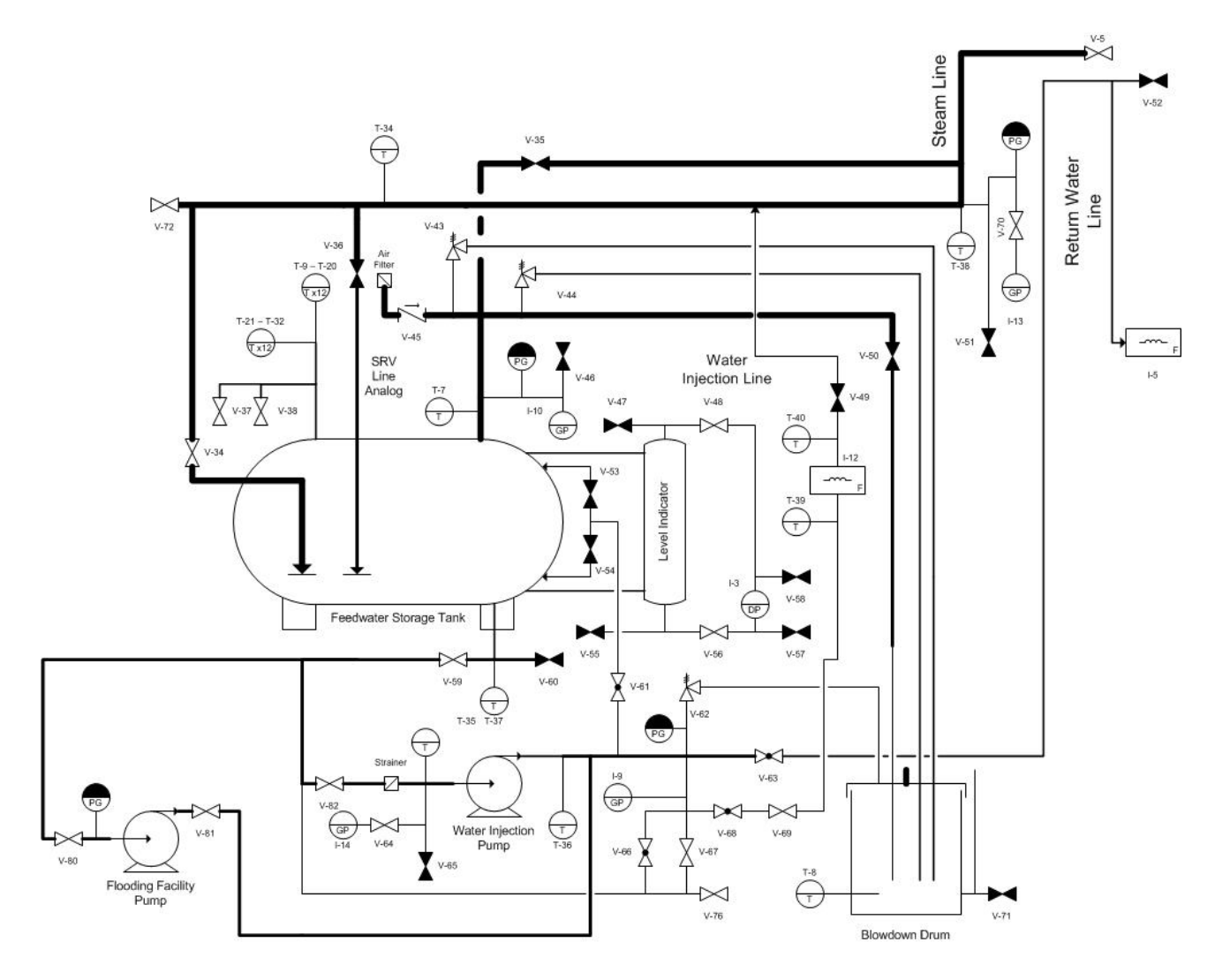


Figure 55 P&ID of feedwater storage tank with associated piping and components

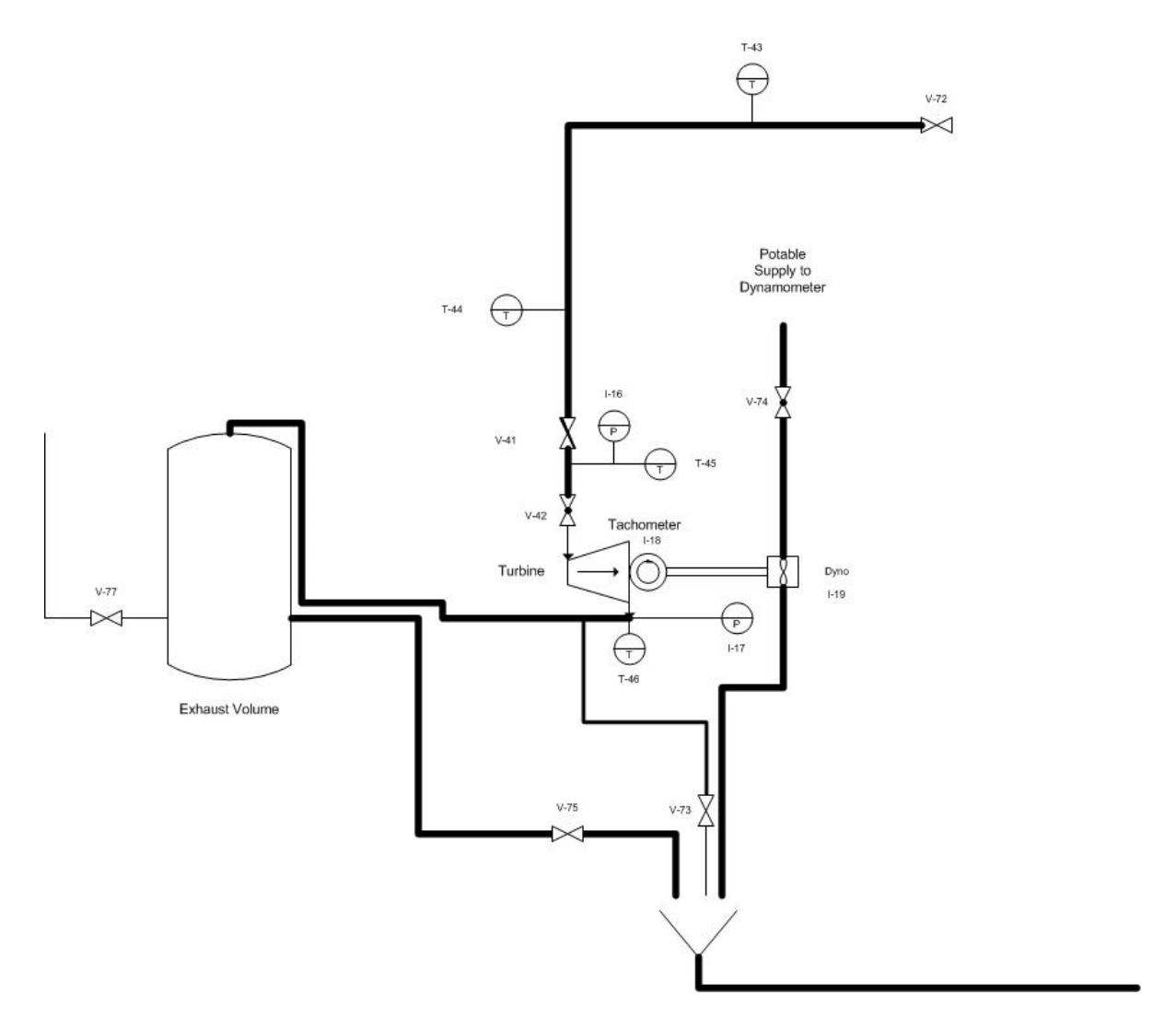


Figure 56 P&ID of turbine with associated piping and components

Table 7 NHTS RCIC Test Facility Instrumentation

Instrument	Manufacturer	Model	Range	Instrument Error
T-1 to T-46	Omega	Type T; SLE	0-350°C	±0.5°C or 0.4% of reading
I-1	Honeywell	ST3000 STA940	0-150 psia	±0.10% of upper range value (URV)
I-2	Honeywell	ST3000 STD924	0-110 inH2O	±0.075% of URV
I-3	Honeywell	ST3000 STD924	0-80inH2O	±0.075% of URV
I-5	Yamatake	MagneW 3000	0-5 GPM	$\pm 0.5\%$ of rate
		PLUS		
I-6	Foxboro	83W	0-2400 Hz	$\pm 1\%$ of reading for flow rates in accurate range
I-7	Honeywell	STA3000 STA940	0-130 psia	±0.10% of URV
I-9	Dwyer	682-3	0-250 psig	±0.13% of URV
I-10	Dwyer	673-7	0-100 psig	± 0.25% URV
I-12	Badger	M2000	0-1 GPM	± 0.25% of rate
I-14	Dwyer	673-7	0-100 psig	± 0.25% of URV
I-16	Rosemount	3051CA	0-75 psia	± 0.04% of URV
I-17	Rosemount	3051CA	0-75 psia	± 0.04% of URV
I-18	Monarch	ACT-3X	5-5,000 RPM	± 0.001% of reading
I-19	Omega	LC-101	0-25 lbf	$\pm$ 0.04% of URV

### **7.1.4.2** *Flow Meters*

Fluid flow was monitored by three flowmeters in this experiment. A Foxboro 83 vortex flowmeter was used in the steam/air line, and a Badger M2000 magnetic flowmeter was used on the water injection line. A Yamatake MagneW3000 PLUS magnetic flowmeter was used to monitor water flowrates when feeding the steam generator [Solom, 2016].

### Vortex Flow Meter

A Foxboro 83W water-style vortex flowmeter is installed in the 1.5-inch steam line. It is located approximately 100 inches downstream of the Main Steam Cutout Valve. This length was to allow at least 30 pipe diameter lengths, which are needed to achieve developed flow and an accurate measurement. The flowmeter transmits a standard analog 4-20 mA signal to the DAQ. The maximum steam flow that can be registered is approximately 96 g/s. The flowmeter can measure both steam and air flow. Pressure and temperature measurements are required to calculate the flow value from the signal of the meter. These are located 6 and 8.25 inches, respectively, downstream of the flowmeter [Solom, 2016].

Vortices are generated within the flowmeter when the fluid encounters the installed baffle. The baffle causes vortex shedding, and the shedding frequency is measured by the instrument using a piezoelectric differential pressure sensor. The shedding frequency is directly related to flow rate. The vortices shed alternately on either side of the obstruction. This results in differential pressures across the sensor that vary with time at the frequency of the shedding [Foxboro, 2000]. The properties of the fluid, measured immediately downstream of the meter, are used to determine density and the correction factors of the meter so that the flow conditions can be characterized. A temperature correction factor corrects for thermal expansion in the meter material.

## Water Injection Flow Meter

Magnetic flowmeters operate by sending a conductive liquid through a magnetic field. Magnetic induction results, generating a voltage perpendicular to both the magnetic field and the flow of the liquid. This magnetic field is picked up by electrodes placed within the detector. The spacing of the electrodes and the magnetic field are known, and so the voltage will be directly proportional to the flow velocity [Solom, 2016].

Two magnetic flowmeters were used. The first is a Badger M2000, which was used to measure lower flowrates injected into the steam flow. It employs a 15-mm flange connection, and can detect flowrates from 0.02 to 5 GPM. Accuracy for this meter can exceed  $\pm$  0.25%. It can also accept process fluid temperatures up to 150°C. The detector requires a minimum fluid conductivity of 5 micromhos/cm [Badger, 2016]. Temperature measurements are taken 6 inches upstream and 2 inches downstream of the detector [Solom, 2016].

The second magnetic flowmeter is a Yamatake MagneW 3000 PLUS detector with a 0.5-inch NPS wafer-style detector. The system comprises an MGG18 detector and a MGG14C converter. The detector can measure flowrates up to 28.01 GPM with an error of  $\pm 0.2\%$  to  $\pm 0.5\%$ . The minimum liquid conductivity for the detector is 3 micromhos/cm [Yamatake, 2004]. The range is set to 0-5 GPM for the 4-20 mA analog output signal. Liquid temperature is measured 4 inches downstream of the meter to more fully characterize the mass flow [Solom, 2016].

### 7.1.4.3 Pressure Transmitters

The turbine facility uses five different models of pressure transmitter. These models are Dwyer 682-3, Dwyer 673-7, Honeywell ST3000 STA940 absolute pressure transmitter, Honeywell ST3000 STD924 differential pressure transmitter, and two Rosemount 3051C absolute pressure transmitters. In addition to the pressure transmitters, there are several analog pressure gages used throughout the facility. The bourdon tube gages are not used for data collection. Rather, they are used as operational aids [Solom, 2016].

The Dwyer 673-7 pressure transmitters come with a fixed range of 0 to 100 psig, and the 682-3 registers 0 to 250 psig. Both transmit an analog 4-20 mA signal. Three of these Dwyer gage pressure transmitters are installed in the facility. One is at the Water Injection Pump discharge, one is at the Water Injection Pump suction, and a third is in the Feedwater Storage Tank vapor space. No adjustments are available for these instruments, so their transmitted data was used only to monitor pressure during operation, not to collect precision measurements [Solom, 2016].

The Honeywell pressure transmitters can interface with the Honeywell Smart Field Communicator. There are multiple benefits to this tool, such as quick connections to the transmitter, rapid output range adjustment, and simple calibration procedures. Adjustment of ranges is done with a few button presses, and no potentiometers adjustments are necessary. Transmitter output can be set to Manual Loop to hold specific values, which aids in calibrating the 4-20 mA current loop [Solom, 2016].

The STD924 model can measure differential presures from -20 to +400 inH20. The detectors can withstand high common-mode case pressure, and so these transmitters are very useful for measuring liquid levels in pressure vessels. One STD924 monitors Steam Generator water level and the other monitors Feedwater Storage Tank level [Solom, 2016].

The STA940 model reads absolute pressure from 0 to 500 psia. Turndown adjustments are used to read lower pressures. One measures steam generator pressure, a second measures pressure in the vapor space of the Feedwater Storage tank, and another measures Main Steam Line pressure downstream of the vortex flowmeter. The Steam Generator pressure transmitter transmits from 0 to 150 psia, the Feedwater Storage Tank transmits from 0 to 100 psia, and the Main Steam line transmits from 0 to 130 psia [Solom, 2016].

The Rosemount 3051C transmitters can transmit from 0 to 150 psia. The 3051C pressure transmitters installed in the system are calibrated from 0 to 75 psia. The instrument overpressure limits are 1500 psia. They can be adjusted and calibrated using the Emerson 475 Field Communicator, which provides benefits similar to the Honeywell Smart Field Communicator. One transmitter is installed in the Turbine inlet plenum near the nozzle inlet, and the second is installed in the turbine exhaust space near the nozzle exhaust [Solom, 2016].

### 7.1.4.4 Thermocouples

For this experiment, thermocouples are used to measure temperatures at several locations. There are six thermocouple sensing points along the steam line between the vortex flowmeter and the turbine steam inlet nozzle, and another is installed the turbine exhaust region. The nozzle inlet sensor port is directly next to the nozzle inlet valve. The exhaust sensor is in the bottom of the exhaust portion of the casing, also near the nozzle exhaust. Five thermocouples monitor water temperature along the line from the Feedwater Storage Tank, through the Feedwater Injection Pump, and into the main steam line. Four thermocouples monitor Steam Generator internal temperatures. One monitors the feed temperature just before injection to the Steam Generator, another is just downstream of the Yamatake flowmeter, and one monitors laboratory ambient temperature [Solom, 2016].

All of these thermocouples are Omega type T thermocouples with special limits of error. The error limit of these thermocouples is the greater of  $\pm 0.5^{\circ}$ C, or  $\pm 0.4\%$  of the total reading. This thermocouple type operates using copper-constantan wire. All are ungrounded, and have stainless steel sheathing. Lengths vary from 12 to 120 inches. Diameters range from 0.032 inches to 0.062 inches. The thermocouples used here are ungrounded. In this case, it is recommended that they be ground referenced on the negative terminal. This has been enabled for all thermocouples in the facility ([Solom, 2016] and [Omega]).

## 7.1.4.5 Vessel Instrumentation

Several instruments are installed to provide indication of conditions within the Feedwater Storage Tank. These include 23 thermocouples for temperature indication. Thermocouples and internal piping are supported by a support structure within the vessel. This support structure is fabricated from stainless steel strut channel and stainless steel threaded fasteners. The feed of the support structure are stainless steel blocks padded with silicone rubber pads. To ensure adherence to the ASME-API certification stamp, there are no mechanical attachments coupling the support structure to the vessel [Solom, 2016].

An Orion magnetic level indicator is located at the front head to provide visual water level indication. A Honeywell differential pressure transmitter is used to take a more precise measurement of water level; this level is transmitted to the data acquisition system. The high pressure side is connected to a reference column which is connected to the top of the pressure vessel vapor space. The low pressure side is connected to the liquid section of the vessel. Vessel level is obtained by measuring the difference in head between the reference leg and the variable leg. A Dwyer 673-7 gauge pressure transmitter is installed in the 1.5-inch flange that monitors vessel pressure [Solom, 2016].

## 7.1.4.6 Tachometer

Turbine rotational speed is detected by a Monarch ROLS-W laser sensor. In Figure , the sensor is visible at the bottom of the photograph, and the red laser dot is visible on turbine shaft. The sensor signal is transformed into a 4-20 mA signal and transmitted to the DAQ by a Monarch ACT-3X tachometer/transmitter, shown in Figure .



Figure 57 Monarch ROLS-W Tachometer sensor



Figure 58 Tachometer display

## 7.1.4.7 Dynamometer

The turbine is loaded using a water brake dynamometer. The Stuska XS-19 model was used for this experiment. The dynamometer, like the turbine, is supported by the test platform. The instrument functions by using the viscous shear of water.

The dynamometer shaft spins at the same speed as the turbine shaft. This causes the water brake, which can be likened to a flywheel, to turn within the dynamometer casing. The dynamometer is loaded by directing water flow to the casing. The water brake imparts a shear tensor to the water, and the water transmits shear to the outer casing. An Omega LC101-25 load cell is attached to a point on the outer casing. The dynamometer is shown in Figure , and the load cell is shown in Figure .

The load cell measures the tensile force between the dynamometer outer casing and the test frame. Together with the distance from the center of the shaft, this force can yield a moment. This moment can combine with the shaft RPM to produce the power generated by the turbine.

Equations for these calculations are given later in Equations Error! Reference source not found. and Error! Reference source not found.

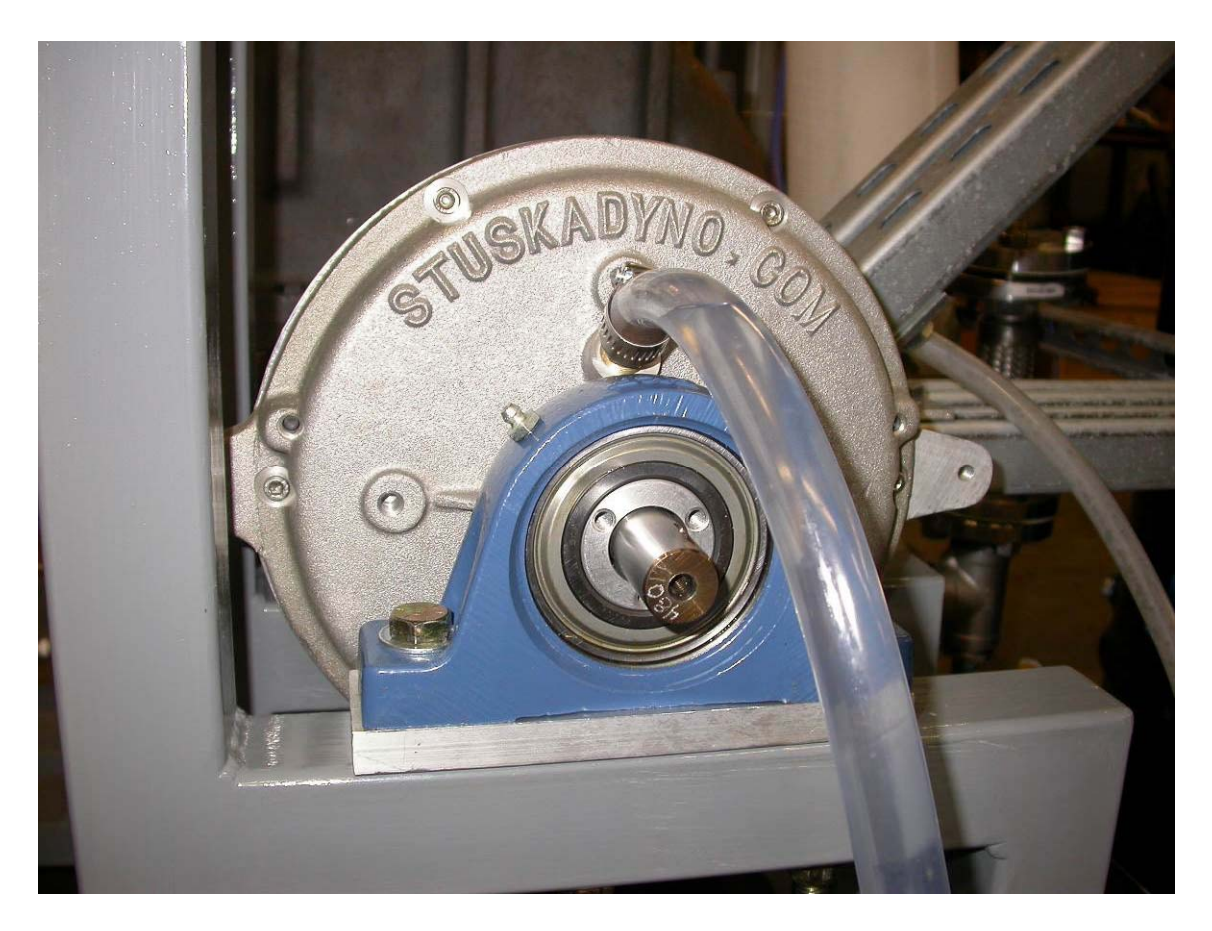


Figure 59 Dynamometer, with water supply tubing attached



Figure 60 Load cell attachment to dynamometer

The turbine, on test platform, with inlet and exhaust piping and instrumentation installed, is shown in Figure .



Figure 61 Turbine, with dynamometer attached

### 7.1.5 Calibration

To provide confidence in the data set, the instruments must have some sort of calibration. To that end, calibrations have been carried out where applicable [Solom, 2016].

The Honeywell ST3000 Series 900 transmitters used for steam line pressure, steam generator pressure, steam generator level, and feedwater storage tank level were calibrated in two phases: first sending them to calibrate their pressure readings; and secondly, performing a signal calibration on their 4-20 mA outputs to implement in the data acquisition software. Once the pressure measurements were calibrated, signal calibration profiles were developed. Signal calibration was done using the same methods for pressure transmitters and magnetic flowmeters. A small LabVIEW VI was developed for this task. It uses a two-point calibration. The Honeywell Smart Field Communicator was used to set the transmitters to transmit 100% of their full-scale 20 mA signals. These signals were recorded by the software and time-averaged for a span of greater than 100 seconds. Then, the instruments were set to output their lowest signal; this is 0%, or 4 mA. The signal was again recorded and time-averaged for greater than 100 seconds. Full linearity straight through from the measurement to the analog output to the analog to digital conversion in the DAQ, this two-point calibration is sufficient to fully derive the curve [Solom, 2016].

Two-point calibrations can be described using an equation of a line, given in Equation Error! Reference source not found.

$$y = a \times (x - b) \tag{194}$$

Calibration data for instruments used in the experiment are given in Table 8.

Table 8 Calibration Profiles for NHTS RCIC Test Facility Instrumentation

Instrument	Instrument Name	a	b
I-1	SG Absolute Pressure Transmitter	0.2510	0.9965
I-2	SG Level Transmitter	0.2510	0.9968
I-3	Feedwater Storage Tank level	0.2510	0.9967
I-5	SG Return Flowmeter	0.2509	0.9958
I-6	Main Steam Line Flowmeter	0.251	0.991
I-7	Main Steam Line Pressure Transmitter	0.25102	0.99650
I-12	Water Injection Flowmeter	0.25112	0.99662
I-16	Turbine Inlet Pressure Transmitter	0.2510	0.9958
I-17	Turbine Exhaust Pressure Transmitter	0.2508	0.9962
I-18	Tachometer	0.251023	0.994734
I-19	Load Cell	0.2513	1.001

The load cell has a range of 0-25 lbf. Calibration data was collected for 0% and 100% loading. For the zero setpoint, the load cell was suspended from a hanger with both eyebolts installed, and no weight suspended. For 100% loading, a set of interlocking test weights was suspended from the bottom eyebolt. The test weights, plus the weight of the hanger, provide a total of 25 lb of mass. This two-point calibration was implemented into the LabVIEW VI. The weights and tolerances are given in Table 9.

Table 9 Load Cell Test Weights

Mass	Quantity	Tolerance
2 lb	2	±0.0002 lbs.
10 lb	2	±0.001 lbs.
1 lb	1	±0.01 lbs.

The Foxboro vortex flowmeter calibration procedure involves calculation of an expected upper range frequency, temporary setting of DIP switches, and removal of electronics from the flowmeter body. The sensor unit is disconnected, and a function generator is installed in its place. The function generator is operated at the calculated upper range frequency, and then at zero while making adjustments to potentiometers. At this point, the temporary connections must be removed, the electronics returned to the housing, and the DIP switches set. For the steam setup, an upper range frequency of 2400 Hz was used. This was determined to be an upper range frequency that would allow the entire band of desired flowrates to be detected. Additionally, the function generator available does not isolate its signal as required by the transmitter. Instead, its signals are ground-referenced. In order to allow the signals to float, the function generator was plugged into an uninterruptible power supply (UPS). The UPS was then unplugged from the wall to remove the ground reference during operation. During the procedure, frequency was read by an oscilloscope to verify that the reported frequency on the function generator was within tolerance [Solom, 2016].

The LabVIEW packages are equipped to read thermocouples. It is assumed that the thermocouples maintained their Special Limit of Error tolerances with minimal drift or

degradation. With regard to thermocouples, the necessary tasks are to ensure the electrical connections are made properly and that the DAQ hardware reads the signals properly. The current DAQ card is an NI PCIe-6341 X Series data acquisition card. This card falls under a two-year calibration compliant with ANSI/NCSL Z540-1-1994. This is the NI "Compliant Calibration" service level [Solom, 2016].

Example calibration certificates are given in the following figures: Figure and Figure are the certificates from the turbine inlet and outlet pressure transmitters, Figure is the tachometer calibration certificate, and Figure is the load cell calibration certificate.



### 23 June, 2016

**Emerson Process Management** Rosemount Inc. 8200 Market Blvd Chanhassen, MN U.S. 55317-9786

### Calibration Data Sheet Consistent with ISO 10474 3.1 or EN 10204 3.1

Customer Information	Manufacturer Information
Name: TEXAS A AND M UNIVERSITY PO: Ref 503123	Sales Order: 4610121 Line: 2
Device Information	Calibration Information
Device Type: Pressure Transmitter PDTag:  Serial No: 2831256 Model No: 3051CA2A22A1AB4Q4	Factory: CHANHASSEN, MN, USA Station Name: CHAN_PRESSURE_CALIBRATION_15 Operator ID: 34934 Calibration Date: 6/23/2016 6:05:26AM
Module Serial No: 6557803 Output: Linear Device ID: 6557803	Internal Ref# 12182729

#### **Equipment Used**

EqNumber:	EqName:	CalDueDate:
E3-56134	Multimeter	7/20/2016 8:50:00AM
E3-58598	Load Box	4/20/2017 1:45:00PM
P3-54296	Pressure Controller	8/2/2016 11:24:00AM

### Calibration Data

Range: 0.000 TO 75.000 PSI

% of Range	Applied Pressure	Requested Applied Pressure	Analog Output (mA)	% Span Error	Pass/Fail
99.999	74.999 PSI	74.9990 PSI	20.00002	0.00138	PASS
80.000	60.000 PSI	60.0000 PSI	16.80066	0.00413	PASS
60.000	45.000 PSI	45.0000 PSI	13.60026	0.00163	PASS
40.000	30.000 PSI	30.0000 PSI	10.40054	0.00338	PASS
20.000	15.000 PSI	15.0000 PSI	7.20040	0.00250	PASS
0.667	0.500 PSI	0.5000 PSI	4.10682	0.00138	PASS

This is to certify that the listed product meets the applicable Rosemount Specifications. Measuring and test equipment used in the manufacture and inspection of the listed product are traceable to the National Institute of Standards and Technology. The calibration system was designed to meet the intent of ANSI Z540-1-1994.

Kelly Klein Vice President of Global Quality, Approvals & EHS

Page 1 of 1

JPG2831256\_Q4-PRESSURE\_RTC\_1

Figure 62 Turbine inlet pressure transmitter calibration certificate



**Emerson Process Management** Rosemount Inc. 8200 Market Blvd Chanhassen, MN U.S. 55317-9786

#### Calibration Data Sheet Consistent with ISO 10474 3.1 or EN 10204 3.1

Customer Information	Manufacturer Information
Name: TEXAS A AND M UNIVERSITY PO: Ref 503123	Sales Order: 4610121 Line: 2
Device Information	Calibration Information
Device Type: Pressure Transmitter PDTag:  Serial No: 2831257 Model No: 3051CA2A22A1AB4Q4	Factory: CHANHASSEN, MN, USA Station Name: CHAN_PRESSURE_CALIBRATION_15 Operator ID: 07369 Calibration Date: 6/23/2016 8:28:41AM
Module Serial No: 6557810 Output: Linear Device ID: 6557810	Internal Ref # 12182730

#### **Equipment Used**

EqNumber:	EqName:	CalDueDate:
E3-56134	Multimeter	7/20/2016 8:50:00AM
E3-58598	Load Box	4/20/2017 1:45:00PM
P3-54296	Pressure Controller	8/2/2016 11:24:00AM

#### **Calibration Data**

Range: 0.000 TO 75.000 PSI

% of Range	Applied Pressure	Requested Applied Pressure	Analog Output (mA)	% Span Error	Pass/Fail
99.999	74.999 PSI	74.9990 PSI	20.00076	0.00600	PASS
80.000	60.000 PSI	60.0000 PSI	16.80088	0.00550	PASS
60.000	45.000 PSI	45.0000 PSI	13.59994	-0.00037	PASS
40.000	30.000 PSI	30.0000 PSI	10.40044	0.00275	PASS
20.000	15.000 PSI	15.0000 PSI	7.19986	-0.00087	PASS
0.667	0.500 PSI	0.5000 PSI	4.10608	-0.00325	PASS

This is to certify that the listed product meets the applicable Rosemount Specifications. Measuring and test equipment used in the manufacture and inspection of the listed product are traceable to the National Institute of Standards and Technology. The calibration system was designed to meet the intent of ANSI Z540-1-1994.

Kelly Klein Vice President of Global Quality, Approvals & EHS

Page 1 of 1

JPG2831257\_Q4-PRESSURE\_RTC\_1

Figure 63 Turbine exhaust pressure transmitter calibration certificate

Certificate of Calibration Model: ACT3X-1-1-4-2-0-0 Serial Number:
Date Calibrated: 05/23/2016 Calibration Exp
Temperature: 22 (Celsius)
Scale: 1 Pulses Per Revo 1483312 Calibration Expires: 11/23/2017 Pulses Per Revolution: NIST Reference: Frequency WWVB This instrument has been calibrated using standards and instruments which are traceable to the National Institute of Standards and Technology and meet the requirements of MIL-STD-45662A. This certificate may only be duplicated in full unless approved by us in writing. This certificate is only valid for the instrument mentioned above and the modes listed below. The instrument was found to be within specification. Equipment used in calibration: MANUFACTURER MODEL # SERIAL # CALIBRATION DATE AFG3021 CO20836 12/29/2015 Tektronix 12/29/2016 Tachometer Calibration (The generated signal is measured by the Instrument) RPM Set | UUT RPM | Acceptable RPM Range | RPM Set | UUT RPM | Acceptable RPM Range | 5 | 5.000 | 4.99995 to 5.00005 | 50 | 50.000 | 49.9995 to 50.0005 | 500 | 500.000 | 499.995 to 500.005 | 5000 | 5000.004 | 499.995 to 5000.05 | 50000 | 5000.030 | 49999.5 to 5000.05 | 100000 | 100000.100 | 99999 to 100001 | 500000 | 500000.300 | 499995 to 500005 | PASS PASS PASS PASS PASS PASS Calibrated by: Monarch Calibration Lab. 15 Columbia Drive. Amherst, NH 03031 Technician: \_\_\_\_ Date: 5-23-/6 SK Document #: CAL-500-002 Rev 3.2 Page 1 of 1 Certificate Serial #: 1483312

Figure 64 Tachometer calibration certificate

```
OMEGA ENGINEERING INC.
                                   LOAD CELL
                                FINAL CALIBRATION
                               0.00 -
                                            25.00 LBS
                              Excitation 10.000 Vdc
       Job: C27955
                                                    Serial: 346735
     Model: LC101-25
                                                Tested By: PEARL
                              Temperature Range: +60 to +160 F
      Date: 8/18/2016
                  0.00 -
                             25.00 LBS
Calibrated:
                                           Specfile: LC101 0-500 LBS
      Force Unit Data Normalized LBS mVdc Data
      LBS
                  mVdc
                               Data
               - 0.118 0.000
14.879 14.997
29.887 30.005
14.892 15.010
- 0.118 0.000
         0.00
                                 0.000
        12.50
        25.00
        12.50
         0.00
Delance - 0.118 mVdc
Sensitivity 30.005 mVdc
In Resist 350.30 Ohms
Out Resist 350.30
                   352.30 Ohms
59K Shunt
                 14.834
                                    Change at 0.00 LBS (-INPUT to -OUTPUT)
                            mVdc
Calibration Factors:
Sensitivity = 3.001 \text{ mV/V} 59K Shunt = 1.483 \text{ mV/V}
         ELECTRICAL LEAKAGE: PASS
ELECTRICAL WIRING/CONNECTOR: RED
                                      = +INPUT (EXC)
                               BLACK = -INPUT (EXC)
GREEN = +OUTPUT
                               WHITE = -OUTPUT
     This Calibration was performed using Instruments and Standards that are
     traceable to the United States National Institute of Standards Technology.
 S/N
Station 3
               Description Range
1001b Dead-Weights 0 - 25.00 LBS
                                                              Reference Cal Cert
                                                              C-2691 C-2451
 US36037962 HP34401A DMM UUT Unit Under Test
 Q.A. Representative : Pearl Stomers
                                                         Date: 8/18/2016
 This transducer is tested to & meets published specifications. After final
 calibration our products are stored in a controlled stock room & considered in
 bonded storage. Depending on environment & severity of use factory calibration
 is recommended every one to three years after initial service installation date.
 COMMENTS: FINAL IN TENSION
 Omega Engineering Inc., One Omega Drive, Stamford, CT 06907
 http://www.omega.com email: info@omega.com phone (800) 826-6342
```

Figure 65 Load cell calibration certificate

# 7.2 Shakedown Testing and Facility Improvements

# 7.2.1 Shakedown Testing

The major equipment installed in the facility for this experiment was the turbine, including with its inlet and exhaust piping, as well as the dynamometer and load cell. Structural support was also required for the turbine, dynamometer, and piping.

#### 7.2.1.1 Turbine

The turbine was first installed to the test platform without any coupling connected to the shaft. The turbine was brought up to speed using compressed air via a 3/4-inch hose. Speed was monitored using a handheld laser tachometer.

After the inlet piping was installed and the permanent tachometer were installed, the turbine was retested again. The dynamometer was aligned with shim plates and installed, and then the turbine was spun up again. Lastly, the exhaust piping was installed.

## 7.2.1.2 Inlet Piping

The inlet piping was installed up until the connection to the turbine. The piping was pressure-tested up to the turbine connection by installing a valve at the turbine connection point. The inlet piping was then pressurized to 120 psia using the air compressor, and inspected for leaks. All noted leaks were repaired. The turbine was then positioned in place, and connected to the inlet piping. The inlet of the turbine up until the nozzle inlet valve was then brought to pressure. Leakage was noted at two points on the casing of the turbine. These were the stem of the TTV and the stem of the nozzle throttle valve. Both of the packing nuts were tightened. The leak at the nozzle inlet valve was able to be sealed, but the TTV was limited in its adjustment because the tightness of the stuffing box began to interfere with the automatic operation of the TTV.

The inlet piping was tested using air, steam, and mixtures of air/water and steam/water. Water hammer was anticipated during the steam/water mixtures were expected to stress the inlet piping. The first tests were air and air/water mix: 60 g/s air, then 55 g/s air with 5 g/s water were admitted to the turbine. After this, 45/15 and 30/30, and 15/45 and finally 60 g/s water were admitted to the turbine. No repairs were necessary, and no significant water hammer was noted. Instrument readings were steady.

### 7.2.1.3 Exhaust Piping

Because it lacks an isolation valve, and is subject to only low pressures, the exhaust portion of the turbine was subjected to only an operational joint tightness test. The exhaust pipe was installed into a water tank, and the turbine was operated using steam. Steam flow was throttled up in increments of 10 g/s to a final flowrate of 60 g/s. Minor leakage of less than two drops per second were noted at the shaft seal drains. No other leaks were noted in the exhaust piping or casing.

Exhaust consisted of a piping leg connected via threaded joints, directed to a 55-gallon drum. The piping employs a 9-inch corrugated stainless steel braided hose to allow for vibrations and misalignments. The exhaust was monitored for vibrations and signs of trouble.

In most steam/water tests, there is no issue with the piping being cleared of liquid, even though there is a significant rise in the piping. This is similar to the RCIC design in reactor plants; the turbopump is located below the suppression chamber to allow a significant NPSH to be applied to the suction of the pump. In consequence, steam is directed downward and then upward again. Condensate can collect in low points. In the plants, barometric condensers are employed to clear the condensate. In the experimental facility, a manual drain is installed at the exhaust low point.

## 7.2.1.4 Dynamometer

The dynamometer was connected and aligned to the turbine shaft. The turbine was brought up to speed using compressed air. Noises were noted while bringing the turbine up to speed. The dynamometer was realigned to the turbine shaft by shimming the pedestal bearings. Again the turbine was brought to speed. The improved alignment alleviated the noise.

The structure and coupling guard were installed to protect the coupling and prevent pieces from becoming missile hazards.

The load cell attaches to the dynamometer and the structural frame using eyebolts that minimize strain in the load cell body. Care was taken in designing the test platform to provide fastening points between the frame and dynamometer that are orthogonal to the axis of the shaft and to the axis of the torque arm. This ensures that the measured torque value is truly the torque delivered by the turbine.

### 7.2.1.5 Instruments

Pressure instruments were connected electronically with 4-20 mA cable to the converter box. Gage line was connected and the instrument bodies were vented. Offset was applied for the height of the instrument piping leg. The gage lines were uninsulated so that steam tests would still have a water leg of consistent height. Instruments were aligned using the Emerson 475 Field Communicator. Calibration was taken at zero 4 and 20 mA points. Offset was then applied through LabVIEW. Ambient readings were taken, and compared to other instruments such as the main steam line absolute pressure transmitter.

### 7.2.2 Modifications

During steam testing, certain thermocouple temperature indications along the steam line were noted to be consistently lower than others. These differences were within the documented uncertainty of the thermocouples. The old thermocouple sensors were replaced with new sensors of identical model for two reasons. First, the old thermocouples were several years old. Second, replacement ensured that all thermocouples along the steam line were from the same batch. The newly installed thermocouples, yielded more consistent temperature values along the steam line.

## 7.2.2.1 Post-Shakedown Repairs

No repairs were necessary after the shakedown testing period.

## 7.2.2.2 System Modifications and Enhancements

After shakedown testing, a non-horizontal branch of piping that had been used in previous tests was removed. This was to remove a confounding element: there was a possibility of losing water from steam/water and air/water mixes down the non-horizontal piping branch. The piping branch was replaced with a plug. This is to prevent loss of water, which could accumulate by falling out into the lower portion of the piping.

## 7.3 Test Description

General notes about the air and air-water tests are provided below.

Air in these tests is not preheated before entering the turbine. After traveling through the compressor, the air passes through a refrigerated air dryer before entering the steam generator. Additionally, expansion as the air passes through the piping and into the steam generator causes further cooling.

Typical air pressures at the turbine inlet, for air-only tests, are 45 psia.

To constitute qualified data, each trial is required be maintained over a certain period with parameters within a given band. The bands are RPM within 50 RPM of the target, gas flow within 2 g/s of the target flowrate, and the water flow within 1 g/s of the target flowrate. These conditions must be maintained for at least thirty seconds to obtain a qualified dataset.

There are several test formats possible for this facility. Air testing is reported herein while steam testing is also possible. Additionally, water injection is possible for either tests type. Water injection is via the five-stage water injection pump.

Loading of the turbine is variable. Assuming mass flowrate is controlled and held constant, loading of the turbine can be adjusted to obtain a desired speed. Loading is planned to be adjusted to power outputs for speeds between 1500 and 3000 RPM, in 500 RPM increments.

The overall testing plan involves testing and comparison of water/air ratios. Low-quality tests limit the speed to lower RPM ranges. Below 50% quality, the tests are limited to coastdown tests. Water injection is expected to add drag, essentially causing lower power to be produced by the turbine. Power will be even less than that required to maintain any steady rotation rate.

Control variables are listed in Table 10.

Table 10 Target Control Variables in Terry Turbine Experiments

Variable	Value
Air flow rate	Up to 60 g/s
Water temperature-air tests	75-306 °F
Inlet Pressure-air tests	35-45 psia
Inlet Quality	0.00-1.00

## 7.3.1 Representative Test Progression

A representative test is given in Figure . This test is with 60 g/s air injection and no water injection. Notable features are the initiation of air flow, followed by a drop in pressure as flow is admitted to the turbine. The turbine is loaded as speed approaches 3000 RPM. Loading results in an increase in load cell force, torque, and power. Test data is collected in the span between approximately 2900 and 2940 seconds. During this period, gas flow and turbine loading are adjusted to maintain turbine in the band between 2949 and 3051 RPM, and gas flow between 58 and 62 g/s.

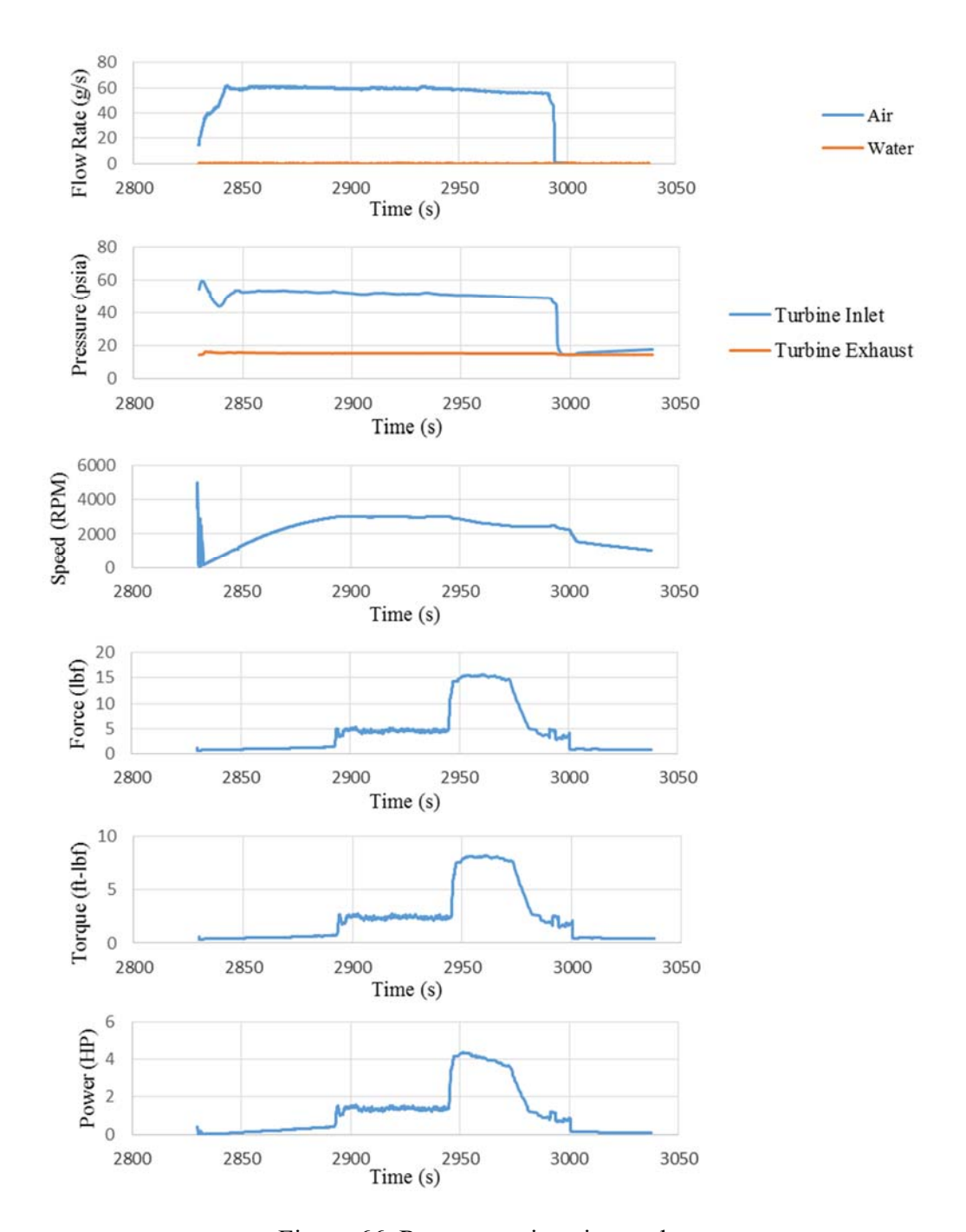


Figure 66 Representative air test data

The combined data from this test can be summarized by plotting power and torque over the test span. A test summary data point for torque is given in Figure , and a test summary data point for power is given in Figure . Torque and power were calculated using Equations **Error! Reference source not found.** [Cengel and Boles, 2008], respectively.

$$\mathbf{T} = Fr \tag{195}$$

$$\dot{W}_{sh} = 2\pi \, \dot{n} \mathbf{T} \tag{196}$$

T: torque (ft-lbf)

F: applied force

*r* : moment arm length

 $\overset{\bullet}{W}_{sh}$ : rate of shaft work

n: shaft revolutions per unit time

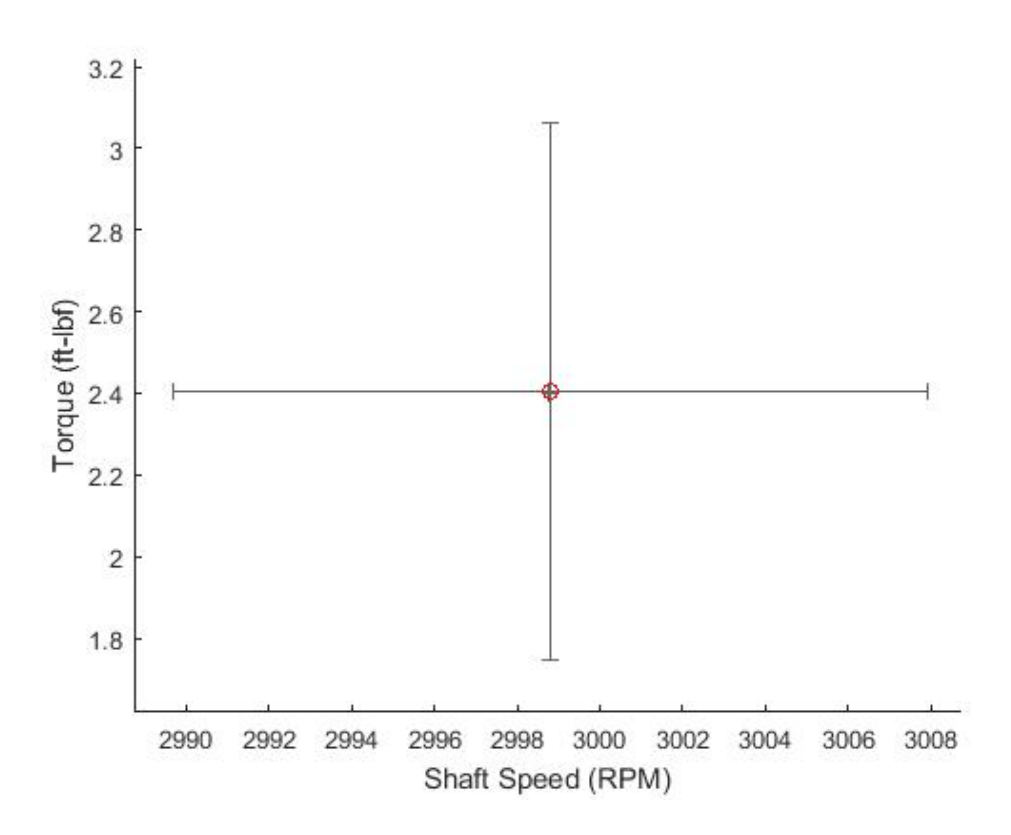


Figure 67 Summary torque data point for 60 g/s dry air test

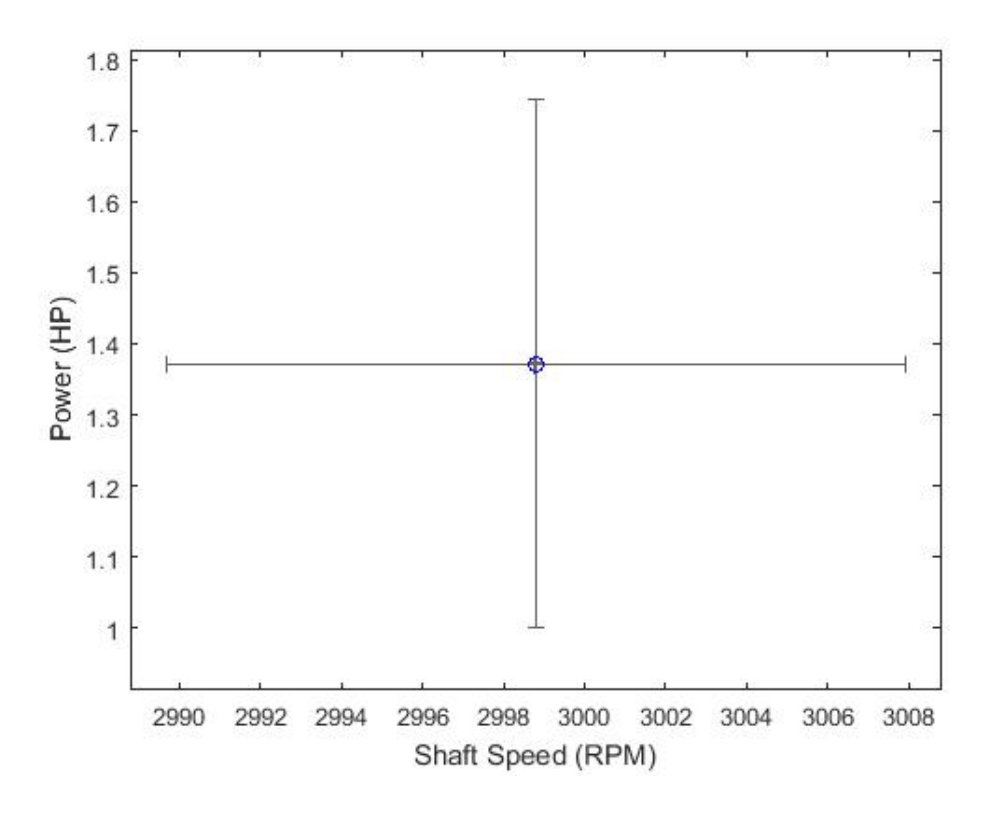


Figure 68 Summary power data point for 60 g/s dry air test

Error bars include sample standard deviation and mean instrument uncertainty over the course of the test. The sample standard deviation is calculated using Equations (197) and 198) [Bevington and Robinson, 2003].

$$\overline{x} = \frac{1}{N} \sum x_i \tag{197}$$

$$s^{2} = \frac{1}{N-1} \sum \left(x_{i} - \overline{x}\right)^{2} \tag{198}$$

x: mean of all measurements

 $x_i$ : individual measurement value

*N* : number of measurements

s: sample standard deviation

Torque and power are derived measurements, so instrument uncertainty was propagated to obtain a derived uncertainty for each of these measurements. Where measurements with associated uncertainties are summed, Equation (199) [Knoll, 2010] was used to propagate uncertainty.

When measurements are multiplied or divided, Equation (200) [Knoll, 2010] was used. Uncertainty limits for the instruments were shown previously in Table 7.

$$\sigma_{u} = \sqrt{\sigma_{x}^{2} + \sigma_{y}^{2}} \tag{199}$$

$$\left(\frac{\sigma_u}{u}\right)^2 = \left(\frac{\sigma_x}{x}\right)^2 + \left(\frac{\sigma_y}{y}\right)^2 \tag{200}$$

x, y: direct measurements

u: derived measurement

 $\sigma$  : uncertainty in measurement

# 7.3.2 Uncertainty Analysis

Uncertainty of measurements stems from multiple origins: accuracy limitations of the instruments, fluctuations due to random error, operator adjustment, and error due to conversion from analog to digital signals. The conversion from analog to digital is treated as negligible; it is very small. The accuracy limitations of the instruments are given in Table 7. Random errors and operator adjustments during data collection are included using standard deviation over the test duration. All plots include two sets of error bars. The wider error bars mark the sum of instrument uncertainty and the standard deviation of the measured quantity over the duration of the test. The more narrow error bars show the range of instrument uncertainty only. In many plots, the instrument uncertainty error bars are so small that they are not discernable on the scale of the plot.

## 7.4 Air Test Results

Air test summary data are given in Figure and Figure . Air tests showed a pronounced lowering of power. The air tests differed from the steam tests in that addition of water to air resulted in an increase of work produced by the turbine. This may be due to a rise in the enthalpy into the turbine with the addition of water. Another possible contributor is the increased differential pressure across the nozzle caused by water injection. Water mass would act to obstruct and slow flow, but the resulting higher differential pressure would also provide more energy to be converted to kinetic energy. This indicates that for air, the higher differential pressure overcomes the losses from addition of water.

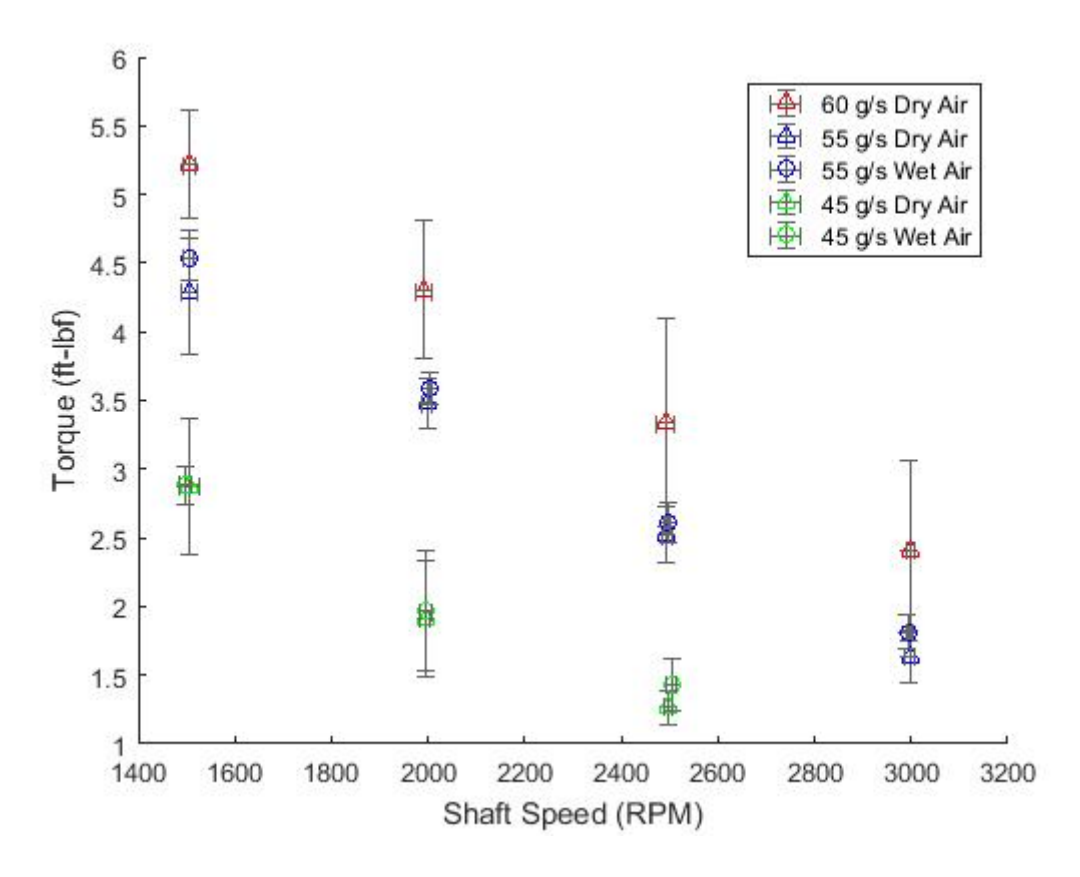


Figure 69 High-flow air torque summary data

There was one tests for which the critical pressure ratio was not obtained across the nozzle. This was the 15 g/s dry steam test. For all other tests, the critical pressure ratio was reached for both air and steam. The 45 g/s air tests in Figure constitute power near the maximum speed that can be achieved for this air flowrate. The turbine was unable to attain steady operation at 3000 RPM with 45 g/s dry air. Whereas the power peak is visible for the higher air flowrates, no peak is visible for the 45 g/s flow.

The torque plots of the air tests yield a linear pattern. The peak power for the 45 g/s air trials is not evident in Figure . Calculating power as a function of shaft speed yields an estimated peak at 1800 RPM.

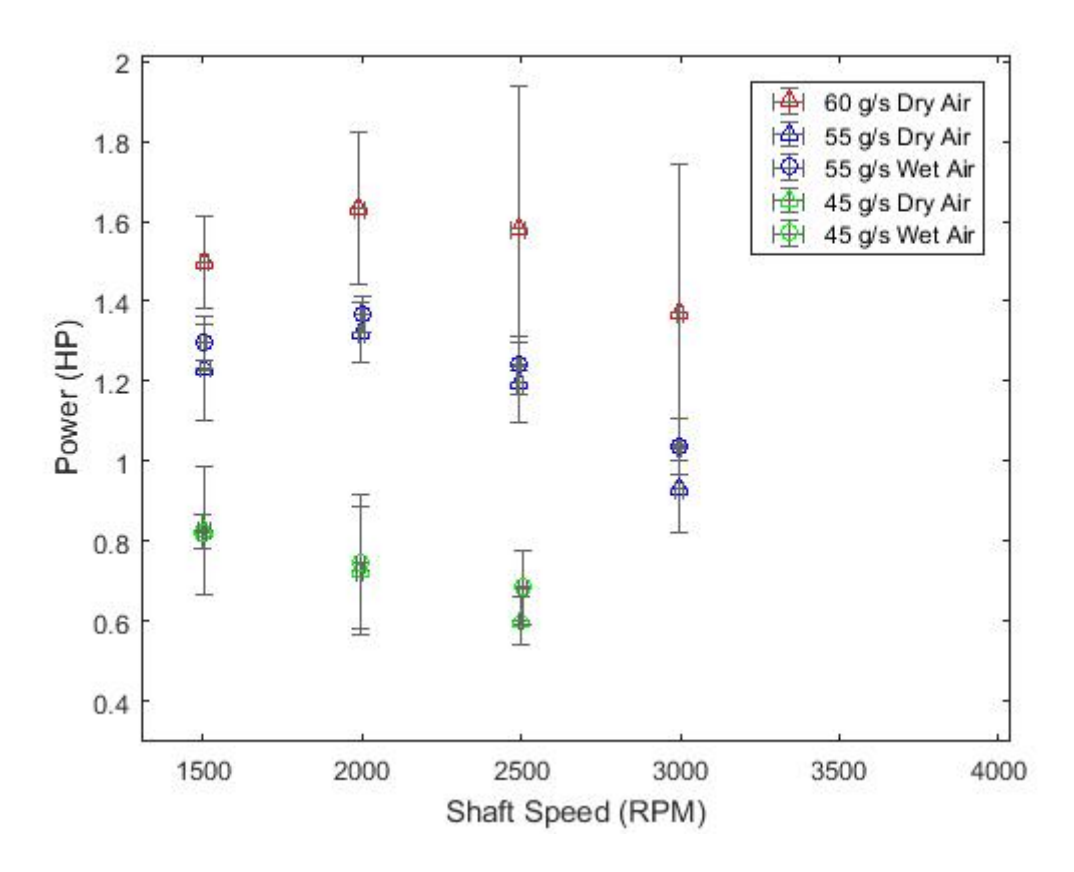


Figure 70 High-flow air power summary data

## 8 Task 6: Benchmarking Against Fukushima Data and Test Data

## 8.1 Terry Turbine Model Comparison against Nuclear Heat Transfer Systems Labs Test Data

# 8.1.1 Nuclear Heat Transfer Systems Labs Experimental Benchmark

The NHTS experimental test section [Luthman, 2017] is designed to send wet or dry air through a ZS-1 model Terry turbine (similar to the larger GS-1 and GS-2 models in use at domestic PWR and BWR installations). Certain characteristics of turbine performance are measured such as rotational speed, shaft torque, and shaft power. By selecting an NHTS experimental run, matching boundary conditions in STAR-CCM+ on a three-dimensional Terry turbine geometry, running a simulation, and comparing results to measurements, the validity of certain CMFD modeling constructs can be examined. Primarily in question is the technique of combining a moving reference frame (set at the experimentally-observed rotational speed) with mixing planes to get a time-averaged depiction of turbine flow.

# 8.1.2 Problem Description and Set-Up

A three-dimensional wedge of a full GS-1 Terry turbine geometry was used for purposes of the NHTS benchmark calculation. Snapshots of the Terry turbine wedge geometry are shown in Figure and Figure . The wedge was crafted with the STAR-CCM+ surface repair tool by essentially cutting a symmetric slice out of the full Terry turbine CAD model and creating periodic boundary conditions on the lateral wedge faces. The geometry was also split into inner (left and right) and outer (left and right) regions to facilitate mixing plane definitions. Inner regions (both left and right) were assigned a moving reference frame to simulate rigid body rotation of the turbine rotor.

Interfaces were set up between regions as necessary. The lateral wedge faces (orange-tinted in Figure ) are periodic interfaces. In-place interfaces were used at all region-wise points of contact. Figure demonstrates mixing plane configurations. The interface area between reversing chambers and accompanying rotor buckets was sub-divided into three roughly equal patches. Each patch was defined as a mixing plane and arranged such that eighteen circumferential bins spanned the width of the patch. Averaging occurs over each bin in each patch, and this choice of configuration produces average solution variable profiles across bucket and reversing chamber width.

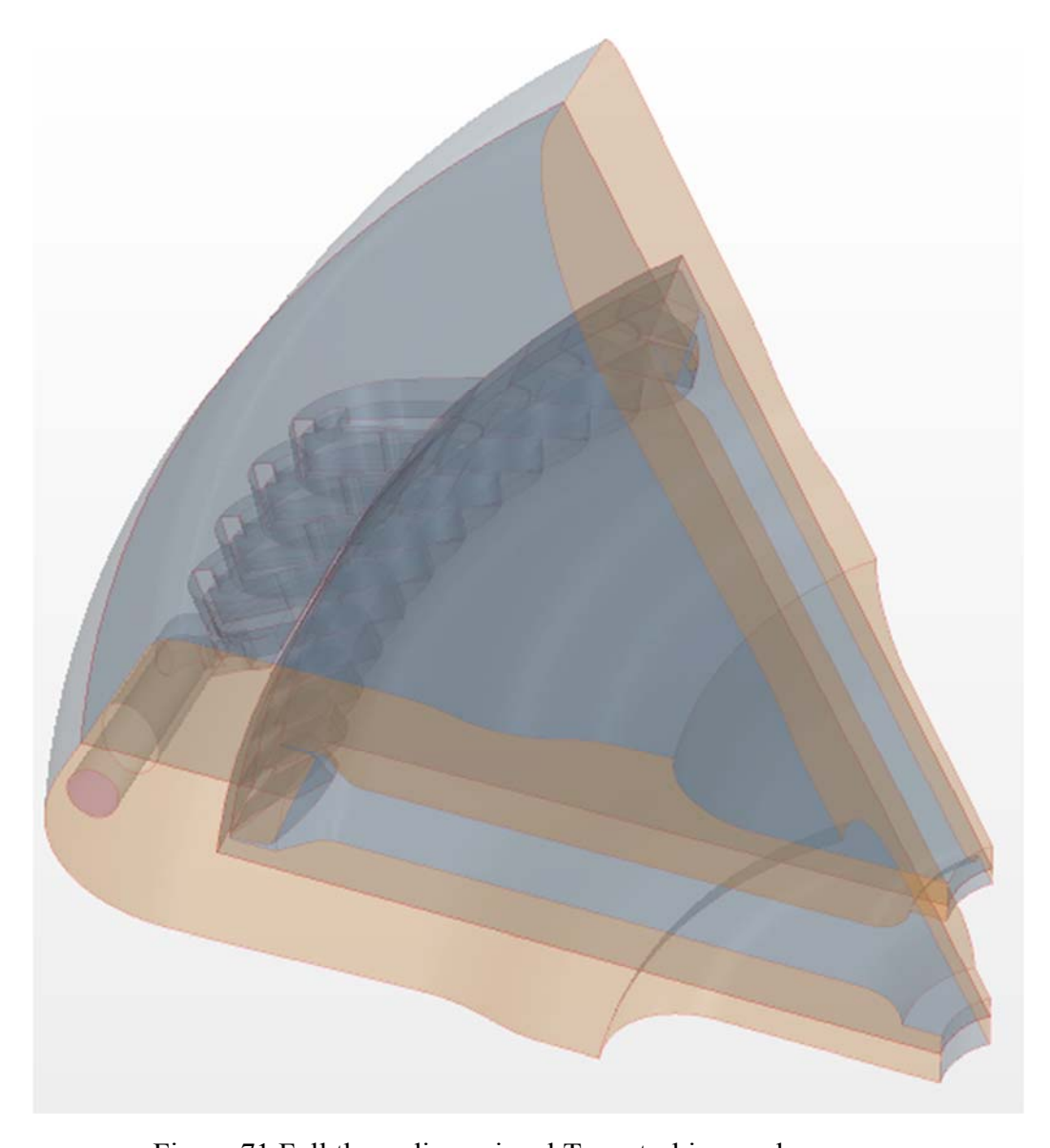


Figure 71 Full three-dimensional Terry turbine wedge

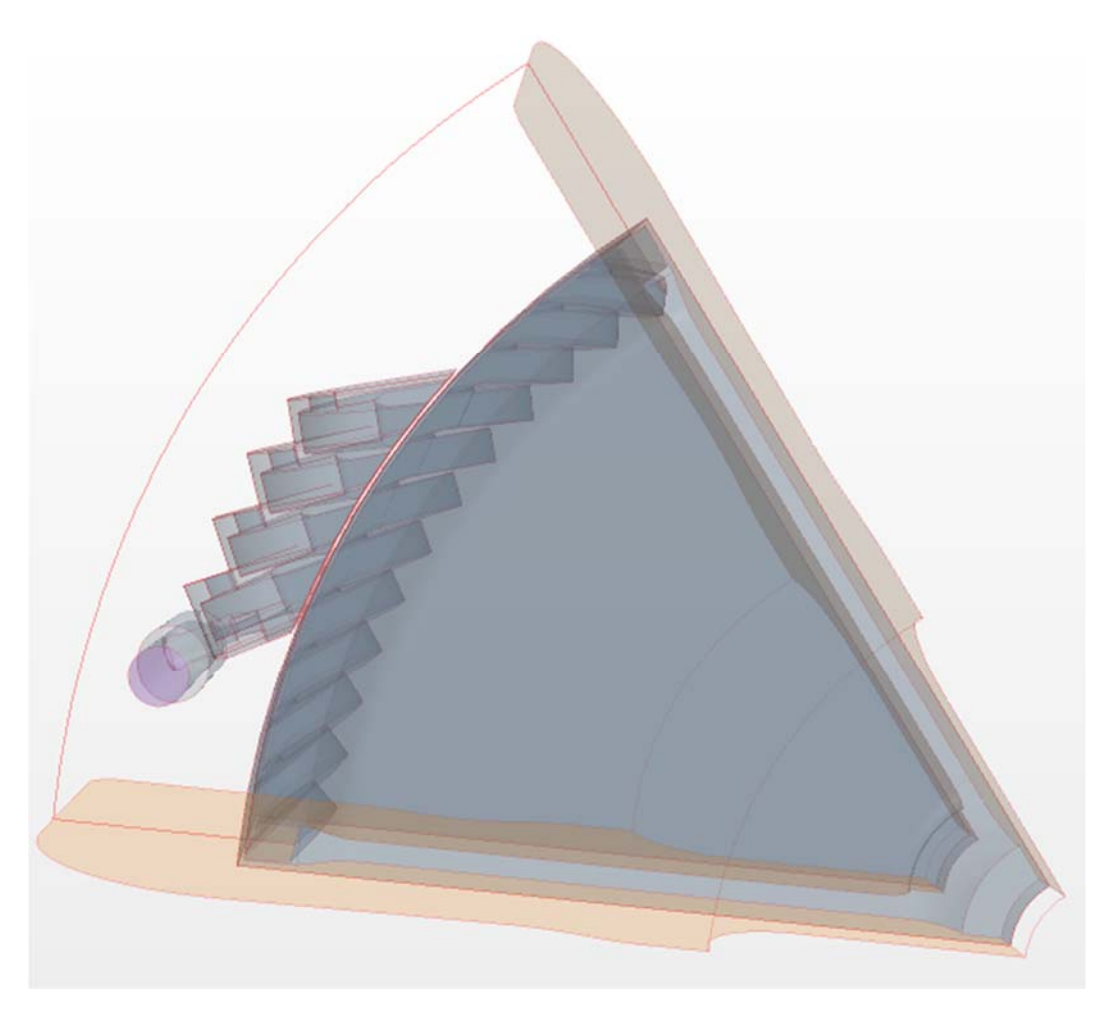


Figure 72 Terry turbine wedge, rotor and reversing chamber

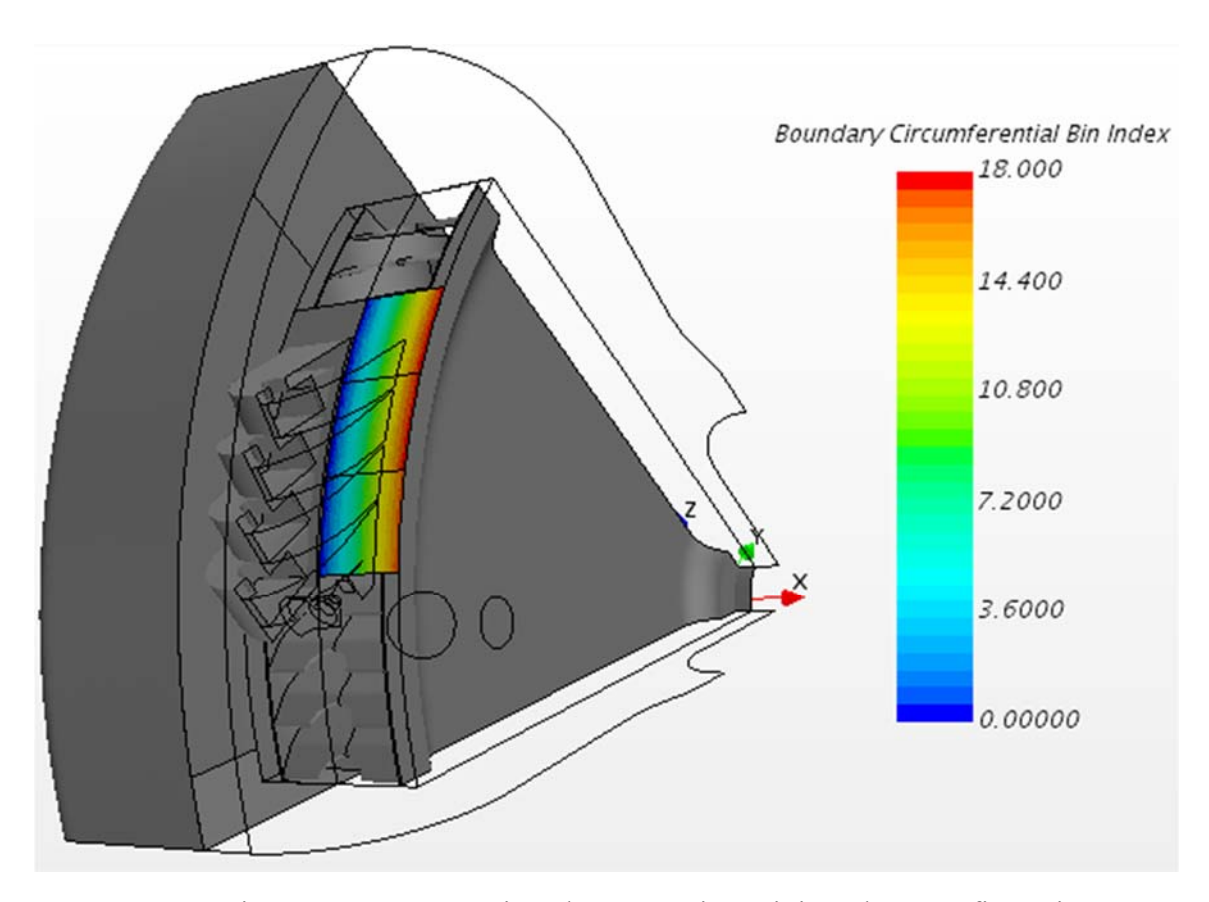


Figure 73 Cut-away view demonstrating mixing plane configuration

Boundary conditions are required at all solid surfaces (no slip, adiabatic), at the Terry turbine nozzle plenum inlet (stagnation inlet conditions), and at the periodic lateral wedge surfaces (pressure outlet). Additionally, a rotational speed must be specified for the moving reference frame assigned to the rotor. In this case, conditions were dictated by NHTS experimental conditions as summarized in Table 11 below.

Table 11 NHTS Experimental Benchmark Conditions [Luthman, 2017]

<b>Boundary/Condition</b>	<u>Value</u>	<u>Units</u>
Inlet/Pressure	360395.8	Pa
Inlet/Temperature	296.55	K
Inlet/Turbulence Intensity	0.01	-
Inlet/Turb Viscosity Ratio	10.0	-
Out/Pressure	106179.3	Pa
Out/Temperature	282.83	K
MRF/Rotational Speed	1500	RPM

### 8.1.3 Results

NHTS dynamometer measurements for torque and power were compared against simulation results. The single average torque value was computed in the simulation with the aid of a force report, which tallies the sum of pressure and shear force on a designated surface (or a collection thereof) by Cartesian coordinate. With all three components of force computed for the rotor bucket u-surfaces, a torque computation can be performed assuming a moment arm position vector with magnitude equal to the rotor radius and direction radially outward through the center of the Terry turbine wedge. Note the NHTS test section consisted of a ZS-1 Terry turbine (18" diameter wheel) containing just one steam nozzle. Therefore, the simulated GS-1 Terry turbine (24" diameter wheel) wedge with just one nozzle directly compares to the experiment, though the turbomachine diameters and bucket sizes do differ. Table 12 below summarizes the torque/power comparison. Some details about the torque computation follow.

<u>Metric</u>	<u>Value</u>	<u>Units</u>
NHTS torque/power	7.077 / 1115.56	N*m / W
Simulation torque/power	8.125 / 1276.27	N*m / W
Simulation $\mathbf{F}_{j}$	0.405	N
Simulation $\mathbf{F}_k$	61.64	N
Moment arm azimuth angle	0.4538	rad

Table 12 NHTS Experimental Torque/Power Comparison and Simulation Results

#### 8.1.4 Discussion

As previously mentioned, STAR-CCM+ furnishes the x, y, and z components of force exerted by air on the rotor bucket u-surfaces. The torque measurement of interest is along a direction tangential to the axis of rotor rotation and acting at a perpendicular distance approximately equal to the rotor radius. In a cylindrical coordinate system, the component of torque that turns the rotor is the azimuthal  $\theta$  component which, according to a change of basis vectors from Cartesian to cylindrical, depends on the j<sup>th</sup> and k<sup>th</sup> Cartesian components of force:

$$F_{\theta} = F_{j}cos(\theta) - F_{k}sin(\theta) \tag{201}$$

Once the report furnishes Cartesian force components, the azimuthal component of force is computed assuming a known angle of the moment arm,  $\theta$  (which lies in the Cartesian XZ plane for purposes of this simulation geometry). Multiplying  $F_{\theta}$  by the moment arm radius yields a torque and multiplying torque by a fixed rotational speed (units of rad/s, not RPM) yields a shaft power.

The agreement in terms of experimental ZS-1 and computational GS-1 shaft torque/power lends some measure of confidence to the analytical approach, namely:

• Use of a moving reference frame (to approximate effects of a spinning rotor on local fluid motion)

• Use of mixing planes (to obtain a time-averaged, steady-state depiction of turbomachine response under all nozzle/rotor configurations)

The comparison in Table 12 was not expected to demonstrate exact agreement because of inherent differences in the experimental apparatus and the simulation geometry. Nevertheless, an air flow of similar temperature and pressure exerts a comparable torque despite difference in rotor size, velocity stages, etc.

# 8.2 Gyarmathy CFD Benchmark for Turbine Steam Nozzle (Pressure Stage) Model

The purpose of Gyarmathy's Laval nozzle experiments [Gyarmathy, 2005] was to study nucleation characteristics in high-pressure saturated/subcooled condensing steam. The experimental test section included a cylindrical steel vessel and several ramp inserts forming different Laval nozzle geometries with disparate expansion rates. An optical measurement technique based on red laser light beam attenuation was used to discern wetness/droplet characteristics. With certain assumptions, measurements were backwards-extrapolated to ascertain Wilson point properties.

## 8.2.1 Problem Description and Set-up

The experimental test section [Gyarmathy, 2005] numbered 4B – pictured in Figure and described in Table 13 was reproduced in two dimensions in STAR-CCM+. Note that the data table gives the height of the "roller coaster" insert above its bottom that forms the bottom surface of the nozzle channel. A physics model including equations/closures for condensing steam outlined in the previous section was applied to the geometry. Some of these equations are available as options in STAR-CCM+ while others (e.g. the nucleation theory and condensation growth equations) were built with user-defined field functions and applied as source terms. A polygonal, unstructured mesh with near-wall prism layers was applied as a spatial discretization of the geometry. Stagnation inlet and pressure outlet boundary conditions (consistent with known experimental conditions) were used. No-slip, adiabatic conditions were applied at walls.

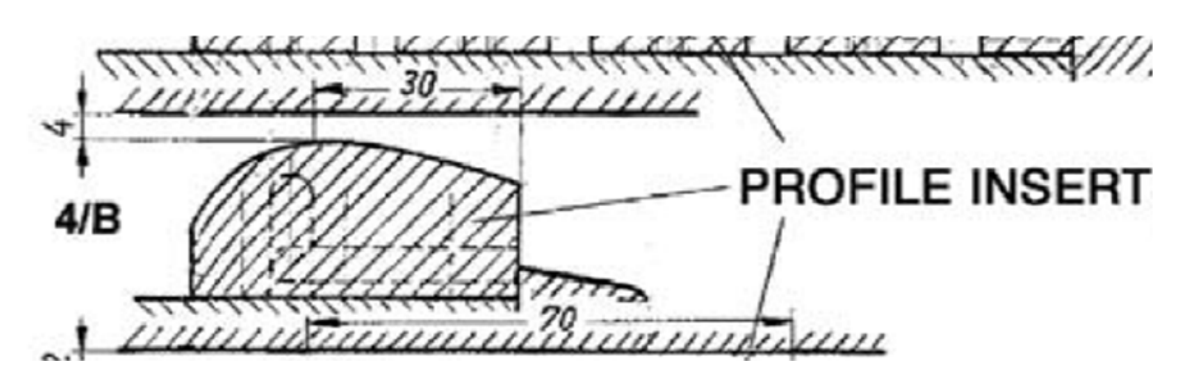


Figure 74 Gyarmathy experimental nozzle 4B geometry [Gyarmathy, 2005]

Table 13 Gyarmathy Nozzle 4B Geometry Data (constant width 20 mm) [Gyarmathy, 2005]

Axial Coord	Insert Height	Axial Coord	Insert Height
[mm]	[mm]	[mm]	[mm]
-20	9.59	16	20.26
-18	12.04	18	19.81
-16	14.24	20	19.34
-14	16.17	22	18.83
-12	17.85	24	18.28
-10	19.27	26	17.69
-8	20.44	28	17.07
-6	21.34	30	16.40
-4	21.98		
-2	22.37		
0 (throat)	22.50 (throat)		
2	22.42		
4	22.23		
6	21.99		
8	21.71		
10	21.40		
12	21.05		
14	20.67		

The steam nozzle 4B (run 19A) expansion rate is reported as approximately 50,000 [1/s] and the throat cross-sectional is: 4 mm in height, 20 mm in width, and 0.8 cm² in area [Gyarmathy, 2005]. Superheated steam inlet conditions were: stagnation (or total) pressure of 6.147\*10<sup>6</sup> [Pa] and stagnation (or total) temperature of 583.55 [K]. A pressure outlet (supersonic) simply extrapolates the boundary values of variables using the neighboring cell values and computed reconstruction gradients. This is consistent with the physics of supersonic flow, as "one-way street" behavior occurs and information does not propagate upstream into the computational domain from the outlet boundary. Initial conditions were linearly-varying estimates of solution variables based on experimental results, isentropic flow hand calculations, or otherwise educated guesses.

# 8.2.2 Benchmarking Results against Gyarmathy Data

In Table 14, certain derived quantities from the simulation are compared to reported values from [Gyarmathy, 2005] which constitute either experimental measurements or extrapolations based on certain assumptions such as isentropic flow. Additionally, profiles of solution quantities are included in Figures 75 through 84. These more detailed descriptions of the flow cannot be directly benchmarked against experimental data because the Gyarmathy experiments yielded point value measurements (from pressure taps, optical scattering, etc.) as opposed to spatial profiles.

Table 14 Gyarmathy Experimental Benchmark, Nozzle 4B, Run 19A

<u>Parameter</u>	<u>Units</u>	<b>Gyarmathy</b>	<u>CMFD</u>
Wilson Point Pressure	MPa	1.57-1.6	1.03
Critical Drop Size	M	4.314-4.469 *10 <sup>-8</sup>	1.318*10 <sup>-8</sup>
Drop Per Mass	Drop/kgsteam	11.99-13.40*10 <sup>16</sup>	5.69*10 <sup>15</sup>
Wilson Point Enthalpy	kJ/kg	2712.72-2716.32	2748.99
Wilson Point Temp	С	177.14-178.92	173.98
Wilson Point Sub-cooling	K	22.46-23.33	17.33

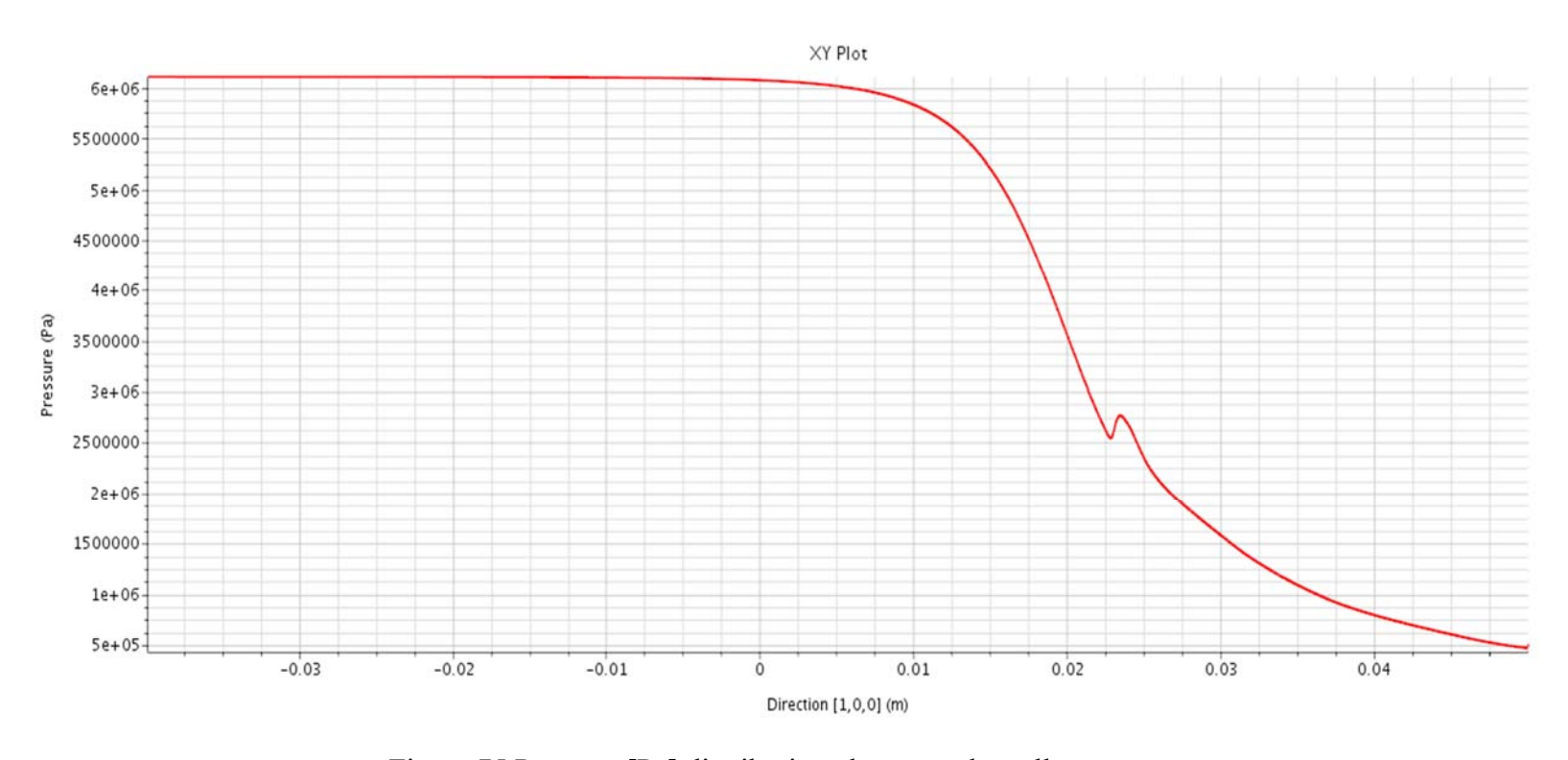


Figure 75 Pressure [Pa] distribution along nozzle wall

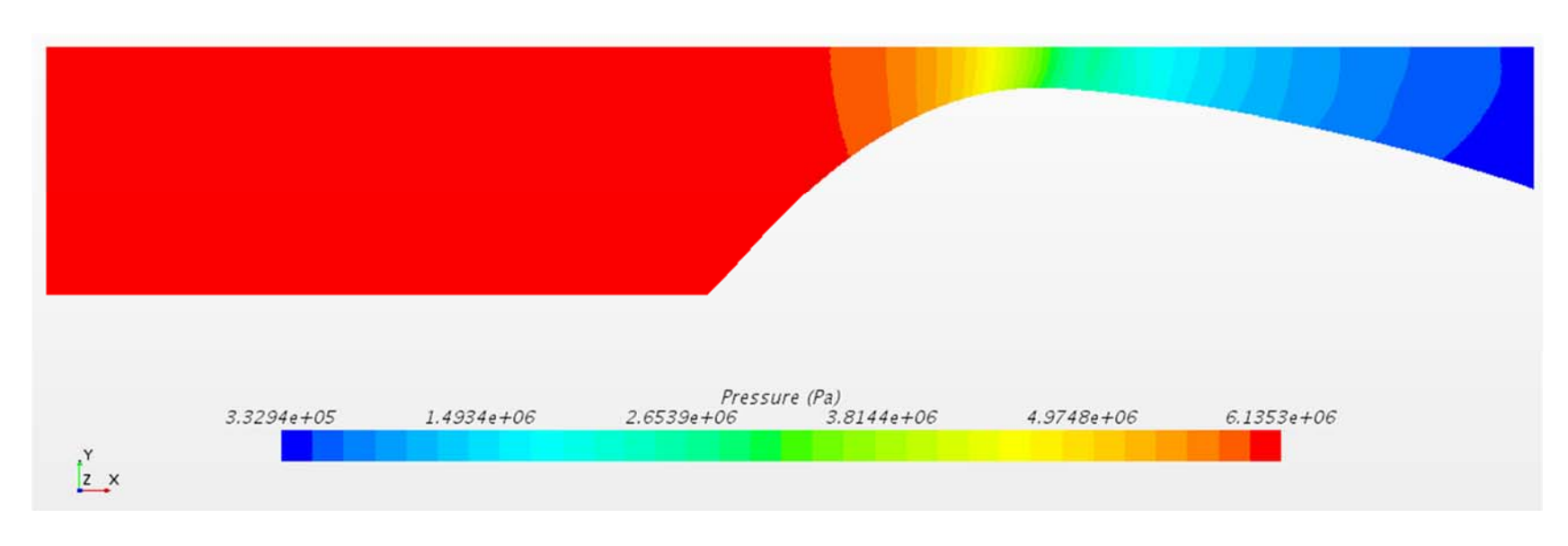


Figure 76 Pressure [Pa] profile in nozzle

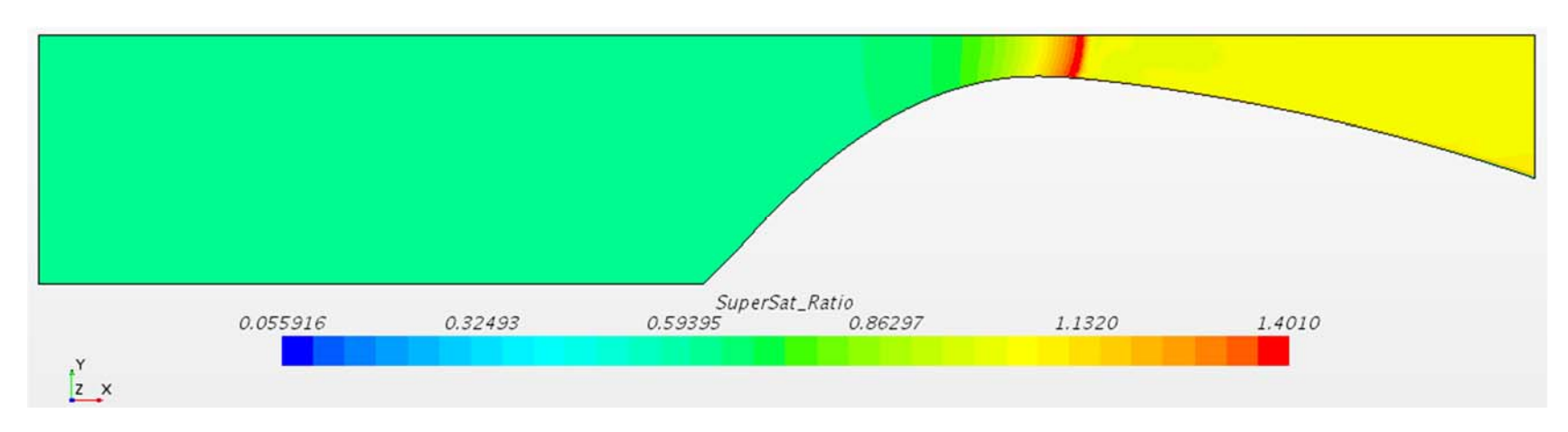


Figure 77 Super-saturation [-] ratio in nozzle

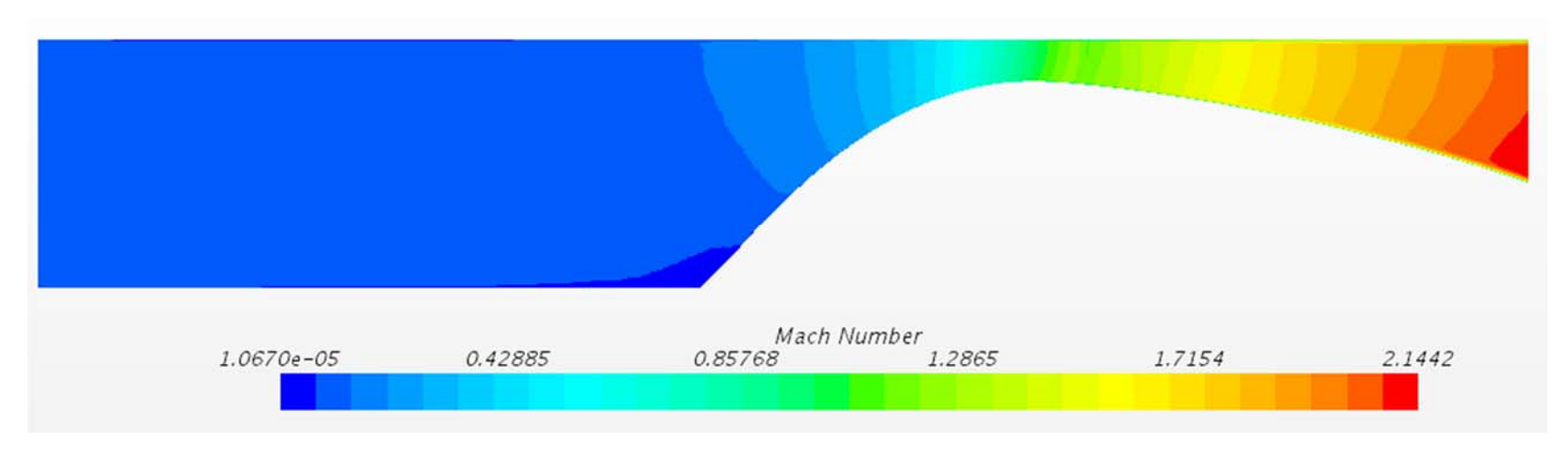


Figure 78 Mach number [-] in nozzle

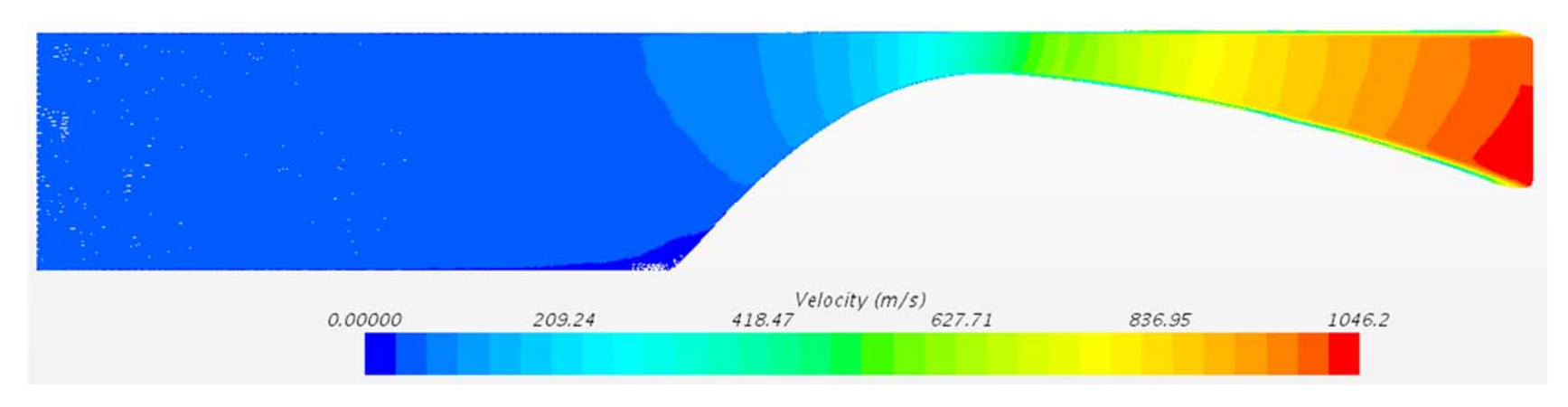


Figure 79 Velocity [m/s] vectors in nozzle

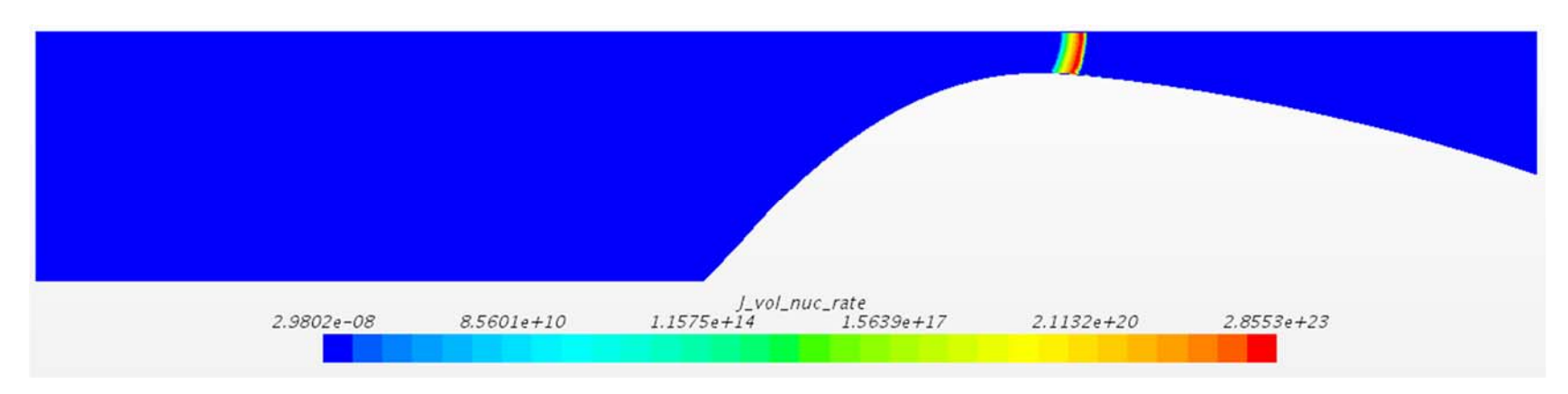


Figure 80 Nucleation rate [drop/m³/s] in nozzle

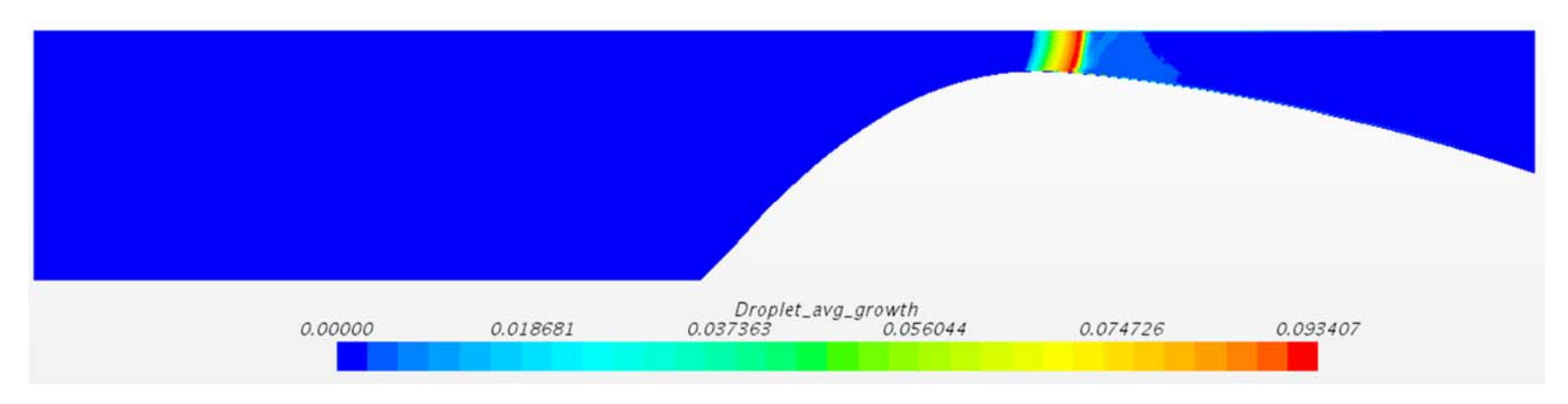


Figure 81 Condensation rate [m/s] in nozzle

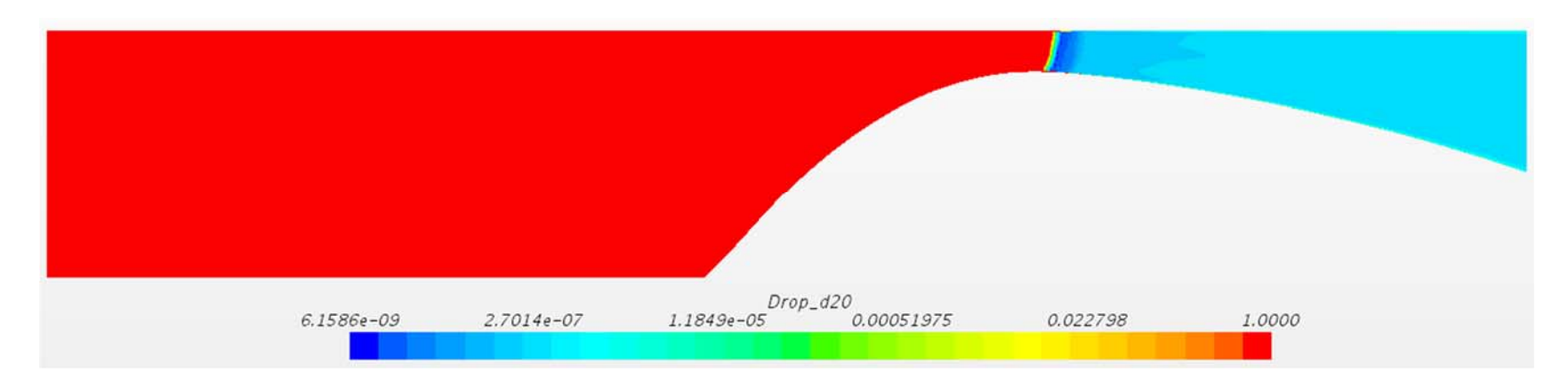


Figure 82 Droplet two-zero (average) diameter [m] in nozzle

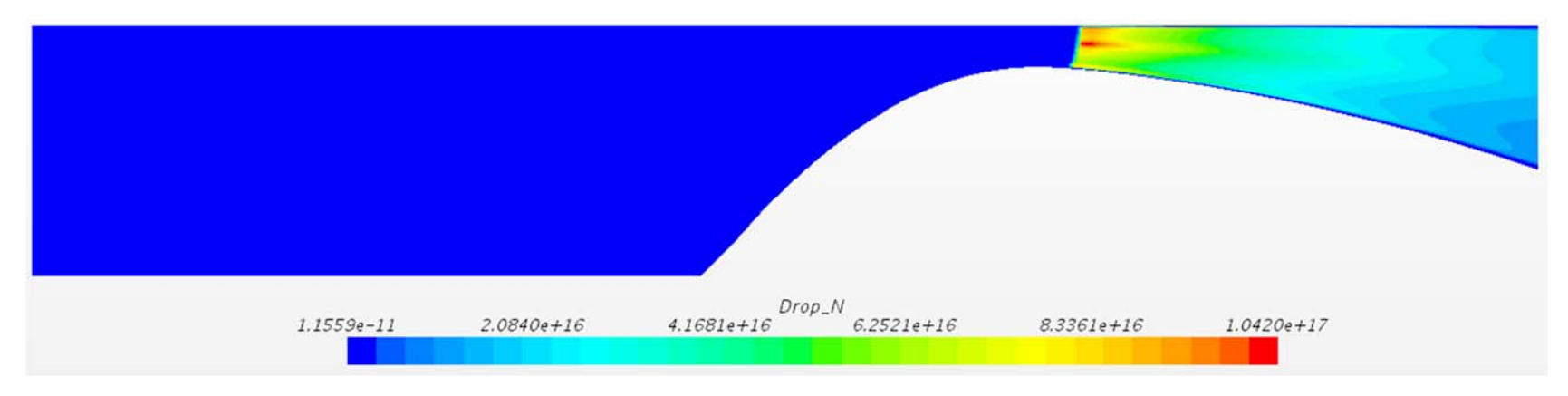


Figure 83 Droplet number density [drop/m³] in nozzle

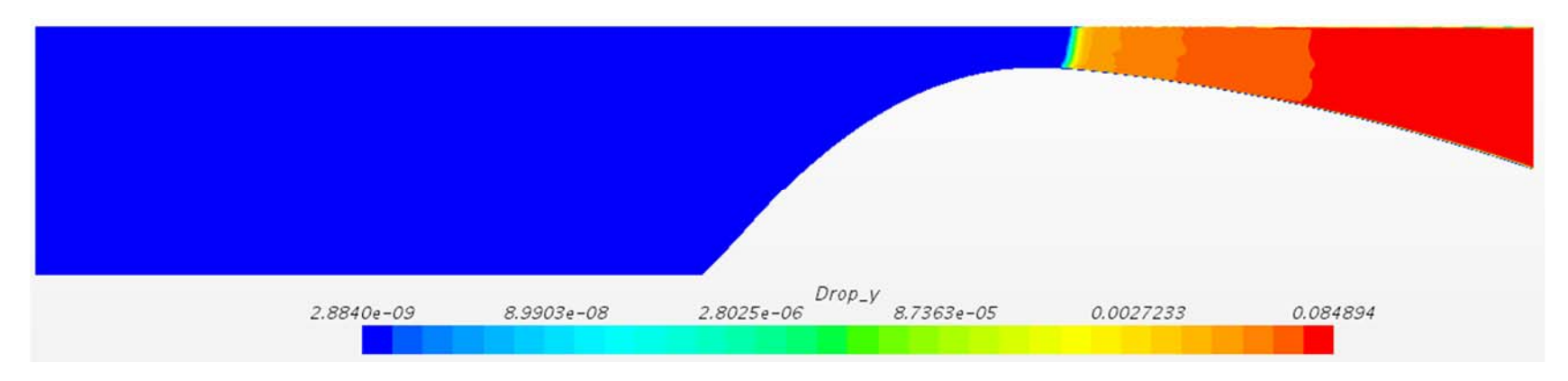


Figure 84 Droplet mass fraction [kg<sub>l</sub>/kg<sub>g</sub>] in nozzle

### 8.2.3 Discussion

The results from Figure 75 through Figure 84 demonstrate the converged solution obtained with steam physics models in STAR-CCM+. The metastability is evidenced by:

- Figure 75 where the pressure effects of condensation shock are visible (i.e. the "pressure bump" in the wall distribution from latent heat release to steam)
- Figure 76 where the effects of condensation shock on spatial pressure distribution are visible from the subtle blue-green-blue transition
- Figure 77 illustrating super-saturation (implying steam sub-cooling) that invariably leads to formation and growth of droplets
- Figure 78 where the steam slow-down due to momentum transfer associated with phase change is visible from the yellow-green-yellow transition
- Figure 79 where again the steam slow-down due to phase change is visible (changes of as much as 100 m/s near nucleation/condensation fronts)
- Figure 80 where predictions of the nucleation closures are shown
- Figure 81 where predictions of the condensation closures are shown, with a condensation front lagging a nucleation front in space (physically reasonable)
- Figure 82 where the passive scalar equation solutions are indirectly evidenced by the "two-zero" diameter (from second and zeroth moments)
- Figure 83 where the passive scalar equation solutions are indirectly evidenced by the droplet number density formed out of the zeroth size distribution moment
- Figure 84 which shows the dispersed mass fraction increasing along the flow direction as droplets grow in size/mass

# 8.3 Pump Model Benchmarking

## 8.3.1 Problem Description and Set-up

The most important performance quality of a pump is the pressure rise, or the hydraulic head. In this study, the pressure at the outlet was set to a reference value of 1000 PSI in all cases. The pressure difference was recorded using a pressure drop function in STAR-CCM+. This function works by subtracting the higher pressure user selection from the lower pressure user selection. In the model the high pressure input is selected as the outlet. While the low pressure output is set as the inlet. The pressure drop uses a surface area average of the pressure of the entire outlet and inlet. Figure 85 depicts the location of the inlet pressure and the outlet pressure in the model.

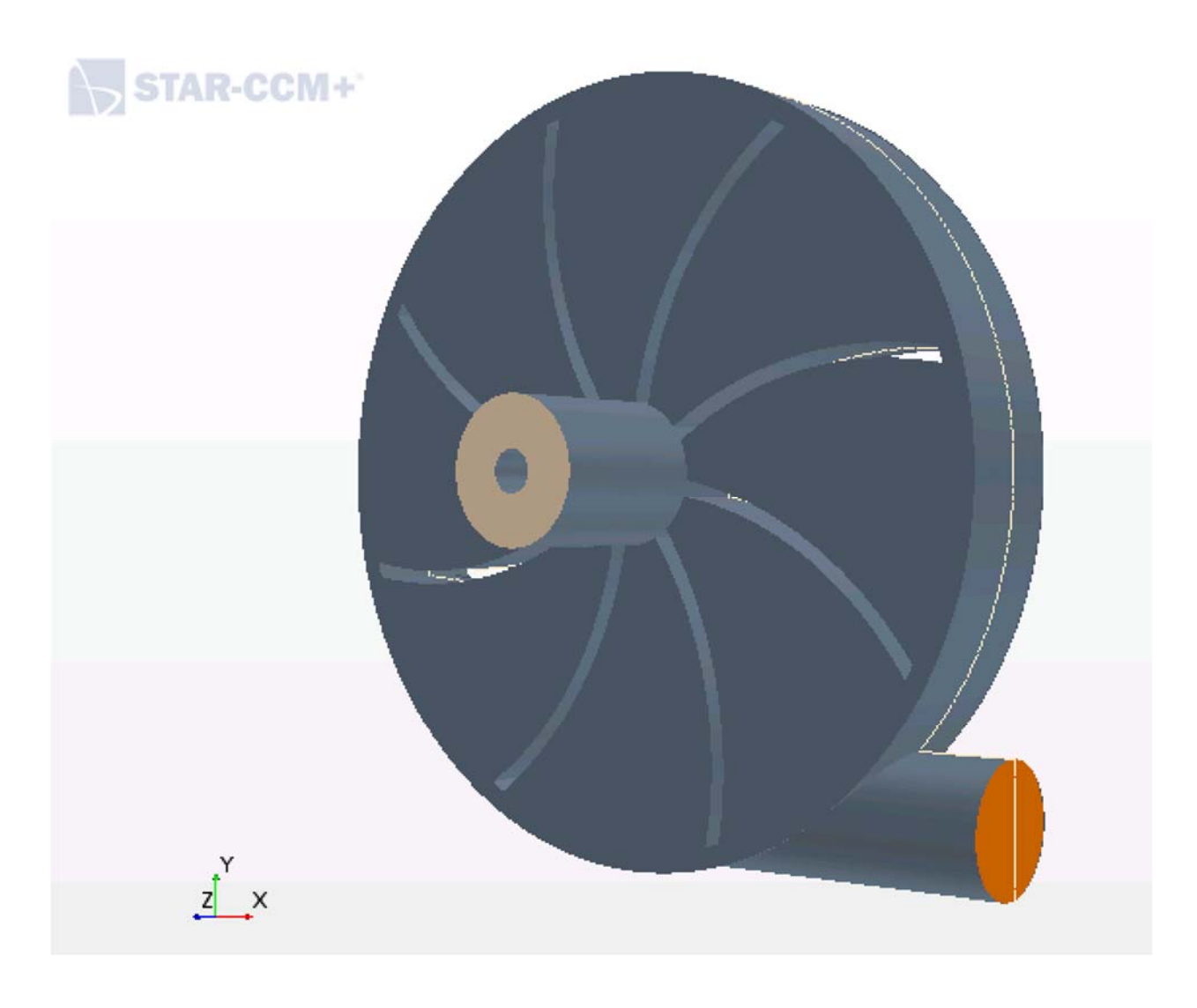


Figure 85 Position of inlet (tan) and outlet (orange) pressure in pump model

Figure 86 depicts the 2-D pressure contour at the outlet. Figure 87 is the pressure contour at the inlet. In Figure 86, since the pressure at the outlet was set to be constant, the pressure contour is also constant. Since the pressure in Figure 87 is not uniform, the benefit of the area-averaged pressure of the pressure drop feature is evident.

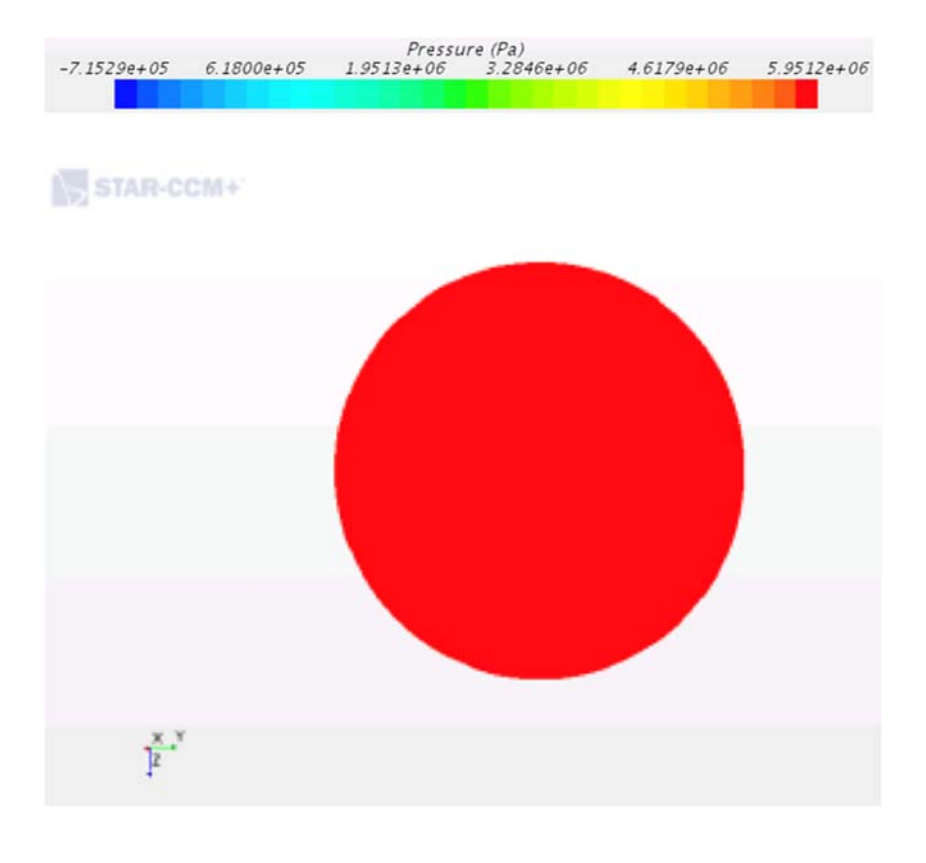


Figure 86 Outlet pressure from CFD pump simulation

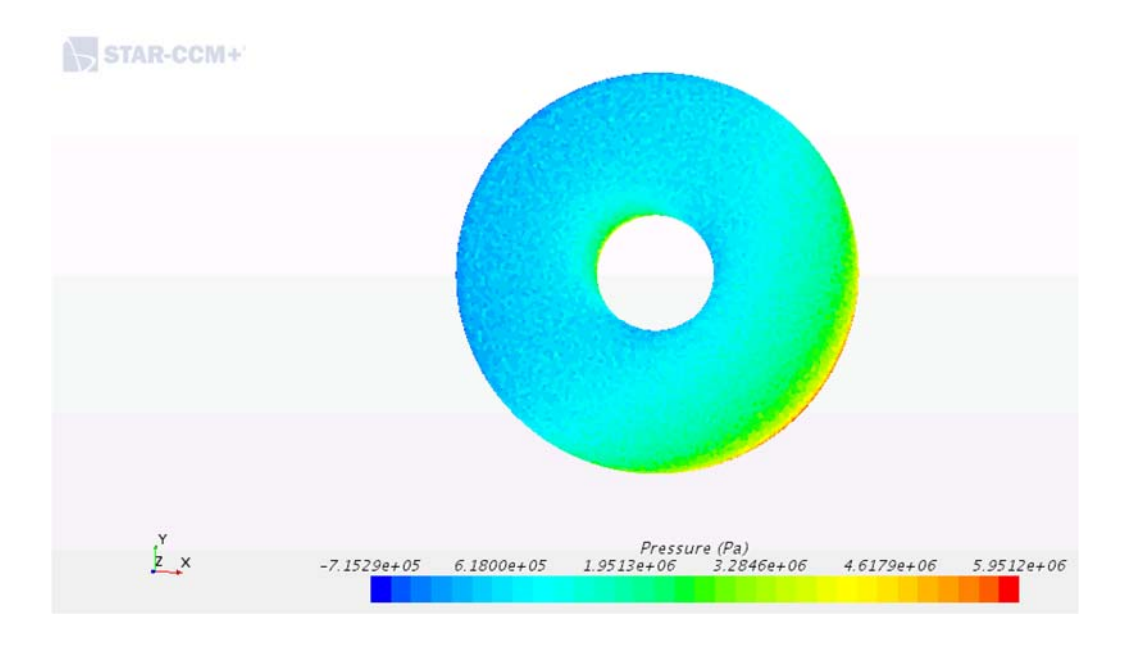


Figure 87 Inlet pressure from the same simulation seen in Figure 86

The pressure rise of the whole stage is calculated as the negative of the pressure drop. This means the lower pressure inlet is subtracted from the higher pressure outlet.

In order to achieve the convergence the simulation was run for 600 iterations. This brought the TKE residuals down to the order of 10<sup>-2</sup>. The residuals were continuing to decrease but at a rate so slowly that the simulation would have become to computationally expensive. The Wall-Y+, seen in Figure 88, was also used to verify the mesh was refined to a sufficient point.



Figure 88 The Wall-Y+ used to quantify the refinement of the mesh

## **8.3.2** Performance Analysis

In order to study how the pump model performs in two-phase condition, an initial pump curve was created for normal operating condition. The pump curve is not as most normal pump curves look (Ft. head vs. Flow Rate) due to the constant flow rate required of the RCIC pump. This means that the variable examined within the model was the variable speed caused by the variable speed of the Terry Turbine. Figure 89 shows the pump curve used as a reference to dictate the effect of two-phase flow induction within the pump. Table 15 shows the results of the simulations to help comparisons as the large y-axis makes comparisons of small changes more difficult.

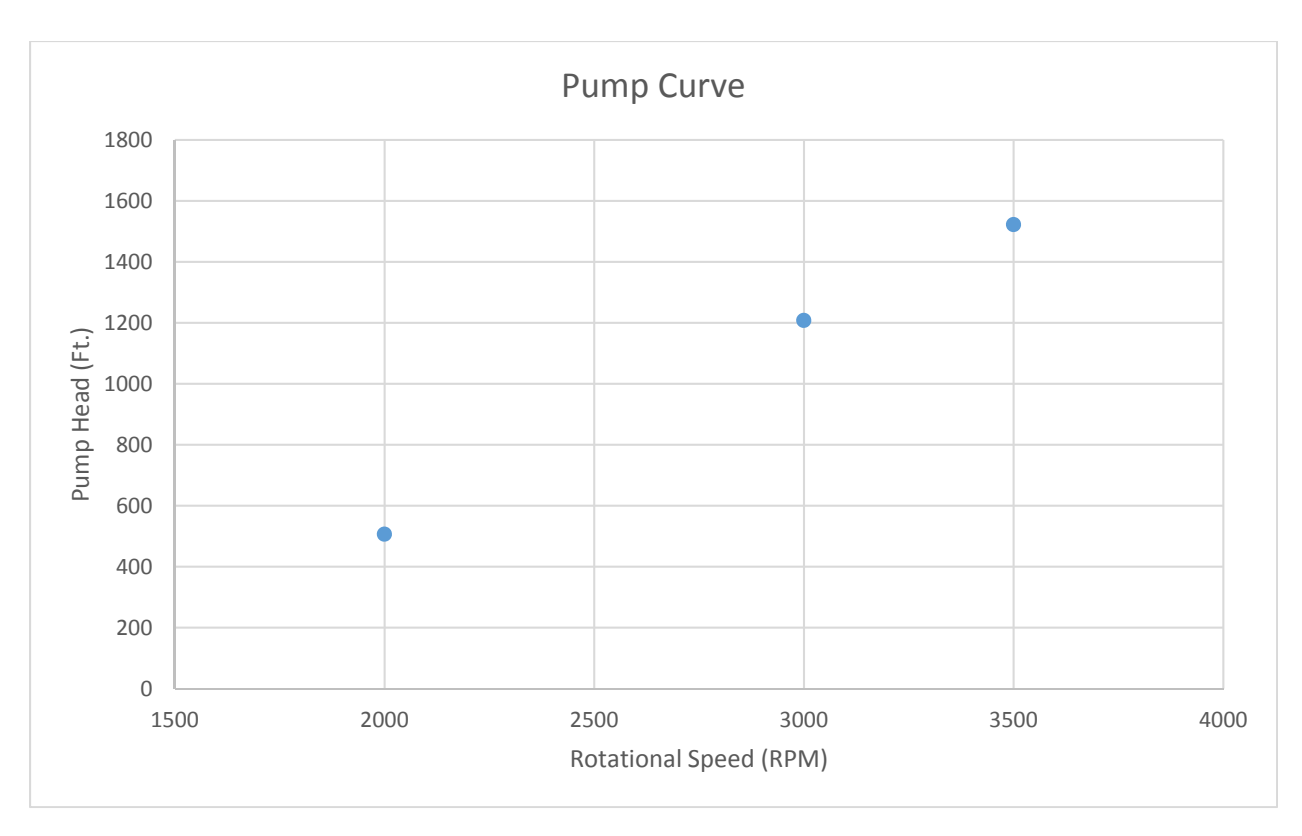


Figure 89 Pump model curve for performance as a function of rotational speed

Table 15 RCIC Pump Model Simulations for the Conditions of 100% Water

RPM	DP	Ft Head
2000	378318	506.27
3000	902656	1207.94
3500	1137562	1522.30

The pump curve seen, displays that the head of the pump increases as the rotational speed increases. This pump curve, initially, looks like a linear increase but if it is closely examined the curve takes more of a power curve. This type of curve means that a greater amount of head is caused by lower variations in rotational speeds at the higher rotational speeds.

Once the standard curve was created and verified to be what was expected out of the model the introduction of two-phase flow was the next step. The first simulation tested was for a pump that had a volume fraction 90% water and 10% steam throughout the entirety of the pump. The pump curve for the simulations containing those conditions can be seen in Figure 90. The exact output of the simulations can also be seen in Table 16.

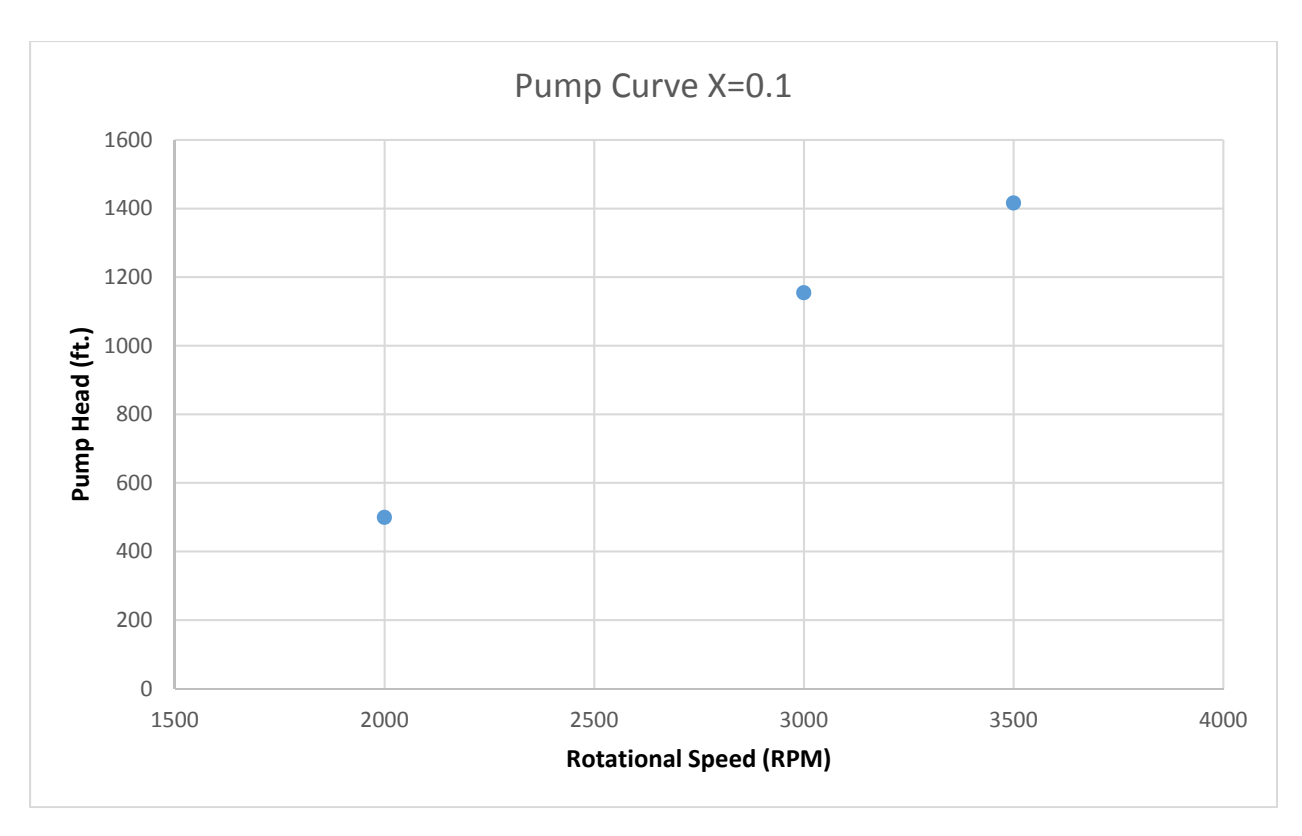


Figure 90 Pump curve for model with 90% water and 10% steam at variable speeds

Table 16 RCIC Pump Model Simulations for 90% Water and 10% Steam

RPM	DP	Ft Head
2000	373128.6	499.32
3000	862463.7	1154.16
3500	1058212.9	1416.11

The differences between Figure 89 and Figure 90 are difficult to see, however, the two tables make the differences more clear. The 2000 RPM simulations don't have a great amount of change as they are only  $\approx$ 7 feet of head difference. The larger the rotational speeds, however, show a larger change in the pump head difference. The largest difference in head is seen at the rated speed of 3500 being 106 feet of head.

The next set of simulations conducted was done with an even greater amount of volume fraction of steam. The set of simulations with the model was operating with a volume fraction 80% water and 20% steam within the pump. The pump curve for these simulations can be seen in Figure 91. The output results of the simulation can be seen in Table 17.

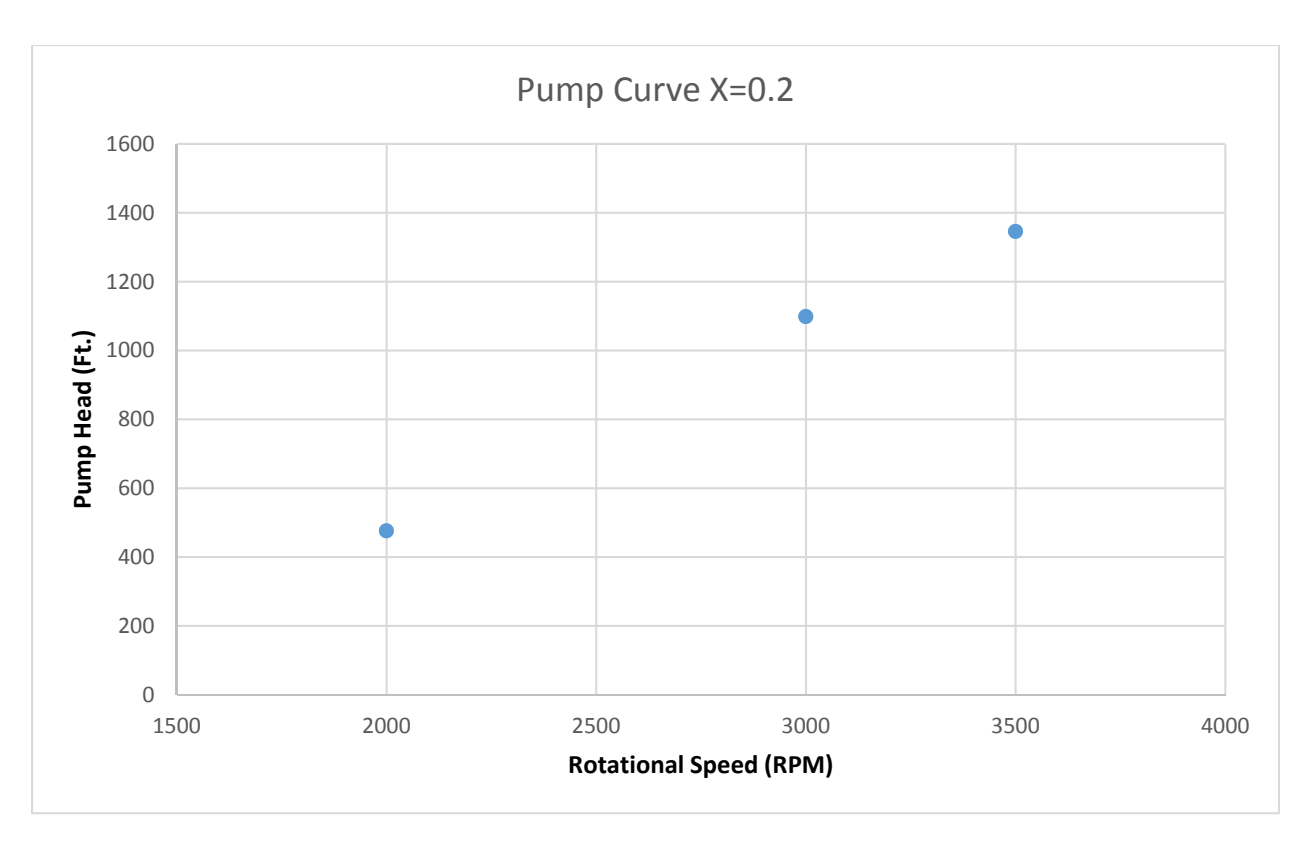


Figure 91 Results from pump model simulations for with 80% water and 20% steam

Table 17 RCIC Pump Model Simulations for 80% Water and 20% Steam

RPM	DP	Ft Head
2000	355594.8	475.86
3000	820628.6	1098.17
3500	1005490.6	1345.56

The simulations with volume fractions of 80% water and 20% steam reflect similar results to that of the simulations with 90% water and 10% steam. The differences are within the degradation quantities as the 2000 RPM speed was degraded the least, with approximately 26 feet of head removed over the entire pump. The 3500 RPM simulation saw almost 200 feet of head removed in comparison to the normal operating conditions of the pump. This shows that the trend of the lower RPM simulations saw less degradation of head than that of the higher RPM simulations.

The next set of simulations saw a similar change as the previous, increasing the volume fraction another 10%. These simulations had 70% water and 30% steam volume fraction throughout the pump. The pump curve of the simulations can be seen in Figure 92. The results of the output of these simulations are contained in Table 18.

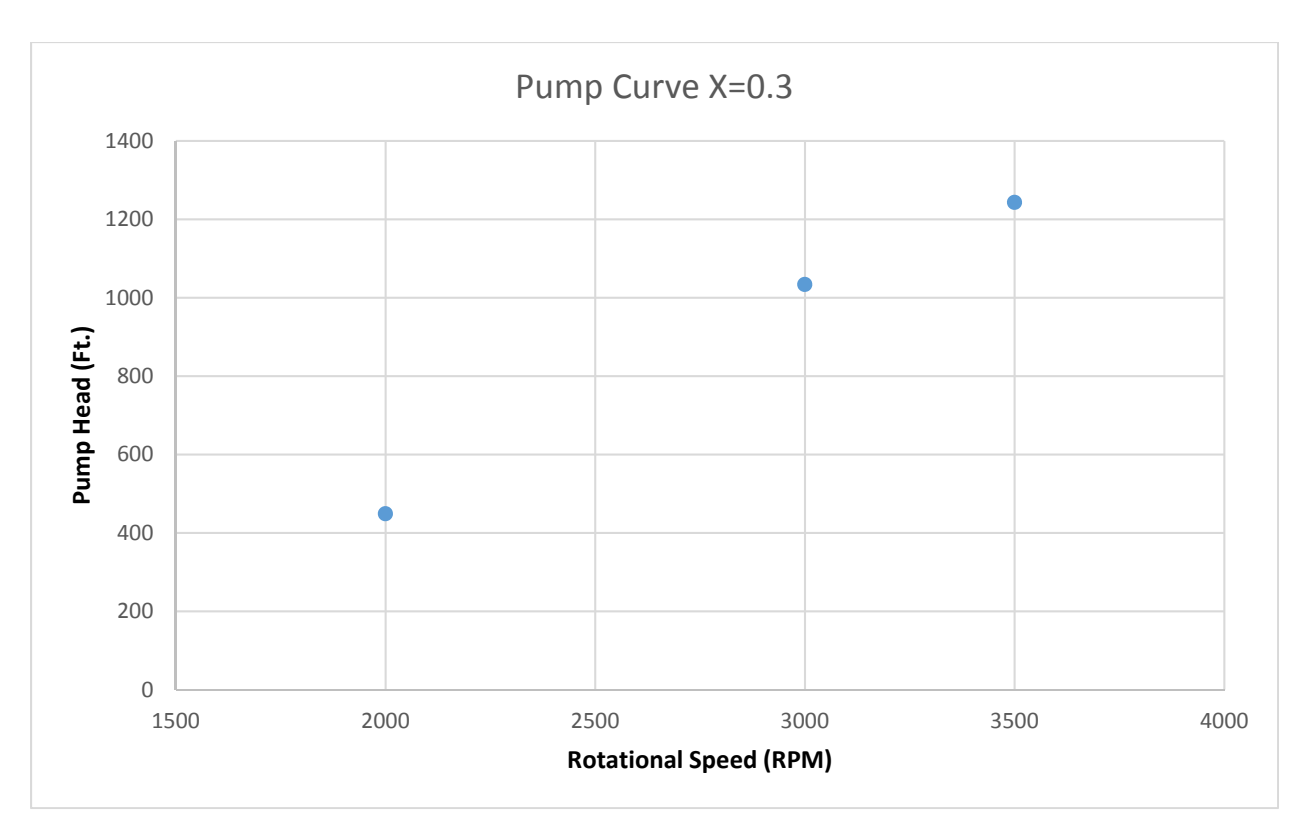


Figure 92 Pump curve for model with 70% water and 30% steam

Table 18 RCIC Pump Model Simulations for 70% Water and 30% Steam

RPM	DP	Ft. Head
2000	335296.7739	448.70
3000	772475.846	1033.74
3500	928853.94	1243.00

The results of the 70% water and 30% steam volume fraction tests display that the results follow that of the previous simulations. The greater RPM simulations display a greater degradation of head. This of course is skewed by the fact that the overall head produced by the pump is greater so one would expect a greater decrease in head. Figure 93 shows all of the pump curves created in this Thesis overlaid into one chart.

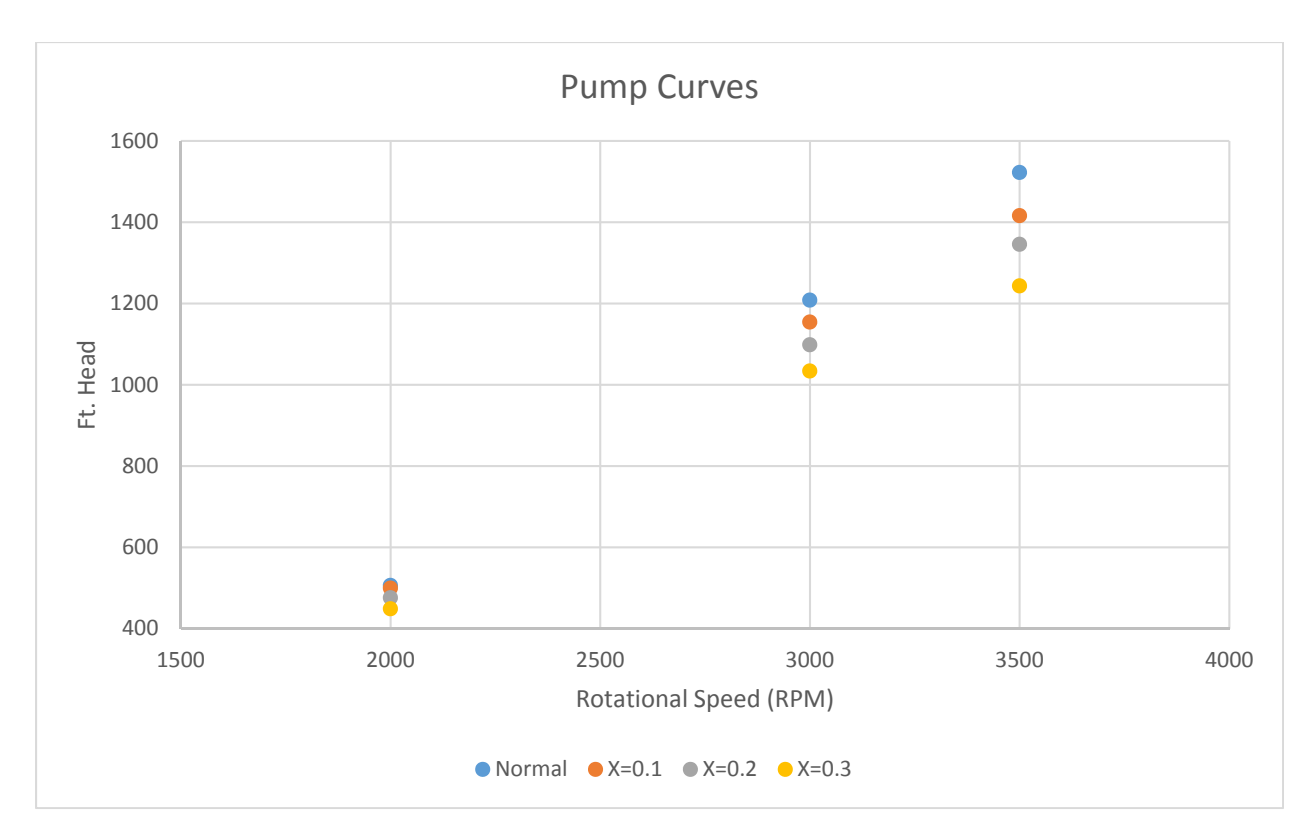


Figure 93 All pump curves compared in a single figure

The difference in pump performance is greatest at the highest rated speed of the pump model. The difference in performance is the least at the lowest rated speed of the pump. The increasing volume fraction causes increased divergence from each pump curve as the pump rotational speed increases. The 10% steam and 20% steam simulations acted similarly in pump head throughout. The 30% steam saw the greatest drop off from performance as one would expect.

#### **8.3.3 Normalized Performance**

As previously discussed, the results of degradation are skewed to the higher RPM simulations due to the increased head at those speeds. In an attempt to combat this a normalization of the head was used to display the results as a percent decrease. Equation (202) displays the way this normalized value was calculated. This allowed for a more direct comparison of how the pump performance was affected by the changing rotational speed. The pressure change was compared for the same rotational rate on the single phase flow to the two-phase flow. Figure 94 displays the normalized performance of the pump model under the volume fraction of 90% water and 10% steam.

$$\varphi = \frac{DP_{TP flow}}{DP_{SP Flow}} \tag{202}$$

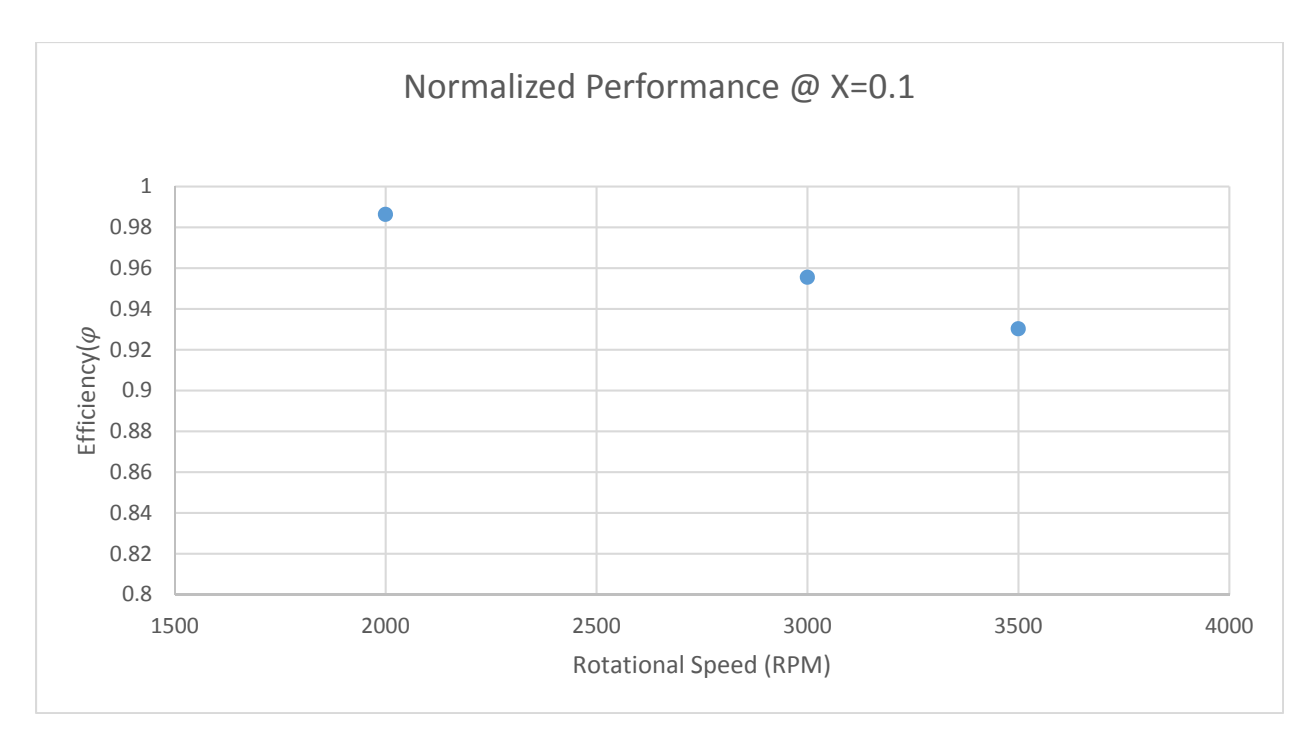


Figure 94 Pump normalized pressure increase for 90% water and 10% steam

The volume fraction of the steam can be seen as immediately impacting the performance of the pump, even at a low volume percentage. At the rated speed the two-phase flow degrades the pump performance by 7% of the optimal value in the model. The 3000 RPM head is degraded by just over 5%. This is the rated speed of the Z1 terry turbine used in Luthman [2017]. The pump performance degrades just less than 2% at the lowest rated speed of the RCIC pump. This would dictate that should the terry turbine powering the pump fail prior to the failure of the pump the performance would not be greatly degraded at this volume fraction. The difference in performance at this volume fraction is approximately 6% between the lowest rated speed and the highest rated speed.

Equation (202) was also applied to the volume fraction split of 80% water and 20% steam. The pressure outputs of the simulation at this volume fraction split were compared to the normal performance of the pump model. The results of the equation application can be seen below in Figure 95.

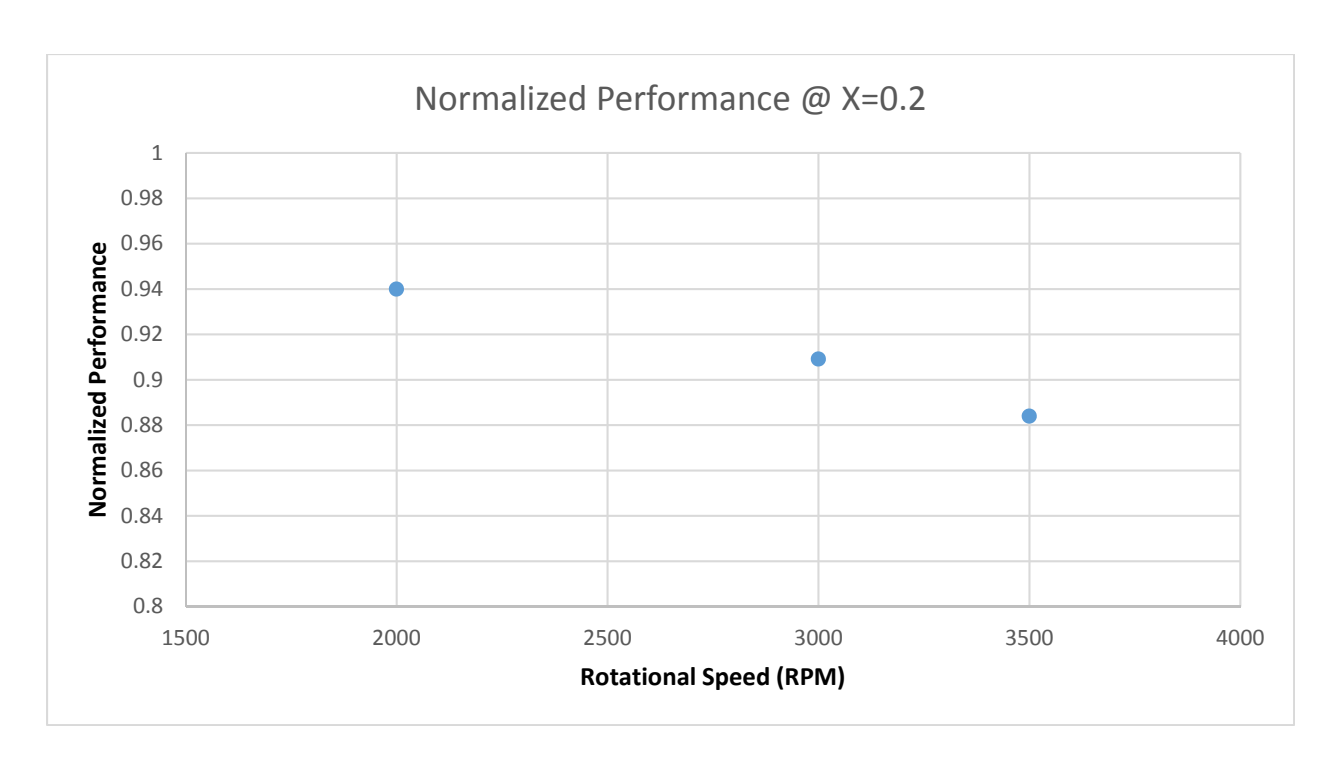


Figure 95 Pump normalized pressure increase for 80% water and 20% steam

Under the conditions of the 20% steam volume fraction, the pump model performance can be degraded over 10% of the rated head. The rated speed of the pump is degraded to almost 12%, with a small head, in relation to most nuclear industry pumps; this can immediately cause major issues. The lowest rated speed of the pump was comparable in percent degradation to the highest rated speed at the 10% volume fraction. The 3000 RPM value was also degraded by approximately 9%. The difference in normalized pressure increase is similar to the drop in normalized pressure increase from 94% down to 88%.

Figure 96 shows the normalized performance Equation (202) as a function of rotational speed with the volume fraction of 70% water and 30% steam.

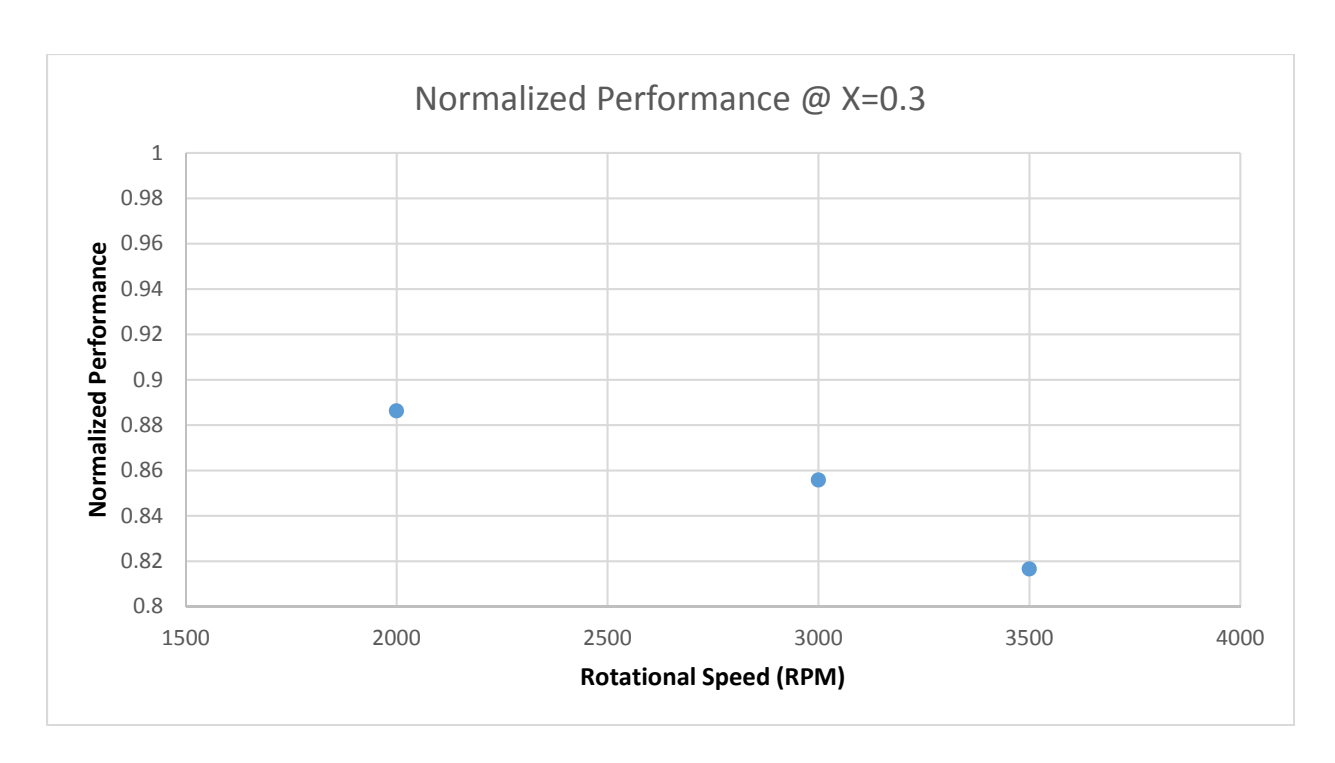


Figure 96 Pump normalized pressure increase for 70% water and 30% steam

The normalized pump performance at the the 30% steam is the lowest in relation to all of the other steam volume percentages. This follows the performance that would be expected; as the volume fraction of steam increases the performance of the pump will decrease. Similarly, to the comparison between the 10% steam and 20% steam the lowest rated speed has a similar performance to the highest rated speed at the 20% steam. The drop-in normalized pressure increase is greater than that of other volume fractions. This is expected as the larger the volume fraction the greater decrease in performance. The optimal performance with the 30% volume fraction steam is 88% at the lowest rated speed of 2000 RPM. The most degraded performance occurs at approximately 82% at the maximum rated speed of 3500 RPM. The net difference in the maximum and minimum performance is 8%. This reduction is rather large for normal operating conditions of the pump. The variation in performance could have catastrophic results.

In an effort to better compare the normalized performance all three volume fractions were plotted together. The plot combining all three together can be seen in Figure 97.

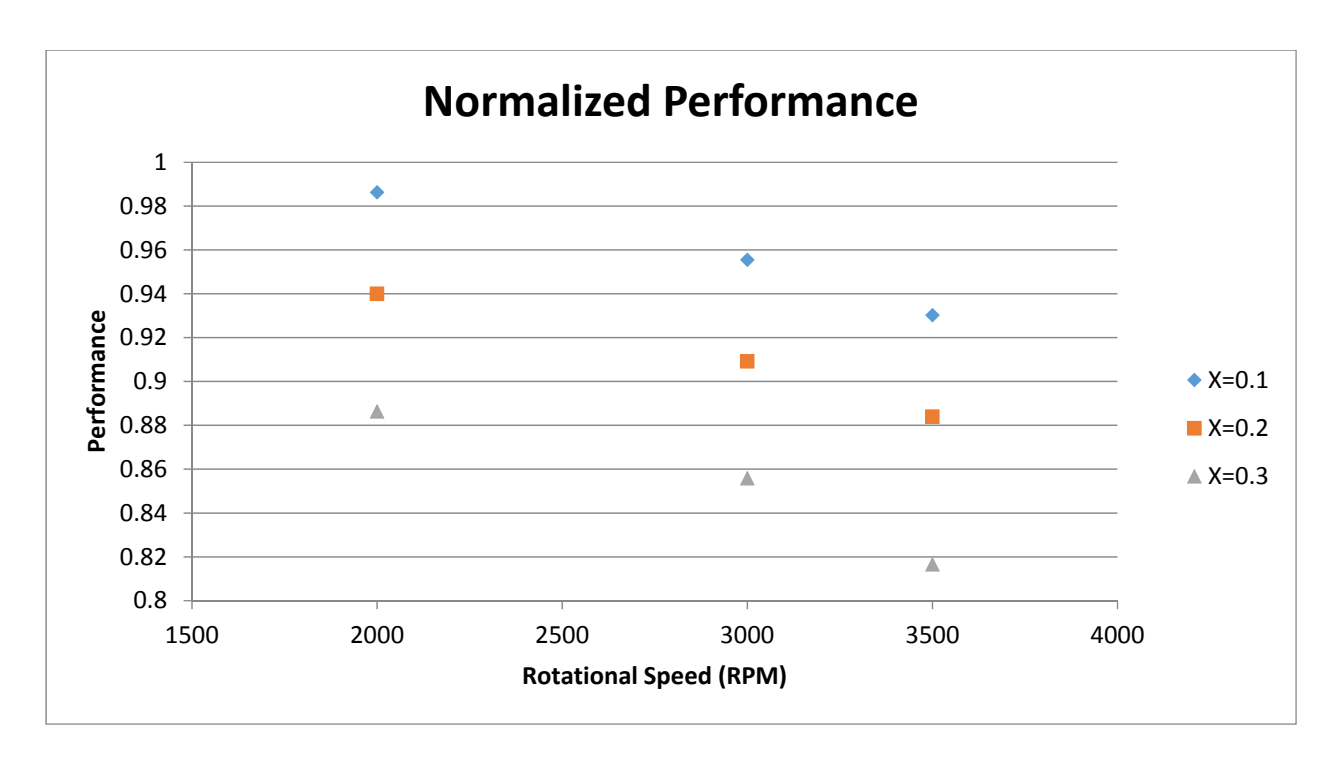


Figure 97 Pump normalized pressure increase for all volume fractions simulated

The first comparison to be made is the greatest drop off in pressure increase at the maximum rated rotation speed for the 30% steam volume fraction. This drop off proves that the larger the volume fraction the greater the pump degradation. The 10% steam has the smallest decrease in pump performance as the net difference in performance is only 6%. The 20% volume fraction steam has a 6.5% difference in performance. The decrease to almost 80% of performance could have catastrophic results. The reduced head could cause the pump head to be reduced to a point low enough that the flow cannot overcome the pressure difference between the pump and the feedwater spargers.

Equation (203) displays the definition of efficiency of pump performance.

$$\eta = \frac{\rho_{avg}gQH}{T\omega} \tag{203}$$

where

 $\rho_{ava}$  is the average density ; g is gravitational constant

Q is the flow rate  $(m^3/s)$ ; H is the pressure increase

T is the torque ;  $\omega$  is the angular speed

While the pump performance will still decrease with varying rotational speed the study also needs to analyze how the pump efficiency will change with void fraction. Figure 98 displays the pump efficiency at the different rotational speeds of the pump. Only two set of data points were included due to the consistency in efficiency over the entire volume fraction models.

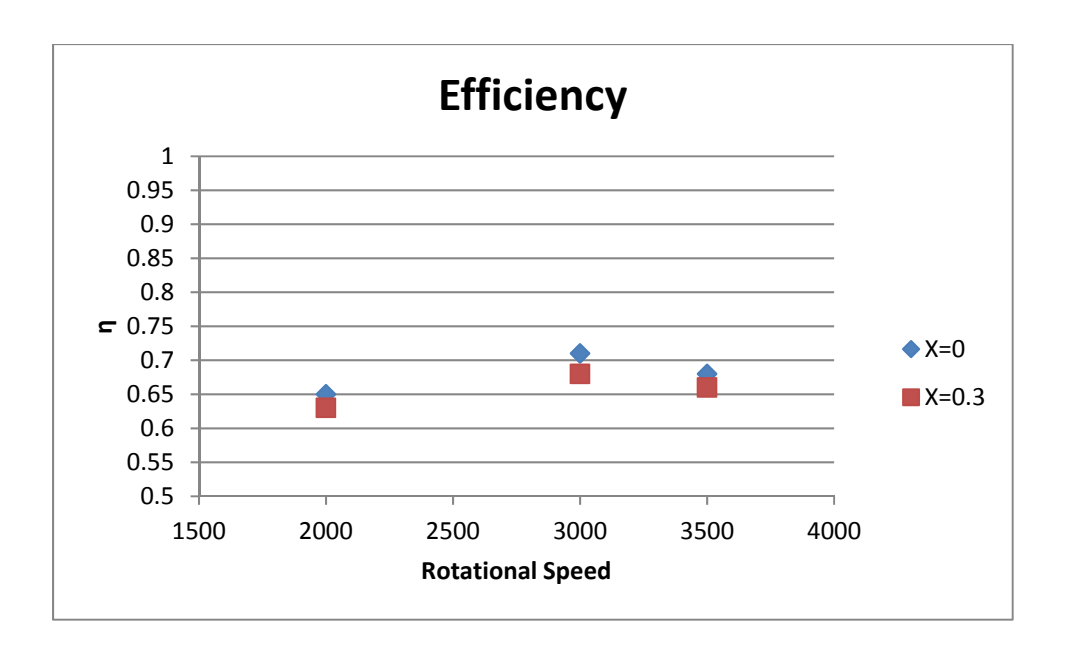


Figure 98 Efficiency curve for pump model at normal operation and 30% water

Figure 98 displays that efficiency of the pump in the simulation didn't vary greatly. This is due to the conservation of the pump affinity laws. The pump affinity laws dictates that efficiency will not appreciably change within the range of normal pump operational speeds. This can be seen as the efficiency doesn't change more than 3% at the maximum difference on the efficiency curve.

# 8.4 Pseudo-Fukushima Reactor Core Isolation Cooling System Benchmark

The MELCOR test problem used to examine the performance of the new Terry turbine systems-level models is a so-called "pseudo-Fukushima" calculation because it models a simplified 2000 MW<sub>th</sub> BWR system that employs boundary conditions (Suppression Chamber pressure) taken from known Fukushima Dai-ichi data points. The problem models decay heat addition to a representative RPV with subsequent water inventory boil-off and RCIC system intervention to replenish lost coolant.

The problem nodalization consists of an RPV and RCIC system piping on both sides of the RCIC system turbo-pump – the driving (turbine-side) loop and the pumping (pump-side) loop. The RCIC system driving loop includes:

- One CV for the RPV or "boiler"
- Two CVs for MSL piping between the boiler and the RCIC turbine
- One CV for RCIC steam line piping
- One CV for the RCIC turbine steam chest
- One CV for the RCIC turbine (i.e. inside the turbine casing)
- One CV for a relief valve sink (relief for MSL)
- Flow paths, 1 per CV pair, connections in the order as listed above

Note that there are no boundary conditions imposed on the driving loop, i.e. the code predicts the evolution of thermal-hydraulic conditions in all CVs of the driving loop. CV sizes and flow path geometry/characteristics are based on best-estimates for typical Fukushima-like BWRs. Note the

RPV CV contains an external source that deposits a volumetric decay heat source into the pool inventory. The pumping loop includes:

- Two property-specified CVs representing the wetwell and/or the CST that essentially impose boundary conditions on the transient
- One CV for the RCIC pump inlet piping
- One CV for the RCIC pump fluid volume
- One CV for the RCIC pump outlet piping
- Flow paths connecting the pump piping CVs to the pump CV, the feedwater boundary condition CV to the pump inlet piping CV, and the pump outlet piping CV to the RPV CV

Figure 99 below contains a diagram illustrating main features of the pseudo-Fukushima input. The overarching goal of the pseudo-Fukushima problem is to replicate key features of the Fukushima-II accident sequence. Ideally, MELCOR will be able to capture the feedback effect between the RPV and the RCIC system under typical SBO conditions.

The problem scenario is an extended SBO with a reactor scram at time zero. The boiler is on the decay heat curve (characteristic of a general 2000 MWth BWR) and receives an according thermal energy input for the duration of the transient. The only safety systems modeled are the RCIC loops and SRV off the MSL. The RCIC system at first runs with power but eventually loses all AC and DC power. RCIC runs uncontrolled thereafter (governor valve not regulating steam admission) with the turbine governor valve full-open. Steam drives the turbine which runs the pump to refill the RPV. Note RCIC pump suction is initially taken from the CST boundary condition CV but later switches over to the wetwell boundary condition CV. In Figure 100 below, boiler pressure curves are shown for:

- 1) Predictions using the fully CF-specified Terry turbine model described in Ross et al., [2015]
- 2) Predictions using the new Terry turbine systems-level models

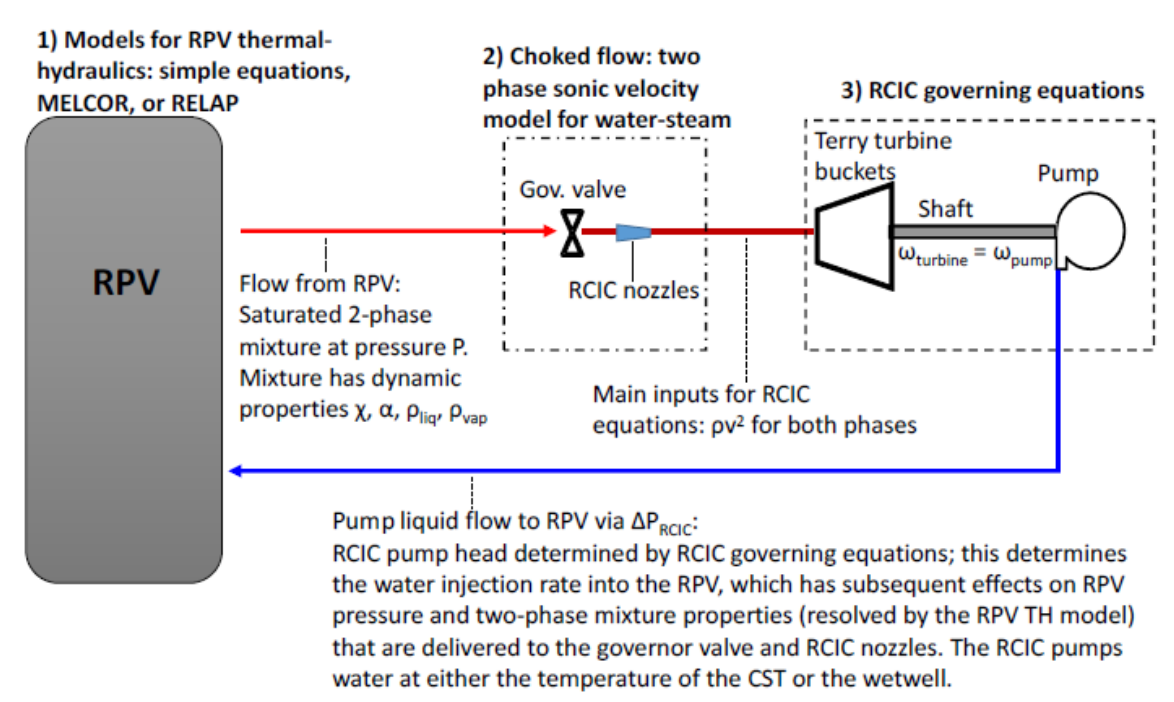


Figure 99 Pseudo-Fukushima RCIC system model diagram

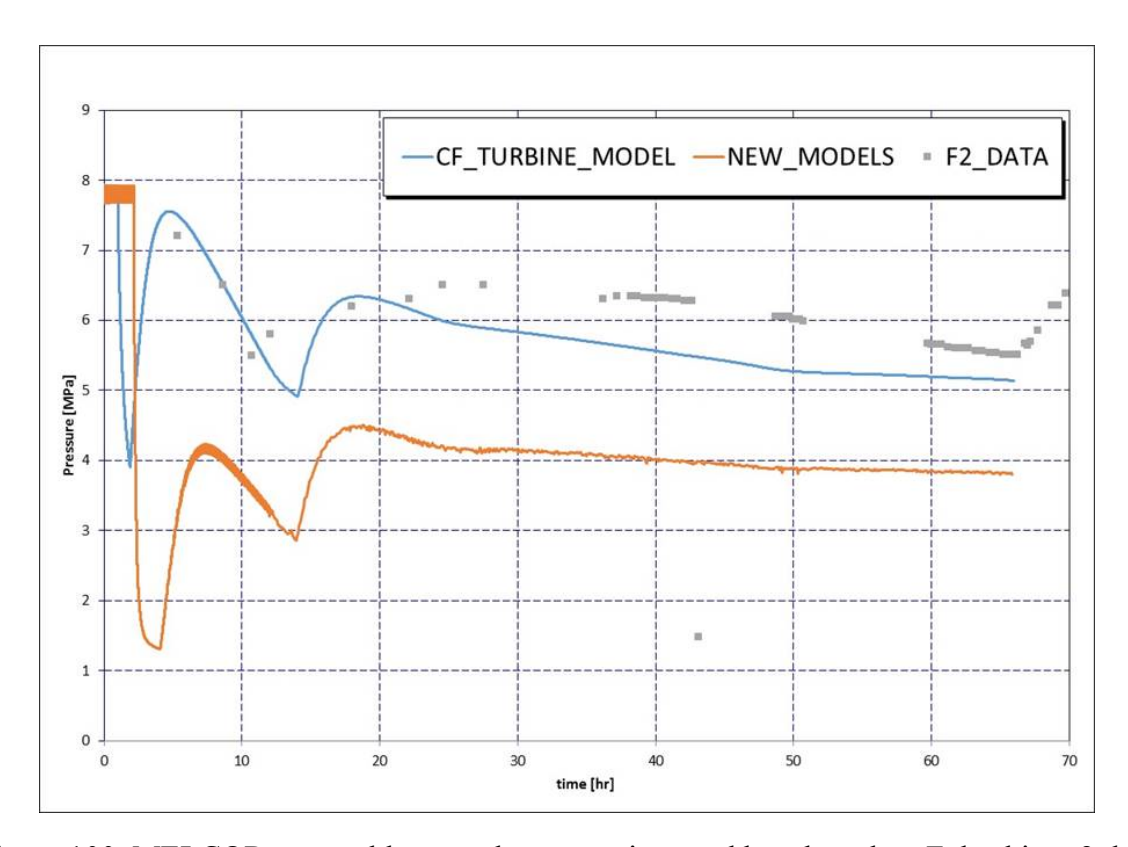


Figure 100 MELCOR test problem results comparison and benchmark to Fukushima-2 data

Figure 100 indicates the progression of the transient from the time of RCIC actuation. At the time when the governor valve goes full-open, both the CF turbine model and the new Terry turbine systems model predict a large pressure drop in the RPV as the RCIC pump – driven by a considerable increase in steam flow through the turbine - delivers a large volume of make-up water. The large up-swings in pressure between 2-5 hr (CF turbine model) and (5-8) hr (new models) correspond to a decrease in make-up coolant delivery from the RCIC system as RPV overfilling occurs. Over-filling leads to water spillover into the RCIC turbine steam lines and an attending degradation in RCIC turbine performance. The RPV remains overfilled from this time on, spilling water into the steam lines continuously. The spill rate and water ingestion rate by the turbine about match the RCIC pump flow rate. Pressure decreases until the point of CST-to-wetwell switchover (about 14 hours problem time). Thereafter, the coolant delivered by the RCIC pump is closer to saturation temperature and more readily boiled by residual heat in the RPV. Thus, pressure comes back up for a time. Ultimately, the wetwell injection catches up with decay heat production and the RCIC system depressurizes the RPV gradually until the problem end time at 66 hr.

Note that both models (the CF turbine and the new model) predict a turbine over-speed (turbine rotor speed exceeds the mechanical trip setpoint) in the seconds following loss of governor valve control. The calculation continued despite this occurrence. The characteristics of both model curves are similar, though the magnitudes of their respective pressure predictions differ. Both curves match the general trends of the recorded Fukushima-2 data, though the new models evidently under-predict both the data and the predictions from the CF turbine model. This could indicate an over-estimation of RCIC system efficiency for the new models because RCIC system action keeps RPV pressure low relative to the data. There are several user inputs to examine for the new Terry turbine models before drawing more definite conclusions. MELCOR

modeling/development is still underway for the pseudo-Fukushima calculation, larger full-plant Fukushima calculations, and the Terry turbine models themselves. Further experimental evidence should allow for further comparisons to data and for refinement of the systems-level models to whatever extent necessary.

# 9. Comparison of Actual Accomplishments with the Project Goals and Objectives

As stated in the main report, the overarching objective of this project was to provide analysis methods for evaluation of the RCIC System performance under severe accident conditions. The objectives of this project were to develop physics-based models of the RCIC System, incorporate them into a multi-phase code and validate the models.

The technical objectives involved integration of models for the key aspects of the RCIC System, some models which were developed anew and others which were adopted from existing techniques. The individual models were validated against experimental data, some of which existed and some of which was generated anew for the turbine model. Finally, the integrated analysis tool was benchmarked against Fukushima Dai-ichi Unit 2 plant data.

All objectives were achieved.

Progress towards these goals and objectives was largely on schedule. Generation of experimental data on the RCIC turbine performance that was of quality for CFD code validation was obtained behind schedule but the validation of CFD models against this data was completed on time.

#### 10. Conclusions

The objectives of this project were to develop physics-based models of the RCIC System, incorporate them into a multi-phase code and validate the models. The technical approach to achieving the project goals was formulated into six technical tasks. Each of these tasks and associated accomplishments are summarized below.

Task 1: Critical evaluation of codes for RCIC System modeling

For system-level modeling, the leading severe accident codes in the US, MAAP and MELCOR, were found to not have any specialized components for RCIC System modeling. However both codes appear to have the capability for models to be incorporated via control functions or other code features. With respect to the RCIC turbine and RCIC pump, the multiphase phenomena expected to occur within the turbine's steam inlet nozzle, the Terry turbine and the pump are complicated and beyond the simulation capabilities of reactor safety codes. Computational Fluid Dynamics (CFD) codes are more appropriate for developing mechanistic models which can be simplified for incorporation into the systems-level codes. Gaps in the current modeling capabilities were identified and approaches were proposed for modeling within the context of CFD codes.

During the second year of the project, a Sandia National Laboratories report was published on system-level MELCOR models for the RCIC System and CFD analysis of the multiphase behavior inside the turbine wheel. This report was evaluated for relevance to the current project.

#### Task 2: Code Selection

For CFD development of the Terry turbine and pump models, the STAR-CCM+ code was selected. The code has sufficient capabilities and user access to enable completion of the turbomachinery model development. Further, the code's methods are similar to those of other commercial codes, such as FLUENT or CFX. Thus any models developed in STAR-CCM+ are likely portable and adaptable to other codes.

During the first year of this project, the conclusion was reached that the CFD models could be simplified directly to the severe accident code level. Simplifying models to the thermal hydraulic code level, as described in the project proposal, and then further to the severe accident level would not bring any significant benefit to the project. Therefore, the decision was made to not develop models specifically for thermal hydraulic codes as originally planned.

MELCOR was chosen as the reference severe accident code for this project. The decision was based on past work to model the RCIC System within MELCOR, code availability and expertise of the investigators with the code.

### Task 3: RCIC System Test Data Survey

Three types of validation data were found for the new models.

- First, several examples of CFD-to-experiment benchmarks for steam nozzle and steam turbine flow were identified. Test problems with the new turbine models were used to validate the models against these data as part of Task 6.
- Second, data for turbine model validation was acquired from the PI's experimental facility during the second and third year of this project. These experimental data were also used to validate the new CFD turbine models as part of Task 6.
- Third, very limited data from the Fukushima Dai-ichi accident are available for benchmarking RCIC System simulations. These data consist of boundary conditions such as Reactor Pressure Vessel water level, system pressures and times of RCIC System operation. These data were used to benchmark system simulations as part of Task 6.

### Task 4: Model Development and Implementation

Phenomenological models for RCIC System analysis were developed under this task. CFD models were developed first for the RCIC System turbine and pump, followed by models for systems-level severe accident codes.

For the CFD Terry turbine model development and implementation, several formulations were investigated in year 1 and, a quasi-two-fluid dispersed phase flow model was developed for implementation into STAR-CCM+. A condensing steam flow physics model was developed and successfully applied on a typical GS-1 Terry turbine pressure stage (steam nozzle) geometry with STAR-CCM+

Regarding the CFD RCIC pump modeling, after extensive searches, proprietary RCIC pump diagrams were obtained that allowed for creation of a Solidworks model followed by a Computer Aided Design (CAD) model that is needed for CFD model development. A CFD model for a single-stage pump was created. This will serve as the starting point for generation of the more complicated multi-stage CFD model that can represent the RCIC pump.

On the system-level modeling with MELCOR, a homologous pump model was developed, coded and integrated into an up-to-date version of MELCOR, as was a systems-level steam nozzle (pressure stage) model based loosely on known analytical Wilson point solutions found in literature. Also, a turbo-shaft model (a torque inertia equation representing the shaft of a turbo-pump) was derived and implemented. To incorporate the pressure stage model into the existing MELCOR phasic velocity equation solution methodology, the time-independent flow path velocity function was co-opted by adding a special flag to the existing input structures. To couple the velocity stage model and the turbo-shaft torque-inertia equation with the semi-implicit homologous pump model, some alterations were made to input structures and the format of the subroutine that handles pump calculations.

### Task 5: Experimental Data Generation

The RCIC System facility in the Texas A&M University PI's laboratory was used to generate validation data for the models developed herein. The facility includes a steam generator, a suppression chamber, a very simple RCIC turbine analog, a RCIC pump and associated piping. Options were explored for installing a suitable RCIC turbine analog and for acquiring a smaller-scale ZS-1 Terry turbine for incorporation into the Texas A&M University RCIC System facility. The latter option proved to be feasible and more likely to generate data representative of RCIC System behavior.

In the first year of the project, a ZS-1 turbine was acquired. In the second year of the project, the turbine refurbishment was completed and the turbine was installed. It was set up in a once-through configuration, so that the exiting gases were not exhausted to the suppression pool. Instrumentation was upgraded to measure turbine performance, and the necessary structural modifications were applied to provide support to the turbine and its associated piping and equipment. The facility was equipped to inject compressed air or steam, along with a water component, into the inlet of the turbine. The turbine shaft work was measured by a water brake dynamometer.

Dry and wet mixes of air and of steam from 60 g/s to 0 g/s were injected into the turbine down to the lower limit of operability. Torque, shaft work, and isentropic efficiency were obtained for 1500, 2000, 2500, and 3000 shaft revolutions per minute (RPM).

#### Task 6: Benchmarking against Fukushima data and test data

The limited data available from the Fukushima Dai-ichi accidents were reviewed and evaluated for utilization in the benchmarking effort. The MELCOR test problem used to examine the

performance of the new Terry turbine systems-level models is a so-called "pseudo-Fukushima" calculation because it models a simplified 2000 MW<sub>th</sub> BWR system that employs boundary conditions (Suppression Chamber pressure) taken from known Fukushima Dai-ichi data points.

The new model predicts a turbine over-speed (turbine rotor speed exceeds the mechanical trip setpoint) in the seconds following loss of governor valve control. The calculation continued despite this occurrence. The predicted pressure curve match the general trends of the recorded Fukushima-2 data, though the new models evidently under-predict the data. This could indicate an overestimation of RCIC system efficiency for the new models because RCIC system action keeps RPV pressure low relative to the data. There are several user inputs to examine for the new Terry turbine models before drawing more definite conclusions.

Development and validation of these RCIC System models is an important advancement with respect to both enhanced reactor safety and the state-of-the-art of severe accident modeling. Major outcomes of the project were:

- Increased knowledge of the RCIC System operational characteristics under accident conditions
- Technically-defensible models of the RCIC System

# 11. Summary of Project Activities

The project activities have been summarized in the Executive Summary and Conclusions sections.

Two departures from planned methodologies occurred:

- Development of RCIC models for thermal hydraulics codes was determined to be unnecessary and therefore was not pursued. (See the Task 2 write-up for details.) The result was time and effort savings that was invested in the CFD and systems-level modeling efforts.
- A RCIC turbine analog was expected to be designed and manufactured. However acquisition of a small-scale model ZS-1 turbine proved to be a better option and this path was followed to generate experimental data for code validation. Use of an actual Terry turbine resulted in data that was more representative of data that could have been produce from an in-house manufactured turbine analog.

### 12. References

- Avetissian, A. R., G. A. Philippov and L. I. Zaichik, "Effects of Turbulence and Inlet Moisture on Two-Phase Spontaneously Condensing Flows in Transonic Nozzles," *International Journal of Heat and Mass Transfer*, vol. 51, pp. 4195-4203, 2008.
- Badger Meter, M-Series M2000 Electromagnetic Flow Meter User Manual, 2016.
- Bakhtar, Ryley, Tubman, Young, "Nucleation Studies in Flowing High Pressure Steam", Proc. of *Instn Mech Engrs*, Vol 189, 1977.
- Bakhtar, F. and M. Piran, "Thermodynamic Properties of Supercooled Steam," *Int J Heat & Fluid Flow*, vol. 1, no. 2, pp. 53-62, 1979.
- Bakhtar, F., J. B. Young, A. J. White and D. A. Simpson, "Classical Nucleation Theory and its Application to Condensing Steam Flow Calculations," *Proceedings of the Institution of Mechanical Engineers, Part C: Journal of Mechanical Engineering Science*, vol. 219, pp. 1315-1333, 2005.
- Beeny, B. A., <u>Computational Multiphase Fluid Dynamics Analyses and Systems-Level Model Development for a Reactor Core Isolation Cooling System Terry Turbine</u>, Ph.D. Dissertation, Department of Nuclear Engineering, Texas A&M University, College Station, 2017.
- Bevington, P. R. and Robinson, D. K., <u>Data Reduction and Error Analysis for the Physical Science</u>, 3rd ed. McGraw-Hill, Boston, MA: 2003.
- Bradshaw, P., <u>An Introduction to Turbulence and Its Measurement</u>, New York: Pergamon Press, 1971.
- Campbell, Bakhtar, "Condensation phenomena in high speed flow of steam", *Proc. of Instn Mech Engrs*, Vol 185, 1970.
- CD ADAPCO, STAR-CCM+ v10.06 Users' Guide, 2016a.
- CD ADAPCO, "STAR-CCM+ Theory Guide, CD ADAPCO, 2016b.
- Cengel, Y. and M. Boles, <u>Thermodynamics: An Engineering Approach</u>, 6th edition, New York: McGraw-Hill, 2008.
- Courtney, W. G., "Remarks on Homogeneous Nucleation," *J Chem Phys*, vol. 35, pp. 2249-2250, 1961.
- Crowe, C., J. Schwarzkopf, M. Sommerfeld and Y. Tsuji, Multiphase Flows with Droplets and Particles, 2nd Edition, Boca Raton: CRC Press, 2012. Dykas, Wroblewski, "Numerical modeling of steam condensing flow in low and high pressure nozzles" *International Journal of Heat and Mass Transfer*, Vol 55, 2012.
- Ding, Wang and Zhao, "An Analytical Method for Wilson Point in Nozzle Flow with Homogeneous Nucleating," *International Journal of Heat and Mass Transfer*, vol. 73, pp. 586-594, 2013.
- Dobbins, R. A., "A Theory of the Wilson Line for Steam at Low Pressures," *Transactions of the ASME* Vol 105, pp. 414-422, December 1983.

- Dykas, Wroblewski. "Numerical Modeling of Steam Condensing Flow in Low and High Pressure Nozzles", *International Journal of Heat and Mass Transfer*, vol. 55, pp. 6191-6199, 2012
- Electric Power Research Institute (EPRI), <u>Terry Turbine Maintenance Guide, RCIC Application</u>, 2012 Technical Report, 2012.
- Foxboro. Instruction Book 3477: 83 F-A and 83W-A Vortex Flowmeters-Analog/Pulse. 2000.
- Gauntt, R. O., et al., <u>Fukushima Daiichi Accident Study (Status as of April 2012)</u>, Sandia National Laboratories, SAND2012-0173, July 2012.
- General Electric Co., "GE BWR\_4 Technology, General Electric Systems Technology Manual, Chapter 2.7, Reactor Core Isolation Cooling System", http://pbadupws.nrc.gov/docs/ML1125/ML11258A311.pdf, last accessed on Nov. 25, 2013.
- General Electric Co., "Boiling Water Reactor, GE BWR/4 Technology Advanced Manual, Chapter 6.0, BWR Differences", http://pbadupws.nrc.gov/docs/ML0230/ML023010606.pdf, last accessed on Dec. 28, 2015.
- Gerber, Kermani, "A Pressure Based Eulerian-Eulerian Multi-Phase Model for Non-equilibrium Condensation in Transonic Steam Flow", *International Journal of Heat and Mass Transfer*, Vol 47, 2004.
- Gerber, "Two-Phase Eulerian-Lagrangian Model for Nucleating Steam Flow", *Journal of Fluids Engineering*, Vol 124, 2002.
- Giordano, M.and P. Cinnella, "Numerical Method for Wet Steam Flows wth Polydispersed Droplet Spectra," American Institute of Aeronautics and Astronautics, Lecce, Italy, 2008.
- Goudie, W., <u>Steam Turbines: A Textbook for Engineering Students</u>, Longmans, Green, and Co, London, 1917.
- Gyarmathy, A., chapter in <u>Two-Phase Steam Flow in Turbines and Separators</u>, edited by M. J. Moore and C. H. Sieverding, Washington: Hemisphere Publishing Company, 1976.
- Gyarmathy, A., "Nucleation of Steam in High Pressure Nozzle Experiments", *Proc. of IMechE Vol. 219 Part A: Power and Energy*, pp. 511-521, 2005.
- Hasril Hasini, M. Z. Y., and A. M. Norhazwani, "Numerical Modeling of Wet Steam Flow in Steam Turbine Channel," Centre for Advanced Computational Engineering, Malaysia, 2012.
- Hill, P. G. "Condensation of Water Vapor During Supersonic Expansion in Nozzles," *J Fluid Mech*, vol. 25, no. 3, pp. 593-620, 1966.
- Idaho National Laboratories (INL), "RELAP5-3D Code Manual Volume II: User's Guide and Input Requirements," INEEL-EXT-98-00834 rev 2.4 p 2-44 2-57, 2005.
- International Association for the Properties of Water and Steam (IAPWS), "Revised Release on the IAPWS Industrial Formulation 1997 for the Thermodynamic Properties of Water and Steam," 2007.

- International Association for the Properties of Water and Steam (IAPWS), "Release on the IAPWS Formulation 2011 for the Thermal Conductivity of Ordinary Water Substance," Plzen, Czech Republic, 2011.
- International Association for the Properties of Water and Steam (IAPWS), "Release on the IAPWS Formulation 2008 for the Viscosity of Ordinary Water Substance," Berlin, Germany, 2008.
- International Association for the Properties of Water and Steam (IAPWS), "Revised Release on Surface Tension of Ordinary Water Substance," 2014.
- Kantrowitz, A., "Nucleation in Very Rapid Vapor Expansion," *J Chem Phys*, vol. 19, pp. 1097-1100, 1951.
- Kazimi, M., and N. Todreas, <u>Nuclear Systems II: Elements of Thermal Hydraulic Design</u>, Taylor and Francis, 2001.
- Knoll, G. F., <u>Radiation Detection and Measurement</u>, edited by Jennifer Welter, Debra Matteson, Elaine S. Chew and Tom Kulesa, 4th ed. John Wiley & Sons, Inc., Hoboken, NJ: 2010.
- Lahssuny and Jedral, "Universal Correlations for Predicting Complete Pump Performance Characteristics," 2004.
- Lane, J. W., L. E. Hochreiter, "Performance Assessment of the Two-Phase Pump Degradation Model in the RELAP5-3D Transient Safety Analysis Code", *Nuclear Technology*, Vol. 161, pp. 277-285, 2008.
- Lee, S., Y. S. Bang, and H. J. Kim, "Prediction of Reactor Coolant Pump Performance Under Two-Phase Flow Conditions", *Journal of the Korean Nuclear Society*, Vol. 26, No. 2, pp. 179-189, 1994.
- Leland, W., Steam Turbines, American School of Correspondence, Chicago, 1910.
- Leland, W. S., <u>Steam Turbines</u>, American Technical Society, Chicago, IL, 1917.
- Luthman Jr., N. G., <u>Evaluation of Impulse Turbine Performance Under Wet Steam Conditions</u>, Master's Thesis, Department of Nuclear Engineering, Texas A&M University, College Station, 2017.
- Luxat, D. L., J. R. Gabor, R. M. Wachowiak, R. L. Yang, "EPRI MAAP5 Fukushima Daiichi Analysis", *Proc. of 16th International Topical Meeting on Nuclear Reactor Thermal Hydraulics (NURETH-16)*, Chicago, IL, pp. 7071-7086, Aug. 30-Sept. 4, 2015.
- Ma, Q.-F., D.-P. Hu, J.-Z. Jiang and Z.-H. Qiu, "A Turbulent Eulerian Multi-Fluid Model for Homogeneous Nucleation of Water Vapour in Transonic Flow," Internation Journal of Computational Fluid Dynamics, vol. 23, no. 3, pp. 221-231, 2009.
- McDonald, J., "Homogeneous Nucleation of Vapor Condensation I: Therodynamic Aspects," Institute of Atmospheric Physics, University of Arizona, Tucson, 1962a.
- McDonald, J., "Homogeneous Nucleation of Vapor Condensation II: Kinetic Aspects," Institute of Atmosperic Physics, University of Arizon, Tucson, 1962b.
- Mikofski, M., "MathWorks," 18 March 2012. [Online]. Available: https://www.mathworks.com/matlabcentral/fileexchange/35710-iapws-if97-functional-

- form-with-no-slip?requestedDomain=www.mathworks.com. (last accessed January 10, 2017).
- Mohsin, R., Z. Abdul Majid, Z. Yacob and S. Ashraf, "Water Condensation in Low Pressure Steam Turbine: A Nucleation Theory Part I," *Journal of Chemical and Natural Resources Engineering*, vol. 2, no. 5, pp. 40-49, 2008.
- Moyer, J.A., <u>Steam Turbines: A Practical and Theoretical Treatise for Engineers and Students</u>, John Wiley & Sons, New York, 1917.
- Narabayashi, T., "Centrifugal Pump Behavior in Steady and Transient Two-Phase Flow," *Journal of Nuclear Science and Technology*, vol. 23, no. 2, pp. 136-150, 1986.
- Olson, <u>Single and Two-Phase Performance Characteristics of the Mod-1 Semiscale Pump Under Steady State and Transient Fluid Conditions</u>, ANCR-1165, 1974.
- Omega, <u>Revised Thermocouple Reference Tables</u>, <u>TYPE T Reference Tables N.I.S.T.</u> Monograph 175 Revised to ITS-90.
- Press, Teukolsky, Vetterling and Flannery, <u>Numerical Recipes in FORTRAN 77: The Art of Scientific Computing</u> 2nd Edition, Cambridge University Press, 1986.
- Reeder, Loft System and Test Description, NUREG/CR-0247, 1978.
- Ross, K. W., et al., <u>Interim MELCOR Simulation of the Fukushima Daiichi Unit 2 Accident Reactor Core Isolation Cooling Operation</u>, SAND2013-9956, Sandia National Laboratories, Nov. 2013.
- Ross, K. W., J. Cardoni, C. Wilson, C. Morrow, D. Osborn and R. Gauntt, <u>Modeling of the Reactor Core Isolation Cooling Response to Beyond Design Basis Operations Phase 1</u>, SAND2015-10662, Sandia National Laboratories, Dec. 2015.
- Sandia National Laboratories (SNL), MELCOR Workshop Presentation, "In Proceedings from the MELCOR Workshop," hosted by U.S. Nuclear Regulatory Commission, Bethesda, 2009.
- Sandia National Laboratories (SNL), <u>MELCOR Computer Code Manuals Vol 1: Primer and Users' Guide, Version 2.1. NUREG/CR-6119</u>," Sandia National Laboratories. 2016a.
- Sandia National Laboratories (SNL), <u>MELCOR Computer Code Manuals Vol 2: Reference Manual, Version 2.1. NUREG/CR-6119</u>," Sandia National Laboratories. 2016b.
- Sawford, B. L., "Reynolds Number Effects in Lagrangina Stochastic Models of Turbulent Dispersion," Phys Fluids, vol. 3, no. 6, pp. 1577-1586, 1991.
- Shames, I. H., Mechanics of Fluids, New York: McGraw Hill Inc, 1982.
- Solom, M., K. Vierow and A. Nosek, "Experimental Investigation of Thermal Hydraulic Limits of BWR RCIC System Operation Under Long-Term Operation", *Proc. of 16th International Topical Meeting on Nuclear Reactor Thermal Hydraulics (NURETH-16)*, Chicago, IL, Aug. 30-Sept. 4, 2015.
- Solom, M., <u>Experimental Study on Suppression Chamber Thermal-Hydraulic Behavior for Long-Term Reactor Core Isolation Cooling System Operation</u>, Ph.D. dissertation, Texas A&M University, Department of Nuclear Engineering, 2016.

- Solom, M., K. Vierow Kirkland, "Experimental investigation of BWR Suppression Pool stratification during RCIC system operation", *Nuclear Engineering and Design*, Vol. 310, pp. 564–569, 2016.
- Strater, Z., <u>Reactor Core Isolation Cooling Pump Performance in Multiphase Conditions</u>, Master's Thesis, Department of Nuclear Engineering, Texas A&M University, College Station, 2017.
- Sulzer, "MSD/MSD2 Axially Split Multistage Pump Brochure," personal correspondence with Sulzer, 2014.
- Tennekes, H., and J. L. Lumley, <u>A First Course in Turbulence</u>, Cambridge: MIT Press, 1972.
- Tokyo Electric Power Company (TEPCO), <u>Evaluation of the situation of cores and containment vessels of Fukushima Daiichi Nuclear Power Station Units-1 to 3 and examination into unsolved issues in the accident progression, Progress Report No. 1, Dec. 13, 2013. http://www.tepco.co.jp/en/press/corp-com/release/betu13\_e/images/131213e0101.pdf, last accessed Dec. 13, 2017.</u>
- Vierow, K., M. Solom and A. Nosek, "Scaling of a RCIC System Experimental Facility," *Proc. of 2015 Japan-U.S. Seminar on Two-Phase Flow Dynamics*, West Lafayette, IN, USA, May 10-15, 2015.
- Wallis, G. B., One-Dimensional Two-Phase Flow, New York, McGraw-Hill Inc, 1969.
- White, A. J., and J. B. Young, "Time-Marching Method for the Prediction of Two-Dimensional, Unsteady Flows of Condensing Steam," *Journal of Propulsion and Power*, vol. 9, no. 4, pp. 579-587, 1993.
- Wilcox, D., <u>Turbulence Modeling for CFD</u>, La Canada: DCW Industries, Inc, 1994.
- Wynne, N. A, <u>Flooding Experiments with Steam/Water and Air/Water at Elevated Pressure in a Large Diameter Vertical Tube</u>, Master's Thesis, Texas A&M University, College Station, TX: 2015.
- Yamatake Corporation, <u>MagneW 3000 PLUS Smart Electromagnetic Flowmeter Detector Model MGG18/19, MGS18, User's Manual, CM2-MGG200-2001</u> (Rev. 4). 2004.
- Young, J. B., "The Spontaneous Condensation of Steam in Supersonic Nozzles," *PhysicoChem Hydrodyn*, vol. 3, pp. 57-82, 1982.
- Zhao, Z. O., "Development and Implementation of Mechanistic Terry Turbine Models in RELAP-7 to Simulate RCIC Normal Operating Conditions," Idaho National Laboratories, Idaho Falls, 2016.
- Zori, L. and F. Kelecy, "Wet Steam Flow Modeling in a General CFD Flow Solver," in *Proc. of 35th AIAA Fluid Dynamics Conference and Exhibit*, Toronto, 2005.

# 13. Cost Status

Table 19 Funding Expenditure Summary

	Tuest 19 Tuning Emperiation Summary								
Phase/Budget Period			DOE	Cost	Total	DOE	Cost	Total	
			Amount	Share		Amount	Share		
			Approved Spending Plan for			Actual Spent to Date by			
			TAMU			ŤAMU			
	From	To							
Year 1	Oct. 1,	Sept. 30,	167,346	0	167,346	79,982	0	79,982	
	2014	2015							
Year 2	Oct. 1,	Sept. 30.	168,005	0	168,005	230,674	0	230,674	
	2015	2016				·			
Year 3	Oct. 1,	Sept. 30.	148,634	0	148,634	153,012	0	153,012	
	2016	2017				,		•	
Actual Totals			483,984	0	483,984	463,236	0	463,236	

# 14. Schedule Status

Table 20 shows a complete list of project milestones, anticipated completion dates and actual completion dates. This table is in accordance with the timetable submitted with the project proposal and the Milestones/Activities schedule on PICS:NE.

Table 20 Project Milestones

Table 20 Floject Whiestones								
Task / Milestone Description	Anticipated Completion	Actual Completion	Comments					
Task 1: Critical evaluation of codes for RCIC System modeling	03/31/15	03/31/15	Completed on schedule.					
Task 2: Code selection	03/31/15	03/31/15	Completed on schedule.					
Task 3: RCIC test data survey	09/30/15	09/30/15	Completed on schedule.					
Task 4: Model development and implementation	09/30/17	09/30/17	Completed on schedule.					
CFD	03/31/17	09/30/17	Completed with delay.					
Thermal Hydraulic Code	03/31/17	04/03/17	Completed. Determined to not be needed, therefore not performed.					
Severe Accident Code	09/30/17	09/30/17	Completed on schedule.					
Task 5: Experimental data generation	03/31/17	04/01/17	Completed with delay.					
Facility Modification	03/31/16	10/14/2016	Completed with delay.					
Experimental Testing	03/31/17	03/31/17	Completed on schedule.					
Task 6: Benchmarking against Fukushima data and test data	09/30/17	09/30/17	Completed on schedule.					
Year 1 Annual Report	01/01/16	12/31/15	Completed on schedule.					
Year 2 Annual Report	01/01/17	12/28/16	Completed on schedule.					
Final Report	12/30/17	12/23/17	Completed on schedule.					
Conference Presentations	09/30/17	09/30/17	Completed on schedule.					
Collaboration with Sandia National Laboratories	09/30/17	09/30/17	Completed on schedule.					

## 15. Changes during the Reporting Period in Project Approach

Two changes from the project approach arose in year 1 and were documented in the Year 1 Annual Progress Report. The first is that models for thermal hydraulic codes will not be developed. As the project proceeded, the team came to realize that the models developed for the severe accident codes can also be implemented into the thermal hydraulic codes. There is no benefit from development of an additional level of models.

Second, although this is not strictly a deviation from the proposal, the team has successfully installed an actual Terry turbine in the lab instead of designing and manufacturing a turbine representation in-house. Several delays were encountered in making this decision due to differing opinions from various parties on the merit of acquiring a smaller scale Terry turbine (details are provided in the Task 5 description of the Year 1 Annual Progress Report). The turbine operated as intended on the existing experimental facility. The data obtained is more representative of the RCIC System turbomachinery than could be obtained from a home-made turbine-like device.

# 16. Actual or Anticipated Problems or Delays

Work on the model development tasks was delayed due to the inability of the PI to recruit a second graduate student for the first year of the project. The award was announced within a few weeks of the start of the fall 2014 semester. Being so close to the new school year, there were no available graduate students who were suitable for this program. The second student for the modeling tasks began on the project in September 2015, a year into the project.

The completion of experimental facility modifications was delayed due to extra time needed for turbine refurbishment. The facility modifications task is noted in Section 14 as being completed late and was reported as delayed on the PICS:NE project reporting site.

# 17. Absence or Changes of Key Personnel

The Sandia National Laboratories co-PI changed from Jesse Phillips, the co-author of the proposal, to Kyle Ross. This change occurred after proposal submittal and prior to project initiation.

### 18. Product Produced or Technology Transfer Activities

#### 18.1 Publications

- Beeny, B. A., <u>Computational Multiphase Fluid Dynamics Analyses and Systems-Level Model Development for a Reactor Core Isolation Cooling System Terry Turbine, Ph.D. Dissertation, Department of Nuclear Engineering, Texas A&M University, College Station, 2017.</u>
- Luthman Jr., N. G., <u>Evaluation of Impulse Turbine Performance Under Wet Steam Conditions</u>, Master's Thesis, Department of Nuclear Engineering, Texas A&M University, College Station, 2017.
- Strater, Z., <u>Reactor Core Isolation Cooling Pump Performance in Multiphase Conditions</u>, Master's Thesis, Department of Nuclear Engineering, Texas A&M University, College Station, 2017.

Future journal papers are expected.

#### 18.2 Networks or collaborations fostered

As a result of this project, the PI and students at Texas A&M University have developed a strong network with Sandia National Laboratories. The PhD student performed his research at the lab for the last few semesters of the project and is now a full-time employee at Sandia.

The students and PI were invited to give presentations at the Terry Turbine User's Group (TTUG) meetings in 2016 and 2017. TTUG is an industry group that is hosted by the Electric Power Research Institute (EPRI). These meetings were valuable networking opportunities with the industry and provided valuable practical feedback on the Texas A&M University research efforts. In particular, the industry representatives gave important feedback on whether the ZS-1 turbine would be appropriate for this project.

#### **19. Project Deliverables**

For projects involving computer modeling, provide the following information with the final report:

- Model description, key assumptions, version, source and intended use;
- Performance criteria for the model related to the intended use; b.
- Test results to demonstrate the model performance criteria were met (e.g., code c. verification/validation, sensitivity analyses, history matching with lab or field data, as appropriate);
- Theory behind the model, expressed in non-mathematical terms; d.
- Mathematics to be used, including formulas and calculation methods; e.
- Whether or not the theory and mathematical algorithms were peer reviewed, and, if so, f. include a summary of theoretical strengths and weaknesses;
- Hardware requirements; and g. h.
- Documentation (e.g., user guide, model code).

For items a, through f., please refer to the descriptions in earlier chapters of Tasks 4 and 6.

For items g. and h., please refer to the Sandia MELCOR website for MELCOR hardware requirements and documentation and the STAR-CCM+ manuals for STAR-CCM+ hardware requirements and documentation.